

MODELING OF MACROSCOPIC ANISOTROPIES DUE TO SURFACE EFFECTS IN MAGNETIC THIN FILMS AND NANOPARTICLES.

by

Rocío Yanes Díaz

Advisor: Oksana Fesenko Morozova
Tutor: Farkhad Aliev

A THESIS SUBMITTED TO UNIVERSIDAD AUTÓNOMA DE MADRID
FOR THE DEGREE OF
DOCTOR EN CIENCIAS FÍSICAS
DEPARTAMENTO FÍSICA DE LA MATERIA CONDENSADA
MARCH 2011



Departamento de Física de la Materia Condensada

Except where acknowledged in the customary manner, the material presented in this thesis is, to the best of my knowledge, original and has not been submitted in whole or part for a degree in any university.

Rocío Yanes Díaz

Es necesario esperar, aunque la esperanza haya de verse siempre frustrada, pues la esperanza misma constituye una dicha, y sus fracasos, por frecuentes que sean, son menos horribles que su extinción.

Samuel Johnson

Contents

Resumen	ix
1 Introduction	1
1.1 Magnetic nanoparticles and thin films	1
1.2 Size effects in nanomagnets	3
1.3 Surface effects in nanomagnets	5
1.4 The magnetic anisotropy	7
1.4.1 Magneto-crystalline anisotropy	8
1.4.2 Surface magnetic anisotropy	9
1.4.3 The shape magnetic anisotropy	12
1.5 Experimental approach	13
1.5.1 Effective and surface anisotropies	13
1.5.2 Surface anisotropy and thin films magnetism	15
1.6 The challenge of modeling of magnetic nanoparticles and thin films	17
1.7 About this thesis	19
2 Multi-spin nanoparticle as an effective one spin problem	21
2.1 Introduction	21
2.2 Model	22
2.2.1 Shape and surface of nanoparticles	22
2.2.2 Localized spin (atomistic or Heisenberg) model	23
2.3 Analytical background	24
2.3.1 Second-order surface-anisotropy energy \mathcal{E}_2	25
2.3.2 First-order surface-anisotropy energy \mathcal{E}_1	27
2.3.3 Mixed contribution to the energy \mathcal{E}_{21}	27
2.3.4 Effective one spin problem (EOSP) approximation	28
2.4 Numerical method	29
2.5 Effective energy landscapes of spherical nanoparticles	30
2.6 Effective energy landscapes of elongated nanoparticles	35
2.7 Effective energy landscape of an octahedral nanoparticle	36
2.8 Effective energy landscape in cobalt nanoparticle	38
2.9 Conclusions	43

Conclusiones	44
3 Energy barriers of magnetic multispin nanoparticles with Néel surface anisotropy	45
3.1 Motivation	45
3.1.1 Phenomenological expression for the effective anisotropy constant in a system with surface anisotropy	46
3.2 Energy barriers from the effective one spin problem (EOSP)	47
3.3 Dependence of the energy barrier on the value of the surface anisotropy constant k_s	49
3.4 Dependence of the energy barrier on the system size	52
3.5 On the applicability of the formula $\mathcal{K}_{\text{eff}} = \mathcal{K}_\infty + 6\mathcal{K}_s/D$	54
3.6 Modeling of energy barriers in cobalt nanoparticle	56
3.7 Conclusions	59
Conclusiones	60
4 The constrained Monte Carlo method and temperature dependence of the macroscopic anisotropy in magnetic thin films	61
4.1 Motivation and introduction	61
4.2 The constrained Monte Carlo method	64
4.2.1 Algorithm	64
4.2.2 Free energy and restoring torque	65
4.2.3 Numerical procedure	66
4.2.4 Tests of the method	68
4.3 Temperature dependence of macroscopic anisotropy in thin films with Néel surface anisotropy	74
4.3.1 The temperature dependence of the total effective anisotropy in thin films with surface anisotropy	74
4.3.2 Temperature dependence of the effective surface anisotropy in thin films	77
4.3.3 Modeling the effect of the anisotropy re-orientation due to the surface effects	80
4.3.4 The scaling of the macroscopic anisotropy with the magnetization	83
4.4 Conclusion	86
Conclusiones	87
5 Temperature dependence of the surface anisotropy in nanoparticles	89
5.1 Introduction	89
5.2 Temperature dependence of macroscopic anisotropy in magnetic nanoparticles	90
5.2.1 Temperature dependence of the effective anisotropies in nanoparticle with sc lattice structure	90

5.2.2	Temperature dependence of the effective anisotropies in nanoparticles with fcc lattice structure	93
5.2.3	Scaling exponent	96
5.3	Conclusions	98
	Conclusiones	100
6	Multiscale modeling of magnetic properties of $Co \setminus Ag$ thin films	101
6.1	Introduction	101
6.2	Density functional theory	103
6.2.1	Hohenberg-Kohn theorems	103
6.2.2	Kohn-Sham scheme	103
6.2.3	Approximation for the exchange-correlation energy $E_{xc}[n]$	104
6.2.4	Screened Korringa-Kohn-Rostoker Green's function method	105
6.3	"Ab-initio" modeling of bulk Co and its interfaces	106
6.3.1	The studied system	107
6.3.2	Work function	109
6.3.3	Spin and orbital moments	110
6.3.4	Exchange interactions	114
6.3.5	Magneto-crystalline anisotropy energy	123
6.4	Temperature-dependent macroscopic properties	129
6.4.1	Magnetostatic interaction	130
6.4.2	Implementation of the exchange tensor interaction	131
6.4.3	Temperature-dependent magnetization	132
6.4.4	Temperature-dependent anisotropy	132
6.5	Conclusions	134
	Conclusiones	136
A	Appendix A	139
A.1	Hamiltonian of the spin system in the adiabatic approximation	139
A.2	Contribution to total uniaxial anisotropy due to "two-site" anisotropy	140
A.3	Determination of one-site anisotropy energy	141
	Bibliography	145
	List of Publications of R. Yanes	161
	Agradecimientos	163

Resumen¹

El rápido desarrollo de la nanotecnología lleva a una drástica reducción del tamaño de los dispositivos magnéticos hasta dimensiones por debajo de la micra, lo que supone un incremento de la relación entre la superficie y el volumen del sistema. Por lo tanto, es lógico suponer que los efectos de superficie en sistemas de dimensiones tan reducidas serán muy relevantes y afectarán al comportamiento magnético global de múltiples formas.

Dentro de los sistemas magnéticos de escala nanoscópica cabe destacar las nanopartículas y las películas ultra-delgadas por sus interesantes propiedades. Estos sistemas pueden presentar una anisotropía de superficie elevada, además de otros efectos de superficie como: reducción de la imanación de saturación, aumento del momento orbital, modificación de la interacción de canje en la superficie, relajación de la red cristalina, oxidación, etc. Múltiples trabajos experimentales demuestran cómo el comportamiento magnético de los sistemas nanoscópicos cambia con respecto al material masivo. Por ejemplo, las nano-partículas magnéticas presentan anisotropía de superficie elevada lo que frecuentemente conduce a un aumento de su temperatura de bloqueo en comparación con el valor correspondiente a los parámetros de volumen.

El trabajo realizado en esta tesis está enfocado en la investigación de los efectos de superficie en sistemas magnéticos, empleando para ello las simulaciones numéricas.

Las simulaciones numéricas ocupan un lugar importante a la hora de determinar el comportamiento de complejos y diversos sistemas magnéticos. Los cálculos numéricos permiten conocer la distribución de la imanación a escala nanométrica en relación con las propiedades intrínsecas y extrínsecas de las nano-partículas y películas delgadas.

Los métodos de simulaciones utilizados en este trabajo están englobados dentro del esquema de simulaciones multiescala que pretenden enlazar cálculos a diferentes escalas.

En esta tesis en concreto se han trabajado en los siguientes temas:

a) *Estudio de partículas individuales como sistemas multiespín.*

Para partículas con diámetros de unos pocos nanómetros es de esperar que la influencia de los efectos superficiales produzca alguna no colinealidad en la configuración de los espines, dependiente de la magnitud de la anisotropía superficial. Estas no colinealidades producen unas anisotropías efectivas, de modo que

¹Las conclusiones en castellano se hayan después de cada capítulo

podemos describir una nanopartícula multiespín como una macroespín pero con anisotropías adicionales. La metodología está basada en el Hamiltoniano de tipo Heisenberg y en el método de multiplicadores de Lagrange para mapear el comportamiento multiespín a un solo macroespín. La anisotropía de superficie fue modelada aplicando un modelo de Néel. Como parte de este estudio se obtuvieron los paisajes de energía (dependencia angular de la energía magnética del sistema con respecto a la dirección de la imanación) de nanopartículas magnéticas. Se estudiaron los paisajes de energía para nanopartículas con diferentes formas, redes cristalinas, anisotropía magnetocristalina así como la intensidad de la anisotropía de superficie. Además se estudiaron las barreras de energía extrayéndose de ellas los valores de la anisotropía efectiva del sistema. Posteriormente se analizó la dependencia de la anisotropía efectiva con el tamaño del sistema y el rango de validez de la fórmula fenomenológica $K^{eff} = KV + \frac{6}{D}KS$ que relaciona la anisotropía efectiva con la anisotropía de volumen, la anisotropía de superficie y el diámetro de la nanopartícula. En concreto, motivados por el trabajo experimental del grupo del Dr. J. Bartolomé modelamos nanopartículas de cobalto con diversos recubrimientos Al_2O_3 , Au, Cu, examinando los paisajes de energía, las barreras de energía y las anisotropías efectivas de dichas nanopartículas, al variar su forma y la fuerza de la anisotropía de superficie.

b) *Estudio del comportamiento de la anisotropía magnética con la temperatura.*

En esta sección se estudió cómo se ve afectada la anisotropía magnética efectiva por la temperatura en nano-partículas y películas ultra-delgadas. Es bien conocido que en un sistema cuya anisotropía efectiva es de carácter uniaxial o cúbico ésta se comporta siguiendo la ley de Callen-Callen, al menos a bajas temperaturas. No obstante, en sistemas más complejos con efectos de superficie importantes, como es el caso de las láminas delgadas o las nano-partículas magnéticas, este comportamiento no está claro. Con el fin de analizar la dependencia de la anisotropía magneto-cristalina efectiva con la temperatura, se llevaron a cabo diversas simulaciones magnéticas utilizando el algoritmo de Monte Carlo con ligadura (CMC) desarrollado recientemente conjuntamente con el Dr. P. Asselin (Seagate Technology) en el curso de este trabajo de tesis. Se analizó la dependencia térmica de la anisotropía efectiva en láminas delgadas y nanopartículas (esféricas y octaedrinas truncadas) con diferentes configuraciones de los ejes fáciles del sistema. Se observó que cuando nuestro sistema en estudio presenta competición entre la anisotropía de superficie y la magnetocristallina, se puede producir por efecto de la temperatura una reorientación de ejes fáciles del sistema.

c) *Estudio multiescala de láminas magnéticas delgadas.*

Desafortunadamente, en este momento una descripción cuántica a todas las escalas (temporal, espacial, etc.) resulta imposible. Adicionalmente, los modelos "ab-initio" no pueden calcular directamente las dependencias térmicas de los parámetros macroscópicos tales como anisotropías efectivas. Sin embargo, los cálculos "ab-initio" pueden obtener los parámetros magnéticos intrínsecos. En este contexto, se han realizado modelizaciones multiescala con el fin de extraer parámetros atomísticos y parametrizar el Hamiltoniano clásico. Dentro de este esquema se han estudiado las propiedades magnéticas de láminas delgadas de Co ((100) y (111)) y Co/Ag (con diferente interfaz (100) o (111)) mono o bicapas de Ag. De los cálculos "ab-initio" se extrajeron parámetros locales tales como anisotropía, momento magnético y canje para posteriormente calcular la anisotropía efectiva macroscópica de la superficie y su dependencia térmica.

1

Introduction

1.1 Magnetic nanoparticles and thin films

The rapid development of nanotechnology leads to a drastic reduction in the size of magnetic devices to dimensions below one micron and thus to an increase in the ratio between the surface and the volume of the system. It is clear that the surface effects in such low dimensional systems will become very important and will affect the overall magnetic behavior in multiple ways. Within the nanoscale magnetic systems, nanoparticles and ultra-thin films are examples of systems where surface effects play an important role in their magnetic properties.

Ultra-thin magnetic films are widely used for technological applications such as magnetic recording or micro-electromechanical applications. The use of magnetic multilayers has offered multiple applications such as magnetic recording heads and sensors. The magnetic layers in magneto-resistive heads or spin valves for example, have thickness below than 10 nm. The ultra-thin films are normally grown on non-magnetic substrates and their coating is a widely used method to protect them from oxidation. Both under and top layers can change the structural and magnetic properties of a magnetically active thin film and allow the engineering of its properties.

Nanoparticles have various important technological applications such as in high-frequency electric circuits for mobile phones [1]; for magnetic refrigerators; data storage devices [2, 3] or in biomedicine [4, 5] (for drug delivery, imaging, sensing and hyperthermia for tumor therapy).

The application of magnetic nano-particles in **data storage devices**, has been a

strong driven force for the development of new methods for growing well-defined magnetic nanoparticles with controllable sizes ranging from a few nanometers up to tens of nanometers. The magnetic storage requires that each magnetic particle behaves as a mono-domain particle and that its magnetic state is thermally stable and switchable. This means that it does not easily lose its magnetization direction once the external magnetic field is removed and that the field necessary to reverse the magnetization of the particle does not exceed the field produced by the read head of the hard disk. Also it is necessary to consider the effect of the interactions between magnetic particles on the signal-noise-ratio (SNR).

The magnetic thermal stability and the blocking temperature are defined by the relevant magnetic energy barrier. The magnetic energy barrier is proportional to the nanoparticle diameter and the macroscopic magnetic anisotropy value. Additional possibility to control the energy barrier is provided by the surface modification, for example, the oxidation of nanoparticle may increase the energy barrier via the exchange-bias effect [6, 7]. Magnetic nanoparticles embedded in non-magnetic matrices, such as Co in Au, Ag or Cu have also been reported to have a larger blocking temperature [8–10], as compared to the value given by pure Co. The combination of materials with different magnetic properties, as in the case of core-shell nanoparticles, allows to control the energy barrier almost independently from the coercive field [7, 11, 12].

In the case of biomedical applications we have to take into account diverse factors: we must not only evaluate the magnetic behavior of the system but also its bio-compatibility, specifically if we work with "*in vivo*" (inside the human body) applications. The nanomagnets also can be used in biomedical applications "*in vitro*" (out of the body) which main use is in diagnostic. Additionally, for biomedicine applications, nanoparticle's surface should be functionalized to act in a biological media or to deliver the drugs. This is known to alter the magnetic properties.

Successful application of magnetic nanoparticles in the areas listed above is strongly dependent on the stability of the particle under a range of different conditions. Additionally it is necessary that the nanoparticles have a narrow shape and size distributions, which implies sophisticated techniques of nanoparticle growth. Magnetic nanoparticles are also very often embedded in non-magnetic matrices to avoid oxidation.

In principle, we can divide the preparation of nanoparticles into two groups, depending on the growth strategy used:

Top-down These methods start from the bulk material which is decomposed into increasingly smaller fragments. The method includes widely used deposition technique such as sputtering, laser ablation, etc.

Bottom-up These methods grow nanoparticles via the nucleation of numerous atoms, obtaining particles with a diameter of 1 to 50 nm and narrow size distribution. The typical example of this kind of growth techniques is the chemical synthesis.

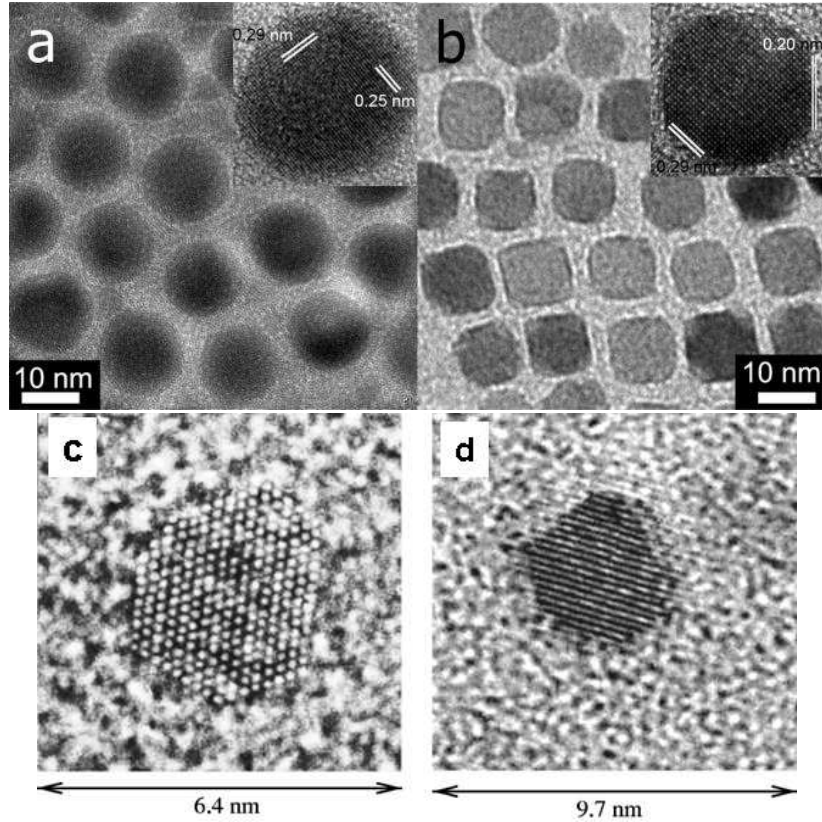


Figure 1.1: Transmission electron microscope (TEM) micrographs of (a) spherical and (b) cubic $\gamma - Fe_2O_3$ nanoparticles. The insets show high resolution transmission electron microscope (HRTEM) images of the respective nanoparticles. (c) HRTEM image of a cobalt nanoparticle along a (110) (d) HRTEM observation of an iron nanoparticle along a (110) direction. (Images extracted from [13] (a-b) and from [14] (c-d))

Depending on the preparation method and chemical environment the nanoparticles with different shapes such as spheres, octahedra, cubes, etc. are possible to prepare. The shape of the nanoparticle also affects its magnetic properties. In Fig. 1.1 we show different examples of magnetic nanoparticles: spherical and cubic nanoparticles of $\gamma - Fe_2O_3$ and octahedral nanoparticles of Co and Fe.

The magnetic properties of nanoparticles could present some differences with respect to those of the bulk material principally by several key issues: the shape, the size and the surface effects [15, 16].

1.2 Size effects in nanomagnets

The finite size effects could yield a modification of the magnetic properties of the system, when one of its dimensions becomes comparable to the exchange correlation

length of the system. The most important finite size effects in nanoparticles are the single domain limit and the super-paramagnetic limit.

The macroscopic materials can present a null net magnetization in the absence of applied magnetic field, inclusive if the material is ferromagnetic, it is due to the fact that when the system size is above a certain value, the division of the system into magnetic domains is energetically favorable. If the size of the system is under a certain cutoff, denominated single domain radius (R_{sd}), the system prefers a mono-domain state. This phenomenon was initially predicted by Frenkel and Doefman [17]. The single domain radius depends on the magnetic parameters of the system (exchange parameter, saturation magnetization, anisotropy constant) and typically lies in the range of a few tens of nanometers.

If the size of the system continues to decrease then the nanoparticle becomes super-paramagnetic (SP), due to thermal fluctuations and the reduction of the energy barrier of the system. In this state a magnetic particle presents a large magnetic moment and behaves like a giant paramagnetic moment with a fast response to an applied magnetic field and negligible coercivity and remanence.

Thermal measurements have become an important part of the characterization of magnetic nanoparticles systems. Often these measurements include a complex influence of interparticle interactions. However, in other cases, measurements on dilute systems can provide information on individual particles. The results show that even in these cases the extracted information is not always consistent with the approximation picturing the particle as a macroscopic magnetic moment, and this is usually attributed to surface effects.

If the nanoparticle size decreases more, the surface effects start to play a important role and deviations from the collinear spin arrangement appear. When the magnetic properties of magnetic nanoparticles are dominated by the surface effects, the ideal model of a macro-spin formed by all the spins of the particle pointing in the direction of the anisotropy easy axis could be no more valid. The schematic representation of the size effects in nanoparticles is presented in Fig. 1.2.

Finite size effects also have important consequences in the magnetization behavior of thin films. Indeed, when the film thickness is smaller than the exchange correlation length, the magnetization is homogeneous through the thin film thickness. In these conditions the magnetostatic interactions tend to place the magnetization in-plane competing with the surface anisotropy effects.

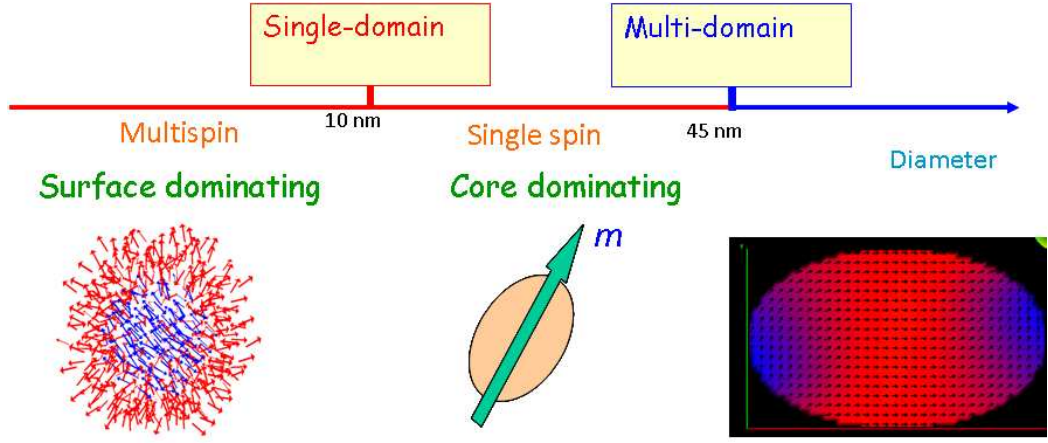


Figure 1.2: Schematic representation of the dependence of the magnetic behavior of the nanoparticle on its diameter.

1.3 Surface effects in nanomagnets

In ferromagnetic bulk materials, the magnetostatic interaction and bulk magneto-crystalline anisotropy are the principal sources of the anisotropy, but when we are working with nano-scale systems, such as thin films, nanoparticles, wires, etc. strong surface effects are expected. As the particle size decreases, the surface and interface effects are enhanced due to the increase of the surface/volume ratio. The surface effects can yield different magnetic properties of a low-dimensional system with respect to the typical bulk ones. The principal surface effects will be briefly discussed in below:

- **Lattice relaxation:** Normally the bond-breaking at the boundaries of the nanomagnet yields the structural relaxation of the system. The atomic positions on the surface of nanoparticle have been reported to correspond to lattice expansion or the contrary contraction [18]. Also nanoparticles embedded in different matrices experience a mismatch of lattice parameters on the surface and the relaxation of the internal lattice structure. Additionally thin films grown on substrates can show large strain effects.
- **Nanoparticles shape and surface reconstruction:** Depending on the chemical environment, nanoparticles with different shapes such as spherical or more exotic cubes or needles can be synthesized [13, 19]. Nanoparticles are often reported in the octahedral and dodecahedral shape [14, 20]. The existence of different surfaces and vertices obviously change local properties on the surface.
- **Charge transfer:** On the surface of nanoparticles we can find defects such as cations, which can promote charge transfer and change the magnetic character of the surface [21]. The charge transfer in the case of magnetic nanoparticles

coated with polymers is also known to occur [22], as well as in nanoparticles with organic molecules or embedded in different non-organic matrices.

- **Oxidation:** Metallic nanoparticles are chemically active and are easily oxidized in air, resulting generally in a reduction or even loss of the total magnetic moment. For instance, cobalt is a typical ferromagnetic (FM) material, nevertheless its oxide CoO has an anti-ferromagnetic (AFM) character [23], in a similar way as Ni and NiO [24]. Additionally, when the surface of Co or Ni nanoparticles is oxidized, we find a system with two different magnetic phases which could lead to new magnetic phenomena. For example, this kind of a composite material (FM-AFM or vice-versa) could present the exchange bias effect [25–27].
- **Variation of the magnetic moment:** In ferromagnetic systems the magnetic moment may be enhanced by reducing the dimensionality [28]. Magnetic moment enhancement with decreasing size has been observed experimentally and theoretically in metallic nano-clusters of Fe, Co, Ni, etc. [29–32]. Therefore in systems like metallic ferromagnet nanoparticles where a large fraction of the spins belong to the surface, one could expect an increment of the system's magnetization.
- **Surface spin disorder:** A reduction of the saturation magnetization, M_s , has been observed experimentally in nanoparticles. Initially, this reduction has been explained by models which postulated the existence of a "dead" magnetic layer at the surface [33], however there are other theories that relate the origin of that effect with the existence of a canted spin configuration at the surface [34], or the spin-glass-like spin state [35]. But up to now, the origin of the canting of the spins in fine particles is an object of a continuing discussion [15].
- **Surface anisotropy** Another surface-driven effect is the enhancement of the magnetic anisotropy with decrease of the system size [32, 36, 37]. That increment is assumed to be originated by the anisotropy at surface and has been detected experimentally in nanoparticles of Co, Fe, etc. [8, 10, 38]. Also a systematic study with different coatings has revealed that they can influence to the effective anisotropy.
- **Variation of the exchange interaction at surface:** The variation of the exchange interaction energy at surface has been reported from a theoretical point of view in thin films [39, 40] and also has been observed in magnetic nanoparticles. For example, $Ni_{1-x}Cu_x$ material has shown a drop of the Curie temperature of the system as the concentration of Cu is increased. Such a decrease of T_c is associated to the variation of the exchange interaction strength at the surface [41].

In practice it is impossible to separate these effects and consequently, all of them are normally embedded in the phenomenological concept of the "surface anisotropy".

The detailed theoretical description of real experimental situation is almost impossible due to competition of many effects and large dispersion of individual nanoparticles properties.

1.4 The magnetic anisotropy

It is known that the magnetization \mathbf{M} tends to orient preferentially along one or several axes in magnetic solids. The magnetic anisotropy energy is defined as the energy term that describes the dependence of the internal energy on the direction of the magnetization, and it may be originated by the crystalline electric field of the solid, by the shape or surface of the magnetic body, by mechanical stress etc. Usually the magnetic anisotropy energy has the symmetry of the crystal structure of the material and it is invariant to the inversion of the magnetization. These facts mean that the magnetic anisotropy energy must be an expansion of even functions of the angles enclosed by the magnetization and the magnetic axes. Hereafter we present the expressions of the magnetic anisotropy energy density (E_{ani}) for the most frequent cases:

Cubic symmetry We denote $\alpha_i; i = 1, 2, 3$ as the cosines of the angles between the magnetization and the axes X;Y;Z parallel to the fourfold axes. Then E_{ani} has the following form:

$$E_{ani} = K_1(\alpha_1^2\alpha_2^2 + \alpha_1^2\alpha_3^2 + \alpha_3^2\alpha_2^2) + K_2\alpha_1^2\alpha_2^2\alpha_3^2 + \dots \quad (1.1)$$

Tetragonal symmetry If we denote θ and φ as the angles in polar coordinates, and Z as the axis parallel to the sixfold axis [001], then E_{ani} has the following form:

$$E_{ani} = K_1 \sin^2(\theta) + K_2 \sin^4(\theta) + K_3 \sin^6(\theta) + K_4 \sin^6(\theta) \cos(6\varphi) + \dots \quad (1.2)$$

Quadratic symmetry In this symmetry there is a fourfold axis [001], and Z is the axis parallel to that axis. Then E_{ani} has the following form:

$$E_{ani} = K_1 \sin^2(\theta) + K_2 \sin^4(\theta) + K_3 \sin^4(\theta) \cos(4\varphi) + \dots \quad (1.3)$$

Uniaxial symmetry The first terms in the expansion of E_{ani} in the case of the tetragonal, rhombohedral and quadratic symmetries are the same. Usually the next term in the expansion is at least one order of magnitude smaller. Then if we restrict the expansion to the first term, we obtain that E_{ani} is of the second order and only depends on the angle between the magnetic moment and the axis of the highest symmetry θ , in the following form:

$$E_{ani} = K_1 \sin^2(\theta). \quad (1.4)$$

This kind of magnetic anisotropy can also be found in amorphous material submitted to stress or isotropic magnetic material annealed under the presence of a magnetic field.

The values above [$K_i(i = 1, 2, 3, 4\dots)$] are the anisotropy constants with dimension [energy/volume]. These parameters depend on the temperature and material and they can range from around 100 erg/cm^3 in soft materials, passing through $10^4 - 10^5 \text{ erg/cm}^3$ for 3d metals of cubic symmetry like Ni, Fe, etc., to $10^7 - 10^8 \text{ erg/cm}^3$ in some rare earth alloys and $L1_0$ compound such as FePt and CoPt. In practice, K_i is usually derived from experiments (ferromagnetic resonance, magnetization curve, etc) as an empirical constant.

The total magnetic anisotropy can be the result of several contributions: the magneto-crystalline anisotropy (MCA), surface anisotropy, shape anisotropy, magnetostriction anisotropy, exchange anisotropy etc.

1.4.1 Magneto-crystalline anisotropy

Magneto-crystalline anisotropy (MCA) is one of the most important energy contributions in magnetic materials and it is generated by the atomic structure and bonding in the magnetic material. Attempts to understand its microscopic origin have been taking place since many years ago. As proposed by Van Vleck [42], the origin to the MCA energy is the spin-orbit coupling interaction (SOC), which is the term that links the spatial and spin parts of the wave functions. In the case of a central potential $V(r)$, its interaction is given as:

$$\mathcal{H}_{SO} = \xi(r)\mathbf{L} \cdot \mathbf{S} \quad (1.5)$$

$$\xi(r) = \frac{1}{4m^2c^2r} \frac{dV(r)}{dr} \quad (1.6)$$

where m is the mass of the electron, c is the speed of light in the vacuum, r is the distance from the nuclei, \mathbf{L} and \mathbf{S} are orbital and spin moments. We would like to note that this form of the SOC term has been used in almost all cases. Although the potential ($V(r)$) is not generally central, nevertheless as $\frac{dV(r)}{dr}$ has its maximum contribution close to the nuclei, where $V(r)$ is approximated as the central potential, thus the approximation of SOC (1.5) is generally accepted.

Theoretically the magneto-crystalline anisotropy is determined from the evaluation of the difference of the system's energy when the magnetization is orientated along the easy and hard axes. If other contributions such as the magnetostatic energy can be neglected, then the MCA is given by the anisotropy due to the spin-orbit coupling:

$$\Delta E_{SO} = \langle \mathcal{H}_{SO} \rangle_{hard} - \langle \mathcal{H}_{SO} \rangle_{easy} = \zeta[\langle \mathbf{L} \cdot \mathbf{S} \rangle_{hard} - \langle \mathbf{L} \cdot \mathbf{S} \rangle_{easy}] > 0 \quad (1.7)$$

where $\zeta = \langle \xi(r) \rangle$ is the spin-orbit coupling constant. This way the magnetization of the system in the hard direction requires an input of energy into the system. The principal difficulty in the study of the MCA is its small size, for example in transition metals MCA is of the order of μeV , which is usually in the limit of accuracy of theoretical calculations.

1.4.2 Surface magnetic anisotropy

As we have mentioned previously, the magnetic anisotropy can be increased when the size of the system is reduced. It is usually explained by the existence of the surface anisotropy different to the bulk one.

Néel in 1954 was the first to suggest the existence of this kind of anisotropy. After that many experimental evidences have corroborated that claim [43], and there exist multiple works on calculation of the surface anisotropy from the first principles [44–46]. An important point that we should take into account is that for small particles or clusters or ultrathin films where the number of spin at surface is large, the surface anisotropy can easily dominate the bulk one, especially in cubic materials.

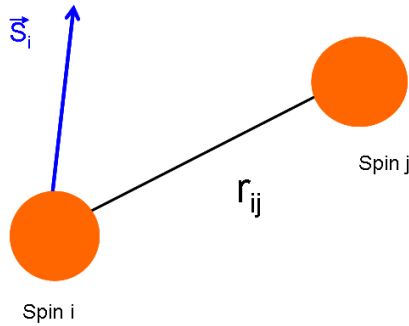


Figure 1.3: Shematic drawing illustrating the Néel pair model.

The Néel model of the surface magnetic anisotropy

The modeling of the surface anisotropy contribution is a complex field of research. Néel proposed a phenomenological model of the surface anisotropy called after that the "Néel surface anisotropy (NSA) model". The model assumes an origin of the anisotropy basing on the lack of the atomic bonds on the surface of a crystal. The surface anisotropy contribution is described as a pair-interaction of spins in the following way:

$$\begin{aligned} \mathcal{H}_i^{NSA} &= \frac{L(r_{ij})}{2} \sum_{j=1}^{z_i} (\vec{s}_i \cdot \vec{e}_{ij})^2, \\ \vec{e}_{ij} &= \frac{\vec{r}_{ij}}{r_{ij}}, \\ \vec{r}_{ij} &= \vec{r}_i - \vec{r}_j. \end{aligned} \quad (1.8)$$

Here z_i is the number of nearest neighbors of the surface spin i , (known as the coordination number), \vec{s}_i is a unit vector pointing along the magnetization direction, r_{ij} is the distance between spin i and j , \vec{e}_{ij} is the unit vector connecting the spin i to its nearest neighbor j , the factor $1/2$ is added in order not to count twice the pair interaction and

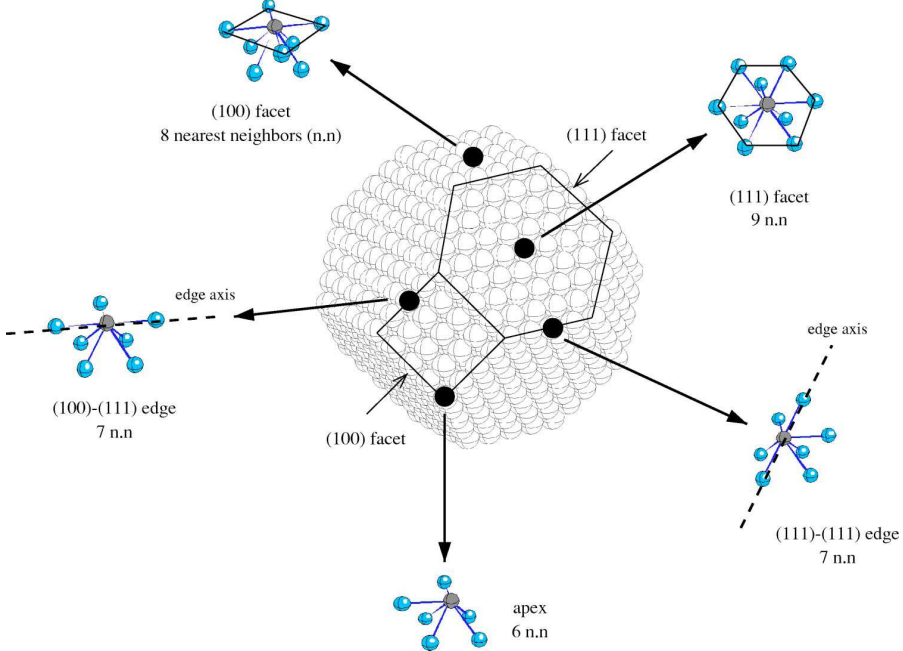


Figure 1.4: The different environment of the atoms in a fcc octahedral nano-particle (from Ref. [14]).

$L(r_{ij})$ is the pair-anisotropy coupling constant, also called the Néel surface anisotropy constant, which depends on the distance between spins [47], see Fig. 1.3.

If $L < 0$ the surface anisotropy is locally in-plane and is out-of-plane if $L > 0$. L depends on the interatomic distance r_{ij} (in the following we will omit the subindex i and j) according to the expression:

$$L(r) = L(r_0) + \left(\frac{dL}{dr} \right)_{r_0} r_0 \eta \quad (1.9)$$

where r_0 is the unstrained bond length and η is the bond strain.

$L(r_0)$ and $r_0 \left(\frac{dL}{dr} \right)_{r_0}$ depend on the magnetostriction and elastic constants, therefore $L(r)$ also depends on these magnitudes. All these relations make obvious that the NSA depends on the orientation of the local magnetization with respect to the surface, the orientation of the surface with respect to the crystalline axes, and the loss of neighbors. This way, atoms located at different positions at the surface can possess a different surface anisotropy value. For example, in Fig. 1.4 (from Ref. [14]) we show the neighborhood of atoms located at different positions in a truncated octahedral nanoparticle, which have different directions of the local easy axes and strengths of the surface anisotropy [14].

Within this model the magnetic surface anisotropy of a given atom can be calculated summing pair-interactions with its nearest neighbors. Despite the fact that this model

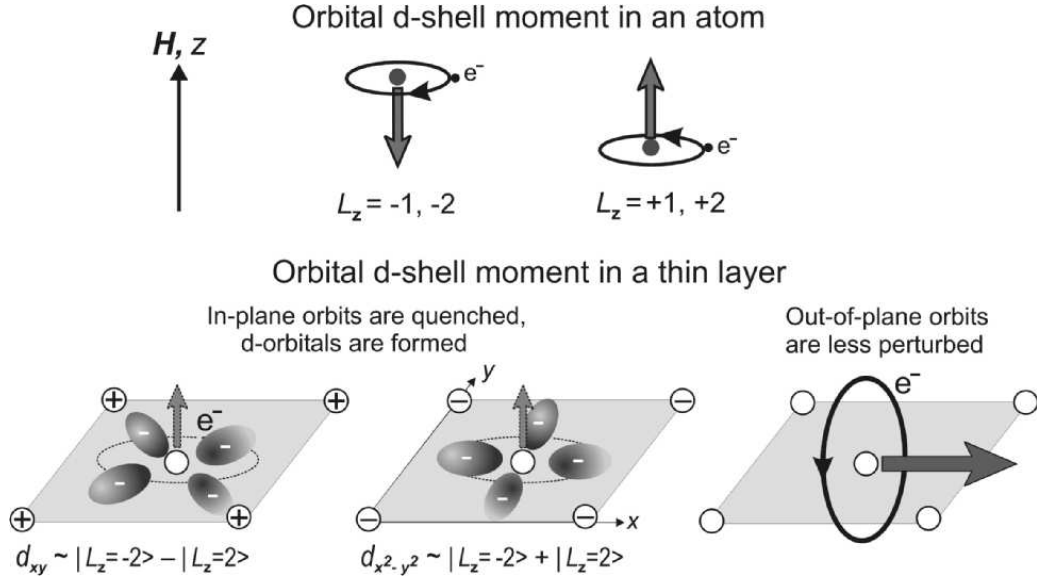


Figure 1.5: Illustration of the directional quenching of the orbital moment of an atom by the ligand field effects in a thin film (from [48]).

provides an adequate description of the symmetry of the surface magnetic anisotropy it doesn't provide a physical understanding of its origin since it has a phenomenological character. With the aim to go deeper in the physical origin of the magnetic surface anisotropy we have to consider the effects of the spin-orbit coupling and the ligand field.

Magneto-crystalline anisotropy: Bruno model

A relatively simple model that takes into account the bonding and magnetic moment is the Bruno model of the magnetic anisotropy of transition metals [45]. Following his concept, MCA for transition metal elements can be related with the anisotropy of the orbital magnetic moment under certain conditions in such way that:

$$\Delta E_{SO} = \zeta [\langle \mathbf{L} \cdot \mathbf{S} \rangle_{hard} - \langle \mathbf{L} \cdot \mathbf{S} \rangle_{easy}] = \frac{\zeta}{4\mu_B} (\mu_L^{easy} - \mu_L^{hard}) > 0 \quad (1.10)$$

where $\mu_L^{hard,easy}$ is the orbital magnetic moment in the hard or easy axis. From that model we can conclude that the easy axis of the magnetization coincides with the direction which has the maximum orbital magnetic moment.

The layered thin films present an inherent in-plane/out-of-plane asymmetry in contrast to the bulk. The magneto-crystalline anisotropy values up to two orders of magnitude larger than that for the typical magnetic elements Fe, Co, Ni have been reported for layered thin films. Therefore these systems are perfect examples to study the origin of the surface anisotropy. According to the Bruno's model, the MCA is related

with the anisotropy bonding and its relation with the ligand field. To illustrate this concept we consider a d electron in a free atom and in an atom contained in a planar geometry with other four atoms which can have negative or positive charge, see Fig. 1.5. In the planar geometry the d electron suffers the effects of the Coulomb repulsion or attraction depending on the charge of its neighbors, altering its orbital with respect to the free one. This way we can see the effects on the magnetic moment due to the ligand field. We can observe a partial break of the degeneracy of the d orbital, one can group the d orbitals into in-plane and out of plane, and we may quantitatively relate the anisotropy of the orbital moment with the anisotropy of the bonding environment. The corresponding orbital moment along the normal of the bonding plane is quenched, however in the case of the moment in-plane with respect to the bond plane this is not so. Due to the loss of neighbors at the surface the orbital motion perpendicular to the bonding plane is less disturbed and the in-plane orbital momentum is unquenched. This leads to an anisotropic orbital moment and to the surface anisotropy, according to the Bruno's model.

Therefore the exchange interaction is responsible for the creation of the spin magnetic moment and the ligand field creates anisotropic orbitals. The spin and orbital moments are linked by the spin-orbit coupling and the orbital moment is locked in a particular direction. The interplay of all these factors creates the surface magnetocrystalline anisotropy.

We should have in mind that the Bruno model is illustrative and may be too simple in real situations. As it has been indicated by Andersson [49], the Bruno model could be not adequate in the analysis of magnetic systems with high spin-orbit coupling.

1.4.3 The shape magnetic anisotropy

Magnetostatic are other sources of the total magnetic anisotropy called the macroscopic shape anisotropy. This concept is clear in the case of homogeneous magnetization in a ellipsoid, where the demagnetization tensor can be introduced in such way that the demagnetization field can be defined as:

$$\mathbf{H}_D = -\mathcal{D}\mathbf{M} \quad (1.11)$$

where \mathcal{D} is the demagnetization tensor, \mathbf{H}_D is the demagnetization field and \mathbf{M} is the magnetization of the system. Thus the density magnetostatic energy can be described as:

$$E_M = 2\pi\mathbf{M}\mathcal{D}\mathbf{M} \quad (1.12)$$

If the semiaxes a , b , and c of the ellipsoid represent the axes of the coordination system the \mathcal{D} is a diagonal tensor. An arbitrary direction of the magnetization with respect to the semiaxes can be characterized by the direction cosine α_a, α_b , and α_c . The tensor

is given by:

$$\mathcal{D} = \begin{pmatrix} \mathcal{D}_a & 0 & 0 \\ 0 & \mathcal{D}_b & 0 \\ 0 & 0 & \mathcal{D}_c \end{pmatrix} \quad (1.13)$$

and the magnetostatic energy density can be written as:

$$\mathcal{E}_M = 2\pi Ms(\mathcal{D}_a\alpha_a^2 + \mathcal{D}_b\alpha_b^2 + \mathcal{D}_c\alpha_c^2). \quad (1.14)$$

For thin films, magnetostatic interaction leads to an additional anisotropy favoring the in-plane anisotropy. In the case of elongated nanoparticles, magnetostatic interactions produce an additional easy axis parallel to the long dimensions.

1.5 Experimental approach

Many techniques are available in our days to measure the magnetic properties of nanomagnets. The challenge lays in measurements of not only macroscopic properties which are generally achieved by the magnetometry measurements but in measurements of local properties at nanoscale. In the past decade several techniques have provided important measurements with the aim to understand surface effects in magnetic films and nanoparticles:

X-ray absorption magnetic circular dichroism (XMCD) This technique was pioneered by Schütz and co-workers [50]. It is based on the changes in the absorption cross section of a magnetic material and uses circularly polarized photons [51]. Through the well-known sum rules it allows to determine the relation between the orbital and the spin magnetic moments μ_L/μ_s . A big advantage of this technique is that it is element specific and it is able to identify moment orientations in ultrathin films and monolayer magnetic materials. The X-ray microscopy also allows imaging with 100 nm. resolution.

(Micro-)Superconducting Quantum Interface Device (μ) – SQUID is a powerful technique to measure the net magnetization on a nanometer-size sample [52]. In 2001 Jamet et. al. have done the first magnetization reversal study on individual Co nanoparticle ($D = 20$ nm.) using a new μ – SQUID setup. From those measurements they deduced the magnetic anisotropy magnitude [20] and that the behavior of individual nanoparticles follows the Néel-Arrhenius law [53].

1.5.1 Effective and surface anisotropies

In experimental situation and basing on macroscopic measurements, different contributions to anisotropy are difficult to distinguish and the concept of the "effective anisotropy" is used. The meaning of the concept is not clear and it is probably highly dependent on the employed experimental method, such as the magnetization work, the

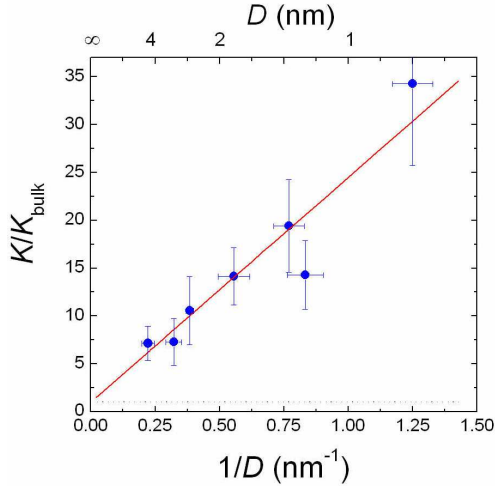


Figure 1.6: Size dependence of the effective anisotropy constant in Co nanoparticles, the line represents the fit to the expression (1.17). (from Ref.[8])

ac- susceptibility measurements, the ferromagnetic resonance, the blocking temperature, etc. It has been suggested [32, 36, 43] that the effective magnetic anisotropy energy \mathcal{K}^{eff} could be phenomenologically separated in a volume and a surface contributions and approximately obeys the relation:

$$\mathcal{K}^{\text{eff}} = K_V + K_S \cdot S/V \quad (1.15)$$

where K_V is the volume anisotropy, K_S is the "effective" surface anisotropy, S is the surface and V is the volume of the system. This means that the magnetic surface anisotropy in thin films can be determined by measuring the total magnetic anisotropy as a function of the film thickness t , showing a $1/t$ dependence [46, 54–56]:

$$\mathcal{K}^{\text{eff}} = K_V + 2K_S/t \quad (1.16)$$

The factor 2 is due to the existence of two surfaces.

In the case of spherical nanoparticles the same relation has been suggested [36], leading to the formula .

$$\mathcal{K}^{\text{eff}} = K_V + 6K_S/D \quad (1.17)$$

where D is the diameter of the nanoparticle.

We would like to emphasize that this formula has been introduced in an "ad hoc" manner, and it is far from evident that the surface should contribute into an effective uniaxial anisotropy in a simple additive manner. Actually one cannot expect K_S to coincide with the atomistic single-site surface anisotropy, especially when strong deviations from non-collinearities leading to "hedgehog-like" structures appear. The effective anisotropy \mathcal{K}^{eff} appears in the literature in relation to the measurements

of energy barriers of nanoparticles, extracted from the magnetic viscosity or dynamic susceptibility measurements. Generally speaking, the surface anisotropy should affect both the minima and the saddle points of the energy landscape in this case. It is clear that while the measurement of viscosity are related to the saddle point, the magnetic resonance measurements depend on the stiffness of the energy minima modified by the surface effects. Thus the meaning of the K^{eff} is different for different measurement techniques.

Despite its rather "ad hoc" character, this formula has become the basis of many experimental studies with the aim to extract the surface anisotropy (see, e.g., Refs. [8, 32, 57]) because of its mere simplicity.

In Fig. 1.6 we present some experimental results (from Ref. [8]) where the effective anisotropy is plotted as a function of the inverse of the diameter of Co nanoparticle (which is supposed to have a spherical shape) and is fitted to the expression of K^{eff} similar to Eq.(1.17).

1.5.2 Surface anisotropy and thin films magnetism

System	Temperature[K]	K_s [erg/cm ²]	Ref.
<i>UHV/Ni(111)</i>	300	-0.48	[58]
Cu, <i>Pd/Ni(111)</i>	300	-0.22	[58]
<i>Re/Ni(111)</i>	300	-0.19	[58]
<i>O₂/Ni(111)</i>	300	$\cong 0$	
<i>UHV/Fe(100)</i>	293	+1	
<i>Ag/Fe(100)</i>	293	+0.6	
<i>UHV/Fe(100)/Ag(100)</i>	293	$\cong 0$	
<i>UHV/Fe(100)/W(110)</i>	293	-0.5	
<i>Ag/Fe(100)/Ag(111)</i>	77 - 293	$\cong 0$	
<i>Au/Fe(100)/Au(111)</i>		> 0	
<i>UHV/Fe/Cu(100)</i>	100	+1	
<i>Cu/Fe(100)/Cu(100)</i>		+0.5	
<i>Au/Co/Au(111)</i>	293	+0.5	
	5	+0.7	
<i>Pd/Co/Pd(111)</i>	293	+0.26	
<i>UHV/Co/Cu(100)</i>	293	≥ 0	

Table 1.1: Experimental data for magnetic surface anisotropy of ferromagnetic transition metals. Data obtained of Ref. [54]

The experimental results show different values of the surface anisotropy in different systems: pure transition metals Ni [59], Fe [55], Co [46, 54, 56, 60] on various substrates,

orientations and overlayers or alloys such as MnSb [61]. The data are shown in Table 1.1.

In general, the easy axis of the magnetization in thin film is determined by the competition between the magnetocrystalline anisotropy, the magnetostatic energy and the surface anisotropy. The experimental progress in growing epitaxial magnetic thin films and multilayer down to monolayer thickness has revealed a wealth of interesting phenomena, such as the perpendicular magnetic anisotropy (PMA), which consist of a preference for the magnetization to lie along the normal to the plane of the magnetic film. The use of a magnetic system that presents PMA as a magnetic storage media has been shown as a good strategy to improve the storage density.

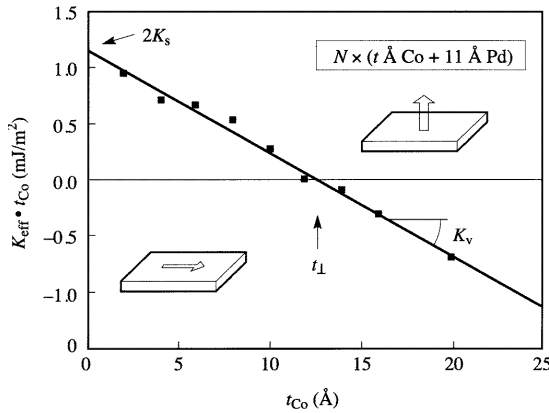


Figure 1.7: $K^{eff} \cdot t_{Co}$ of a Co thin film layer in a Co/Pd multilayer as a function of the Co thickness t_{Co} . (from Ref. [62]).

The balance between different anisotropies can be changed as the temperature or global thickness of a thin films are varied [56, 63, 64], leading to a re-orientation of the global anisotropy axis. A change from perpendicular orientation of the easy axis for film thickness (t) below a few monolayers to an in-plane orientation for larger t has been reported, for example in Fe/Ag(001) [65] and Fe/Cu(001) etc. [66]. A contrary crossover from in-plane to perpendicular orientation of the easy axis has been reported for example in Ni/Cu(001) [63]. A detailed analysis of the magnetization near the re-orientation transition in ultrathin films has shown that the surface magnetization pattern can be very complex, consisting, for example, of perpendicularly magnetized stripes [67–69] or ripple structures [70].

In order to illustrate the spin reorientation transition we present in Fig. 1.7 the case of Co/Pd multilayer. This system shows a shape anisotropy with in-plane easy axis and a surface anisotropy with an easy axis perpendicular to the surface. The system shows a reorientation transition of its global easy axis from perpendicular to the surface to in-plane as the thickness of the Co layer is increased [62]. In Fig. 1.7 we show the values of the $K^{eff} \cdot t_{Co}$ as a function of t_{Co} (the thickness of the Co layer).

The reorientation transition is indicated in the figure by the change of K^{eff} sign. If $K^{eff} > 0$ the easy axis of the system is perpendicular to the surface, and the easy axis of the system is in plane if $K^{eff} < 0$.

1.6 The challenge of modeling of magnetic nanoparticles and thin films

The understanding of the origin of the surface anisotropy and its influence on the magnetic behavior of thin films and nanoparticles relies on the modeling. Electronic structure calculations have been proven to explain the physical reasons behind the existence of several surface effects such as the spin polarization. The main problem, however, lies in the fact that although these calculations are reasonably good in determining the difference between spin up and spin down populations, they are often not accurate enough to calculate the anisotropy value. Besides this fact, the calculations are mostly limited to small systems only and to zero temperatures.

The full quantum mechanical treatment of a 5 nm nanoparticle is still not feasible. The modeling of magnetic nanoparticles from the first-principle side is, therefore, normally limited to small clusters of hundreds of atoms [71, 72] and cannot take into account to a full extend the spin non-collinearities, their dynamics and temperature. Larger magnetic nanoparticles of 10 nm diameter are normally modeled using the Heisenberg model. An important role of spin non-collinearities [73] in understanding the magnetic behavior of nanoparticles has been reported using these types of studies. This so-called "atomistic" description [74–79] is relied on the Heisenberg-type Hamiltonian and can include spin dynamics and temperature. As a handicap these calculations use phenomenological surface anisotropy models, such as the transverse anisotropy one [75]. One of the most justified models for the surface anisotropy is the widely-used Néel surface anisotropy model [14, 47, 74] which will be also used in the present thesis.

The challenge, however, is the understanding of not only individual nanoparticles but their ensembles, where the distributions of individual properties and interactions play an important role. This is normally done using the representation of each nanoparticle as one macrospin [80, 81].

As for the thin films modeling, although intrinsic surface effects, based on the electronic interactions are localized on few layers, the magnetic exchange correlation length makes the surface anisotropy to influence the magnetic structure down to nanometers distance inside the material and may cause the inhomogeneous magnetization. The correct account for the domain structure belongs to the area of micromagnetism - a "continuous" approximation which has been proven to be very useful, especially in understanding the hysteresis and dynamics of nanostructures with dimensions up to several microns [82].

Therefore, one of the challenges of theoretical modeling in magnetism is the proper

account of its multiscale character. The physics of magnetism in materials involve many length, energy and time scales. And, unfortunately at this moment, a unified description of all these scales on the same footing is impossible.

Our "ideal" multiscale scheme is presented in Fig. 1.8. In the case of thin films the microscopic on-site parameters are calculated from ab-intio calculations limited to several atomic cells. The output of these calculations is the parameterized Heisenberg Hamiltonian which can be used to evaluate temperature-dependent parameters. These are used for large-scale micromagnetic modeling where also the microstructure such as the distribution of grains can be taken into account. In "theory" the atomic-scale defects should be taken into account either on the ab-initio or on the atomistic scale, also the atomistic discretization could be used near defects and the micromagnetic one - far from it, as in Ref. [83].

For the nanoparticles the "ideal" scheme consists first of the calculation of the nanoparticle structure, basing, for example, on the molecular dynamics with suitably parameterized potentials [84]. The "ab-initio" calculations for site-resolved magnetic

Multiscale modelling : cells → grain (nanoparticle) → thin film (ensemble)

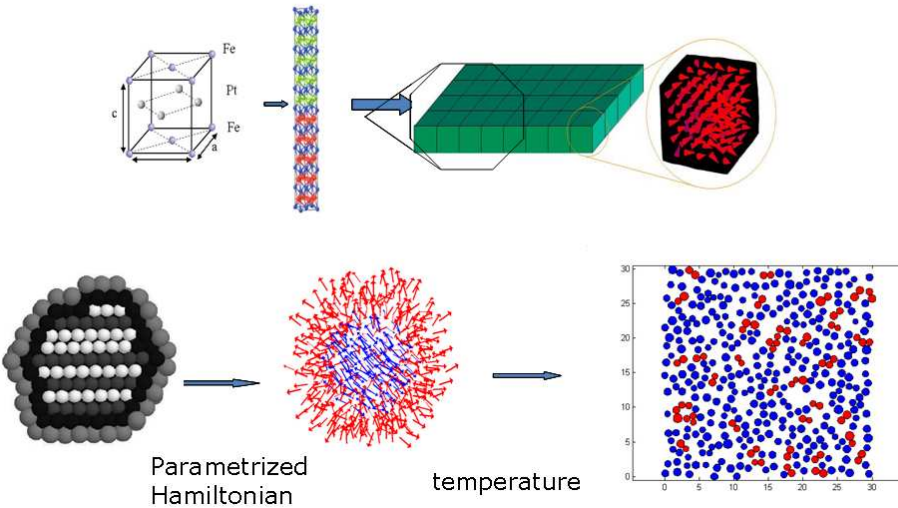


Figure 1.8: Scheme showing the "ideal" multiscale model .

parameters can be either directly performed on this structure if the size allows this, or the approximate values based on the local environment can be used [85]. Thus the Heisenberg model could be parameterized and the temperature introduced. The use of the Heisenberg model should provide a way to parameterize an individual magnetic nanoparticle as one macrospin with effective parameters. These macrospins could be

used for the modeling of an ensemble of nanoparticles to study the effects of interactions.

We should note that even this scheme is too ambitious for the present state of art and its development is making the first steps. Also this scheme is too simplified, since as we mentioned above, the surface anisotropy, for example, has multiple ingredients, many of them related to the presence of defects. The precise knowledge of defects on the atomistic scale and its consequences is basically not available.

1.7 About this thesis

We would like to indicate that a unified treatment of the whole magnetic problem and its temporal, length and energy scales is in nowadays a challenge. We have concentrated our efforts in some parts and problems related to the total multiscale scheme.

This thesis presents a theoretical study of the magnetic behavior of the low dimensional systems such as nanoparticles and thin films. Most of the magnetic parameters used in the study correspond to the cobalt fcc ones. We have selected the Co because it is one of the typical and widely used for applications magnetic material.

This thesis presents the way to parameterize multispin particle as an effective macrospin with mixed anisotropy (a combination of an uniaxial and a cubic contributions), which has been done in **Chapter 2** and **Chapter 3**. Since the ab-initio calculations on nanoparticles of reasonable sizes, taking account of all on-site parameters are not feasible at the present moment, we have used a phenomenological Néel surface anisotropy model. The variety of nanoparticles with different shapes, underlying structures, strengths of the surface anisotropy, etc has been investigated. Such approximation will in the future open the doors for modeling of an ensemble of nanoparticles as a set of effective macrospins which implicitly takes into account the effects of the surface, underlying lattice structure and shape.

During the work on this thesis the method of the constrained Monte Carlo has been developed in collaboration with Dr. P. Asselin (Seagate Technology, USA) and co-workers. This new method allows to evaluate numerically the dependence on temperature of the magnetic anisotropy in magnetic nanoparticles and thin films. We have used it in the study of the dependence on temperature of the magnetic anisotropy in magnetic thin films and nanoparticles with Néel surface anisotropy, in **Chapter 4** and **Chapter 5**. In those chapters of the thesis we have analyzed the applicability of the new method, have studied the deviations from the Callen-Callen law of the dependence on temperature of macroscopic magnetic anisotropy in the presence of the surface anisotropy. We have also studied the re-orientation transition in thin films with the surface anisotropy. Finally, we also show the possibility to have a temperature-induced transition from cubic (due to surface effects) to uniaxial macroscopic anisotropy in nanoparticles.

In **Chapter 6** we use a multiscale scheme, starting from the "ab-initio" calculations and using a fully relativistic screened Khon-Korringa-Rostocker (SKKR) method [86].

The "ab-initio" simulations have been performed with a code supplied by Dr. L. Szunyogh from Budapest University, Hungary. The magnetic properties of Co (bulk), semi-infinite Co ((100) and (111)), $Co((100) \setminus Ag$ and $Co(111) \setminus Ag$ system are studied. The use of this method allows to extract local magnetic parameters and parameterize the Heisenberg Hamiltonian. Inside the multi-scale scheme, the constrained Monte Carlo method is applied to evaluate the temperature-dependent parameters, including the macroscopic anisotropy in the presence of the Ag surface.

2

Multi-spin nanoparticle as an effective one spin problem

2.1 Introduction

Since the "ab-initio" treatment of a magnetic nanoparticle remains a future challenge, in this chapter we consider a nanoparticle treated as a multi-spin problem but within a classical atomic spin approach. Even in this case, the investigation of the thermal magnetization switching of a multi-spin nanoparticle is a real challenge. We are faced with complex many-body aspects with the inherent difficulties related with the analysis of the energy potential and its extrema. This analysis is unavoidable since it is a crucial step in the calculation of the relaxation time and thereby in the study of the magnetization stability against thermal fluctuations. As such, a question arises whether it is possible to map the behavior of a multi-spin nanoparticle onto that of a simpler model system as one effective magnetic moment, without loosing its main features such as surface anisotropy, lattice structure, size and shape, and more importantly the spin non-collinearities they entail. A first answer to this question was given in Ref. [74] where it was shown that when the surface anisotropy is much smaller than the exchange parameter and in the absence of the core anisotropy, the single-site Néel surface anisotropy contribution to the particle's effective energy is of the fourth order in the net magnetization components, of the second order in the surface anisotropy constant, and is proportional to a surface integral. The latter accounts for the lattice structure and the particle's shape. Later it has been shown that in a more general situation with the core anisotropy, taken as uniaxial, the energy of the multi-spin

particle could be modelled by that of an effective potential containing both uniaxial and cubic anisotropy terms [87].

In this chapter we investigate this issue in a more extensive way by considering other lattice structures, particle's shapes and different anisotropies in the core. For this purpose, we compute the energy potential of the multi-spin particle using the Lagrangian multiplier method [74] and fit it to the appropriate effective energy potential.

2.2 Model

2.2.1 Shape and surface of nanoparticles

In this study we show that the magnetic behavior of small particles is very sensitive to the surface arrangement, shape of the particles and underlying crystallographic structure. To investigate the various tendencies, we have considered particles cut from lattices with the simple cubic (sc) and face-centered cubic (fcc). Although experi-

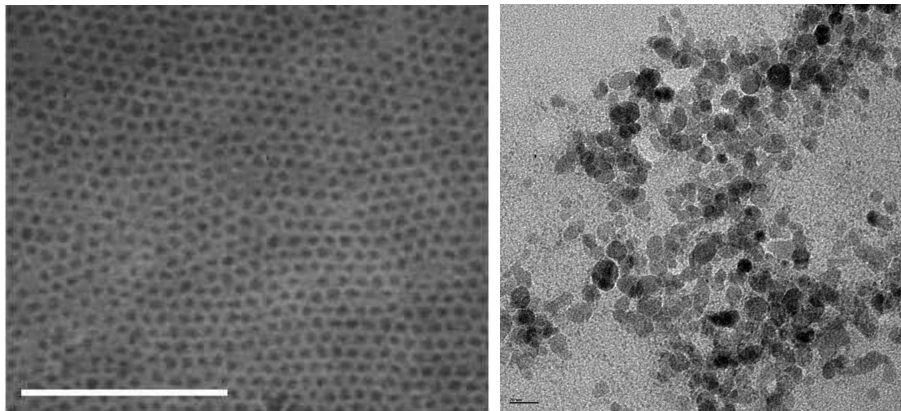


Figure 2.1: Image TEM of magnetic nanoparticles: (left) nanoparticles of $\gamma - Fe_2O_3$ (from Ref.[88]) and (right) azide functionalized Fe_3O_4 nanoparticles (right) (from Ref. [89]).

mental studies providing transmission electron microscopy images often show particles resembling truncated octahedra [14, 20] (see Figs. 1.1 in section 1.1 of the chapter Introduction). The real particles are not regular see for example Fig. 2.1, where we can find TEM images of different kind of nanoparticles. Making realistic particle shapes and surface arrangements in a computer simulations proves to be rather complex, "ab initio" simulations are available only for small clusters [71, 72]. Truncated octahedra have been included in our studies as an ideal case for fcc crystals, but the reality is somewhat subtler. In Ref. [14], in order to interpret the experimental results of the 3D-dimensional switching field curve, the so called Stoner-Wohlfarth astroid, it was assumed that a few outer layers in the truncated octahedral particle were magnetically "dead", leading to an effective elongation and thereby to a non-perfect octahedron.

Producing such a faceted elongated particle by somehow cutting the latter is an arbitrary procedure. In order to minimize the changes in the surface structure caused by elongation, we assumed a spherical particle or introduced elliptical elongation along the easy axis. This kind of structure has been the basis of many theoretical studies using the Heisenberg Hamiltonian (see, e.g., Refs. [74, 75, 87, 90–94]).

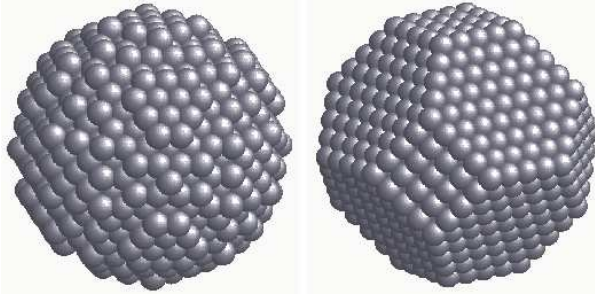


Figure 2.2: Two particles cut from fcc structure: spherical (left) and truncated octahedron (right).

Regarding the arrangement on the particle's surface, an appropriate approach would be to use molecular-dynamic techniques [84, 95, 96] based on the empirical potentials for specific materials. This would produce more realistic non-perfect surface structures, more representative of what it is hinted to experimentally. However, these potentials exist only for some specific materials and do not fully include the complex character of the surface. Moreover, the particles thus obtained (see, e.g. Ref. [18]), may have non-symmetric structures, and may present some dislocations. All these phenomena lead to rich and different behavior of differently prepared particles.

In the present chapter, and in order to illustrate the general tendency of the magnetic behavior, we mostly present results for particles with "pure" non-modified surfaces, namely spheres, ellipsoids and truncated octahedra cut from regular lattices. Even in this case, the surface arrangement may appear to be very different (see Fig. 2.2) leading to a rich magnetic behavior.

2.2.2 Localized spin (atomistic or Heisenberg) model

We consider a magnetic nanoparticle of \mathcal{N} spins in the many-spin approach, i.e., taking account of its intrinsic properties such as the lattice structure, shape, and size. This also includes the (nearest-neighbor) exchange interactions, single-site core and surface anisotropy. The magnetic properties of such a multi-spin particle (MSP) can be described by the anisotropic Heisenberg model of classical spins \mathbf{S}_i (with $|\mathbf{S}_i| = 1$).

$$\mathcal{H} = -\frac{1}{2}J \sum_{i,j} \mathbf{S}_i \cdot \mathbf{S}_j + \mathcal{H}_{\text{anis}}. \quad (2.1)$$

where J is the exchange parameter.

The anisotropy energy $\mathcal{H}_{\text{anis}}$ will be different if we are working with core spins or surface spins. For core spins, i.e., those spins with full coordination, the anisotropy energy $\mathcal{H}_{\text{anis}}$ is taken either as uniaxial with easy axis along z and a constant K_c (per atom), that is

$$\mathcal{H}_{\text{anis}}^{\text{uni}} = -K_c \sum_{i=1}^{N_c} S_{i,z}^2 \quad (2.2)$$

or cubic,

$$\mathcal{H}_{\text{anis}}^{\text{cub}} = \frac{1}{2} K_c \sum_{i=1}^{N_c} (S_{i,x}^4 + S_{i,y}^4 + S_{i,z}^4) \quad (2.3)$$

where N_c is the number of core spins in the particle. For surface spins the anisotropy is taken according to the Néel's surface anisotropy model (referred to in the sequel as NSA), expressed as:

$$\mathcal{H}_{\text{anis}}^{\text{NSA}} = \frac{K_s}{2} \sum_{i=1}^{N_s} \sum_{j=1}^{z_i} (\mathbf{S}_i \cdot \mathbf{u}_{ij})^2, \quad (2.4)$$

where N_s is the number of surface spins, z_i the number of nearest neighbors of site i , and \mathbf{u}_{ij} - a unit vector connecting this site to its nearest neighbors labeled by j .

Dipolar interactions are known to produce an additional "shape" anisotropy. However, in the atomistic description, their role in describing the spin non-collinearities is negligible as compared to that of all other contributions. In order to compare particles with the same strength of anisotropy in the core, we assume that the shape anisotropy is included in the core uniaxial anisotropy and neglect the dipolar energy contribution to the spin non-collinearities. We also assume that in the ellipsoidal nanoparticles the anisotropy easy axis is parallel to the elongation direction.

All physical constants will be measured with respect to the exchange coupling J (unless explicitly stated otherwise), so we define the reduced constants,

$$k_c \equiv K_c/J, \quad k_s \equiv K_s/J. \quad (2.5)$$

The core anisotropy constant will be taken as $k_c \simeq 0.01$, and $k_c \simeq 0.0025$. The latter constant in real units corresponds to $K_c \simeq 3.2 \times 10^{-17}$ erg/atom and is similar to cobalt fcc value. On the other hand, the surface anisotropy constant k_s is unknown "a priori" and will be varied.

2.3 Analytical background

In Refs. [73, 74, 87, 97] analytical as well as numerical calculations showed that a multi-spin particle, cut from a sc lattice, and when its surface anisotropy is small with respect to the exchange coupling, may be modeled by an effective one-spin particle (EOSP), i.e., a single macroscopic magnetic moment \mathbf{m} representing the net magnetic

moment of the multi-spin particle. The energy of this EOSP (normalized to $J\mathcal{N}$) may be written as

$$\mathcal{E}_{\text{EOSP}} = (\mathcal{E}_c + \mathcal{E}_1 + \mathcal{E}_2 + \mathcal{E}_{21}). \quad (2.6)$$

The \mathcal{E}_1 is the first-order anisotropy energy with surface contribution, \mathcal{E}_2 is the second-order anisotropy energy with surface contribution, \mathcal{E}_{21} is a mixed contribution to the energy that is second order in surface anisotropy and first order in core anisotropy and \mathcal{E}_c is the core anisotropy energy (per spin).

The \mathcal{E}_c energy has the following form:

$$\mathcal{E}_c = \frac{N_c}{\mathcal{N}} k_c \begin{cases} -m_z^2 & \text{uniaxial,} \\ \frac{1}{2}(m_x^4 + m_y^4 + m_z^4) & \text{cubic,} \end{cases} \quad (2.7)$$

The other three contributions (\mathcal{E}_1 , \mathcal{E}_2 and \mathcal{E}_{21}) stem from the surface, which we discuss now.

2.3.1 Second-order surface-anisotropy energy \mathcal{E}_2

In Ref. [74] a spherical multi-spin nanoparticle was considered, the anisotropy in the core was ignored and the surface anisotropy was taken as NSA. Using the continuous approximation for $N \gg 1$ the authors evaluated the surface energy density $E_S(\mathbf{m}, \mathbf{n})$, where \mathbf{m} is the magnetization and \mathbf{n} is the normal to the surface. The equilibrium magnetization satisfied the Brown's condition [98]:

$$\mathbf{m} \times \mathbf{H}_{eff} = 0, \quad \mathbf{H}_{eff} = \mathbf{H}_A + J\Delta\mathbf{m} \quad (2.8)$$

here \mathbf{H}_{eff} is the total effective field, J is the exchange constant, Δ is the Laplace operator and \mathbf{H}_A is the anisotropy field, that in this case is due entirely to the surface.

$$\mathbf{H}_A = -\frac{dE_S}{d\mathbf{m}} \delta(r - R), \quad (2.9)$$

here R represents the radius of the spherical particle.

For the case of $Ks \ll J$ we can suppose that the deviations of \mathbf{m} of the homogeneous state \mathbf{m}_0 are small and the problem can be linearized.

$$\mathbf{m}(\mathbf{r}) \cong \mathbf{m}_0 + \psi(\mathbf{r}, \mathbf{m}_0), \quad \psi = |\psi| \ll 1 \quad (2.10)$$

The correction ψ is the solution of the internal Neumann boundary problem for a sphere:

$$\Delta\psi = 0, \quad \left. \frac{\delta\psi}{\delta r} \right|_{r=R} = \mathbf{f}(\mathbf{m}, \mathbf{n}) \quad (2.11)$$

$$\mathbf{f}(\mathbf{m}, \mathbf{n}) = -\frac{1}{J} \left[\frac{dE_S(\mathbf{m}_0, \mathbf{r})}{d\mathbf{m}} - \left(\frac{dE_S(\mathbf{m}_0, \mathbf{r})}{d\mathbf{m}} \cdot \mathbf{m}_0 \right) \mathbf{m}_0 \right] \quad (2.12)$$

Then, solving the corresponding Neumann problem by the Green's function technique, we obtain:

$$\psi(\mathbf{r}, \mathbf{m}) = \frac{1}{4\pi} \int_S d^2\mathbf{r}' \mathbf{G}(\mathbf{r}, \mathbf{r}') \mathbf{f}(\mathbf{m}, \mathbf{n}) \quad (2.13)$$

where $\mathbf{G}(\mathbf{r}, \mathbf{r}')$ is the Green function. Computing the energy of the multi-spin particle, it was found that the corresponding effective energy is of the 4th-order in the components of the net magnetic moment \mathbf{m} and the 2nd-order in the surface anisotropy constant k_s , that is

$$\mathcal{E}_2 = k_2 \sum_{\alpha=x,y,z} m_\alpha^4, \quad (2.14)$$

with

$$k_2 = \kappa \frac{k_s^2}{z}. \quad (2.15)$$

κ is a surface integral that depends on the underlying lattice, shape, and the size of the particle and also on the surface-anisotropy model. For instance, $\kappa \simeq 0.53466$ for a spherical particle cut from an sc lattice, with NSA. We would like to note that the contribution (2.14) scales with the system's volume and thus could renormalize the volume anisotropy of the nanoparticle.

The equation (2.15) was obtained analytically for $K_s \ll J$ in the range of the particle size large enough ($\mathcal{N} \gg 1$) but small enough so that $\delta\psi$ remains small. Being $\delta\psi \sim \mathcal{N}^{1/3} K_s / J$, the angle of order which describes the noncollinearity of the spins that results from the competition of the exchange interaction and the surface anisotropy ¹.

Since k_2 is nearly size independent (i.e. the whole energy of the particle scales with the volume), it is difficult to experimentally distinguish between the core cubic anisotropy and the one due to the second order surface contribution (see discussion later on). The physical reason for the independence of k_2 on the system size is the deep penetration of the spin non-collinearities into the core of the particle. This means that the angular dependence of the non-collinearities also contributes to the effective anisotropy. Interestingly this implies that the influence of the surface anisotropy on the overall effective anisotropy is not an isolated surface phenomena and is dependent on the magnetic state of the particle. We note that this effect is quenched by the presence of the core anisotropy which could screen the effect at a distance of the order of domain wall width from the surface.

The energy contribution \mathcal{E}_2 has also been derived in the presence of core anisotropy [73] and numerically tested in Ref. [87]. Similar conclusions also apply for the case of the transverse surface anisotropy, Ref. [87].

¹Since the applicability conditions for Eqs. (2.14, 2.15) are usually not fully satisfied, numerical calculations yield k_2 slightly dependent on the system size [74].

2.3.2 First-order surface-anisotropy energy \mathcal{E}_1

In Ref. [74] the case of non-symmetrical particles was also discussed. More precisely, for small deviations from spheres and cubes, i.e., for weakly ellipsoidal or weakly rectangular particles, there is a corresponding weak first-order contribution \mathcal{E}_1 that adds up to \mathcal{E}_2 . Hence, for an ellipsoid of revolution with axes a and $b = a(1 + \epsilon)$, $\epsilon \ll 1$, cut out of an sc lattice so that the ellipsoid's axes are parallel to the crystallographic direction, one has that the first order anisotropy is given by [97]:

$$\mathcal{E}_1 = -k_1 m_z^2 . \quad (2.16)$$

where

$$k_1 \sim k_s \mathcal{N}^{-1/3} \epsilon , \quad (2.17)$$

i.e. the \mathcal{E}_1 energy contribution scales with the surface of the system.

It is necessary to mention that for crystal shapes such as spheres and cubes the contribution \mathcal{E}_1 vanishes by symmetry.

The ratio of the second to the first order surface contributions is:

$$\frac{\mathcal{E}_2}{\mathcal{E}_1} \sim k_s \frac{\mathcal{N}^{1/3}}{\epsilon} , \quad (2.18)$$

It can be significant even for $K_s \ll J$ due to the combined influence of the large particle size and the small deviation from symmetry, $\epsilon \ll 1$.

2.3.3 Mixed contribution to the energy \mathcal{E}_{21}

Taking into account the core anisotropy analytically to describe corrections to Eq. (2.14) due to the screening of the spin noncollinearities in the general case is difficult. However, one can consider this effects perturbatively, at least to clarify the validity limits of expression (2.14). In Ref. [97], the use of the general method outlined above (see section 2.3.1) led to a Helmholtz equation. In this case, there is no exact Green's function and as such the perturbation theory was used to write the Green's function G in the presence of core anisotropy as the sum of the exact Green's function $G^{(0)}$, obtained in the absence of core anisotropy, and a correction $G^{(1)}$. The perturbation parameter:

$$(2.19)$$

Therefore, upon using $G = G^{(0)} + p_\alpha^2 G^{(1)}$ in the energy, it was found that $G^{(1)}$ leads to a new contribution of the surface anisotropy which is also of the 2nd-order in the surface anisotropy constant k_s and the first order in k_c .

$$\mathcal{E}_{21} = k_{21} g(\mathbf{m}) \quad (2.20)$$

with

$$k_{21} = \tilde{\kappa} (k_c N_s) k_s^2 \quad (2.21)$$

where $\tilde{\kappa}$ is another surface integral whose integrand contains $G^{(1)}$. $g(\mathbf{m})$ is a function of m_α [97] which comprises, among other contributions, both the 2nd- and the 4th-order contributions in spin components. For example, if we work with spherical coordinates (θ, φ) for an sc lattice

$$g(\theta, \varphi = 0) = -\cos^2 \theta + 3 \cos^4 \theta - 2 \cos^6 \theta,$$

which is shown later to give an agreement with the numerical simulations, see Fig. 2.5.

The contribution (2.20), called here the *core-surface mixing* (CSM) contribution, should satisfy $k_{21} \lesssim k_2$ which requires:

$$N_s K_c / J \lesssim 1 \quad (2.22)$$

This is exactly the condition that the screening length is still much greater than the linear size of the particle. For larger system sizes the perturbative treatment becomes invalid.

2.3.4 Effective one spin problem (EOSP) approximation

Consequently, collecting all the contributions, one can model the energy of a multi-spin particle with an effective energy potential in the form:

$$\mathcal{E}_{\text{EOSP}} = -k_{\text{ua}}^{\text{eff}} m_z^2 - \frac{1}{2} k_{\text{ca}}^{\text{eff}} \sum_{\alpha=x,y,z} m_\alpha^4. \quad (2.23)$$

The subscripts ua/ca stand for uniaxial/cubic anisotropy, respectively.

Now, we note that due to the contributions (2.16) and (2.20), even when the core anisotropy is not uniaxial, the effective energy contains two uniaxial contributions induced by the surface, one is due to elongation given by (2.16) and the other to the mixing between the core and the surface given by (2.20). Hence, the 2nd-order term $k_{\text{ua}}^{\text{eff}}$ in (2.23) takes into account these two contributions. Similarly, the 4th-order term $k_{\text{ca}}^{\text{eff}}$ is a result of the surface contributions (2.14) and part of (2.20), and may also contain a contribution from the core if the latter has a cubic anisotropy.

To clarify the dependence on the system size and the surface anisotropy constants of the different energy contributions to EOSP we summarized them in Tab. 2.1.

Although the analytical expressions are only established so far for sc lattices, they do provide us with a general form of the effective energy potential which allows us to investigate the different tendencies of the nanoparticle behavior, taking account of various contributions to its energy. These approximate expressions are also very useful in the interpretation of numerical results.

Contribution	System size dependence	Dependence on (k_s)
E_c	Nc	-
E_1 (elongated particles only)	Ns	$\propto k_s$
E_2	\mathcal{N}	$\propto k_s^2$
E_{21}	Ns	$\propto k_c k_s^2$

Table 2.1: Dependence of different contributions to the effective macrospin energy $E = \mathcal{E} \cdot (J\mathcal{N})$ on the surface anisotropy constant k_s and its scaling with the system size.

2.4 Numerical method

Since we are dealing with a multi-spin particle, the energy potential is multidimensional. Accordingly, in Ref. [74] the technique of Lagrange multiplier was introduced to represent the energy potential in terms of the coordinates of the particle's net magnetization $\vec{\nu} \equiv \sum_i \mathbf{S}_i / |\sum_i \mathbf{S}_i|$. This technique consists of adding the term $-\mathcal{N}\vec{\lambda}(\vec{\nu} - \vec{\nu}_0)$, to the total energy Eq. (2.1). This term produces an additional torque that forces the net magnetization to lie along the prescribed direction $\vec{\nu}_0$. The equilibrium state of the spin system is determined by solving the Landau-Lifshitz equation (without the precession term):

$$\frac{d\mathbf{S}_i}{dt} = -\alpha \mathbf{S}_i \times (\mathbf{S}_i \times \mathbf{H}_i). \quad (2.24)$$

The effective field $\mathbf{H}_i = -\delta\mathcal{H}/\delta\mathbf{S}_i$ now contains an additional term due to the Lagrange constraint. For the three components of the Lagrange parameter $\vec{\lambda}$ the set of equations (2.24) is augmented by the equations $d\vec{\lambda}/dt = \delta\mathcal{H}/\delta\vec{\lambda}$. The stationary points found with this method are also stationary points of the Hamiltonian (2.1), since for these points $\vec{\lambda} = 0$. However, if the system has many metastable states, only part of these points, compatible with the behavior assumed by the direction of the net magnetization is determined. More precisely, in individual small particles where the exchange interaction is dominating, the deviations from the collinear state are small and thereby the individual spins adiabatically adjust to the net direction when the latter is rotated. In this case, it is possible to define a net magnetization and parameterize it, e.g., in the spherical system of coordinates as $\nu_0(\theta, \varphi)$. The advantage of this technique is that it can produce highly non-collinear multi-dimensional stationary points [74, 87, 99]. Accordingly, in the present work and unlike the studies presented in Ref. [14], spin non-collinearities are taken into account. Moreover, in order to check the correct loci of the saddle points, we computed the eigenvalues and gradient of the Hessian matrix associated with the Hamiltonian (2.1).

2.5 Effective energy landscapes of spherical nanoparticles

In this section we compute the 3D energy potential as a function of the polar angle θ and azimuthal angle φ of net magnetization of the multi-spin particle. First, we do this for a spherical particle with uniaxial anisotropy in the core and NSA, cut from an sc and fcc lattices, and for different values of the surface anisotropy constant, k_s .

We apply the Lagrange multiplier technique to analyze the case of a spherical multi-spin particle of $\mathcal{N} = 1736$ spins on an sc lattice with uniaxial anisotropy in the core ($k_c = 0.0025$) and NSA. In Fig. 2.3 we show the obtained energy landscapes. One can

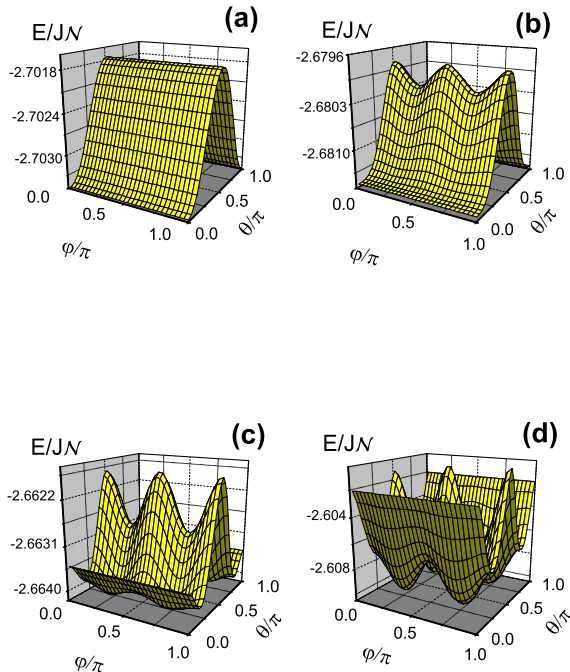


Figure 2.3: Energy potentials of a spherical multi-spin particle of $\mathcal{N} = 1736$ spins on an sc lattice with uniaxial anisotropy in the core ($k_c = 0.0025$) and NSA with constant (a) $k_s = 0.005$, (b) $k_s = 0.112$, (c) $k_s = 0.2$, (d) $k_s = 0.5$.

see that as k_s increases from $k_s = 2k_c$ to $k_s = 200k_c$, the global minima move away from those defined by the uniaxial core anisotropy, i.e., at $\theta = 0, \pi$ and any ϕ , and become maxima, while new minima and saddle points develop which are reminiscent of cubic anisotropy.

With the aim to extract the value of the effective uniaxial and cubic anisotropy constants, we cut the 3D energy landscape at $\varphi = 0$ and obtain the 2D energy potential, later we fit it to formula (2.23). In Fig. 2.4 we present the 2D energy potential ($\varphi = 0$) of a multi-spin particle with uniaxial anisotropy in the core ($k_c = 0.01$) and NSA with $k_s = 0.1$ (left), 0.5 (right). The solid lines are numerical fits to formula (2.23). From this graph we see that the energy of the multi-spin particle is well recovered by Eq. (2.23) when k_s is small. Consequently, such multi-spin particle can be treated as an EOSP with an energy that contains uniaxial and cubic anisotropies. However, as it is started to be seen in the right panel, and as was shown in Ref. [87], when the surface anisotropy increases, this mapping of the multi-spin particle onto an effective one-spin particle is less satisfactory.

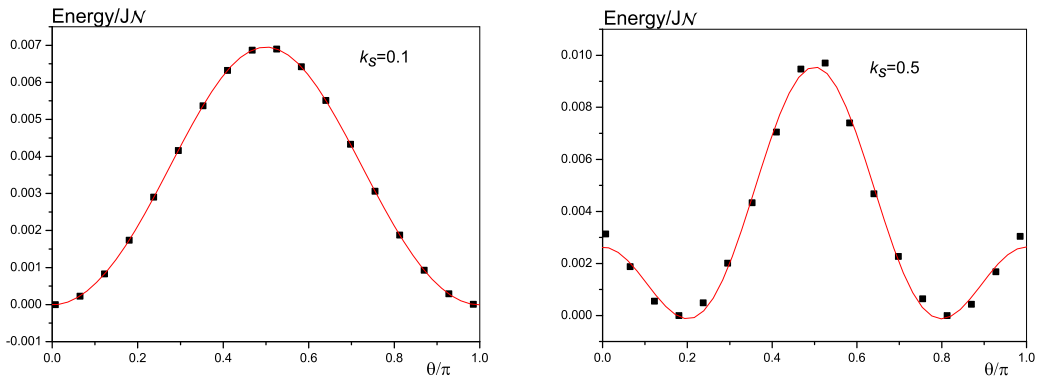


Figure 2.4: 2D energy potentials of a spherical multi-spin particle of $N = 1736$ spins on an sc lattice with uniaxial anisotropy in the core ($k_c = 0.01$) and NSA with constant $k_s = 0.1$ (left), 0.5 (right). The solid lines are numerical fits to formula (2.23).

Repeating this fitting procedure for other values of k_s we obtain the plots of k_{ua}^{eff} and k_{ca}^{eff} as a function of k_s , see Fig. 2.5. Here we first see that these effective constants are quadratic in k_s , in accordance with Eqs. (2.15) and (2.21). In addition, the plot on the right shows an agreement between the constant k_{ua}^{eff} obtained numerically and the analytical expression (2.21), upon subtracting the pure core contribution \mathcal{E}_c , see Eq. (2.6). The agreement is better in the regime of small k_s . These results confirm those of Refs. [73, 87, 97] that the core anisotropy is renormalized by the surface anisotropy, though only slightly in the present case.

Spherical particles cut from the sc lattice exhibit an effective four-fold anisotropy with $k_{ca}^{\text{eff}} < 0$, as we can check from the numerical results in Fig. 2.5 and analytical expression Eq. (2.23). As such, the contribution of the latter to the effective energy is positive.

Next we will analyze the case of a spherical particle with fcc lattice structure. First, in the same way that we have done in the case of an sc particle, we calculate the 3D

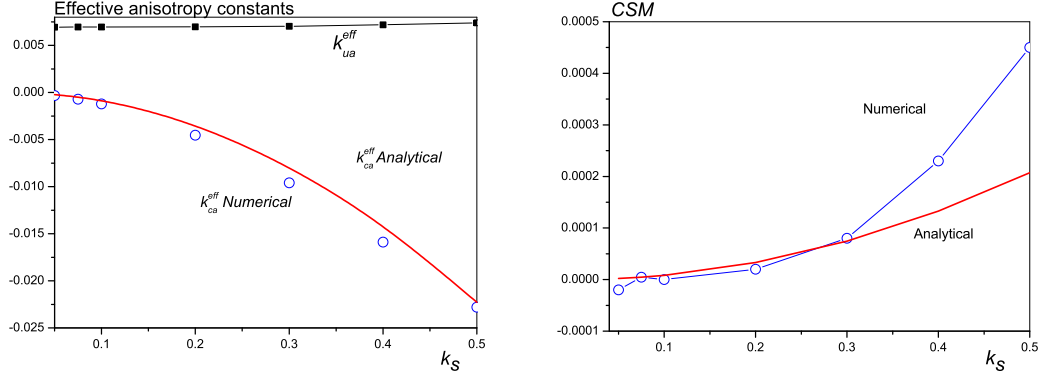


Figure 2.5: Effective anisotropy constants for a spherical multi-spin particle of $\mathcal{N} = 1736$ spins cut from an sc lattice against k_s . The panel on the right shows the *core-surface mixing* (CSM) contribution obtained numerically as $k_{\text{ua}}^{\text{eff}}$ upon subtracting the original core contribution \mathcal{E}_c in Eq. (2.3). The thick solid lines are plots of the analytical expressions (2.15), (2.21).

energy landscape, see Fig. 2.6. Comparing the energy potential in Fig. 2.3 for the sc and Fig. 2.6 for the fcc lattice one realizes that, because of the different underlying structure and thereby different spin surface arrangements, the corresponding energy potentials exhibit different topologies. For instance, it can be seen that the point $\theta = \pi/2, \varphi = \pi/4$ is a saddle in MSPs cut from an sc lattice and a maximum in those cut from the fcc lattice.

In Figs. 2.7, we plot the 2D energy potential for a spherical particle with fcc structure, for two values of k_s : $k_s = 10k_c$ in the left graph and $k_s = 120k_c$ in the right graph. The solid line represents numerical fits to formula (2.23). We can observe an agreement between the numerical results and the fittings to formula (2.23). Now, we extract the values $k_{\text{ua}}^{\text{eff}}$ and $k_{\text{ca}}^{\text{eff}}$ as a function of k_s for a fcc spherical particle. The effective cubic constant $k_{\text{ca}}^{\text{eff}}$ appears to be positive in contrast to sc case, see Fig. 2.8, and as for the sc lattice, it is quadratic in k_s . As mentioned earlier, the coefficient κ in Eq. (2.15) depends on the lattice structure and for fcc it may become negative. To check this, one first has to find an analytical expression for the spin density on the fcc lattice, in the same way that the sc lattice density was obtained in Ref. [74] (see Eq. (6) therein). Likewise, the coefficient $\tilde{\kappa}$ in Eq. (2.21) should change on the fcc lattice, thus changing the uniaxial and cubic contributions as well.

In fact that not only the value of the effective constant $k_{\text{ca}}^{\text{eff}}$ but even its sign depend on the underlying structure, more exactly the surface arrangement. It is an important point for general modelling. Very often and for simplicity the nanoparticles are considered cut from sc lattice, disregarding the fact that realistic nanoparticles never have this structure.

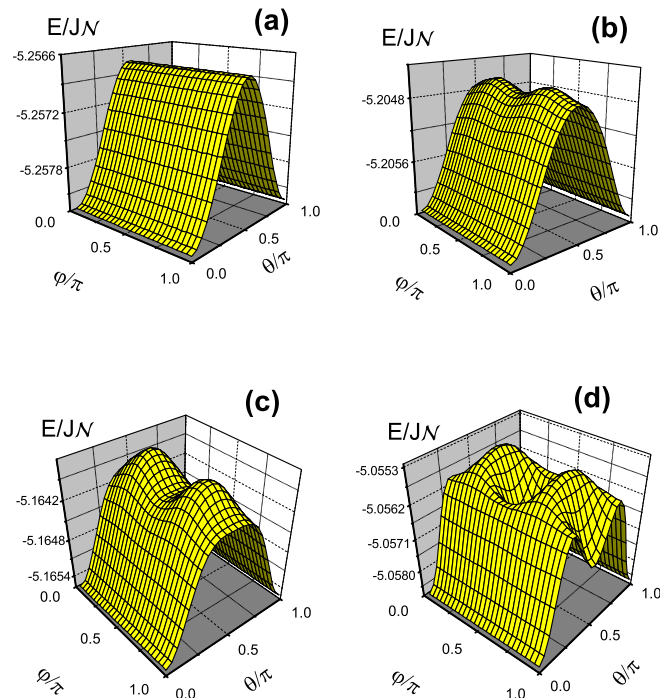


Figure 2.6: Energy potentials of a spherical multi-spin particle with uniaxial anisotropy in the core ($k_c = 0.0025$) and NSA with constant (a) $k_s = 0.005$, (b) $k_s = 0.1$, (c) $k_s = 0.175$ and (d) $k_s = 0.375$. The particle contains $\mathcal{N} = 1264$ spins on an fcc lattice.

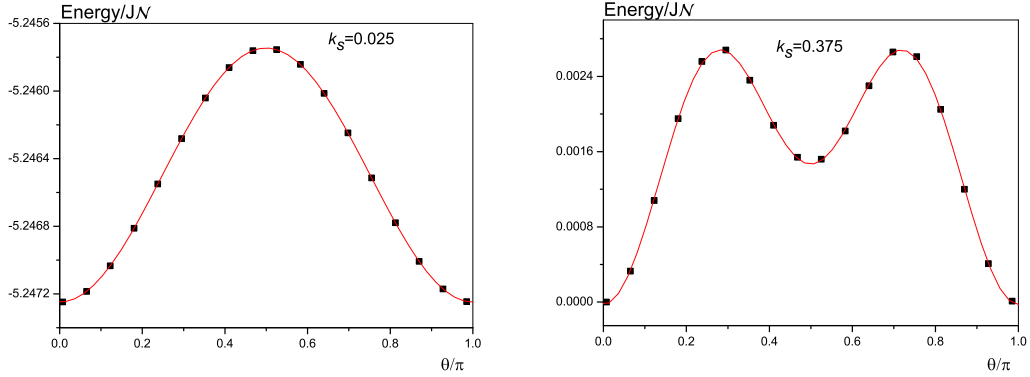


Figure 2.7: 2D energy potentials of a spherical multi-spin particle of $\mathcal{N} = 1264$ spins on an fcc lattice with uniaxial anisotropy in the core ($k_c = 0.0025$) and NSA with constant $k_s = 0.025$ (left), 0.375 (right). The solid lines are numerical fits to formula (2.23).

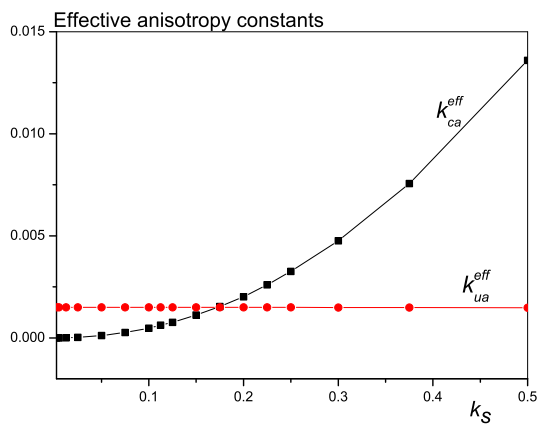


Figure 2.8: Effective anisotropy constants against k_s for a spherical particle of $\mathcal{N} = 1264$ spins cut from an fcc lattice with uniaxial core anisotropy $k_c = 0.0025$. The lines are guides for the eyes.

2.6 Effective energy landscapes of elongated nanoparticles

Now we investigate the effect of elongation. As discussed earlier, due to the contribution in Eq. (2.16), even a small elongation may have a strong effect on the energy barrier of the multi-spin particle, and in particular on the effective uniaxial constant $k_{\text{ua}}^{\text{eff}}$, as will be seen below. Fig. 2.9 shows the energy potential of an ellipsoidal multi-spin particle with aspect ratio 2:3, cut from an fcc lattice. Unlike the energy potentials of spherical multi-spin particle, the result here shows that for large surface anisotropy the energy minimum corresponds to $\theta = \pi/2$, see Fig. 2.9(d). Indeed, due to a large number of local easy axes on the surface pointing perpendicular to the core easy axis, the total effect is to change this point from a saddle for small k_s to a minimum when k_s has large values.

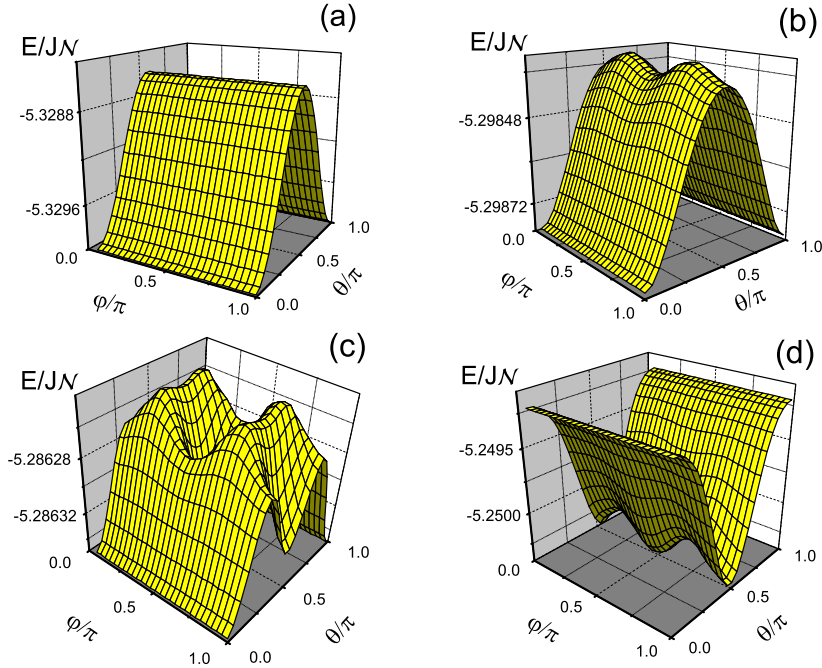


Figure 2.9: Energy potentials of an ellipsoidal particle cut from an fcc lattice and with uniaxial anisotropy in the core ($k_c = 0.0025$) and NSA with constant (a) $k_s = 0.0125$, (b) $k_s = 0.075$, (c) $k_s = 0.1$ and (d) $k_s = 0.175$.

The effective uniaxial and cubic anisotropy constants are shown in Fig. 2.10, for nanoparticles cut from fcc and sc lattice. As expected, the effective uniaxial constant

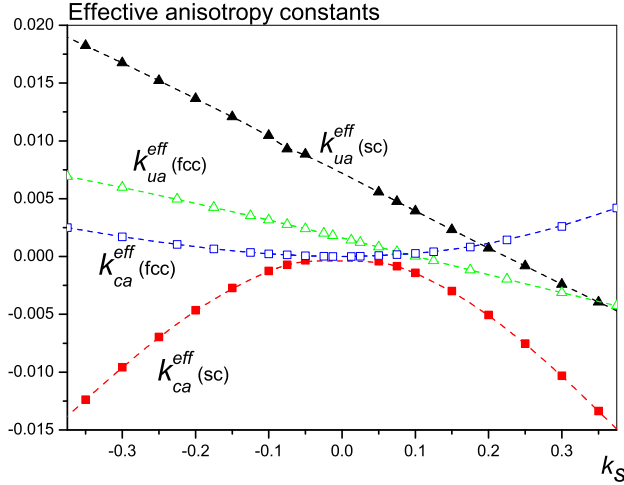


Figure 2.10: Effective anisotropy constants against k_s for an ellipsoidal particle of $\mathcal{N} = 2044$ spins on sc and fcc lattices, with uniaxial core anisotropy $k_c = 0.0025$. The lines are guides.

is linear in k_s shows a strong variation and even changes sign at some value of k_s , as opposed to the case of a spherical multi-spin particle. On the other hand, as for the latter case, the constant k_{ca}^{eff} retains its behavior as a function of k_s , i.e. is proportional k_s^2 . Again, in the case of an sc lattice $k_{ca}^{\text{eff}} < 0$ and on an fcc lattice $k_{ca}^{\text{eff}} > 0$.

2.7 Effective energy landscape of an octahedral nanoparticle

In this section we analyze the energy landscape of a magnetic nanoparticle with the so-called truncated octahedral shape. The Co particles are usually reported as having this structure with fcc underlying lattice, see for example Ref. [8, 14, 20] and image in Figs. 1.1(c-d).

Regular truncated octahedrons having six squares and eight hexagons on the surface have been constructed cutting the ideal fcc lattice in an octahedral (two equal mutually perpendicular pyramids with square bases parallel to XY plane) and subsequent truncation. Equal surface densities in all hexagons and squares can be obtained if the fcc lattice is initially rotated 45° in the XY plane, i.e. when the X axis is taken parallel to the (110) direction and the Z axis to the (001) direction. We perform the same calculations as before for a multi-spin particle cut from an fcc lattice, with cubic single-site anisotropy in the core and NSA.

In Fig. 2.11 we presents the values of the effective uniaxial and cubic anisotropy constants as a function of surface anisotropy value k_s . The results show that the

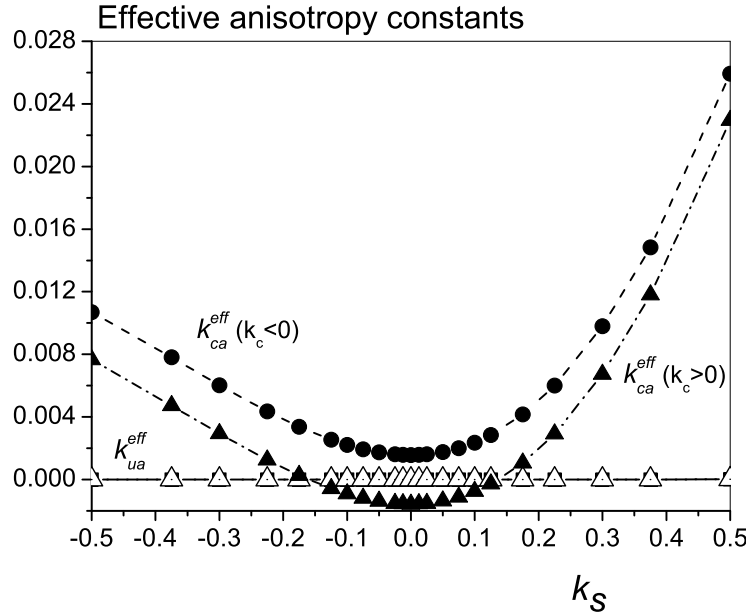


Figure 2.11: Effective anisotropy constants against k_s for a regular truncated octahedral particle $\mathcal{N} = 1289$ spins, fcc structure, and cubic anisotropy in the core with $k_c = 0.01$ and $k_c = -0.01$.

effective uniaxial contribution in this system is practically zero. We can also observe that the effective cubic anisotropy is modified with respect to the core by surface effects. It can be seen that, similarly to the results discussed above for spherical particles, the effective cubic anisotropy constant is again proportional to k_s^2 for small k_s . This is mainly due to the two contributions, one coming from the initial core cubic anisotropy and the other from the surface contribution as in Eq. (2.14). It is interesting to note that the surface contribution can change the sign of the effective cubic anisotropy constant from the initially negative cubic core anisotropy. We can also observe an asymmetric behavior of the effective anisotropy constants with respect to the change of the sign of the surface anisotropy which we found, in general, in all particles with fcc underlying lattice.

If the fcc lattice is initially orientated with crystallographic lattice axes parallel to those of the system of coordinates, then different atomic densities are created on different surfaces. This way the surface density along the XY circumference is different from that along XZ one. In Fig. 2.12 we plot the dependence of the effective cubic constant k_{ca}^{eff} as a function of k_s for $k_c > 0$ and $k_c < 0$. It can be seen that, similarly to the results discussed above, the effective cubic constant is again proportional to k_s^2 but now its increase with k_s is slower. The surface contribution can again change the sign of the initially negative cubic core anisotropy. Besides, we clearly see that the multi-spin particle develops a negative uniaxial anisotropy contribution, induced by

the surface in the presence of core anisotropy, according to Eq. (2.20).

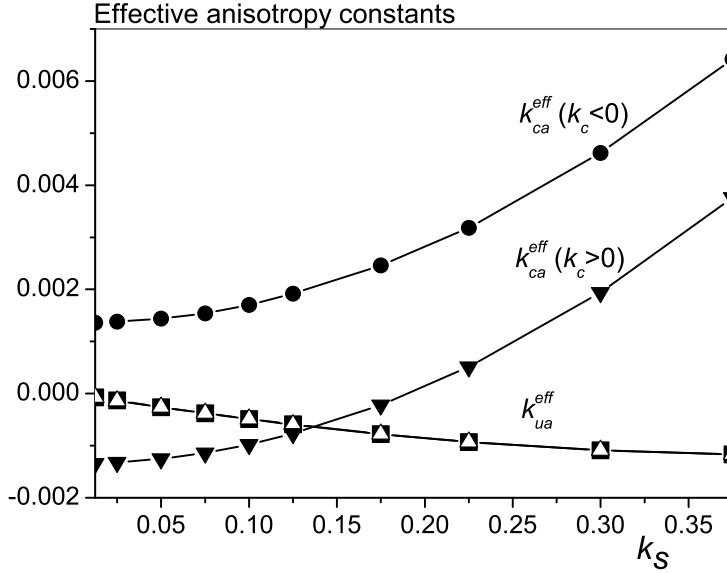


Figure 2.12: Effective anisotropy constants against k_s for a truncated octahedral particle of $\mathcal{N} = 1080$ spins, fcc structure and cubic anisotropy in the core with $k_c = 0.01$ and $k_c = -0.01$.

2.8 Effective energy landscape in cobalt nanoparticle

In the present section we aim at the modeling of nanoparticles experimentally prepared in Ref. [8–10, 100, 101]. In those articles it has been reported that the magnetic anisotropy of the Co cluster prepared by sequential sputtering of Co and Al_2O_3 (or Cu; or Au; or Ag) suffers an increment when the diameter of the cluster is reduced which is associated to the surface anisotropy. The same group suggested that such an increment of the effective anisotropy produces an increase of the effective energy barrier, stabilizing the magnetization against thermal fluctuations.

With the aim to study the effective energy landscape of such nanoparticles, we consider a Co nanoparticle with fcc internal structure, cubic magnetocrystalline anisotropy, varying the strength of the surface anisotropy. To compare with the experimental results in this sub-section the anisotropy parameter was taken from the experimental value and is measured as the anisotropy density per volume, $K_c = -2.8 \times 10^6 \text{ ergcm}^{-3}$. The Co nanoparticles are "numerically prepared" in two forms: truncated octahedral, see Fig. 2.13(a) and elongated truncated octahedral, see Fig. 2.13(b). For truncated octahedra, we use a symmetrical construction which allowed the same surface atom arrangements in all rectangular facets, as it was described above. In the case of

perfect truncated octahedral nanoparticle, the nanoparticle's diameter is $D = 4.5\text{nm}$ ($\mathcal{N} = 2951$), \mathcal{N} is the total number of spin. For the elongated truncated octahedron the planes, perpendicular to z-axis, used to cut the polygon from the fcc lattice, were additionally separated to obtain the desired elongation, in our case that elongation has been chosen as $e = Dz/Dx = 1.228$, where Dz and Dx are dimensions in z and x directions, respectively (corresponding to experimentally prepared nanoparticles). The nanoparticle size in x direction was considered $Dx = 3.1\text{nm}$ (the total spin number is equal to $\mathcal{N} = 1439$).

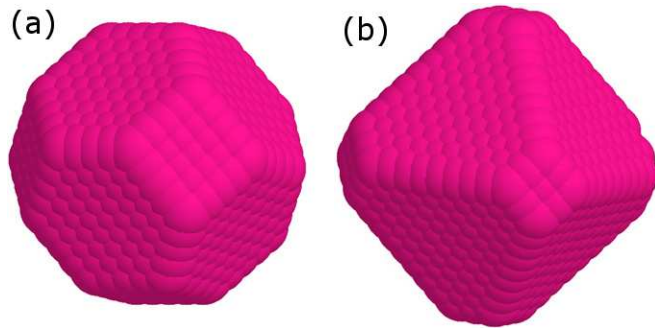


Figure 2.13: Modeled Co nanoparticles with fcc lattice and (a) octahedral shape. (b) elongated octahedral shape.

Some examples of the 3D effective energy landscapes for several values of the Néel surface anisotropy constants are presented in Fig. 2.14. We have observed that for relatively small values of the surface anisotropy $k_s \lesssim 50|k_c|$, see Figs. 2.14(a) and 2.15(a), the overall anisotropy is in agreement with the previous results, i. e. can be described by formula (2.23). For large value of the surface anisotropy $k_s \gtrsim 60|k_c|$, see Figs. 2.14(b-d) and 2.15(b-d), we note the change of the character of the energy landscape. Moreover, we observe a change of the character of the special point at $\theta_0 = \pi/2, \varphi = \pi/4$ from the saddle one to the maximum. Interestingly, the special point corresponding to the minimum energy path in Figs. 2.14(d) and 2.15(d), is not a usual one: locally near this point in one of the normal mode directions the energy increases and in another one it decreases (similar to x^3 expansion). This point is known as a "monkey saddle" and its existence invalidates the standard Kramers-type approach (in particular, leading to the Arrhenius-Neel law), where the full-harmonic expansion of the energy near the saddle point is necessary [53].

In Figs. 2.15 we present 2D energy landscapes, corresponding to $\varphi_0 = 0$ (squares) and $\varphi_0 = \pi/4$ (circles). Namely, the energy landscape cannot be fitted to the cubic anisotropy with the first cubic anisotropy constant only. We have found that these landscapes could be fitted to the effective macro-spin energy, slightly different from

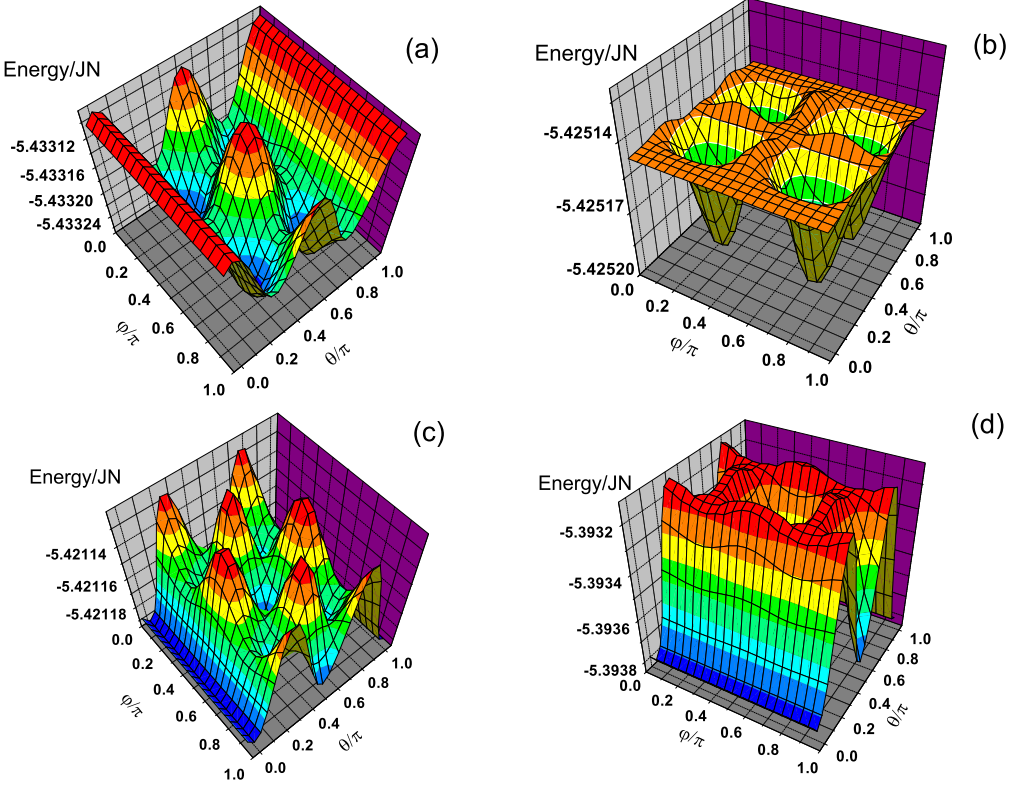


Figure 2.14: Effective 3D energy landscapes of octahedral Co nanoparticle with $D=4.5\text{ nm}$ (a) $k_s/k_c = -50$, (b) $k_s/k_c = -60$, (c) $k_s/k_c = -65$ and (d) $k_s/k_c = -100$.

that of Eq. (2.23):

$$\mathcal{E}_{\text{EOSP}} = -k_{\text{ua}}^{\text{eff}} m_z^2 - \frac{1}{2} k_{\text{ca}}^{\text{eff}} \sum_{\alpha=x,y,z} m_\alpha^4 + k_{2,\text{ca}}^{\text{eff}} m_x^2 m_y^2 m_z^2, \quad (2.25)$$

where $k_{\text{ua}}^{\text{eff}}$ is the effective uniaxial anisotropy constant; $k_{\text{ca}}^{\text{eff}}$ and $k_{2,\text{ca}}^{\text{eff}}$ are the effective first and second cubic anisotropy constants.

For symmetric particles, $k_{\text{ua}}^{\text{eff}} \approx 0$ (see previous sections) and we have observed that $k_{2,\text{ca}}^{\text{eff}}$ is relevant when k_s has a large value, when $k_s > 50|k_c|$, as we can see in Fig. 2.17 and Fig. 2.18.

In Fig. 2.16 we present the minimum and the saddle point spin configurations (on $y = 0$ plane) for $k_s = 350 |k_c|$. We would like to mention that when the surface anisotropy is increased ($k_s \sim 350 |k_c|$) in comparison with the exchange parameter J , then the spin arrangement shows a high non-collinearity. Those spin non-collinearities are similar to the ones reported previously for strong surface anisotropy

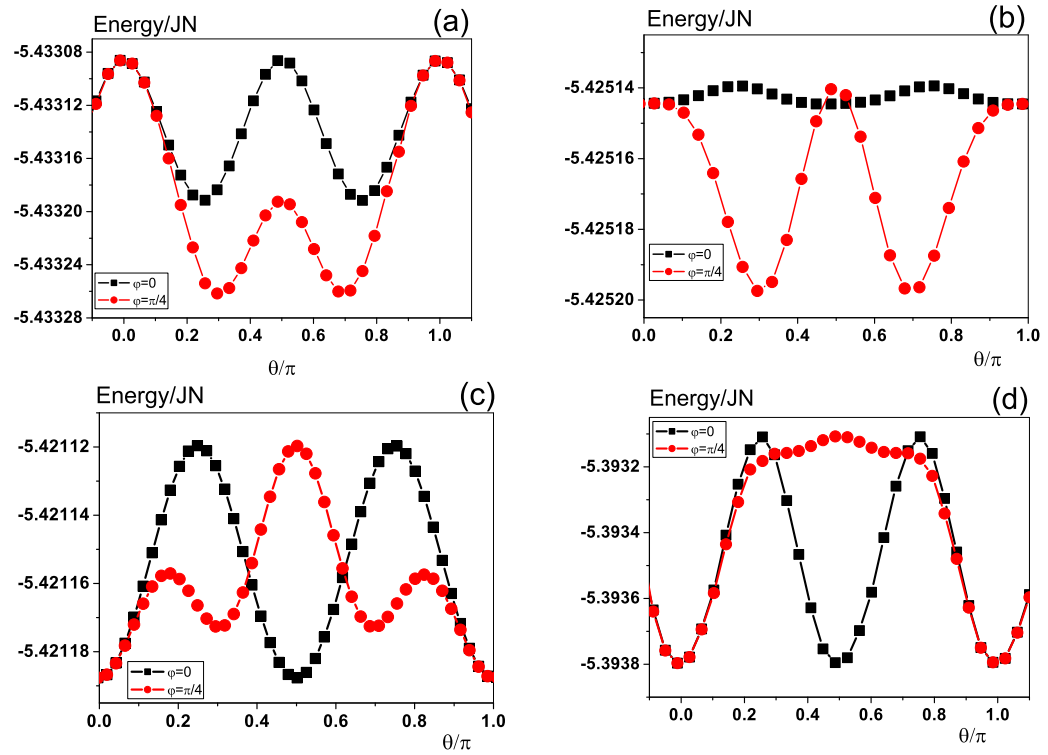


Figure 2.15: 2D energy landscapes of an octahedral many-spin Co particle with $D = 4.5\text{nm}$ for (a) $k_s/k_c = -50$, (b) $k_s/k_c = -60$, (c) $k_s/k_c = -65$ and (d) $k_s/k_c = -100$.

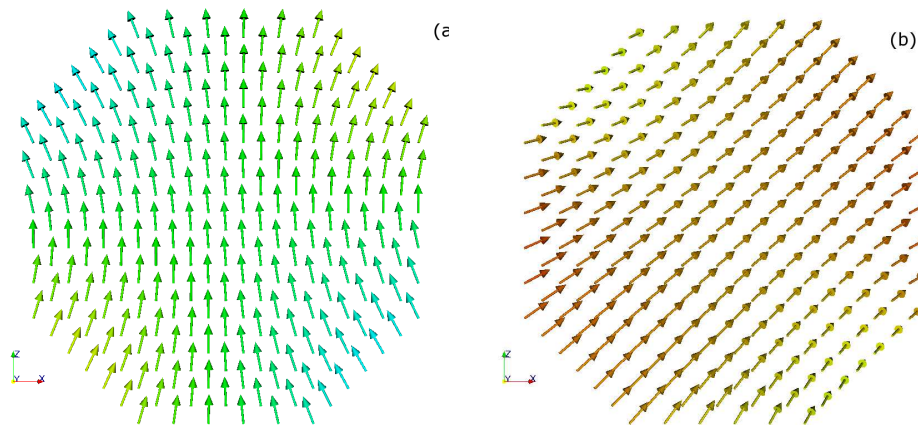


Figure 2.16: Magnetic moment configurations(on $Y = 0$ plane) in Co fcc truncated octahedral nanoparticle with $D = 4.5 \text{ nm}$. and $k_s = 350 | k_c |$: (a) The minimum energy configuration. (b) The saddle point configuration.

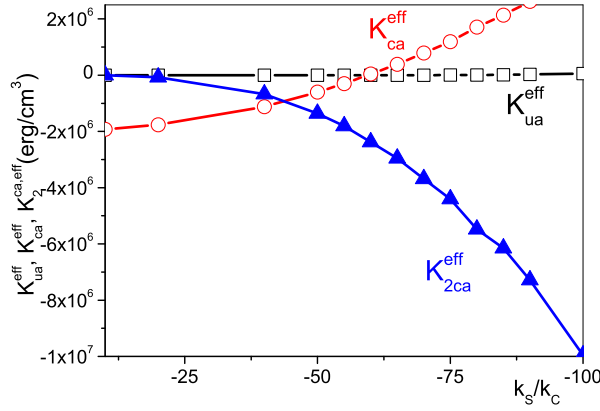


Figure 2.17: Effective anisotropy constants for fcc Co nanoparticles with octahedral shape and $D = 4.5\text{nm}$ as a function of the Néel surface anisotropy K_s , normalized to the core anisotropy K_c .

cases [74, 90, 102, 103], and it is possible that the EOSP approximation is no more valid [73].

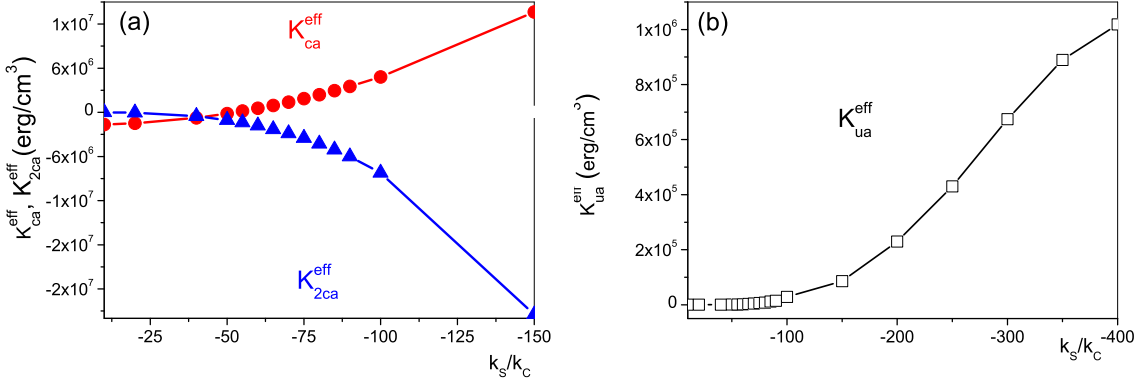


Figure 2.18: Effective anisotropy constants as a function of the surface anisotropy value k_s/k_c for fcc Co octahedral elongated nanoparticle with $e = 1.228$ and $D = 3.1\text{nm}$ (smaller dimension). (a) Cubic constants (left) and (b) uniaxial constant .

In Figs. 2.17 and 2.18 we present the values of the uniaxial and cubic macroscopic anisotropy constants extracted by fitting the 2D landscapes to expression (2.25). To make the comparison with experimental values easier we supply the values of the macroscopic anisotropy as energy density. The effective uniaxial anisotropy constant is zero in practice in the case of a perfect truncated octahedral particle. Nevertheless, for elongated particle, there is a non-zero uniaxial contribution coming from the surface

effect, see Fig. 2.18(b). However its value is much smaller than the additional cubic anisotropy.

In both cases of octahedral and elongated particles the effective macroscopic first cubic anisotropy constant changes the sign, see Figs. 2.17 and 2.18(a), and therefore the easy axis of the system changes its position, as have been shown clearly in Figs. 2.15 and 2.14.

2.9 Conclusions

The main results of the study of the energy landscape in magnetic nanoparticles with different lattices, shapes and the Néel surface anisotropy model are summarized as follows:

- Our numerical calculations have shown that the magnetic behavior of the nanoparticles with Néel surface anisotropy is consistent with the effective one spin particle (EOSP) model with uniaxial and cubic anisotropies. The strength and sign of these additional effective anisotropy constants are dependent on many parameters, including the shape and elongation of the particle, and the underlying crystal structure which produces different spin surface arrangement.
- We have compared the analytical and numerical results for the energy landscapes for many-spin particles cut from sc lattice obtaining a very good agreement.
- We have observed that the cubic anisotropy contribution due to the surface of magnetic nanoparticles has an opposite sign in the case of sc and fcc underlying lattice structures.
- We have studied numerically the effective energy of Co multi-spin nanoparticle with an octahedral shape, fcc lattice structure and cubic core anisotropy as a function of the surface anisotropy magnitude. The results indicate that the surface anisotropy introduces an additional first and second order cubic anisotropy. For elongated particles they also induce an additional uniaxial anisotropy.

Conclusiones

Se ha estudiado la dependencia angular de la energía total con respecto a la dirección de la imanación (paisajes de energía) de nanopartículas magnéticas con diferentes formas, redes cristalinas y valores de la anisotropía de superficie. En estos sistemas la anisotropía de superficie se ha modelado usando el modelo de interacciones a pares tipo Néel. Los principales resultados son los siguientes:

- Nuestras simulaciones muestran que el comportamiento magnético de las nanopartículas con anisotropía de superficie tipo Néel se puede modelar como el de una partícula macroespín efectiva con anisotropía mixta (combinación de anisotropía uniaxial y cúbica). El valor y el signo de las anisotropías efectivas dependen de múltiples parámetros, por un lado de la forma y el alargamiento de las nanopartículas y por otro -de la estructura cristalina que origina diferentes ordenamientos de los momentos magnéticos en la superficie.
- Se obtiene un buen acuerdo al comparar los cálculos analíticos con los numéricos para los paisajes de energía de las nanopartículas multi-espín con estructura cristalina tipo simple cúbica.
- Se observan signos opuestos para el término de anisotropía cúbica originada por la superficie si la nanopartícula posee una red cristalina sc o fcc.
- Se han estudiado las nanopartículas de cobalto con una forma octaédrica truncada perfecta o alargada con estructura cristalina tipo fcc, anisotropía en el núcleo de la partícula tipo cúbica y anisotropía de superficie tipo Néel. Los resultados obtenidos de los paisajes de energía indican que la anisotropía de superficie induce dos contribuciones a la anisotropía cúbica efectiva del sistema: de primer y segundo orden. En el caso de partículas alargadas se observa que la anisotropía de superficie induce además una anisotropía uniaxial.

3

Energy barriers of magnetic multispin nanoparticles with Néel surface anisotropy

3.1 Motivation

How long the magnetization can remain fixed in a determinate direction is one of the key questions in magnetism, or equivalently the determination of the stability of a magnetic system. It is worth pointing out here that any discussion of magnetic stability will involve evaluation of the energy barrier separating the two magnetic states, because this controls the energy required to change magnetic moment of a system from one direction to another by means of thermal activation. The probability of the switching of the magnetization is related to the energy barrier through the Arrhenius-Néel law [53].

$$f(t) = f_0 \exp^{-\frac{\Delta E}{K_B T}}. \quad (3.1)$$

Here the prefactor f_0 is the attempt frequency, ΔE is the energy barrier, K_B is the Boltzmann constant, and T is the temperature of the system.

Experimentally the relevant energy barrier ΔE may be extracted from the measurement of the blocking temperature T_B . It has been widely reported that the surface effects can modify the energy barrier through a modification of the "effective anisotropy", \mathcal{K}^{eff} [9, 14, 20, 32, 36]. The effective anisotropy constant simply may be defined through the energy barrier as:

$$\mathcal{K}^{eff} = \Delta E/V, \quad (3.2)$$

where V is the volume of the nanoparticle. In the case of magnetic nanoparticle modeled by a macro-spin approximation with bulk uniaxial or cubic magnetocrystalline anisotropy, the energy barrier has the following dependence on the core anisotropy constant (K_c), defined here as a macroscopic anisotropy energy density:

$$\Delta E/V = \begin{cases} K_c & \text{uniaxial anisotropy} \\ \frac{K_c}{4} & \text{cubic anisotropy with } K_c > 0 \\ \frac{|K_c|}{12} & \text{cubic anisotropy with } K_c < 0 \end{cases} \quad (3.3)$$

Therefore, the analysis of the energy potential is unavoidable since it is a crucial step in calculating relaxation rates and thereby in the study of the magnetization stability against thermal-activated reversal.

3.1.1 Phenomenological expression for the effective anisotropy constant in a system with surface anisotropy

The influence of the surface manifests itself in the fact that the values $\Delta E/V$ are often found experimentally to be different from that of the bulk, i.e. there is an effective anisotropy \mathcal{K}^{eff} that is not exactly proportional to the particle's volume V . One can expect that the effect of the surface reduces when the particle size increases. The volume dependence of the effective anisotropy is often analyzed on the basis of a simple model:

$$\mathcal{K}^{eff} = \mathcal{K}_\infty + \frac{S}{V} \mathcal{K}_S \quad (3.4)$$

where \mathcal{K}_∞ is the anisotropy constant for an infinite system, presumably it is equal to the bulk anisotropy constant, and \mathcal{K}_S is the effective surface anisotropy constant, S and V are the surface and the volume of the system respectively. For spherical particles with diameter D it has been suggested that the effective anisotropy constants also adjust to a similar phenomenological expression [36]:

$$\mathcal{K}^{eff} = \mathcal{K}_\infty + \frac{6}{D} \mathcal{K}_S \quad (3.5)$$

We can find a modified version of this formula. For example, Luis et.al., in the study of the magnetic behavior of fcc Co nanoparticles embedded in different non-magnetic matrices [10], supposed the following relation between the effective anisotropy and the bulk and surface anisotropies, corrected by the fact that the surface spins do not feel the bulk anisotropy.

$$\mathcal{K}^{eff} = (1 - f) \mathcal{K}_V + f \cdot \mathcal{K}_S^* \quad (3.6)$$

where f is the surface atom fraction, $f \approx 1 - (1 - a/D)^3$ and a is the lattice parameter. Here \mathcal{K}_S^* represents the surface anisotropy contribution to the effective anisotropy. Note that it has different dimensions than the surface anisotropy in Eq. (3.5).

3.2 Energy barriers from the effective one spin problem (EOSP)

In what follows we consider a magnetic system of \mathcal{N} spins in the classical many-spin approach, i.e., taking into account its intrinsic properties such as the lattice structure, shape and size. The magnetic properties of such system are described by the anisotropic Heisenberg model of classical spins \mathbf{S}_i (with $|\mathbf{S}_i| = 1$), described in Eq. (2.1), where the the anisotropy constants are measured in energy units per spin.

As we have shown in the previous chapter, under certain conditions the energy potential of such muti-spin particle can be mapped onto an EOSP model, in such way that the effective energy potential has the form:

$$\mathcal{E}_{\text{EOSP}} = -k_{\text{ua}}^{\text{eff}} m_z^2 - \frac{1}{2} k_{\text{ca}}^{\text{eff}} \sum_{\alpha=x,y,z} m_{\alpha}^4 \quad (3.7)$$

First, we investigate the minima, maxima and saddle points of the effective potential (3.7) for different values and signs of the parameters $k_{\text{ua}}^{\text{eff}}$ and $k_{\text{ca}}^{\text{eff}}$, and calculate analytically the energy barriers in each case. The results are presented in Tab. 3.1.

In the previous chapter we have shown that although the magnetic behavior of the multi-spin particle can be mapped onto an effective one spin problem, its energy landscape can have a very complex character if the effective potential has two competing anisotropies, this fact is reflect in the results shows in Tab. 3.1. In some cases there are multiple energy barriers, but in foregoing we will consider only the relevant energy barrier for switching, corresponding to the lowest energy path between the global minima. Nevertheless, we would like remark that for large surface anisotropy $|\zeta| \gg 1$, where $\zeta = k_{\text{ca}}^{\text{eff}}/k_{\text{ua}}^{\text{eff}}$, all energy barriers are simple linear combinations of the two effective anisotropy constants. The energy barriers for the case $k_{\text{ua}}^{\text{eff}} > 0$ are plotted in Fig. 3.1 as a function of the parameter ζ .

Here we only present analytical expressions based on the potential (3.7) with direct relevance to the results presented in the previous chapter for spherical, octahedral and elongated nanoparticles. We have seen that in the case of a spherical particle cut from an sc lattice, and in accordance with the EOSP energy potential (3.7), $k_{\text{ua}}^{\text{eff}} > 0$ and $k_{\text{ca}}^{\text{eff}} < 0$ (see Fig. 2.5). For a spherical particle with an fcc lattice, $k_{\text{ua}}^{\text{eff}} > 0, k_{\text{ca}}^{\text{eff}} > 0$, as can be seen in Fig. 2.8. Finally for ellipsoidal and truncated octahedral multi-spin particles (MSPs), the results in Figs. 2.10 and 2.12 show that $k_{\text{ua}}^{\text{eff}}$ may become negative at some value of k_s , since then the contributions similar to (2.21) and (2.16) become important.

So, when $k_{\text{ua}}^{\text{eff}} > 0$ and $k_{\text{ca}}^{\text{eff}} < 0$, from Eq. (3.7) we find

$$\Delta E_{\text{EOSP}} = \begin{cases} k_{\text{ua}}^{\text{eff}} + \frac{1}{4} k_{\text{ca}}^{\text{eff}}, & (a) \quad |\zeta| < 1 \\ \frac{1}{3} k_{\text{ua}}^{\text{eff}} - \frac{1}{12} k_{\text{ca}}^{\text{eff}} - \frac{(k_{\text{ua}}^{\text{eff}})^2}{3k_{\text{ca}}^{\text{eff}}}, & (b) \quad |\zeta| > 1 \end{cases} \quad (3.8)$$

Table 3.1: Energy barriers for effective one-spin particle. The critical angle $\theta_c(\varphi)$ is defined by $\cos^2 \theta_c(\varphi) = (k_{\text{ua}}^{\text{eff}} + k_{\text{ua}}^{\text{eff}}(\sin^4 \varphi + \cos^4 \varphi))/(k_{\text{ca}}^{\text{eff}}(1 + \sin^4 \varphi + \cos^4 \varphi))$ and φ is the azimuthal angle.

$k_{\text{ua}}^{\text{eff}} > 0$				
$\zeta = k_{\text{ca}}^{\text{eff}}/k_{\text{ua}}^{\text{eff}}$	Minima (θ, φ)	Saddle points (θ, φ)	Energy barriers, ΔE_{EOSP}	
$-\infty < \zeta < -1$	$\theta_c(\pi/4); \pi/4$	$\pi/2; \pi/4$	$\frac{k_{\text{ua}}^{\text{eff}}}{3} - \frac{k_{\text{ca}}^{\text{eff}}}{12} - \frac{(k_{\text{ua}}^{\text{eff}})^2}{3k_{\text{ca}}^{\text{eff}}}$	(1.1)
	$\theta_c(\pi/4); \pi/4$	$\theta_c(\pi/2); \pi/2$	$-\frac{k_{\text{ua}}^{\text{eff}}}{6} - \frac{k_{\text{ca}}^{\text{eff}}}{12} - \frac{(k_{\text{ua}}^{\text{eff}})^2}{12k_{\text{ca}}^{\text{eff}}}$	(1.2)
$-1 < \zeta < 0$	$0; 0$	$\pi/2; 0$	$k_{\text{ua}}^{\text{eff}} + \frac{k_{\text{ca}}^{\text{eff}}}{4}$	(2)
$0 < \zeta < 1$	$0; \pi/2$	$\pi/2; \pi/2$	$k_{\text{ua}}^{\text{eff}}$	(3)
$1 < \zeta < 2$	$\theta_c(0); \pi/2$	$\theta_c(\pi/2); \pi/2$	$\frac{k_{\text{ua}}^{\text{eff}}}{2} + \frac{k_{\text{ca}}^{\text{eff}}}{4} + \frac{(k_{\text{ua}}^{\text{eff}})^2}{4k_{\text{ca}}^{\text{eff}}}$	(4.1)
	$\pi/2; \pi/2$	$\theta_c(\pi/2); \pi/2$	$-\frac{k_{\text{ua}}^{\text{eff}}}{2} + \frac{k_{\text{ca}}^{\text{eff}}}{4} + \frac{(k_{\text{ua}}^{\text{eff}})^2}{4k_{\text{ca}}^{\text{eff}}}$	(4.2)
$2 < \zeta < \infty$	$0; \pi/2$	$\theta_c(\pi/2); \pi/2$	$\frac{k_{\text{ua}}^{\text{eff}}}{2} + \frac{k_{\text{ca}}^{\text{eff}}}{4} + \frac{(k_{\text{ua}}^{\text{eff}})^2}{4k_{\text{ca}}^{\text{eff}}}$	(5.1)
	$\pi/2; \pi/2$	$\pi/2; \pi/4$	$\frac{k_{\text{ca}}^{\text{eff}}}{4}$	(5.2)
	$\pi/2; \pi/2$	$\theta_c(\pi/2); \pi/2$	$-\frac{k_{\text{ua}}^{\text{eff}}}{2} + \frac{k_{\text{ca}}^{\text{eff}}}{4} + \frac{(k_{\text{ua}}^{\text{eff}})^2}{4k_{\text{ca}}^{\text{eff}}}$	(5.3)
$k_{\text{ua}}^{\text{eff}} < 0$				
$-\infty < \zeta < -1$	$\pi/2; \pi/2$	$\theta_c(\pi/2); \pi/2$	$-\frac{k_{\text{ua}}^{\text{eff}}}{2} + \frac{k_{\text{ca}}^{\text{eff}}}{4} + \frac{(k_{\text{ua}}^{\text{eff}})^2}{4k_{\text{ca}}^{\text{eff}}}$	(6.1)
	$\pi/2; 0$	$\pi/2; \pi/4$	$\frac{k_{\text{ca}}^{\text{eff}}}{4}$	(6.2)
	$0; \pi/2$	$\theta_c(\pi/2); \pi/4$	$\frac{k_{\text{ua}}^{\text{eff}}}{2} + \frac{k_{\text{ca}}^{\text{eff}}}{4} + \frac{(k_{\text{ua}}^{\text{eff}})^2}{4k_{\text{ca}}^{\text{eff}}}$	(6.3)
$-1 < \zeta < 0$	$\pi/2; 0$	$\pi/2; \pi/4$	$\frac{k_{\text{ca}}^{\text{eff}}}{4}$	(7)
$0 < \zeta < 1$	$\pi/2; \pi/4$	$\pi/2; \pi/2$	$\frac{k_{\text{ca}}^{\text{eff}}}{4}$	(8)
$1 < \zeta < 2$	$\pi/2; \pi/4$	$\theta_c(\pi/2); \pi/2$	$-\frac{k_{\text{ua}}^{\text{eff}}}{2} + \frac{(k_{\text{ua}}^{\text{eff}})^2}{4k_{\text{ca}}^{\text{eff}}}$	(9)
$2 < \zeta < \infty$	$\theta_c(\pi/4); \pi/4$	$\pi/2; \pi/4$	$-\frac{k_{\text{ua}}^{\text{eff}}}{6} - \frac{k_{\text{ca}}^{\text{eff}}}{12} - \frac{(k_{\text{ua}}^{\text{eff}})^2}{3k_{\text{ca}}^{\text{eff}}}$	(10.1)
	$\theta_c(\pi/4); \pi/4$	$\theta_c(\pi/2); \pi/2$	$\frac{k_{\text{ua}}^{\text{eff}}}{3} - \frac{k_{\text{ca}}^{\text{eff}}}{12} - \frac{(k_{\text{ua}}^{\text{eff}})^2}{12k_{\text{ca}}^{\text{eff}}}$	(10.2)

In the case $k_{\text{ca}}^{\text{eff}} > 0$, the energy barriers read,

$$\Delta E_{\text{EOSP}} = \begin{cases} k_{\text{ua}}^{\text{eff}}, & k_{\text{ua}}^{\text{eff}} > 0 \quad (a) \\ \frac{1}{4}k_{\text{ca}}^{\text{eff}}, & k_{\text{ua}}^{\text{eff}} < 0 \quad (b) \\ \frac{1}{2}k_{\text{ua}}^{\text{eff}} + \frac{1}{4}k_{\text{ca}}^{\text{eff}} + \frac{(k_{\text{ua}}^{\text{eff}})^2}{4k_{\text{ca}}^{\text{eff}}} & \quad (c) \end{cases} \quad |\zeta| < 1 \quad | \zeta | > 1.$$
(3.9)

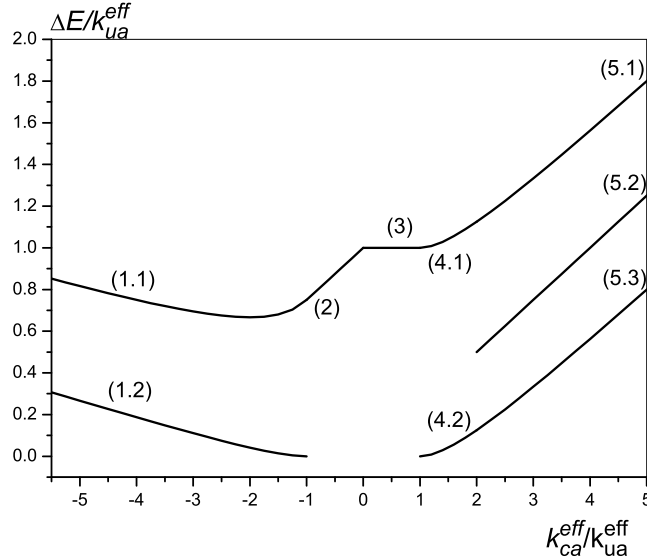


Figure 3.1: The relevant (i.e. lowest) energy barriers of the EOSP estimated analytically from the potential (3.7) as a function of $\zeta = k_{ca}^{\text{eff}}/k_{ua}^{\text{eff}}$ with $k_{ua}^{\text{eff}} > 0$. The number in brackets correspond to the formula number in Tab. 3.1

3.3 Dependence of the energy barrier on the value of the surface anisotropy constant k_s

As we have shown in the previous chapter, the numerical evaluation of the energy barrier should be done in a multidimensional space and it is a difficult task. With this aim we use the Lagrange-multiplier method described in section 2.4. We evaluate the energy barriers of multi-spin particles (MSPs) by numerically computing the difference between the energy at the saddle point and at the minimum, and compare them with analytical results obtained from the EOSP approximation.

Note that in the wide range of the parameters several energy barriers (corresponding to different paths of magnetization rotation) coexist in the system in accordance with the complex character of the effective potential with two competitive anisotropies, see Figs. 2.3(c) and 2.9(c). In what follows, in most cases we will only discuss the energy barrier which corresponds to the change in θ direction. In the case corresponding to elongated nanoparticles cut from fcc lattice and uniaxial anisotropy in the core, see Fig. 2.9(d), the only energy barrier corresponds to the rotation around φ direction.

Fig. 3.2 shows the energy barrier of a spherical particle cut from an sc lattice as a function of k_s . The nonlinear behavior of the energy barrier with k_s follows quantitatively that of the EOSP potential (3.7). Indeed, the solid line in this plot is

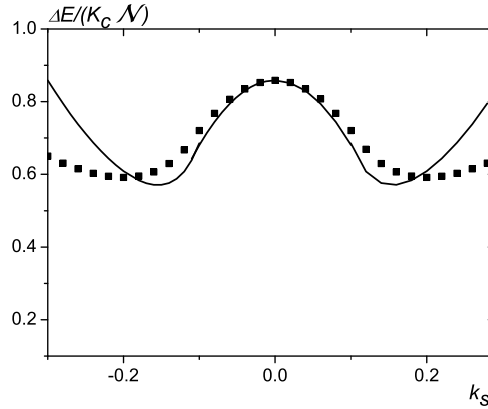


Figure 3.2: Energy barrier as a function of k_s for a spherical particle cut from an sc lattice. The particle contains $\mathcal{N} = 20479$ spins and has the uniaxial core anisotropy $k_c = 0.0025$. The solid line is a plot of the analytical expression (3.8).

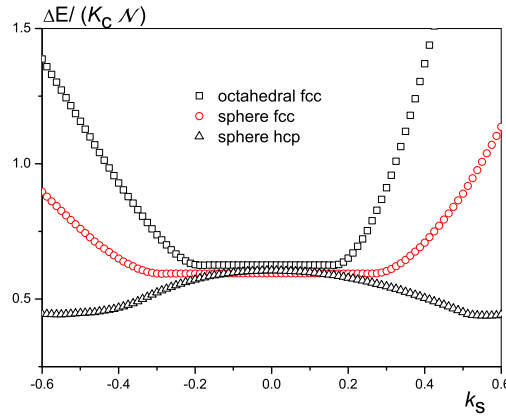


Figure 3.3: Energy barriers against k_s for truncated octahedral multi-spin particle cut from an fcc lattice ($\mathcal{N} = 1688$) and spherical particles cut from the fcc ($\mathcal{N} = 1289$) and hcp ($\mathcal{N} = 1261$) lattices. Uniaxial core anisotropy with $k_c = 0.0025$ is assumed.

the analytical result (3.8), using analytical expressions of Eqs. (2.14-2.15) together with the pure core anisotropy contribution. The discrepancy at the relatively large k_s is due to the fact that the analytical expressions are valid only if the condition (2.22) is fulfilled; the core-surface mixing (CSM) contribution has not been taken into account.

In Fig. 3.3 we represent the energy barriers as a function of k_s for MSPs with different shapes and internal structures. First of all, one can see a different dependence

on k_s as compared to MSPs with the sc lattice. In the present case, i.e., $k_{\text{ua}}^{\text{eff}} > 0, k_{\text{ca}}^{\text{eff}} > 0$, the energy barriers are given by Eqs. (3.9)(a) and (c). For small values of k_s , for which $|\zeta| < 1$, the energy barrier, in the first approximation neglecting the CSM term, is independent of k_s . Accordingly, the nearly constant value of the energy barrier, coinciding with that of the core, is observed for multi-spin particles in a large range of k_s . For larger k_s , the energy barrier increases, since $k_{\text{ua}}^{\text{eff}} > 0$ for multi-spin particles cut from an fcc lattice. At very large values of k_s , i.e., $k_s \gtrsim 100k_c$ the energy barriers depend approximately linearly on k_s and may have values larger than that inferred from the pure core anisotropy.

The energy barriers for ellipsoidal multi-spin particles are shown in Fig. 3.4. Note

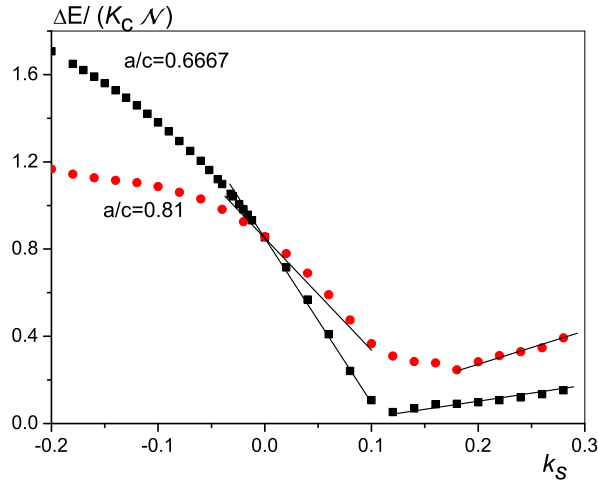


Figure 3.4: Energy barriers versus k_s of ellipsoidal multi-spin particles with different aspect ratio ($a/c = 0.6667, \mathcal{N} = 21121$, and $a/c = 0.81, \mathcal{N} = 21171$, with uniaxial core anisotropy $k_c = 0.0025$). The solid lines are linear fits.

that in this case the effective uniaxial anisotropy constant $k_{\text{ua}}^{\text{eff}}$ is a linear function of k_s , according to the analytical results (2.16), (2.17) and the numerical results presented in Fig. 2.10. In this case the value of the energy barrier is not symmetric with respect to the change of the sign of k_s . This is due to the fact that for $k_s < 0$ the effective uniaxial constant is a sum of the core anisotropy and the first-order contribution owing to elongation. On the contrary, when $k_s > 0$, the "effective core anisotropy" $k_{\text{ua}}^{\text{eff}}$ is smaller than the pure core anisotropy \mathcal{E}_c in Eq. (2.6). This means that at some k_s the effective uniaxial anisotropy constant ($k_{\text{ua}}^{\text{eff}}$) may change sign. At the same time the effective cubic anisotropy $k_{\text{ca}}^{\text{eff}}$ remains positive and is proportional to k_s^2 . Accordingly, at the vicinity of the point at which $k_{\text{ca}}^{\text{eff}} \approx 0$, rapid changes of the character of the energy landscape occur as we have shown in Fig. 2.10 in the previous chapter.

The analysis, based on the effective one spin problem potential shows that when $k_{ua}^{\text{eff}} > 0$ the energy barriers of ellipsoidal multi-spin particles are defined by Eqs. 3.9(a) and (c), and for negative $k_{ua}^{\text{eff}} < 0$ these are given by Eq. 3.9(b) and (c).

We would like to note that a regime of linear behavior in k_s exists for both $k_s < 0$ and $k_s > 0$ (see Fig. 3.4). In some region of the effective anisotropy constants, e.g., $k_{ua}^{\text{eff}} > 0$, $|\zeta| < 1$, the energy barrier $\Delta E_{\text{EOSP}} = k_{ua}^{\text{eff}}$, i.e., it is independent of the cubic contribution (neglecting again the CSM term). Consequently, it is linear in k_s , according to Eq. (2.17). The interval of these parameters is especially large in MSPs with $k_s < 0$ for which k_{ua}^{eff} does not change sign.

3.4 Dependence of the energy barrier on the system size

As $\mathcal{N} \rightarrow \infty$, the influence of the surface effects should become weaker and the energy barriers should recover the full value $K_c \mathcal{N}$, this convergence has been shown to be slow [74].

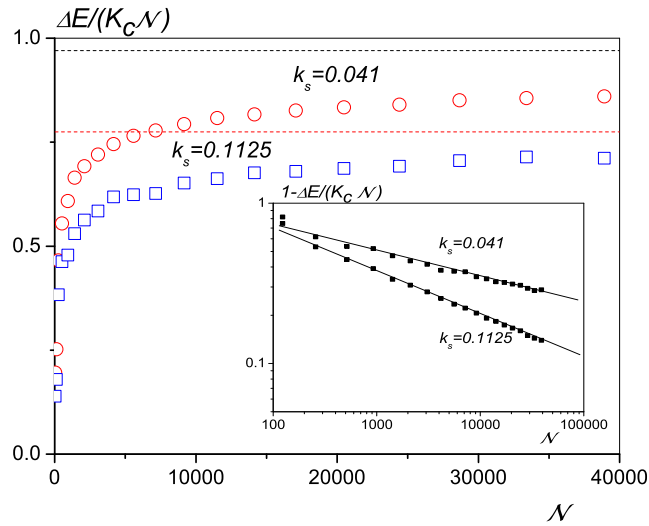


Figure 3.5: Energy barrier as a function of the total number of spins \mathcal{N} for two different values of the surface anisotropy, spherical particles cut from the sc lattice with uniaxial anisotropy $k_c = 0.0025$ in the core. The inset shows a slow dependence of the difference between these results and the uniaxial one-particle energy barrier $K_c \mathcal{N}$ in the logarithmic scale. The lines in the inset are the analytical expressions 2.3 and 2.14, see section 2.3

Fig. 3.5 shows the values of the energy barriers as a function of the total number of spins \mathcal{N} in particles with spherical shape cut from an sc lattice and with two values of $k_s > 0$. First of all, we note that in this case the main contribution to the effective

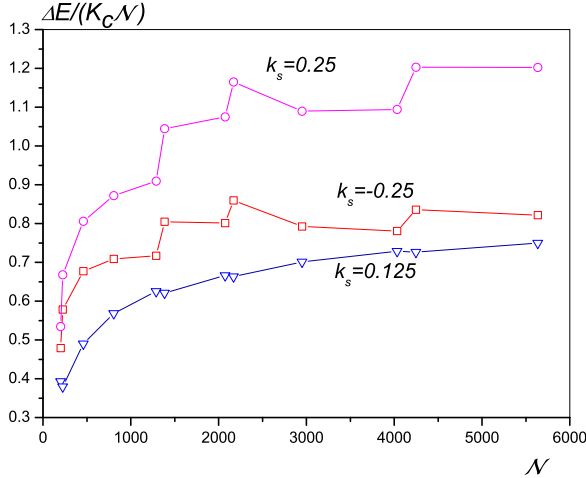


Figure 3.6: Energy barriers versus \mathcal{N} for truncated octahedra with internal fcc structure and uniaxial core anisotropy $k_c = 0.0025$.

anisotropy consists of two terms: the core anisotropy and the surface second-order contribution (2.14). In agreement with this all energy barriers of these particles are always smaller than $K_c \mathcal{N}$, since as we showed previously for the sc lattice, k_{ca}^{eff} is negative and the energy barriers in this case are defined by Eq. (3.8).

Both uniaxial core anisotropy \mathcal{E}_c and the main contribution to the effective cubic anisotropy \mathcal{E}_2 scale with \mathcal{N} , see section 2.3. As $\mathcal{N} \rightarrow \infty$, the core anisotropy contribution slowly recovers its full value, i.e., $\mathcal{E}_c/(K_c \mathcal{N}) \rightarrow 1$. However, from the analytical expressions 2.3 and 2.14, when neglecting the CSM contribution, $\Delta E/(K_c \mathcal{N})$ should approach the value $1 - \kappa k_s^2 / 12k_c$, which is independent of the system size. Hence, we may conclude that it is the CSM contribution (2.20) that is responsible for the recovering of the full one-spin uniaxial potential. However, being very small, this contribution produces a very slow increment of the energy barrier. In fact, we have estimated that even spherical particles of diameter $D = 20$ nm (an estimation based on the atomic distance of 4 Å) would have an effective anisotropy $\Delta E/(K_c \mathcal{N})$ that is 13% smaller than that of the bulk.

Truncated octahedra particles, see Fig. 3.6, show a behavior similar to that of the spherical particles. The energy barriers in this case behave very irregularly due to the rough variation of the number of atoms on the surface. The same effect was observed in other particles of small sizes. For truncated octahedra particles this effect arises as a consequence of non-monotonic variation of the number of spins on the surface for particles cut from regular lattices. The effective anisotropy of truncated octahedra particles with large $k_s > 0$ is larger than the core anisotropy in accordance with the fact

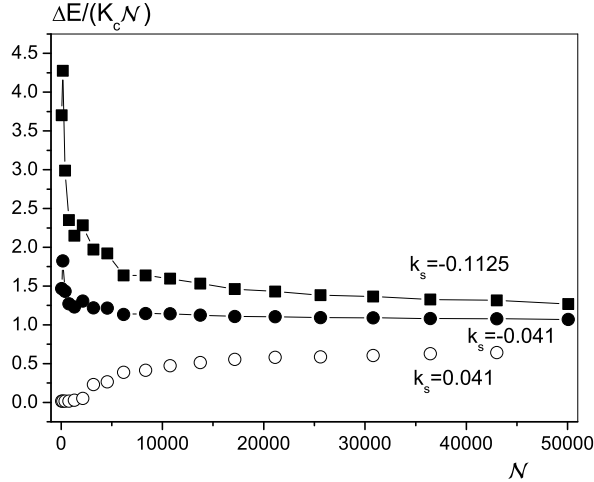


Figure 3.7: Energy barriers as a function of the particle size for ellipsoidal particles with internal sc structure, uniaxial anisotropy $k_c = 0.0025$ and different values of k_s .

that k_{ca}^{eff} is positive for fcc structures and the energy barriers are defined by Eqs. (3.9).

Finally, in Fig. 3.7 we present the energy barriers of ellipsoidal particles with different values of k_s . According to formulas (3.9)(b) and (c), particles with $k_s < 0$ have energy barriers larger than that inferred from the core anisotropy, and for those with $k_s > 0$ the energy barriers are smaller. In this case, the energy barrier scales with the number of surface spins N_s (see Fig. 3.8), in agreement with the first-order contribution from elongation (2.17).

3.5 On the applicability of the formula $\mathcal{K}_{\text{eff}} = \mathcal{K}_\infty + 6\mathcal{K}_s/D$

The results presented above show that in the most general case, studied here, of a multi-spin particle with Néel surface anisotropy, this formula is not applicable, for the following reasons:

- (i) It assumes that the overall anisotropy of the particle remains uniaxial. However, we have shown that the surface anisotropy induces an additional cubic contribution.
- (ii) It assumes that the surface anisotropy always enhances that in the core. In this and the previous sections we saw that both situations can arise.
- (iii) It is implicitly based on the hypothesis that the core and surface anisotropies are additive contributions. As we have seen above for large k_s the energy barrier indeed can be represented as a sum of the effective cubic and uniaxial anisotropies.

However, the cubic anisotropy term is proportional to k_s^2 , which is inconsistent with formula (3.5).

- (iv) It assumes linear dependence of energy barriers on the parameter $1/D$, or equivalently N_s/\mathcal{N} .

Consequently, spherical or octahedral particles cannot be described by formula (3.5), since in this case:

- (i) No term linear in k_s is obtained.
- (ii) No term scales as the ratio of the surface-to-volume number of spins N_s/\mathcal{N} .

However, in the case of elongated particles with a not too large surface anisotropy, i.e., $|\zeta| < 1$, the energy barriers are independent of the effective cubic anisotropy. In this case, for weakly ellipsoidal particles, for example, we may write

$$\Delta E_{EOSP} = k_{\text{ua}}^{\text{eff}} \approx k_c N_c / \mathcal{N} + A |k_s| / \mathcal{N}^{1/3} \quad (3.10)$$

where A is a parameter that depends on the particle's elongation and surface arrangement, and which is positive for $k_s < 0$ and negative in the opposite case. Hence, the behavior is as predicted by this formula (3.5). The approximately linear behavior in N_s/\mathcal{N} was also observed in the case of large surface anisotropy $\zeta \gg 1$ (see Fig. 3.1). However, in this case at $\mathcal{N} \rightarrow \infty$, the “uniaxial anisotropy term” \mathcal{K}_{∞} is renormalized by the effective cubic anisotropy $k_{\text{ca}}^{\text{eff}} \sim k_s^2$. In Fig. 3.8 we plot the energy barriers of small ellipsoidal particles with sc structure, aspect ratio 2:3, and $k_s < 0$ from Fig. 3.7. For such particles, the formula (3.5) should be modified as $\mathcal{K}_{\text{eff}} = \mathcal{K}_{\infty} + |\mathcal{K}_s| N_s / \mathcal{N}$. Accordingly, in Fig. 3.8 we plot the energy barrier against N_s/\mathcal{N} . These data are well fitted to straight lines, especially when small particle sizes are removed. We note that in the case of relatively small surface anisotropy $k_s = -0.041$ (though 17 times larger than that in the core), the full core anisotropy $\mathcal{K}_{\infty} = K_c/v$ (v is the atomic volume) can be extracted. However, for the larger surface anisotropy $k_s = -0.1125$, \mathcal{K}_{∞} is renormalized by the surface contribution, defined by Eq. (2.15). On the other hand, it is not possible to extract the value of k_s , since the exact proportionality coefficient of Eq. (2.17) (the value of A in Eq. 3.10) is dependent on the particles surface arrangement and elongation. The effective anisotropy constant \mathcal{K}_s obtained from this fit is much smaller than the input value, namely, for $k_s/k_c = 45$ we obtain from the fit $(k_s/k_c)_{\text{eff}} = 4.3$.

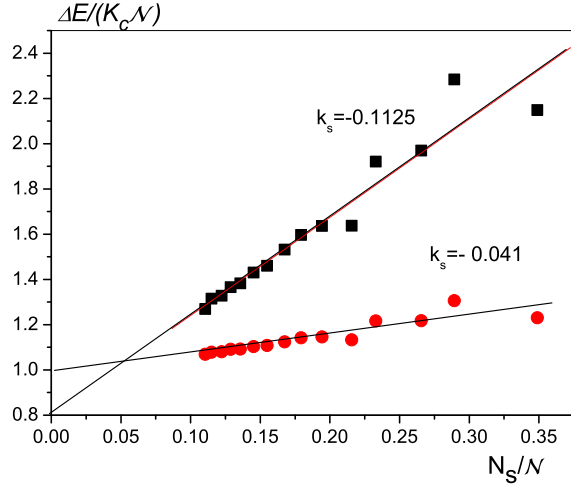


Figure 3.8: Linear fit of energy barriers, versus the ratio of the surface-to-total number of spins N_S/\mathcal{N} , of ellipsoidal particles with aspect ratio 2:3 with $k_s = -0.041$ (circles) and $k_s = -0.1125$ (squares).

3.6 Modeling of energy barriers in cobalt nanoparticle

Experimentally, it has been reported that the surface effects in nanoparticles can lead to a change in the "effective anisotropy" [9, 14, 20, 32, 36], and therefore the surface effects can alter the magnetic behavior of the nanoparticles. Luis. et al. [10] have shown that the fcc Co nanoparticles embedded in different non-magnetic matrices experienced an increment of the effective anisotropy, obtaining $\mathcal{K}^*_S = 25K_V$ (for Al_2O_3 capping), $\mathcal{K}^*_S = 40K_V$ (for Cu capping) and $\mathcal{K}^*_S = 70K_V$ (for Au capping), where $K_V = K_c/4$ and K_c correspond to fcc Co bulk anisotropy. Note that in this case and in agreement with the expression (3.6) used in the experimental study, both surface and volume anisotropies are measured in the same units erg/cm^3 . To comply with the experimental approach in this subsection we also use this definition. In Fig 3.6 we show the reported experimental value of the dependence of the effective anisotropy with the diameter of the cobalt nanoparticles with different cappings. Generally speaking, our results above show that there is no reason to expect this value of the surface anisotropy \mathcal{K}^*_S to coincide with the local on-site surface anisotropy value.

In this section we directly model the effective energy landscapes of multi-spin Co nanoparticles, with typical experimental parameters, varying the strength of the local surface anisotropy value. The obtained effective anisotropy, defined as $K^{eff} = \Delta E/V$, where ΔE is the energy barrier and V is the particle volume, is then compared with those experimentally determined in [10]. Consequently, we get rid of formula

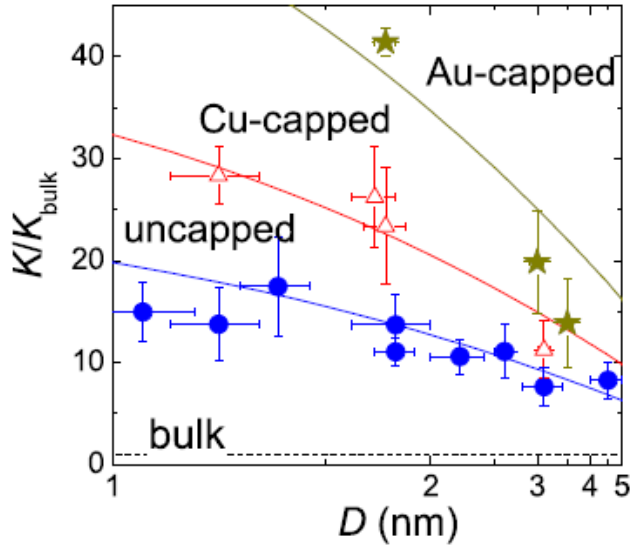


Figure 3.9: Size dependence of the effective anisotropy constant, for cobalt fcc nanoparticles with different cappings (from Ref.[10]).

(3.6) and obtain the local on-site surface anisotropy from a "direct" comparison of the experimental and numerical effective anisotropy constants.

In Figs. 3.10 we present the effective anisotropy constant $K^{eff} = \Delta E/V$ evaluated for truncated octahedral nanoparticles with two diameters $D = 3.1$ nm. and $D = 4.5$ nm., and for an elongated nanoparticle with $e=1.228$ and the smaller dimension $D = 3.1$ nm (experimental parameters). One can see that for $k_s > 100|k_c|$ the energy barriers of multispin particles increase with surface anisotropy increment, confirming multiple experimental results. The horizontal lines in these figures indicate the experimental results for the energy barriers obtained in Refs. [8, 10]. From this comparison we have estimated the corresponding local surface anisotropy values. The uncapped Co nanoparticle would have the same value of the effective anisotropy as bulk Co, provided that $k_s \sim -90k_c$ ($2.5 \times 10^8 \text{ erg cm}^{-3}$); this value is only slightly higher than that estimated from the calculations ($2.2 \times 10^8 \text{ erg cm}^{-3}$) of Daalderop et al [104]. The results for capped nanoparticles are presented in Tab. 3.2. The estimated surface anisotropy values are 20-40 times higher than those obtained via formula (3.6) and are almost of the order of the exchange parameter $k_s \sim 0.4 - 0.7J$. These values look higher than those normally expected. On the other hand they are in agreement with estimations for the surface anisotropy based on first principles in thin films [105].

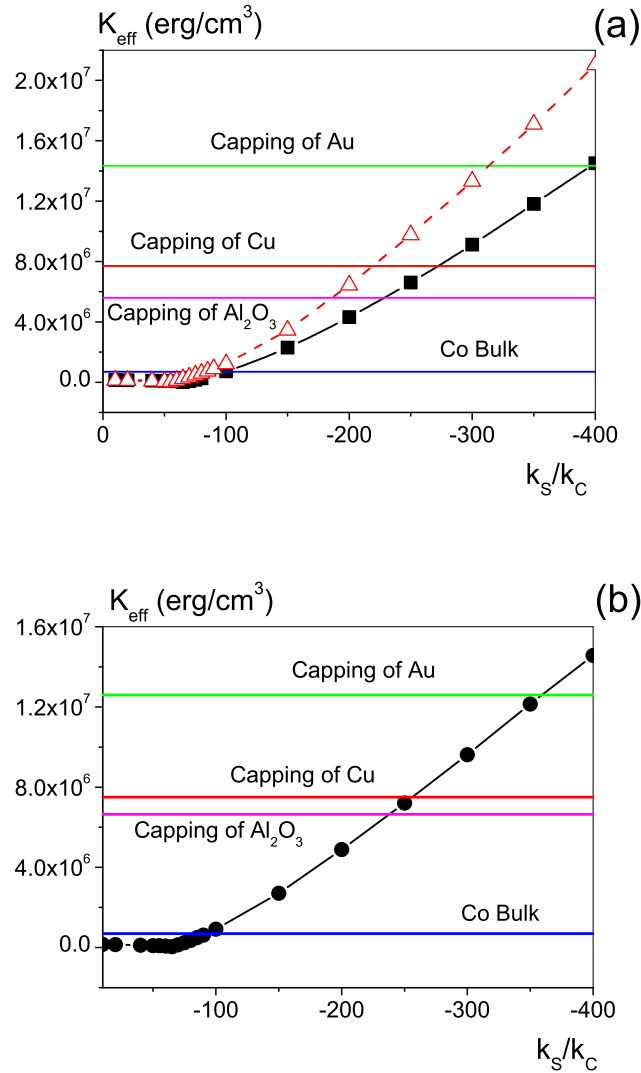


Figure 3.10: Effective anisotropy values $K_{eff} = \Delta E/V$, obtained through energy barrier of Co nanoparticle: (a) Particle with $D = 3.1\text{nm}$ with (dashed line) and without (solid line) elongation $e = 1.228$, (b) octahedral symmetric particle with $D = 4.5\text{nm}$ without elongation. The straight lines indicate experimental results of Ref.[10]

Table 3.2: Surface anisotropy constant for Co nanoparticle with different capping, extracted by comparison between simulation and experimental results in Ref.[10].

Capping	<i>Al₂O₃</i>		Cu		Au	
	$k_s/ k_c $	K_s/J	$k_s/ k_c $	K_s/J	$k_s/ k_c $	K_s/J
Octahedral D=3.1nm	228.92	0.447	273.01	0.532	396.29	0.773
Octahedral D=4.5nm	237.63	0.467	257.60	0.503	360.45	0.703
Elongated particle	187.258	0.365	219.37	0.428	314.076	0.613

3.7 Conclusions

In summary we have evaluated the energy barriers for multispin magnetic nanoparticles with different underlying lattice, shapes, sizes and with the Néel surface anisotropy model. The main results are summarized as follows:

- The energy barriers evaluated in a multidimensional space are complex functions of the system parameters and multiple saddle points can exist. Only in the case of $|\zeta| \gg 1$, where $\zeta = k_{ca}^{\text{eff}}/k_{ua}^{\text{eff}}$, all energy barriers are simple linear combinations of the two effective anisotropy constants.
- We have found energy barriers larger than $K_c\mathcal{N}$ value for all studied symmetric nanoparticles with very large surface anisotropy, $k_s \gtrsim 100k_c$, or for elongated particles with $k_s < 0$. This confirms a well-known fact that the surface anisotropy may contribute to the enhancement of the thermal stability of a magnetic particle.
- We have analyzed the behavior of the energy barriers of different magnetic nanoparticles as a function of their sizes. We have observed that the influence of the surface become weaker when the size of the particle is increased. The energy barriers value recovers the full value $K_c\mathcal{N}$ when $\mathcal{N} \rightarrow \infty$, with very slow convergence.
- We have found that the effective anisotropy values extracted from the energy barriers measurements are consistent with the formula $\mathcal{K}^{\text{eff}} = \mathcal{K}_\infty + \frac{6}{D}\mathcal{K}_S$ only for elongated nanoparticles. This formula is never fulfilled in perfect spherical or truncated octahedral nanoparticles.
- We have studied Co fcc nanoparticles prepared experimentally in Ref. [10] varying the strength of the surface anisotropy constant. The energy barriers were fitted to the experimentally measured energy barriers values for nanoparticles with different cappings, *Al₂O₃*, Cu and Au [8, 10]. From this comparison we obtained the local surface anisotropy values which are almost of the order of the exchange parameter $k_s \sim 0.4 \div 0.7J$.

Conclusiones

En este capítulo hemos evaluado las barreras de energía de nanopartículas magnéticas multiespín con diferentes redes cristalinas, formas, tamaños y anisotropía de superficie tipo Néel. Los principales resultados de este estudio se resumen a continuación:

- Las barreras de energía evaluadas en un espacio multidimensional son funciones muy complejas de los parámetros del sistema. Sólo en el caso $|\zeta| \gg 1$, donde $\zeta = k_{\text{ca}}^{\text{eff}}/k_{\text{ua}}^{\text{eff}}$, todas las barreras de energía son una simple combinación lineal de la anisotropía cúbica y uniaxial.
- En el caso de las nanopartículas simétricas estudiadas, hemos encontrado que los valores de las barreras de energía son mayores de $K_c\mathcal{N}$ para valores de la anisotropía de superficie altos, $k_s \gtrsim 100k_c$, y también en el caso de las nanopartículas alargadas con $k_s < 0$. Esto confirma el hecho de que la anisotropía de superficie puede contribuir al incremento de la estabilidad térmica de las partículas magnéticas.
- Hemos estudiado el comportamiento de las barreras de energía para diversos tipos de nanopartículas magnéticas en función de su tamaño. Observamos que a medida que el tamaño del sistema aumenta la influencia de la superficie disminuye, de tal forma que para $\mathcal{N} \rightarrow \infty$ la barrera de energía recupera el valor $K_c\mathcal{N}$.
- Hemos analizado la validez de la fórmula $\mathcal{K}^{\text{eff}} = \mathcal{K}_\infty + \frac{6}{D}\mathcal{K}_S$. Para ello hemos obtenido el valor de la anisotropía efectiva a partir de la barrera de energía, observando que la fórmula sólo es válida en el caso de nanopartículas alargadas y nunca se cumple en el caso de nanopartículas perfectamente esféricas u octaédricas truncadas.
- Hemos modelado nanopartículas de cobalto con estructura cristalina fcc similares a las preparadas experimentalmente en Ref. [10]. Las nanopartículas estaban recubiertas de diferentes materiales. Hemos modelado este efecto variando la magnitud de la anisotropía de superficie. A partir del valor de la barrera de energía hemos obtenido numéricamente el valor de la anisotropía magnética efectiva de las nanopartículas, y de la comparación directa con los datos experimentales obtuvimos el valor de la anisotropía de superficie local asociada a cada recubrimiento Al_2O_3 , Cu y Au. El valor de la anisotropía de superficie local obtenida oscilaba entre $k_s \sim 0.4 \div 0.7$ J.

4

The constrained Monte Carlo method and temperature dependence of the macroscopic anisotropy in magnetic thin films

4.1 Motivation and introduction

The temperature dependence of magnetocrystalline anisotropy of pure ferromagnets has been well known for decades, following the Callen-Callen theory [106], who established a scaling law of the anisotropy K with magnetization M . Examples of the systems following this law and classed as pure ferromagnets in the anisotropic sense include Gd with uniaxial anisotropy ($K \propto M^3$) and Fe with cubic anisotropy ($K \propto M^{10}$), in contrast there are other systems such as magnetic transition metal alloys that exhibit more complex temperature dependence. For example, the anisotropy of FePt alloy has been demonstrated to follow $K \propto M^{2,09}$ law [107] or CoPt alloy that shows a $K \propto M^2$ dependence [108].

Recently, the high temperature behavior of magnetic anisotropy has become important due to the applications in heat-assisted magnetic recording (HAMR) [109–111]. The idea of HAMR is based on the heating of the recording media to decrease the writing field of the high anisotropy media (such as FePt) to values compatible with the writing fields provided by conventional recording heads. Since the writing field is proportional to the anisotropy field $H_k = 2K(T)/M(T)$, the knowledge of the scaling behavior of the anisotropy K with the magnetization M has become a paramount

consideration for HAMR[112]. It should be noted that even in relatively simple systems, a simple scaling behavior predicted by the Callen-Callen theory is only valid at temperatures far from the Curie temperature. The systems proposed for HAMR applications can also include more complex composite media such as soft/hard bilayers [113], FePt/FeRh with metamagnetic phase transition [114, 115], or exchange-bias systems [7].

The evaluation of the temperature dependence of magnetic anisotropy is also important for the modeling of the laser-induced demagnetization processes. The thermal decrease of the anisotropy during the laser-induced demagnetization has been shown to be responsible for the optically-induced magnetization precession [116]. Thus the ability to evaluate the temperature dependence of the anisotropy in complex systems at arbitrary temperatures is highly desired from the fundamental and applied perspectives.

In this sense magnetic thin films with surface anisotropy are a representative example of this more complicated situation. Since the surface anisotropy has a different temperature dependence from the bulk, multiple experiments on thin films have demonstrated the occurrence of the spin re-orientation transition from an out-of-plane to in-plane magnetization as a function of the temperature and the thin film thickness [54, 56, 63, 66, 117–120]. The possibility to engineer the re-orientation transition also requires the capability to evaluate the temperature dependence of the surface anisotropy independently from the bulk.

In this chapter we introduce the constrained Monte Carlo method (in the following CMC) for the calculation of the macroscopic temperature dependence of the magnetic anisotropy. We will show the possibility to calculate the temperature-dependent anisotropies in principle with this method. When CMC is combined with detailed magnetic information, such as that available from ab-initio methods (see Ref. [121] and also chapter 6), forms a very powerful method of engineering the temperature dependent properties of a magnetic system. The flexibility of the constrained Monte Carlo method allows for a thorough investigation of the temperature dependence of the Néel surface anisotropy. Since the constrained Monte Carlo is a new method first we test the method and later we investigate the temperature behavior of the surface anisotropy in thin films.

Thin films have attracted a lot of research interest over the past 50 years and so a large body of experimental data exists [66, 118, 122]. Nevertheless, achieving good experimental data on the temperature dependence of surface anisotropy requires the creation of very thin films with very sharp interfaces, which has only been technologically feasible within the last decade. This is because the influence of surface anisotropy is usually determined by varying the thickness of the magnetic layer, so that volume and surface contributions can be separated. For thick films the volume component strongly dominates the overall anisotropy, leading to a large degree of uncertainty in the strength of the surface contribution.

The present chapter is divided into the following sections:

- In section 4.2 we describe the constrained Monte Carlo algorithm and perform several tests.
- In the section 4.3 we present the results of the temperature dependence of the effective magnetic anisotropy in thin films with Néel surface anisotropy.
- And finally, in section 4.4 we summarize the conclusions of these studies.

Atomistic model

We consider a magnetic system of \mathcal{N} spins in the classical many-spin approach, i.e., taking account of its intrinsic properties such as the lattice structure and system size. The magnetic properties of such system are described by the anisotropic Heisenberg model for classical spins \mathbf{S}_i (with $|\mathbf{S}_i| = 1$). The Hamiltonian includes the (nearest-neighbor) exchange interactions, single-site bulk (K_c) and Néel surface anisotropy (K_s):

$$\mathcal{H} = -\frac{1}{2}J \sum_{i,j} \mathbf{S}_i \cdot \mathbf{S}_j + \mathcal{H}_{\text{anis}}. \quad (4.1)$$

where J is the exchange parameter.

The anisotropy energy $\mathcal{H}_{\text{anis}}$ will be different if we are working with bulk spins or surface spins. For bulk spins, i.e., those spins with full coordination, the anisotropy energy $\mathcal{H}_{\text{anis}}$ is taken either as uniaxial with easy axis along z and anisotropy constant K_c (per atomic volume), that is

$$\mathcal{H}_{\text{anis}}^{\text{uni}} = -K_c \sum_{i=1}^{N_c} V_i S_{i,z}^2 \quad (4.2)$$

or cubic,

$$\mathcal{H}_{\text{anis}}^{\text{cub}} = -\frac{1}{2}K_c \sum_{i=1}^{N_c} V_i (S_{i,x}^4 + S_{i,y}^4 + S_{i,z}^4) \quad (4.3)$$

where V_i is the volume of the atomic atom i , N_c is the number of bulk spins in the thin film. For surface spins the anisotropy is taken according to the Néel's model, expressed as:

$$\mathcal{H}_{\text{anis}}^{\text{NSA}} = \frac{K_s}{2} \sum_{i=1}^{N_s} \sum_{j=1}^{z_i} V_i (\mathbf{S}_i \cdot \mathbf{u}_{ij})^2, \quad (4.4)$$

where N_s is the number of surface spins, z_i the number of nearest neighbors of site i , and \mathbf{u}_{ij} a unit vector connecting this site to its nearest neighbors labeled by j .

The magnetic systems modeled in this chapter are thin films. The magnetic parameters of the system under study are presented in table 4.1.

Lattice	$a(\text{nm})$	$K_c (10^6 \text{erg/cc})$	$J(10^{-14} \text{erg})$	$M_S(\text{emu/cc})$
sc	0.3548	4.16	10	1260.38
fcc	0.3548	4.16	5.6	1260.38

Table 4.1: Lattice parameter (a), zero-temperature "on-site" magnetic anisotropy constant K_c , exchange constant J and saturation magnetization M_S at $T = 0K$, used in the simulations.

4.2 The constrained Monte Carlo method

4.2.1 Algorithm

An ordinary Monte Carlo (MC) algorithm is widely used to compute thermodynamic properties by averaging over the Boltzmann distribution using the Metropolis algorithm [123]. The Metropolis algorithm works by generating trial moves at random and accepting or rejecting each move based on the Boltzman probability density $\exp(-\beta \cdot \Delta E)$, where $\beta = \frac{1}{k_B \cdot T}$ (k_B is the Boltzmann constant and T is the temperature). The ratio $(\frac{\Delta E}{k_B \cdot T})$ depends on the energy difference between two states, $\Delta E = \mathcal{H}' - \mathcal{H}$ (\mathcal{H} is the Hamiltonian of the system). In the usual Monte Carlo method for magnetic systems we generate our trial moves by drawing a vector \mathbf{v} from an isotropic normal distribution, choosing a spin \mathbf{S}_i at random, adding $\mathbf{S}_i \times \mathbf{v}$ to it and normalizing the result to obtain a trial spin \mathbf{S}'_i .

The probability density of the move depends only on the angle between \mathbf{S}_i and \mathbf{S}'_i , which ensures reversibility. The variance of the \mathbf{v} distribution controls the average step size and can be chosen at will to improve the ratio of accepted to rejected moves, similarly to the MC angle in Refs. [123, 124]. For our Hamiltonian, the energy difference involves only spin i and few neighboring spins to which it is coupled by exchange interaction, so that the decision to accept or reject the move can be made quickly. A sequence of N moves, counting null moves, constitutes a *sweep* (or one Monte Carlo step); we compute quantities of interest once per sweep to average them.

The constrained Monte Carlo method has been suggested by P. Asselin from Seagate technology [125, 126] in relation to the necessity to model high temperature spin dynamics in the heat-assisted magnetic recording. The innovation of the constrained Monte Carlo method is to modify the elementary steps of the random walk so as to conserve the average magnetization direction $\mathbf{M} \equiv (\sum_i \mathbf{S}_i)/\|\sum_i \mathbf{S}_i\|$. In this way we sample the Boltzmann distribution over a submanifold of the full phase space. Thus we keep the system out of thermodynamic equilibrium in a controlled manner, while allowing its microscopic degrees of freedom to thermalize.

In the constrained Monte Carlo method the trial moves act on two spins at a time. The extra degrees of freedom allow us to fix \mathbf{M} to any given unit vector, which we take here to be the positive z axis since we can always reduce the problem to this case by means of a global rotation. In detail, the algorithm is the following:

1. Choose a *primary spin* \mathbf{S}_i and a *compensation spin* \mathbf{S}_j , not necessarily neighbors.
2. Rotate the primary spin normally similar to normal Metropolis MC algorithm, obtaining a new spin \mathbf{S}'_i .
3. Adjust the compensation spin's x and y components to preserve $M_x = M_y = 0$,

$$S'_{jx} = S_{jx} + S_{ix} - S'_{ix} \quad (4.5)$$

$$S'_{jy} = S_{jy} + S_{iy} - S'_{iy} \quad (4.6)$$

4. Adjust the z component,

$$S'_{jz} = \text{sign}(S_{jz}) \sqrt{1 - S'^2_{jx} - S'^2_{jy}} \quad . \quad (4.7)$$

If the argument of the square root is negative, stop and take a null move (reject the move).

5. Compute the new magnetization,

$$M'_z = M_z + S'_{iz} + S'_{jz} - S_{iz} - S_{jz} \quad . \quad (4.8)$$

If $M'_z \leq 0$, stop and take a null move.

6. Compute the energy difference $\Delta\mathcal{H} = \mathcal{H}' - \mathcal{H}$.
7. Compute the acceptance probability P ,

$$P = \min \left[1, \left(\frac{M'_z}{M_z} \right)^2 \frac{|S_{jz}|}{|S'_{jz}|} \exp(-\beta\Delta\mathcal{H}) \right] \quad . \quad (4.9)$$

8. Accept the move with probability P or take a null move with probability $1 - P$.

In effect, we use the compensation spin to project the system back to its admissible manifold. The projection is not orthogonal and does not preserve measure. Consequently the Boltzmann ratio in step 7 is multiplied by a geometric correction, the ratio of two Jacobians (derived in details in Ref. [126]). The reversibility and the ergodicity of this new Monte Carlo method have been rigorously proved, see Ref. [126].

4.2.2 Free energy and restoring torque

We begin with a brief summary of principal thermodynamic relations and the relevant thermodynamic potential.

The free energy also called the Helmholtz energy or Helmholtz free energy, \mathcal{F} , is a thermodynamic potential defined as:

$$\mathcal{F} = \mathcal{U} - TS, \quad (4.10)$$

where \mathcal{U} is the internal energy and S is the entropy, both of them correspond to state functions. In basis of the first law of thermodynamics, the variation of the internal energy could be expressed as:

$$d\mathcal{U} = \delta W + \delta Q. \quad (4.11)$$

δW is the work performed on the system, and δQ is the heat absorbed by it, and using the second law of the thermodynamics we obtain that $\delta Q \geq TdS$.

Then we can express the variation of the free energy in the following way.

$$d\mathcal{F} = d\mathcal{U} - TdS - SdT, \quad (4.12)$$

$$d\mathcal{F} = \delta W + \delta Q - TdS - SdT, \quad (4.13)$$

$$d\mathcal{F} \geq \delta W - SdT. \quad (4.14)$$

The work done on the system can be redefined as a function of the appropriate conjugate work variables H and X , in such way that:

$$\delta W = H \cdot dX = \left[\frac{\partial \mathcal{F}}{\partial X} \right] \cdot dX. \quad (4.15)$$

If we consider a magnetic system in contact with a thermal bath at a constant temperature, and neglect the possible thermal expansion and magnetostriction effects, the work performed on the system could be described by the following expression:

$$\delta W = \left[\frac{\partial \mathcal{F}}{\partial \mathbf{m}} \right] \cdot d\mathbf{m}. \quad (4.16)$$

On the other hand, it is known that the work done on the system is equivalent to the restoring force also called internal torque, and we can build the torque of our system as:

$$\mathcal{T} = \left\langle - \sum_i \mathbf{S}_i \times \partial \mathcal{H} / \partial \mathbf{S}_i \right\rangle. \quad (4.17)$$

In constrained Monte Carlo method the system cannot reach full equilibrium. The average of the total internal torque does not vanish and this is equal to the macroscopic torque $-\mathbf{M} \times \partial \mathcal{F} / \partial \mathbf{M}$ (see detailed proof in Ref. [126]), where $\mathcal{F}(\mathbf{M})$ is the Helmholtz free energy, now a function of \mathbf{M} . Even though we cannot compute \mathcal{F} directly, we can reconstruct its angular dependence by integration (if the system behaves reversibly) and this in turn gives us the anisotropy constants at any temperature.

4.2.3 Numerical procedure

The evaluation of the free energy with temperature is not straightforward. Consequently, the anisotropy could be retrieved by calculating the average restoring torque in the equilibrium as a function of the constrained angles θ, φ , which represents the

polar and azimuthal angles of the magnetization from the easy axis. The torque acting on a system with mixed anisotropy (combination of uniaxial and cubic anisotropies) depends on the azimuthal and rotational angles in the following way:

$$\mathcal{T}(\theta, \varphi) = -K_{ua}^{eff}(T) \sin(2\theta) - \frac{1}{2} K_{ca}^{eff}(T) \sin(2\theta) \left(\sin^2(\theta) \left(\sin^4(\varphi) + \cos^4(\varphi) \right) - \cos^2(\theta) \right). \quad (4.18)$$

If we evaluate the restoring torque at $\varphi = 0$, we obtain that:

$$\mathcal{T}(\theta, 0) = -K_{ua}^{eff}(T) \sin(2\theta) - \frac{1}{2} K_{ca}^{eff}(T) \sin(4\theta). \quad (4.19)$$

Thus, it is possible to obtain the values of anisotropy constants of the system and their behavior at different temperatures evaluating the torque curve.

In practice we first initialize the system with uniform magnetization in a direction of our choice (θ, φ) , away from the anisotropy axes, where we expect a nonzero torque. Next we evolve the system by constrained Monte Carlo until the length of the magnetization reaches equilibrium. We then take a thermodynamic average of the torque over the number of constrained Monte Carlo “sweeps”. We repeat at other orientations and we finally reconstruct the anisotropy constants from the angular dependence of the torque.

Torque curves for a generic system with uniaxial and cubic anisotropy are shown in Fig. 4.1. The symbols show the calculated torque and the curves are fitted to a $\sin(2\theta)$ dependence in the uniaxial case and to a $\sin(4\theta)$ dependence when the system has cubic anisotropy, where θ is the angle from the easy axis. The $\sin(2\theta)$ [$\sin(4\theta)$]

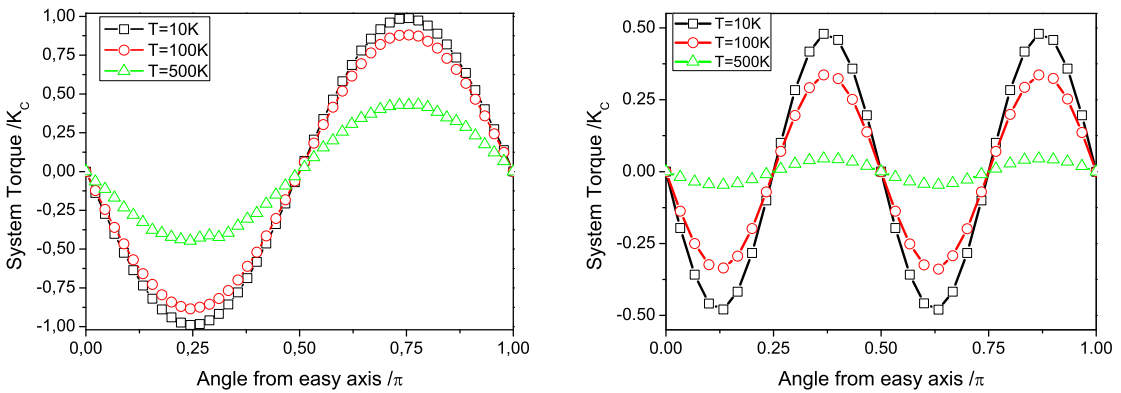


Figure 4.1: Simulated angular dependence of the restoring torque for a thin film with a simple cubic lattice, periodic boundary conditions and T_c close to 1100K, at temperatures 10 K, 100 K, and 500 K. (Left) Thin film with uniaxial anisotropy with easy axis parallel to Z axis. (Right) Thin film with cubic anisotropy with one of the easy axes parallel to Z axis.

law is seen to hold at all temperatures for the case of uniaxial [*cubic*] anisotropy and the fit of the restoring torque curves gives $K_{ua}^{eff}(T)$ [$K_{ca}^{eff}(T)$].

In a situation like this, where all the torque curves have the same shape and the anisotropy is described by a single parameter, it is sufficient to compute the torque at 45 degrees in the uniaxial case and $\theta = 22.5^\circ$ in the xz -plane for the cubic anisotropy case, where the maximum is known to occur. In more general cases it is necessary to compute the torque at several angular positions. Finally, with every new system it is prudent to verify the shape of the torque curves over many angles, both polar and azimuthal, before reducing the number of evaluated points.

4.2.4 Tests of the method

Given the originality of the constrained Monte Carlo method, it is important to ensure that the method is reliable and conforms with existing results. For this purpose we have done several tests:

- We have checked that with this method we are able to reproduce the correct T_c of several systems.
- We have checked that the anisotropy constants obtained by the constrained Monte Carlo method at low temperatures are in agreement with those obtained by the Lagrange Multiplier technique at $T = 0$ (see previous chapter).
- We have checked that the scaling behavior ($K \sim M^\gamma$) for thin films with pure (uniaxial or cubic) anisotropy at low temperatures obtained by the CMC method are consistent with those predicted by the Callen-Callen theory.

Curie temperature

The Curie temperature T_c is the temperature beyond which a ferromagnetic material becomes paramagnetic and perhaps the loss of the ferromagnetic character with the temperature is the most important temperature effect in magnetic systems. For this reason, to determine the Curie temperature through the constrained Monte Carlo method is a good test. The Curie temperature is related to the value of the exchange constant and in the Mean Field Approximation (MFA) it could be expressed as follows:

$$T_c = \frac{z \cdot J}{3k_B} \quad (4.20)$$

where J is the exchange constant, z is the number of the first neighbors and k_B is the Boltzmann constant. On the other hand, it is well known that MFA overestimates the value of the Curie temperature, this overestimation is due to the inaccuracy in the consideration of the correlations between spins within this approximation. In the literature we find other approaches, such as the classical spectral density method (CSDM)

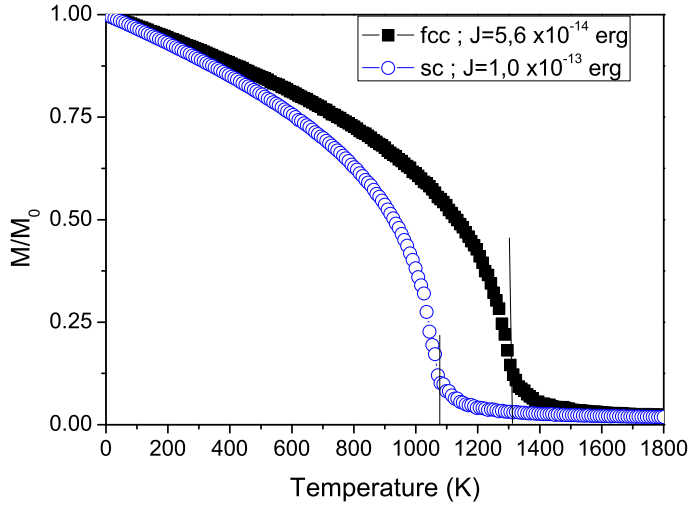


Figure 4.2: Temperature dependence of the magnetization in a ferromagnetic material with 8000 spins with periodic boundary conditions in 3D and with a sc and fcc lattice structures.

[127] or the hight temperatures expansion method (HTS) [128] which is used to extract the well known expression for the Curie temperatures for simple cubic lattices.

$$T_c = 1.44 \frac{J}{k_B} \quad (4.21)$$

We have considered two systems: a bulk system with periodic boundary conditions in 3D with a simple cubic or fcc lattice and evaluated the magnetization as a function of the temperature. We consider that the Curie temperature is defined when the magnetization becomes zero (see Fig. 4.2), excluding the finite-size effects. The exchange constants in both systems are different. In the case of a simple cubic lattice, each spin has 6 first neighbors, the exchange constant is $J = 10 \times 10^{-14} \text{erg}$ and the Curie temperature obtained by the constrained Monte-Carlo simulation is close to $T_c = 1100 \text{K}$. For a thin film with fcc lattice with a $J = 5.6 \times 10^{-14} \text{erg}$, the number of first neighbors is 12 and the Curie temperature determined by (CMC) simulations is close to $T_c = 1320 \text{K}$.

The Curie temperature obtained by the constrained Monte Carlo simulation for sc and fcc thin films presents an important discrepancy with the theoretical Mean Field prediction. In contrast, our values of T_c are in a good agreement with the values predicted by the classical spectral density method [127] (see Table 4.2).

Lattice	(MFA)	(CSDM)	(CMC)
sc	1448.58	1064.71	~ 1080
fcc	1622.41	1309.29	~ 1320

Table 4.2: Curie Temperature (T_c) values for thin films with sc ($J = 10 \times 10^{-14}$ erg) and fcc ($J = 5.6 \times 10^{-14}$ erg) lattices, predicted by the Mean Field Approximation (MFA), Classical Spectral Density Method (CSDM) and extracted from the constrained Monte Carlo (CMC) simulation.

Comparison of the constrained Monte Carlo method at low temperature with the Lagrange multiplier method

At this stage of our study we decided to check and compare the results of the effective anisotropy constants obtained with the constrained Monte Carlo method with those obtained with the Lagrange multiplier method for $T = 0K$. For this purpose we have simulated a set of thin films. This set is made up of thin layers of different thicknesses from $Lz = 3$ with $N = 4800$ total spins to $Lz = 10$ with $N = 16000$ total spins. Here Lz is the number of atomic layers of the system, consequently the films have different ratios of surface to volume number of spins N_s/N . All thin films have a sc structure with periodic boundary conditions in 2D, uniaxial anisotropy in the bulk with the easy axis of the system parallel to the Z axis and a Néel surface anisotropy constant $K_s = 10 \cdot K_c$. The bulk anisotropy constant, exchange constant, and the saturation magnetization value are presented in Tab. 4.1.

First we obtain the effective anisotropy constant at $T = 0K$ by the Lagrange multiplier method for each of the thin films that conform the set (for more details about this method see section 2.4). After that, we extract the effective anisotropy constants of the same systems but with the constrained Monte Carlo method at $T = 0.01K$ (note that due to the limitation of the method it is impossible to perform simulations of the CMC at $T = 0$). And finally we compare the effective uniaxial anisotropy constants obtained by both methods. In the case of the Lagrange multiplier method the effective uniaxial anisotropy constant (K_{ua}^{eff}) is calculated from the expression of the energy barrier of the system, in the CMC method from the restoring torque curve.

The results of this test are plotted in Fig. 4.3, the squared dots represent the data obtained by the Lagrange multiplier method and the circular ones are obtained by the CMC method. The value of the effective uniaxial anisotropy constant is normalized by the value of the macroscopic volume anisotropy constant at $T = 0$ ($K_V = K_c$). As we can see, the data show total agreement between both methods at low temperature. The results show a linear behavior of the effective anisotropy as a function of N_s/N ratio as predicted by the formula:

$$K^{eff} = K_V + \frac{N_s}{N}(K_s - K_V) \quad (4.22)$$

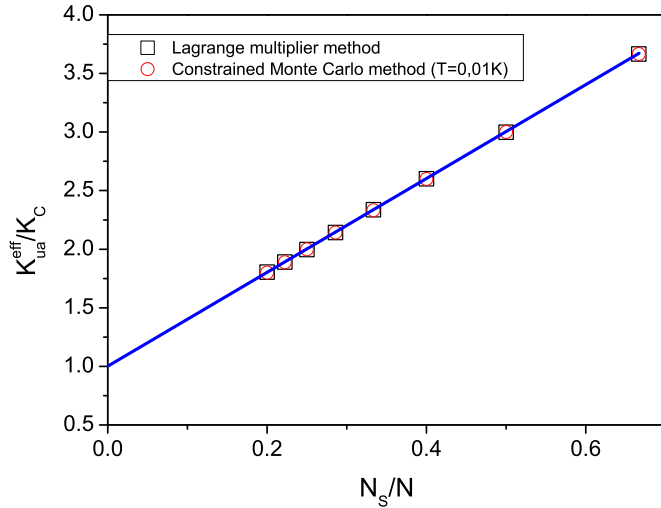


Figure 4.3: The effective anisotropy constant (K_{ua}^{eff}/K_c) obtained by the Lagrange multiplier method (squared dots) and constrained Monte Carlo method at $T = 0.01 K$ (circular dots) as a function of the ratio between surface and total number of spins, of a set of thin films with thickness ranging from $Lz = 3$ to $Lz = 10$ with sc lattice and periodic boundary conditions in 2D.

at $\frac{N_s}{N} \rightarrow 0$ the bulk anisotropy is recovered $K_V = K_c$, as we can see in Fig. 4.3.

Temperature dependence of the bulk anisotropy

Next we check well known results for the low temperature dependence of the bulk anisotropy, as predicted by Callen and Callen theory in Refs. [106, 129], where uniaxial anisotropy was shown to have an M^3 dependence, and cubic anisotropy to have an M^{10} dependence. In the constrained Monte Carlo method we evaluate the torque curves at different temperatures from which we extract the value of the macroscopic anisotropy constant at different temperatures. We simulate a generic ferromagnetic material with 1000 spins, simple cubic crystalline structure, the magnetic parameters are those exposed in Tab 4.1. We analyze both cases of uniaxial and cubic anisotropy and the "on-site" anisotropy constant values are the same for both cases. We also consider periodic boundary conditions in 3D.

The magnetization and macroscopic uniaxial and cubic anisotropy are plotted against temperature in Fig. 4.4. We can observe that the cubic anisotropy constant has a more pronounced dependence on temperature than the uniaxial one.

In Figs. 4.5 and 4.6 the macroscopic anisotropies are plotted against the magnetization on logarithmic scales. In this way we can extract the scaling exponent γ ($K \propto M^\gamma$) at low-temperatures. As it can be seen, the results are consistent with the

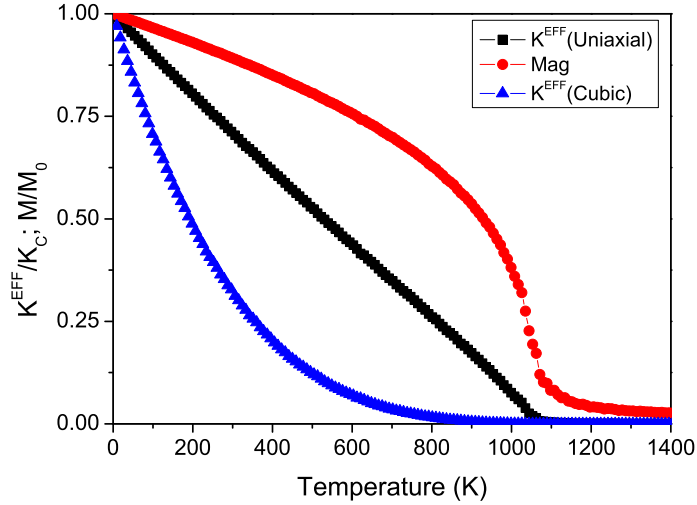


Figure 4.4: Temperature dependence of magnetization, macroscopic uniaxial and cubic anisotropies, for a ferromagnetic material with $N = 1000$ spins and a simple cubic lattice with periodic boundary conditions in 3D.

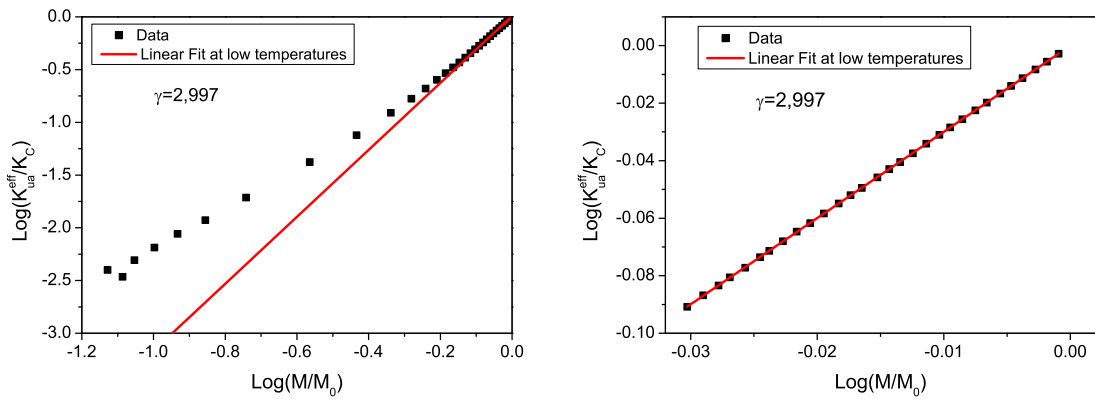


Figure 4.5: Temperature scaling of the anisotropy versus magnetization of a ferromagnetic material with $N = 1000$ moments, a simple cubic lattice, uniaxial anisotropy and periodic boundary conditions in 3D, for the whole temperature range (Left) and the fitting at low-temperatures (Right).

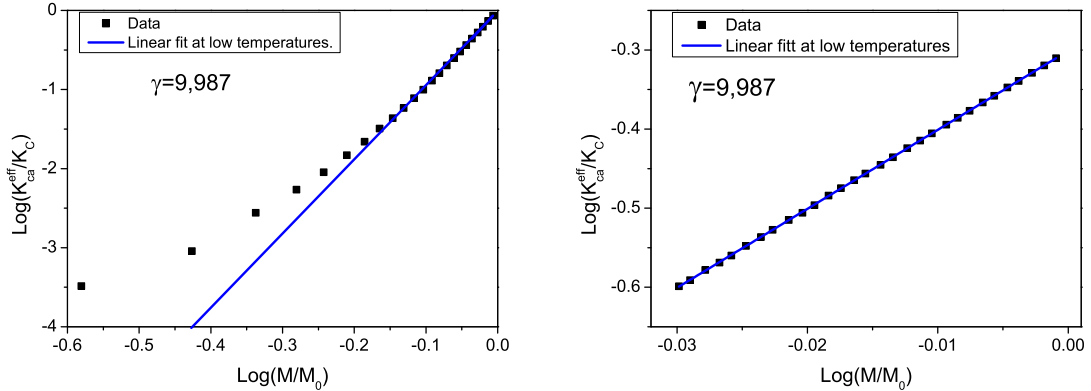


Figure 4.6: Temperature scaling of the effective anisotropy versus magnetization of a ferromagnetic material with a simple cubic lattice, $N = 1000$ moments, cubic anisotropy and periodic boundary conditions in 3D, for the whole temperature range (Left), and the fitting at low-temperatures (Right).

scaling behavior predicted by Callen and Callen [106]. Namely, in the system with uniaxial anisotropy we found $K_{ua}^{eff} \sim M^{2.997}$ (see Fig. 4.5) and for the cubic anisotropy case $K_{ca}^{eff} \sim M^{9.987}$ (see Fig. 4.6) at low temperatures.

Next we simulate a generic ferromagnetic material with fcc crystalline structure with periodic boundary conditions in 3D. The magnetic parameters of the system are again those shown in the Tab. 4.1 and we investigate the cases of uniaxial and cubic magneto-crystalline anisotropy. For uniaxial anisotropy we found that $K_{ua}^{eff} \sim M^{2.997}$ (see Fig. 4.7 left) and for cubic anisotropy $K_{ca}^{eff} \sim M^{10}$, at low temperatures (see Fig. 4.7 right).

Given the results we can say that the behavior of the macroscopic anisotropy at low temperatures, obtained by the CMC method, corresponds with the predicted by Callen and Callen, both in the cases of sc and fcc lattices.

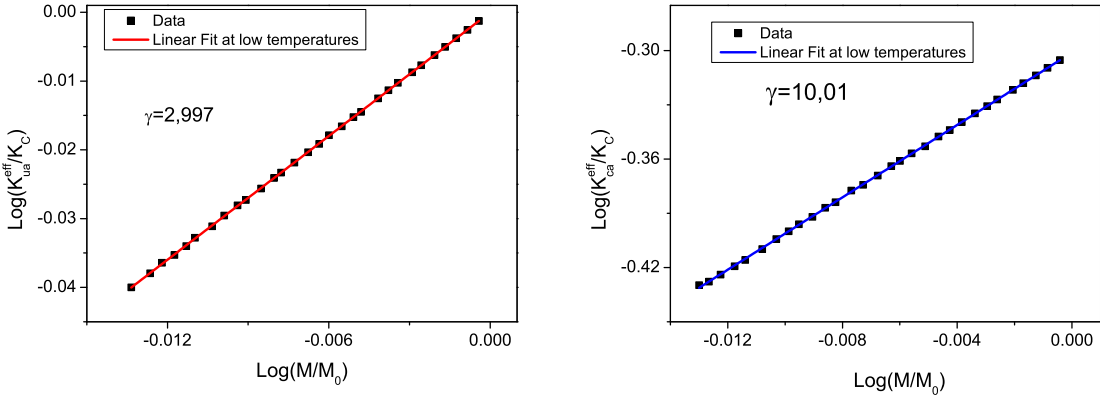


Figure 4.7: Low-temperatures scaling of the effective anisotropy versus magnetization of a pure ferromagnet (with $N = 1000$ moments) with fcc structure, periodic boundary conditions in 3D with uniaxial anisotropy (left) and cubic anisotropy (right).

4.3 Temperature dependence of macroscopic anisotropy in thin films with Néel surface anisotropy

Due to the flexibility of the constrained Monte Carlo method it is a perfect tool to investigate and understand the temperature dependence of the Néel surface anisotropy (NSA).

The surface anisotropy is normally found to be much stronger than bulk anisotropy, so that a value of $K_s = 10 \cdot K_c$ was chosen. In the simulation of thin films we have imposed periodic boundary conditions in 2D with the aim to avoid the edge effects. When studying thin films with surface anisotropy, a number of basic combinations of anisotropies are possible. Principally, in the case of bulk uniaxial anisotropy, the surface and bulk anisotropies can have aligned or opposite directions of easy axes, depending on the sign of the constants. Alternatively, a material could possess a cubic bulk anisotropy and uniaxial surface anisotropy. In the following we present calculations of temperature dependent effects in these thin film systems with surface anisotropy.

4.3.1 The temperature dependence of the total effective anisotropy in thin films with surface anisotropy.

In this section we study the temperature dependence of the total effective anisotropy. We have simulated several types of thin films, with sc or fcc lattice structures and with uniaxial or cubic anisotropy in the bulk. In the previous section 4.2.4 we studied the temperature dependence of the bulk anisotropy without taking into account the surface effects, the natural next step is to analyze the temperature dependence of a pure surface system, in which all the moments belong to the surface so that only surface anisotropy is present. In Fig. 4.8 we show the temperature dependence of the magnetization and

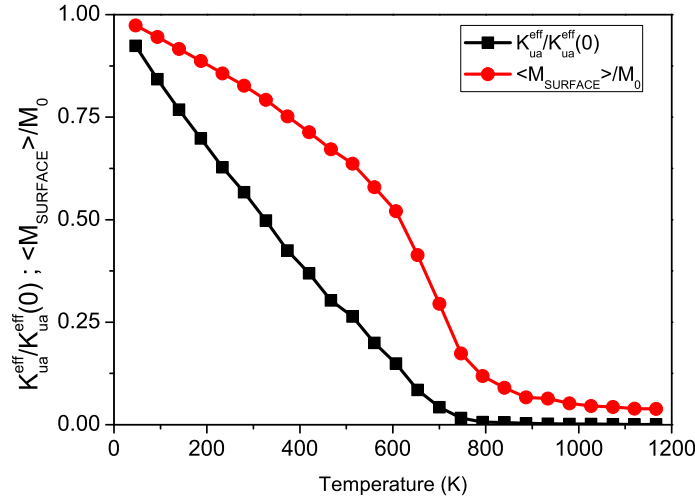


Figure 4.8: Temperature dependence of the surface magnetization and effective uniaxial anisotropy of a thin film $N = N_s = 3200$, $Lz = 2$ with Néel surface anisotropy and $K_s = 10 \cdot K_c$, where K_c has the value from Tab. 4.1.

effective uniaxial anisotropy of such a system, i. e. a thin film with $Lz = 2$. Due to the reduction of the number of first neighbors the Curie temperature of the system is lower than that corresponding to the bulk system with the same exchange constant. The effective uniaxial anisotropy has its origin in the surface effects. It is normalized to the effective anisotropy constant at $T = 0$, which following the expression (4.4) for a sc structure is ($K_{ua}^{\text{eff}}(0) = \frac{K_s}{2} = 5 \cdot K_c$). The effective uniaxial anisotropy shows a linear dependence on temperature.

Once we analyzed the temperature dependence of the magnetization and the magnetic anisotropy of a thin film with only surface moments, we continue our study with a more complex system. Namely, we model a thin film with simple cubic lattice structure with 16000 spins ($Lz = 10$). Now we distinguish between bulk and surface spins. We first investigate the case where the bulk anisotropy is of the uniaxial type and the easy axis is parallel to Z axis. The Néel surface anisotropy has an easy axis parallel to the easy axis of the bulk anisotropy and perpendicular to the surface of the thin film (see Fig. 4.9).

When both bulk and surface anisotropies are uniaxial, the torque curves are similar to those corresponding to a pure uniaxial system. However, the effective anisotropy constant is different from the bulk or the surface ones. It can be calculated by fitting the torque curves to the expression (4.19). We calculate the total, bulk and the surface magnetization, see Fig. 4.10 (left graph) and the total anisotropy, see Fig. 4.10 (right graph), dependencies on temperature. The surface magnetization is more sensitive

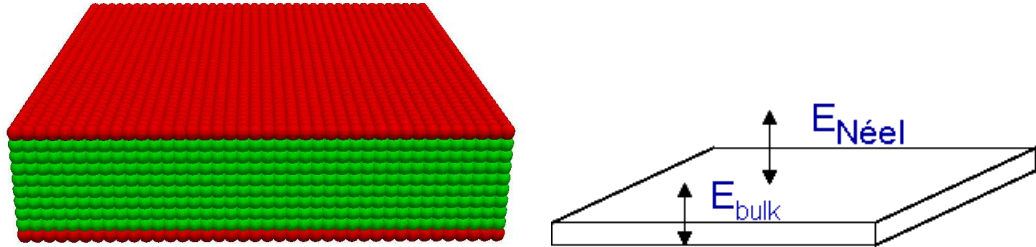


Figure 4.9: Sketch for the geometry: (left) Thin film with 16000 moments, $Lz = 10$ and with a sc crystalline structure. The uniaxial anisotropies with easy axis in the bulk and on the surface are depicted on the right hand side.

than the total magnetization to the temperature increase, but both have the same Curie temperature, we can find similar results in the literature [130, 131]. This stronger

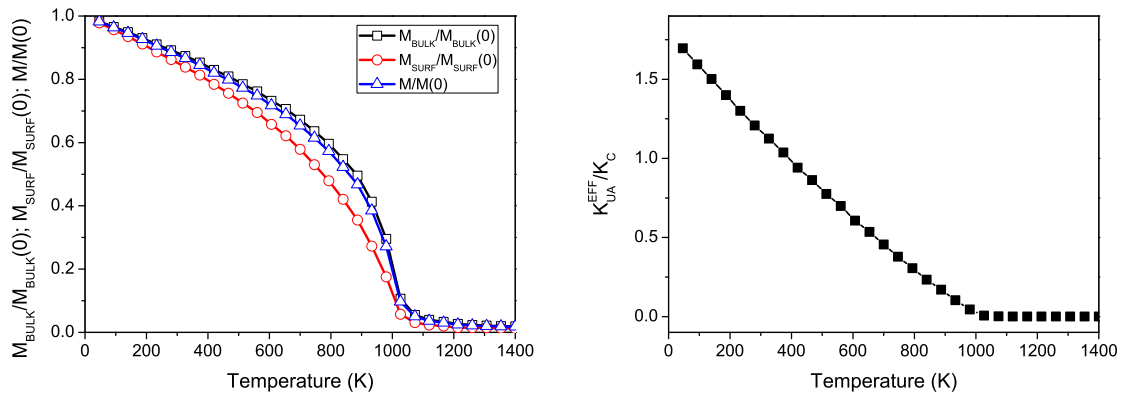


Figure 4.10: Temperature dependence of magnetization and effective uniaxial anisotropy constant (left and right graphic respectively) of a thin film with $Lz = 10$, with uniaxial anisotropy in the bulk and Néel surface anisotropy $K_s = 10 \cdot K_c$.

sensibility of the surface magnetization arises from a reduction in coordination number at the surface. An isolated surface layer also has a reduced Curie temperature, see Fig. 4.8. But in the present case the surface layer is polarized by the bulk and thus the surface and the bulk moments share the same T_c of around 1050K.

Next we present a more complicated situation, where an fcc thin film has cubic bulk anisotropy and a Néel surface anisotropy. The plane of the thin films is cut along the (001) direction, thus for an fcc crystalline structure the spins that belong to the surface have lost 4 first neighbors. This yields a further reduction of the exchange field and therefore the sensibility of the surface magnetization with temperature is increased. One of the easy axes of the cubic anisotropy coincides with the surface anisotropy axis and is perpendicular to the thin film surface. The torque curve is clearly a sum of the uniaxial and cubic contributions as is seen in Fig. 4.11 (Left).

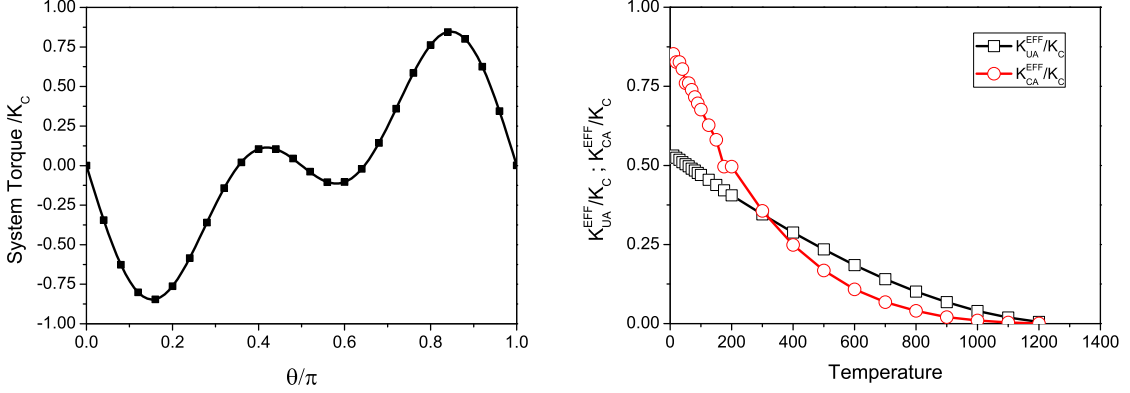


Figure 4.11: For a thin film of $L_z = 10$ atomic planes with fcc structure, cubic bulk anisotropy and Néel surface anisotropy ($K_s = 10 \cdot K_c$) perpendicular to the thin film plane and parallel to one of the bulk anisotropy easy axes: (Left) Angular dependence of the component Y of the restoring torque. (Right) Temperature dependence of uniaxial and cubic effective anisotropies.

The temperature dependence of the uniaxial and cubic macroscopic contributions to the anisotropies of the system are present in Fig. 4.11 (Right). According to the general theory and our previous results, the cubic anisotropy is decreasing faster with temperature than the uniaxial surface one. Consequently, at low temperatures the cubic anisotropy dominates, while at high temperatures the uniaxial surface one. This leads to a change in the global easy axis of the system with temperature.

4.3.2 Temperature dependence of the effective surface anisotropy in thin films.

The total effective anisotropy in the presence of the surface effects is not an intrinsic parameter since it is strongly dependent on the thin film thickness. In this section we present two methods, "Scaling method" and "Separation of the surface torque method", suitable to separate the surface from the bulk anisotropy contributions as a function of the temperature in thin films. For simplicity, the thin films have parallel surface and bulk uniaxial anisotropy axes, both easy axes perpendicular to the thin film plane. We applied these two methods to extract the effective surface anisotropy constant of magnetic thin films with a simple cubic crystal structure and the Néel surface anisotropy constant $K_s = 10 \cdot K_c$. The size of the modeled system is increased from $Lz = 3$ (4800 spins) to $Lz = 10$ (16000 spins).

Scaling with the system size

The first method is based on the phenomenological expression [132] that allows to determine the effective surface anisotropy from the total effective anisotropy varying the size of the system (see section 3.1.1). We assume that this formula is valid for all temperatures:

$$K^{eff}(T) = K_V(T) + \frac{N_s}{N} \cdot (K_s^{eff}(T) - K_V(T)) \quad (4.23)$$

where $K_V(T)$ is the temperature-dependent macroscopic volume anisotropy constant, $K_s^{eff}(T)$ is the temperature-dependent effective surface anisotropy constant, N_s is the number of moments that belongs to the surface and N is the number of total moments in the magnetic system. Then if we know the fraction of moments that belongs to the surface, and the value of the total anisotropy, $K^{eff}(T)$ as a function of the size of the system, we will be able to determine $K_s^{eff}(T)$.

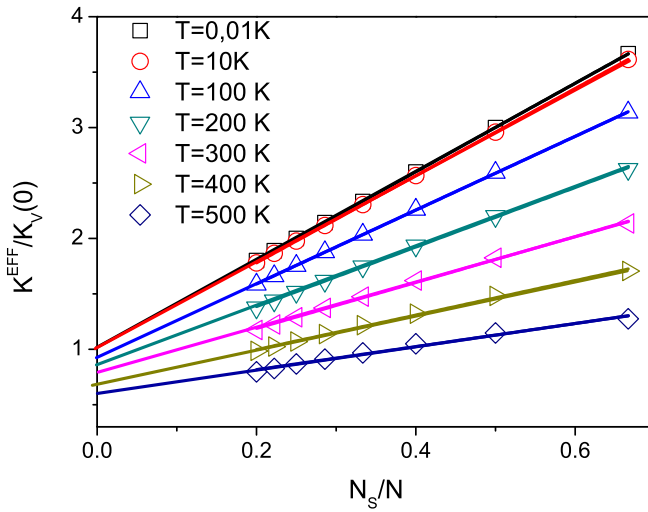


Figure 4.12: The scaling of the K^{eff} (normalized to the uniaxial anisotropy in the bulk at $T = 0K$, $K_V(0)$) with the ratio between the number of surface spins and total spins at several temperatures.

The modeling at different temperatures of a set of thin films (see Fig. 4.12) provide the effective bulk and surface anisotropy constants. The data are perfectly scaled with the ratio N_s/N . The fitting of $K^{eff}(T)$ to the expression (4.23) allows to extract the effective surface and volume anisotropies as a function of the temperature, see Fig. 4.13.

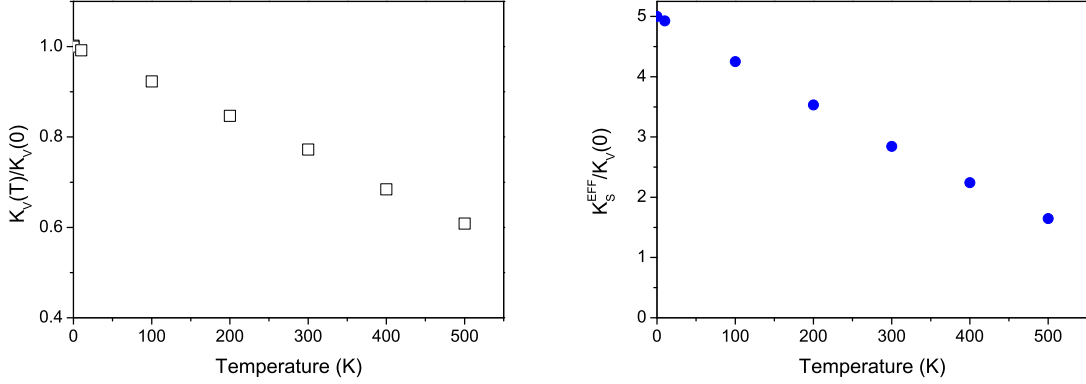


Figure 4.13: (Left) The bulk anisotropy $K_V(T)$ (normalized to the uniaxial anisotropy in the bulk at $T = 0\text{K}$ $K_V(0) = K_c$) obtained by the scaling method at several temperatures. On the right graph we present the effective surface anisotropy constant K_s^{eff} obtained at these temperatures.

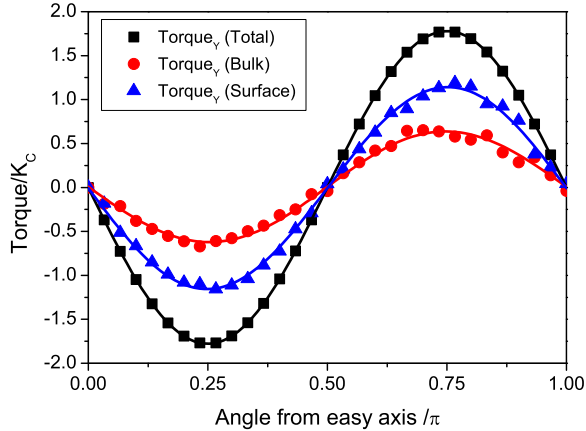


Figure 4.14: Total, surface and bulk torques in a thin film with $N = 16000$, $Lz = 10$, uniaxial anisotropy in the bulk and Néel Surface anisotropy $K_s = 10 \cdot K_c$. The bulk easy axis is parallel to Z axis.

Separation of the surface torque

The second method is based on the possibility to separate the contributions of the surface to the restoring torque.

Fig. 4.14 represents the total, bulk and surface torque curves, evaluated for a thin film with $Lz = 10$, sc structure and the relative orientation between the bulk and surface easy axes, parallel to each other. Each curve is fitted separately to expression (4.19). The comparison between the values of effective surface anisotropy obtained by the two methods shows a good agreement, see Fig. 4.15.

In practice, the surface torque is a noisy quantity due to the relatively small number of atoms. In order to obtain a good thermodynamic average it is generally necessary to use a large number of steps in the CMC algorithm ($N_{\text{sweeps}} = 70000$). However, the total torque converges much more rapidly and requires relatively few steps.

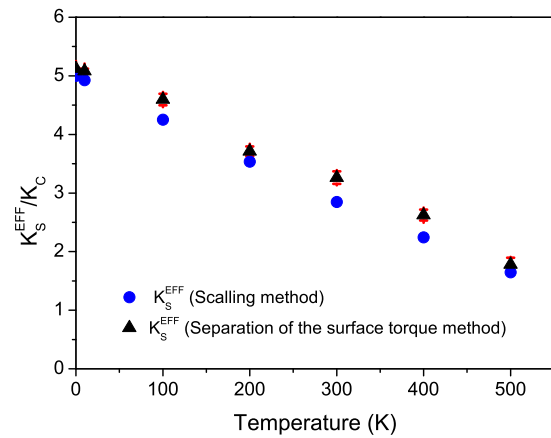


Figure 4.15: The effective surface anisotropy constant K_s^{eff} obtained at several temperatures by the separation of the surface torque (triangular dots) and the scaling method (circular dots).

The experimental results for Gd, Fe, Ni show a largely linear temperature dependence of surface anisotropy [119, 133, 134]. Note that low temperature behavior of the surface anisotropy presented in Fig. 4.15 resemble a linear behavior. However, when comparing with our results, various factors should be taken into account, including structural changes with increased temperatures or a lattice mismatch which could influence the bulk-type anisotropy. One other possibility is that of an enhanced exchange interaction at the surface of the material [135] (see also section 6.3.4 of the next chapter). An increased exchange interaction would lead to a *reduction* in the criticality of the surface layer and similarly the temperature scaling of the surface anisotropy will be affected.

4.3.3 Modeling the effect of the anisotropy re-orientation due to the surface effects

In many cases the direction of the easy axes in the system suffers a change due to the existence of the surface effects [136, 137]. Such effect can occur when the easy directions of the surface and bulk anisotropies compete, see Fig. 4.16. The temperature re-orientation of the easy axis in magnetic thin films has previously been refereed in a huge number of papers [54, 56, 63, 117–120, 138].

We first analyze the existence of the re-orientation transition in magnetic thin films

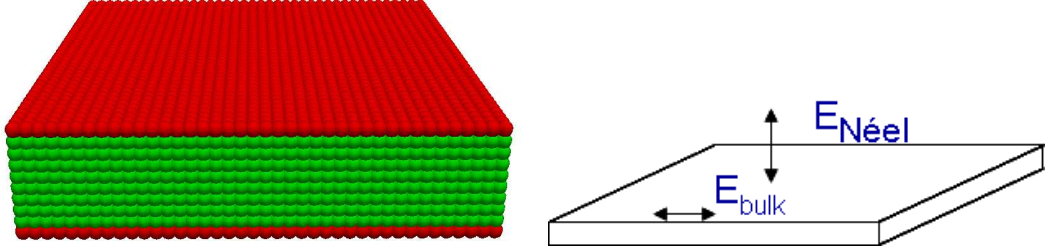


Figure 4.16: (Left) System Geometry of a thin film with $L_z = 10$ with a sc crystalline structure. Uniaxial anisotropies with easy axis in the bulk and on the surface are depicted on the right side (perpendicular to each other).

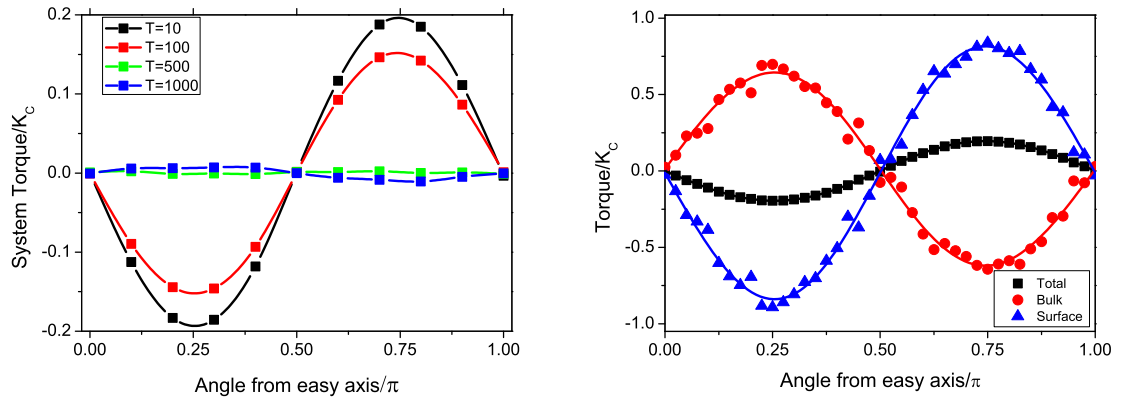


Figure 4.17: The system torque evaluated for thin film with $L_z = 10$, uniaxial anisotropy in the bulk and Néel Surface anisotropy $K_s = 10 \cdot K_c$, sketched in Fig. 4.16. The bulk easy axis is parallel to X axis. (Left graphic) Curve of the component Y of the total torque as a function of θ angle for several temperatures $T = 10, 100, 500, 1000 \text{ K}$. (Right graphic) Total, surface and bulk torques at $T = 10 \text{ K}$.

as a function of the temperature. As it can be seen in Fig. 4.17 (right) (thin film with $L_z = 10$), in the case of perpendicular configuration of the easy axes the surface, the torque also follows the $\sin(2\theta)$ behavior and the effective surface anisotropy could be extracted. The sign of the effective surface anisotropy constant obtained by fitting of the surface restoring torque curve is opposite to the bulk one, it indicates the different orientations of easy axis in the bulk which easy axis geometry of Fig. 4.16.

In this system at low temperatures the magnetization lies along the surface easy direction, perpendicular to the plane. As the temperature is increased the surface contribution to the anisotropy energy rapidly decreases, so that the system magnetization is re-oriented along the bulk easy direction, i.e. in the plane. This is illustrated in Fig. 4.17 (left), where we plot the Y component of the total torque acting on the same thin film at different temperatures. As it can be seen, at low temperatures the

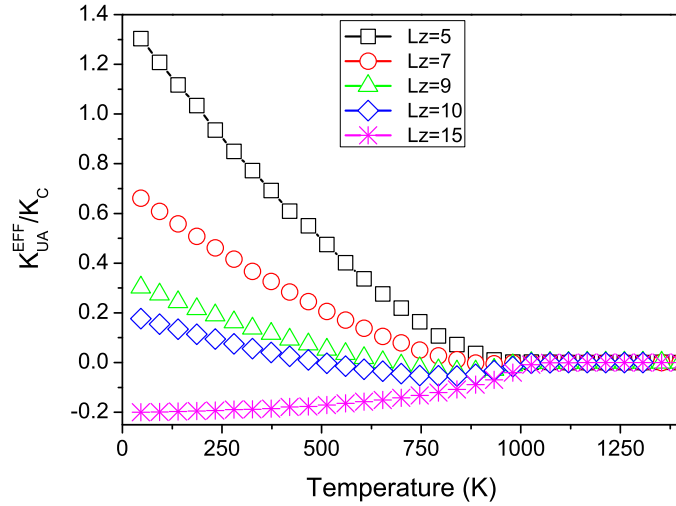


Figure 4.18: Temperature dependence of the effective anisotropy constant for different thin film thicknesses.

positions of the maximum of the torque corresponds to that of the uniaxial out-of-plane anisotropy while at high temperatures the situation corresponds to that of the in-plane anisotropy.

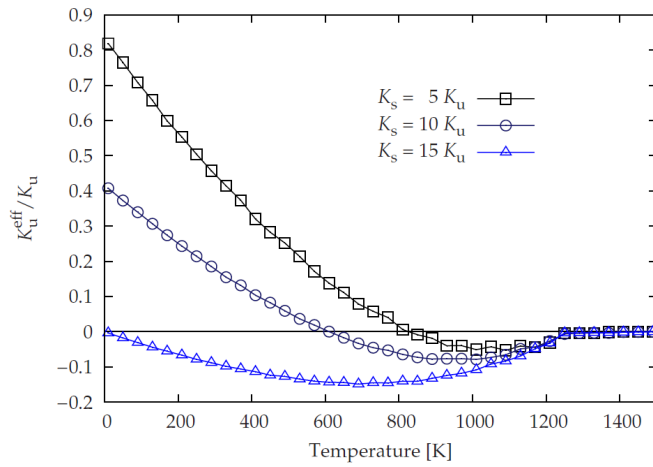


Figure 4.19: Temperature dependence of effective anisotropy for a thin film with competing surface (easy plane) and bulk (parallel to Z axis) anisotropies for different magnitudes of $K_{\text{Néel}}$.

Next we analyze the existence of the re-orientation transition in magnetic thin films as a function of their thickness. We increase the thickness from 5 to 15 atomic layer.

The temperature dependence of the effective anisotropy is plotted in Fig. 4.18. In ultra-thin films the total anisotropy of the system is governed by the surface anisotropy up to the Curie temperature. If the thickness of the thin film is large, then the total anisotropy is dominated by the bulk anisotropy and the easy axis is parallel to bulk one. The re-orientation transition occurs in an intermediate region of thickness and the re-orientation temperature depends on the thin film thickness.

One interesting property of the temperature dependent re-orientation transition is that, depending on the choice of non-magnetic interface material, the temperature of the transition can be tuned. To illustrate this phenomenon, Fig 4.19 shows a plot of the temperature dependence of the total anisotropy for different Néel anisotropy constants, emulating the effect of changing the coating of the material. Note that in this case the easy axis of the surface anisotropy is in-plane and the bulk anisotropy is assumed to be perpendicular to the plane (as in coated materials for perpendicular magnetic recording applications).

4.3.4 The scaling of the macroscopic anisotropy with the magnetization

In this section we investigate the temperature scaling of the macroscopic anisotropy with respect to the magnetization $K \propto M^\gamma$. As it has been reported in the literature for a pure magnetic material the scaling factor γ at low temperature follows the well known Callen-Callen law [106, 129]. However, when the magnetic system has a more complex structure than a pure ferromagnet the scaling is unknown *a priori* and is a coordination number, thin film thickness, configuration of easy axes and material dependent. Nevertheless, it is this scaling which would be measured experimentally. To illustrate this effect we have calculated the scaling exponent at low-temperatures for various thin films with different easy axes configurations.

First we analyze the scaling exponent γ as a function of the thin film thickness when the bulk has a uniaxial magneto-crystalline anisotropy and the surface anisotropy is modeled by the Néel surface anisotropy with a $K_s = 10 \cdot K_c$. We consider two cases, the Néel surface anisotropy is perpendicular to the thin film plane in both cases while the bulk easy axis is in the first case (Fig. 4.20) also perpendicular to the surface and in the second case (Fig 4.21) lies in the plane parallel to X axis.

The scaling exponent γ is shown in the Fig. 4.20. We can observe that when our system is a pure surface system it is well modeled by an uniaxial anisotropy and $\gamma \approx 3$, practically we recover the value expected from the Callen- Callen theory. But when the size of the system is increased and we have both surface and bulk moments the system presents two different anisotropy constants from the surface and bulk magnetization which have different dependence on temperature, and this affects the γ value.

Next, we consider that the configuration of the easy axis of the bulk and surface corresponds to that shown in Fig. 4.16 (right). As we have analyzed in the previous

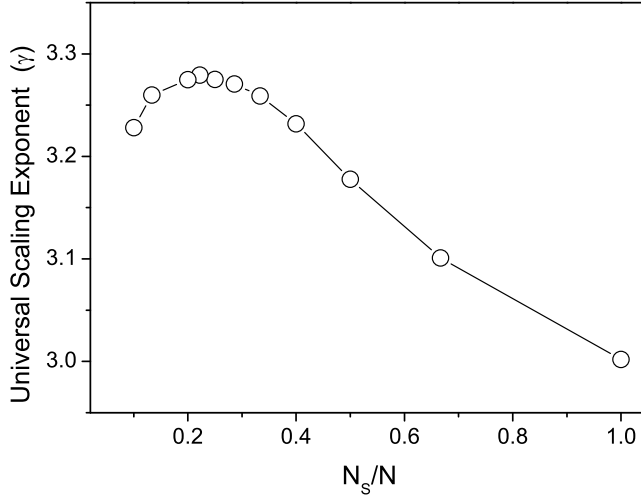


Figure 4.20: The scaling exponent as a function of the ratio N_s/N for a set of thin films with sc lattice, uniaxial anisotropy in the bulk and Néel surface anisotropy $K_s = 10 \cdot K_c$, the bulk and surface easy axis are out-of-plane.

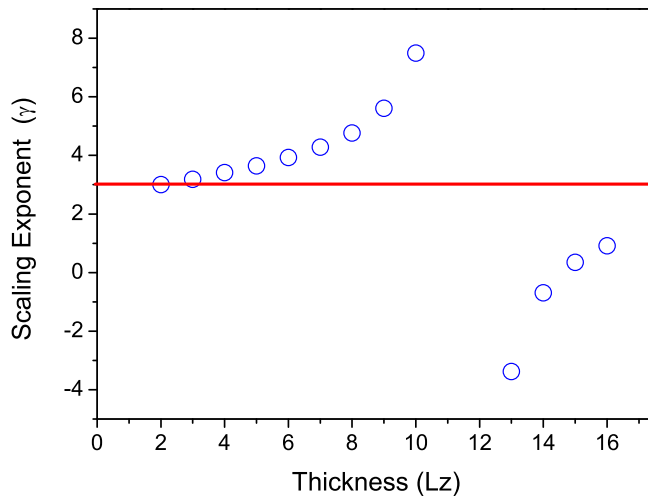


Figure 4.21: The scaling exponent γ as a function of system size of a thin film with sc lattice, uniaxial anisotropy in the bulk with the easy axis parallel to X axis, and Néel surface anisotropy with $K_s = 10 \cdot K_c$ and easy axis out-of-plane.

section 4.3.3, the existence of several easy axes with different origins could lead to a

re-orientation transition with temperature. The re-orientation transition has the consequence that the scaling exponent of the effective anisotropy constant with the average magnetization is not monotonic, as we can see in Fig. 4.21, where the scaling exponent of systems with $Lz = 2 \div 16$ is plotted. The scaling exponent increases from $\gamma \gtrsim 3$ (when the total anisotropy is dominated by the surface anisotropy), diverges at the re-orientation transition and later recovers the value $\gamma \sim 3$ (when the total anisotropy is dominated by the bulk one) with increased thin film thickness (see Fig. 4.21). The negative value of the scaling exponent is related to a non-monotonic dependence of the effective anisotropy on temperature, related to the orientation transition, as seen in Fig. 4.19.

In general the magnetic behavior of a thin film depends on the character of its surface, if it is coated, if it is free, etc. It is natural to ask the question on how the scaling exponent is affected by the surface. With the aim to answer this question, we have simulated the effect of different cappings on our thin film, varying the value of the Néel surface anisotropy parameter. We have modeled a thin film with a sc lattice structure ($Lz = 5$), the bulk anisotropy is uniaxial and the Néel surface anisotropy constant is changed in the range from $K_s = K_c$ to $K_s = 100 \cdot K_c$. In Fig. 4.22 we present the calculated value of the scaling exponent. When the value of the surface anisotropy per spin is smaller than the bulk one, the scaling factor is smaller than that predicted by the Callen-Callen theory ($\gamma = 3$). If the effective surface anisotropy per spin is larger than the bulk one, the scaling factor calculated is larger than 3 and $\gamma \approx 3$ at $K_s = 2K_c$.

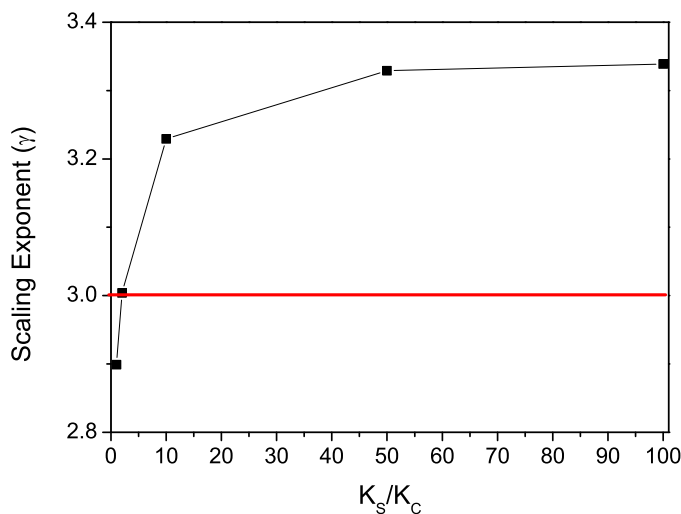


Figure 4.22: Scaling exponent of a thin film, with sc lattice structure, $Lz = 5$ as a function of the Néel surface anisotropy normalized to the bulk anisotropy constant (K_c).

To summarize this section we conclude that the scaling exponent for thin films with uniaxial anisotropy in the bulk and surface anisotropy at low temperatures is different than that predicted by the Callen-Callen theory, and depends on the system size. The increment of γ has its origin in the fact that the moments on the surface have a reduction of the number of the nearest neighbors, therefore the surface magnetization is more sensible to the temperature than the total magnetization. Also we have to note that the value of the surface anisotropy constant itself is different from the bulk one, and this could induce a change in the value of γ .

4.4 Conclusion

From our results we can conclude the following:

- The constrained Monte Carlo method is capable to evaluate temperature-dependent properties. We have shown its novel capability to evaluate the temperature dependence of the magnetic anisotropy, which is an important quantity for technological applications in hard magnetic materials. In the case of bulk materials we recovered numerically the analytical scaling law of Callen and Callen.
- We have also shown that the method enables the separation of the temperature dependent surface anisotropy as an intrinsic system parameter, independent of the thin film thickness. Our results demonstrate a linear temperature dependence of the surface anisotropy, consistent with the experimental results in Gd [133, 134], Ni [134] and Fe [119] grown on different substrates.
- We have also shown that the competition between the surface and the bulk anisotropies could produce a re-orientation of the effective easy axis. The re-orientation temperature depends on the system size.
- We have investigated the scaling of the anisotropy in thin films with magnetization. In ultrathin films without bulk moments, the surface anisotropy scales with the surface magnetization following the Callen-Callen law as corresponds to the uniaxial case. In other cases with both surface and bulk anisotropy contributions we report no universal scaling behavior of the effective anisotropy.

Conclusiones

En esta sección de la tesis hemos hecho un estudio numérico del comportamiento térmico de láminas delgadas ferromagnéticas con anisotropía de superficie tipo Néel. De nuestros resultados se puede concluir lo siguiente:

- Hemos demostrado que el nuevo método "Monte Carlo con ligaduras" es capaz de evaluar la dependencia térmica de propiedades magnéticas tales como la imanación del sistema. Además utilizamos esta capacidad para evaluar la dependencia con la temperatura de la anisotropía magnética, parámetro muy importante por sus posibles aplicaciones tecnológicas en materiales magnéticos duros. En el caso de anisotropía magnética de un sistema bulk recuperamos numéricamente el escalado de la ley de Callen-Callen.
- Además hemos mostrado que este nuevo método es capaz de obtener la dependencia térmica de la ansiotropía de superficie como parámetro intrínseco del sistema, independientemente del grosor de la película delgada. Nuestros resultados muestran una dependencia lineal de la anisotropía de superficie con la temperatura, consistente con resultados experimentales como en el caso de Gd [133, 134], Ni [134] y Fe [119], crecidos sobre diferentes substratos.
- Por otro lado, se ha mostrado que la competición entre la anisotropía de superficie y la de volumen puede producir una re-orientación de los ejes fáciles magnéticos del sistema con la temperatura. A su vez se ha observado que la temperatura de re-orientación presenta una dependencia del grosor de la película.
- Hemos investigado el escalado de la anisotropía con la imanación en láminas delgadas, observando que, para películas magnéticas ultra-delgadas donde todos los momentos magnéticos pertenecen a la superficie la anisotropía escala con la imanación de superficie siguiendo la ley de Callen-Callen a bajas temperaturas. En otros casos con ambas contribuciones (de superficie y de volumen) a la anisotropía, observamos que no existe un comportamiento universal del escalado de la anisotropía efectiva del sistema.

THE CONSTRAINED MONTE CARLO METHOD AND TEMPERATURE DEPENDENCE OF
88 THE MACROSCOPIC ANISOTROPY IN MAGNETIC THIN FILMS

5

Temperature dependence of the surface anisotropy in nanoparticles

5.1 Introduction

We have demonstrated in the previous chapters the relevance of surface effects in nanoparticles and nanostructures: the Néel surface anisotropy can induce additional macroscopic anisotropies which affect the magnetic behavior of the system. For nanoparticles in chapter 2 we have investigated the influence of surface anisotropy at zero temperature, in particular highlighting the effects of spin non-collinearities. The most noticeable effect of these non-collinearities is the appearance of effective cubic anisotropy caused by large values of the surface anisotropy constant K_s . It is reasonable to ask the question, what happens to these effective anisotropies with the additional spin non-collinearities due to the thermal disordering. Also from the Callen-Callen theory one can see that cubic and uniaxial type anisotropies have very different temperature dependencies. Thus it is an open question whether the surface induced cubic anisotropy in nanoparticles also shows such a strong temperature dependence. This is what we aim to address in the present chapter.

In the present chapter we consider spherical and truncated octahedral nanoparticles cut from the face-centered cubic (fcc) and simple cubic (sc) internal structures. Nanoparticles have the diameter $D \approx 3\text{nm}$ with approximately $N = 1200 \div 1500$ atoms depending on the underlying structure and shape, and $D \approx 7\text{nm}$ with approximately $N = 6300$ atoms. To model the magnetic behavior we use an anisotropic Heisenberg model similar to that described in section 4.1.

We have taken into account the exchange interaction with nearest-neighbor exchange energy only (we use $J = 1.0 \times 10^{-13} \text{erg}$ for sc and $J = 5.6 \times 10^{-14} \text{erg}$ for fcc lattices). For core spins, we use the magneto-crystalline anisotropy in the uniaxial or cubic form, with the core anisotropy value $K_c = 4.16 \times 10^6 \text{erg/cm}^3$. For surface spins (spins with not full coordination number) we use the Ne  l surface anisotropy model, with varying K_s .

5.2 Temperature dependence of macroscopic anisotropy in magnetic nanoparticles

To evaluate the temperature dependence of the macroscopic anisotropy constant we use the constrained Monte Carlo method (CMC) introduced in the section 4.2 of the previous chapter. The CMC is an algorithm of the Monte Carlo type which allows to include both thermodynamic fluctuations and entropy into the evaluation of macroscopic quantities such as the temperature dependent magnetic anisotropy. Differently to chapter 2, the internal energy in this case is substituted by the free energy \mathcal{F} . We retrieve the anisotropy constants by calculating the average restoring torque in the equilibrium as a function of the constrained magnetization direction $\mathbf{M}_0(\theta, \varphi)$, where (θ, φ) are the constrained polar and azimuthal angles. θ, φ .

$$\mathcal{T} = \left\langle - \sum_i \mathbf{S}_i \times \partial \mathcal{H} / \partial \mathbf{S}_i \right\rangle \approx -\mathbf{M} \times \partial \mathcal{F} / \partial \mathbf{M}. \quad (5.1)$$

where \mathcal{T} is the restoring torque, \mathbf{S}_i is the localized spin moment at site i ($|\mathbf{S}_i| = 1$), and \mathbf{M} is the average magnetization $\mathbf{M} \equiv (\sum_i \mathbf{S}_i) / \|\sum_i \mathbf{S}_i\|$. The simulated angular dependence of the torque at $\varphi = 0$ is then fitted to

$$\mathcal{T}(\theta) = -K_{ua}^{eff}(T) \sin(2\theta) - \frac{1}{2} K_{ca}^{eff}(T) \sin(4\theta). \quad (5.2)$$

from which the effective uniaxial (K_{ua}^{eff}) and cubic K_{ca}^{eff} anisotropies are extracted as a function of temperature.

5.2.1 Temperature dependence of the effective anisotropies in nanoparticle with sc lattice structure

The first study that we have to do when we analyze the temperature dependence of the effective anisotropy of the nanoparticle is to evaluate this parameter at $T = 0K$, similar to chapter 2. In Fig. 5.1 we present the plot of 2D energy landscapes for a spherical nanoparticle with uniaxial anisotropy cut from sc internal lattice as a function of the constrained angle θ for two values of the constrained angle $\varphi = 0, \pi/4$ and the surface anisotropy constants $K_s = 10K_c, 50K_c, 100K_c$. The onset of the additional cubic anisotropy is clearly seen in a different value of the energy in the maximum at

$\varphi = \pi/4$ (the saddle point) and $\varphi = 0$ (the absolute maximum). For large surface anisotropy value $K_s = 100K_c$ the energy landscape has predominantly cubic form, characterized by a four-fold anisotropy. The effective uniaxial and cubic anisotropy constants can be extracted from these figures, as we have shown in chapter 2. The surface introduces an additional cubic anisotropy with $K_{ca} < 0$ for spherical particles cut from sc internal structure and $K_{ca} > 0$ for the ones from the fcc lattice. The same is true for the truncated octahedron, although depending on the orientation of the facets and strength of the surface anisotropy (see section 2.8) we may need an additional cubic constant $K_{2,ca}^{\text{eff}}$ for the fitting.

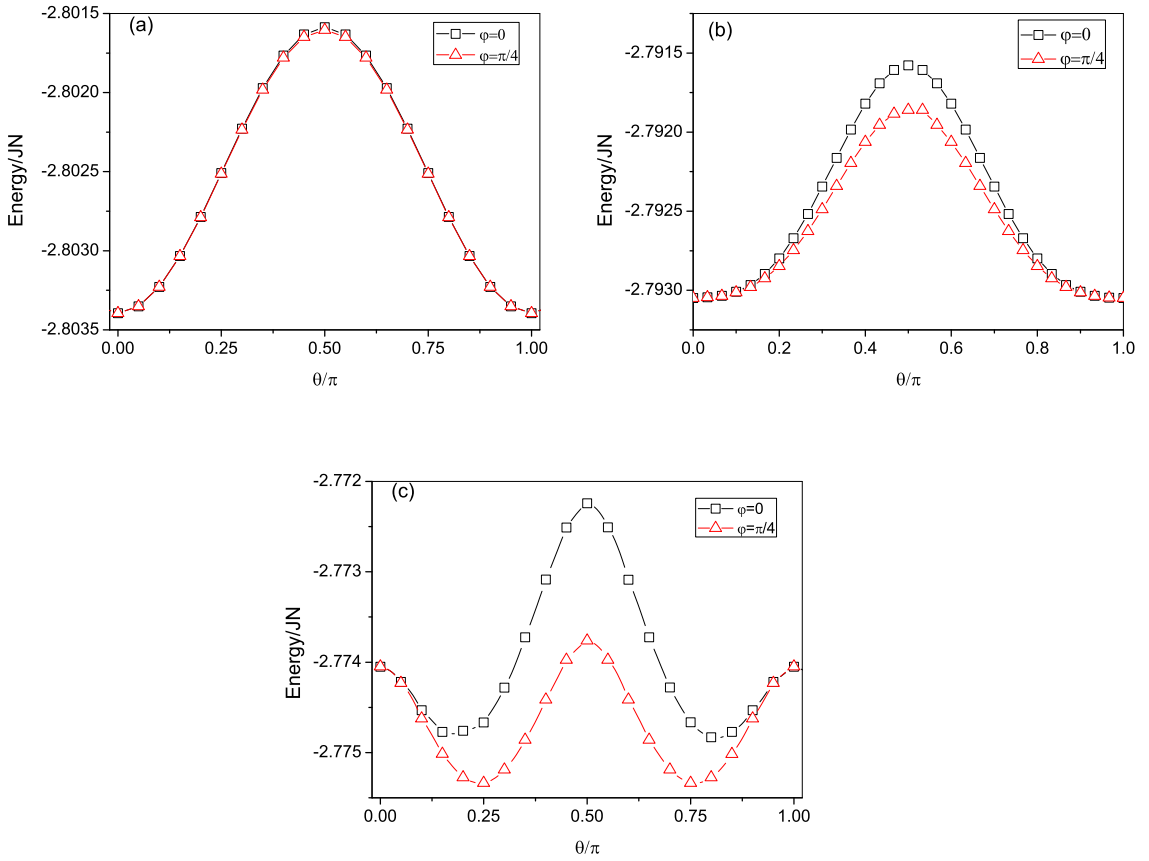


Figure 5.1: Internal energy for $T = 0K$ for $\varphi = 0$ and $\varphi = \pi/4$ as a function of the constrained angle θ in a spherical nanoparticle with uniaxial anisotropy in the core, sc internal structure ($N = 6272$, $N_c = 4968$ and $N_s = 1304$) and three values of the Néel surface anisotropy (a) $K_s = 10K_c$, (b) $K_s = 50K_c$ and (c) $K_s = 100K_c$.

In Fig. 5.2 we present the results for the Y -component of the average restoring torque at $T \neq 0K$ for the nanoparticles whose energy landscapes are presented in Figs. 5.1. The shapes of the torque curves are well described by the expression (5.2) for all

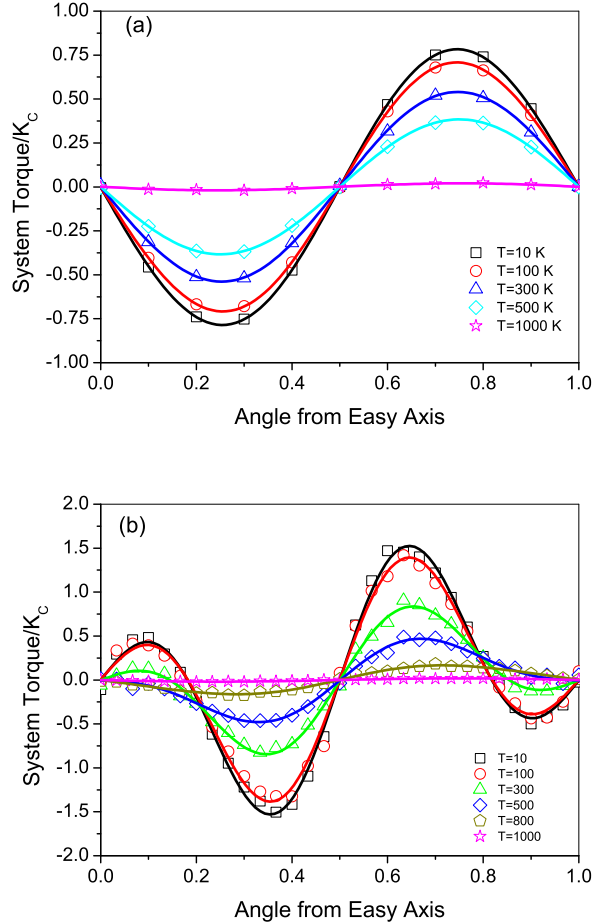


Figure 5.2: The Y-component of the torque for $\varphi = 0$ as a function of the constrained angle θ for various temperatures in a spherical nanoparticle with uniaxial anisotropy in the core, sc internal structure ($N = 6272$, $N_c = 4968$ and $N_s = 1304$) and two values of the Néel surface anisotropy $K_s = 10K_c$ (upper graph) and $K_s = 100K_c$ (lower graph). The line is a fitting curve to Eq.(5.2).

temperatures with the macroscopic anisotropy constants decreasing with temperature. For relatively small strength of the surface anisotropy $K_s = 10K_c$ (see Fig. 5.2(a)), practically only uniaxial anisotropy is present. For large strength of the anisotropy constant $K_s = 100K_c$ we observed the competition of two anisotropies: uniaxial and additional cubic due to surface effects (see Fig. 5.2(b)). At high temperatures, however, the cubic anisotropy contribution disappears.

The torque curves presented in Figs. 5.2 allow to investigate the temperature dependence of the effective anisotropies in nanoparticles. Fig. 5.3 presents the corresponding temperature dependence of uniaxial and additional cubic anisotropy for the two values of the surface anisotropy constants. The macroscopic uniaxial anisotropy

is independent on the surface anisotropy value, as expected. The macroscopic cubic anisotropy, coming from the surface anisotropy, is practically zero for small strength of the surface anisotropy $K_s = 10K_c$. In the case of strong surface anisotropy $K_s = 100K_c$ this additional cubic anisotropy is negative and its absolute value is decreasing with temperature. As it happens with the bulk cubic anisotropy, the surface-induced cubic anisotropy is decreasing faster with temperature as the uniaxial core contribution. Consequently, at high temperatures the cubic counterpart disappears leaving the uniaxial core anisotropy as the dominant factor. A transition in the magnetic behavior then can take place. It is similar to the observed in thin films with strong surface effects: at low temperatures the surface effects predominate and the magnetization of the film is perpendicular to the thin film plane while at higher temperatures the surface anisotropy vanishes and the magnetization stays in plane, see section 4.3.3 in previous chapter. In the case of nanoparticles a similar effect occurs: at low temperatures the surface effects dominate determining the overall cubic behavior, at high temperatures the surface contribution vanishes and the nanoparticle behaves as a uniaxial one.

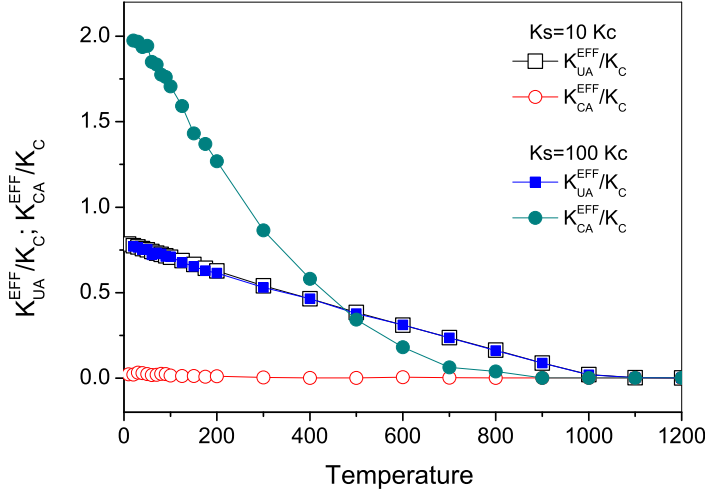


Figure 5.3: Temperature dependence of the macroscopic anisotropies in a spherical nanoparticle with uniaxial anisotropy in the core, sc internal structure ($N = 6272$, $N_c = 4968$ and $N_s = 1304$) and two values of the Néel surface anisotropy (a) $K_s = 10K_c$ and (b) $K_s = 100K_c$. The values are normalized by the core anisotropy K_c .

5.2.2 Temperature dependence of the effective anisotropies in nanoparticles with fcc lattice structure

In the case of nanoparticles with cubic core anisotropy, the surface anisotropy induces an additional contribution which is also cubic in nature being positive for nanoparticles

cut from fcc lattice and negative for nanoparticles cut from sc lattice. The contribution of this anisotropy is additive to the bulk one, although one should note [74], see also section 2.3.1, that it is proportional to K_s^2 , rather than to K_s . An example of the average torque curves is plotted in Fig. 5.4. for various temperatures. The shape of the curves remains corresponding to the cubic anisotropy for all temperatures and surface anisotropy values.

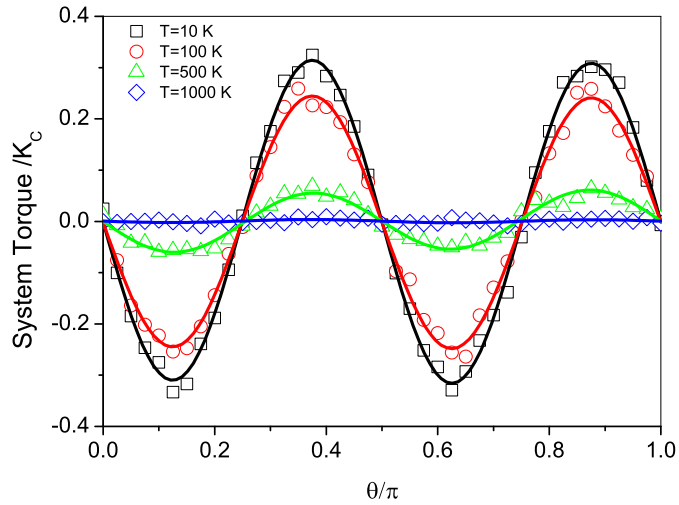


Figure 5.4: Angular dependence of the Y -component of the total system torque in a truncated octahedral nanoparticle with fcc internal structure ($N = 1289$, $N_c = 482$ and $N_s = 807$), Néel surface anisotropy $K_s = 10K_c$ and various values of the temperature.

In Fig. 5.5 we present the temperature dependence of the effective cubic anisotropy constant in a truncated octahedral nanoparticle cut from fcc crystalline structure for various values of the Néel surface anisotropy constant. The appearance of an additional positive cubic anisotropy contribution coming from the surface is seen starting from the value $K_s \approx 20K_c$. The low-temperature values of the effective anisotropy coincide with the ones obtained through the Lagrange multiplier technique at $T = 0K$. In Fig. 5.6 we present the temperature dependence of total cubic anisotropy in spherical and truncated octahedral nanoparticles both with fcc internal structures and for various values of the Néel surface anisotropy K_s . These values are normalized by the value of the effective anisotropy at $T = 0K$ (K_{ca}^{eff}) which is different for each case. The universal dependence on temperature corresponding to the overall cubic anisotropy is observed.

Fig. 5.7 presents the dependence of the effective anisotropy on the value of the surface anisotropy K_s for various temperatures for truncated octahedra cut from the fcc

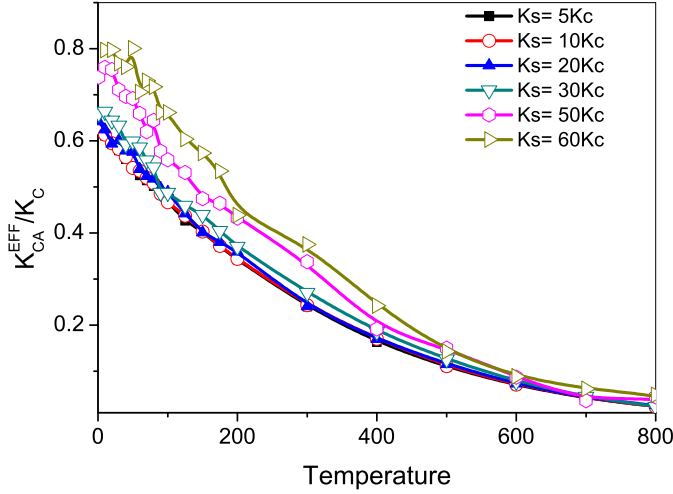


Figure 5.5: Temperature dependence of the effective cubic anisotropy, normalized to the core anisotropy value in truncated octahedra nanoparticles with cubic anisotropy in the core, fcc internal structure ($N = 1289$, $N_c = 482$ and $N_s = 807$) and various values of the Néel surface anisotropy.

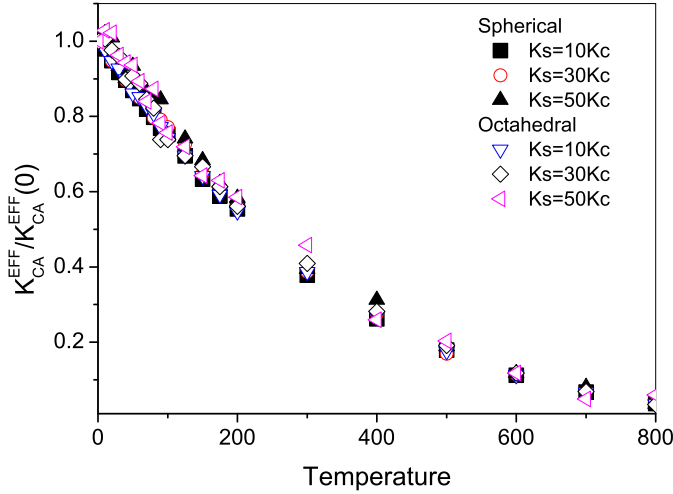


Figure 5.6: Temperature dependence of the effective cubic anisotropy, normalized to its value at $T = 0K$ in spherical ($N = 1505$) and truncated octahedra ($N = 1289$) nanoparticles with cubic anisotropy in the core, fcc internal structure and various values of the Néel surface anisotropy.

lattice with cubic anisotropy in the core. As it is mentioned above, in this case the surface anisotropy contribution is of the same cubic nature as the core one. The additional

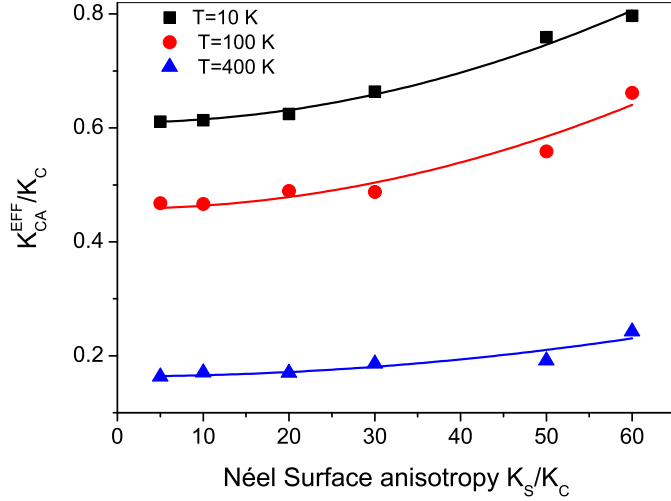


Figure 5.7: The effective cubic anisotropy as a function of the Néel surface anisotropy parameter in truncated octahedra nanoparticle with cubic anisotropy in the core, fcc internal structure ($N = 1289$, $N_c = 482$ and $N_s = 807$) and for various temperatures.

surface contribution is expected to be proportional to K_s^2 , see section 2.3.1 in chapter 2. Consequently, all the data were fitted to this theoretically predicted dependence. The extracted values $K_c^{eff}(T)$ are consistent with the ones calculated independently. The corresponding formula $K^{eff}(T) = K_c^{eff}(T) + AK_{Surf}(T)$ ($K_{Surf}(T) \sim K_s^2$) may be viewed as the one substituting the original formula (3.5). Unfortunately, the parameter A dependence on the system size is not trivial as is discussed in section 3.5 in chapter 3, since it depends on the surface density of spins. The latter is not smooth as a function of the nanoparticle diameter, due to the fact that small nanoparticles do not have uniform spin density on their surfaces.

5.2.3 Scaling exponent

Finally, we would like to discuss the scaling behavior of the effective anisotropy on the nanoparticle magnetisation $K \propto M^\gamma$. The Callen-Callen theory [106] states that in the bulk $\gamma = 3$ for uniaxial anisotropy and $\gamma = 10$ for the cubic one.

Similar to what happens in magnetic thin films, in magnetic nanoparticles the surface magnetization has a faster temperature dependence than the core one, see Fig. 5.8, sharing the same Curie temperature. This arises due to a reduction in coordination number at the surface leading to a reduced exchange and a strong surface anisotropy pointing perpendicularly to the surface. At the same time the fully coordinated core effectively polarizes the surface layer, resulting in a shared value for T_c . The surface anisotropy value has very little effect on the temperature dependence of the overall

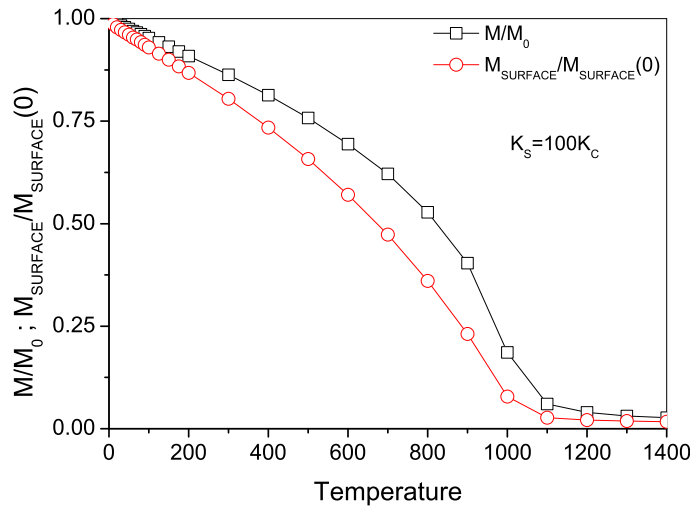


Figure 5.8: Temperature dependence of core and surface magnetization, normalized to $T = 0K$ values in a spherical nanoparticle with sc lattice ($N=1505$).

anisotropy, see Fig. 5.6. The total effect is that the scaling exponents are always smaller than the corresponding bulk value and decreases with the surface anisotropy value.

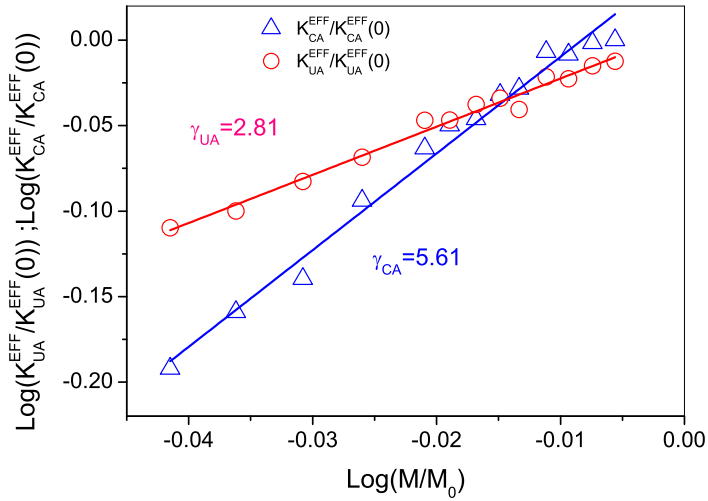


Figure 5.9: Low-temperature scaling of the effective anisotropies with magnetization in a spherical nanoparticles cut from the sc lattice ($N = 1505$), uniaxial anisotropy and Néel surface anisotropy parameter $K_s = 100K_c$.

For example, in Fig. 5.9 we present the scaling of the uniaxial and cubic anisotropy constants with the magnetization at low temperatures (up to $\approx 200K$) in a spherical nanoparticle with uniaxial core anisotropy. Note that no scaling behavior is observed in the whole temperature range. The low temperature scaling exponents are lower than the corresponding bulk values and depend on the surface anisotropy value.

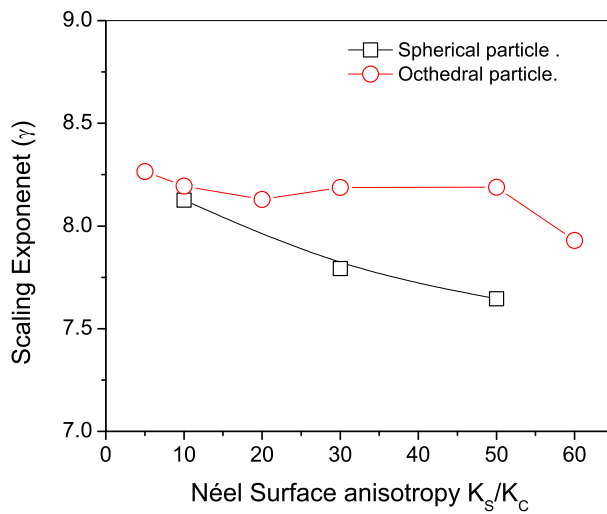


Figure 5.10: Scaling exponents as a function of Néel surface anisotropy constant in spherical ($N = 1505$) and truncated octahedra ($N = 1289$) nanoparticles with cubic anisotropy in the core and fcc internal structure.

A similar effect is produced in spherical and truncated octahedral nanoparticles with cubic core anisotropy. In Fig. 5.10 we present the scaling exponent as a function of Néel surface anisotropy constant in nanoparticles with spherical and octahedral shapes, fcc internal structure, cubic anisotropy in the core and approximately the same nanoparticle's diameter $D \approx 3nm$. The scaling exponents are lower than the corresponding bulk values and weakly depend on the surface anisotropy value, see Fig. 5.10. In fact, the scaling exponent decreases as a function of the surface anisotropy value due to a faster decrease of the magnetization on the surface.

5.3 Conclusions

The main results of the study of the temperature dependence of the macroscopic anisotropy in nanoparticles within the Néel surface anisotropy model, with different lattices and shapes are summarized as follows:

- By means of the constrained Monte Carlo method, we have been able to evaluate the temperature dependence of macroscopic anisotropies in nanoparticles with

different shapes and internal structures. An additional cubic anisotropy, due to the spin non-collinearities produced by the surface anisotropy was detected in chapter 2 at $T = 0K$. This effect persists when the temperature is included.

- The additional cubic anisotropy shows a faster dependence of temperature than the uniaxial core anisotropy. Therefore, the temperature-induced re-orientation transition from the cubic anisotropy to the bulk one can be observed. This effect is similar to the reorientation transition in thin films. It has a pure surface origin and it is independent from the structural changes which may occur in nanoparticles with temperature.
- The scaling exponent of the anisotropy with magnetization depends on the surface anisotropy value and is always lower than the bulk scaling exponent due to strong magnetization fluctuations at the surface.

Conclusiones

En esta sección estudiamos la dependencia de la anisotropía macroscópica con la temperatura en nanopartículas magnéticas con diferentes redes cristalinas, formas y fuerza de la anisotropía de superficie Néel. Los principales resultados han sido sintetizados en los siguientes puntos:

- Por medio del algoritmo ”Monte Carlo con ligaduras” hemos sido capaces de evaluar la dependencia térmica de la anisotropía magnética de nanopartículas con diferentes formas y redes cristalinas. En nuestro estudio observamos que la anisotropía cúbica efectiva adicional que aparecía en el comportamiento global de la nanopartícula, debido a las no-colinealidades en la configuración de espines originadas por la anisotropía de superficie a $T = 0K$ (ver capítulo 2), persiste cuando se tienen en cuenta los efectos de temperatura.
- La anisotropía cúbica efectiva muestra una mayor dependencia con la temperatura que la anisotropía uniaxial. Por tanto, los efectos de temperatura pueden producir una transición desde una anisotropía efectiva cúbica (originada por la superficie) a la correspondiente al volumen. Este efecto es similar a la re-orientación observada en láminas delgadas, tratándose de un efecto puramente de superficie e independiente de posibles cambios estructurales que puedan ocurrir en la red por efectos de temperatura.
- El exponente del escalado de la anisotropía con la imanación del sistema depende del valor de la anisotropía de superficie y es siempre inferior al valor del escalado para el caso de volumen, esto es debido a las fuertes fluctuaciones de la imanación en la superficie.

6

Multiscale modeling of magnetic properties of *Co \ Ag* thin films

6.1 Introduction

Magnetism has a quantum origin and magnetization processes depend on the atomic magnetic moments, the exchange interaction, the spin-orbit coupling, etc. For this reason the "ab-initio" calculations can be useful to obtain the intrinsic magnetic parameters. But from the computational point of view these calculations are very expensive, they require long time and limit the system size to several hundred atoms. Therefore an "ab-initio" study of a macroscopic system is intractable. Additionally, the complete account of temperature fluctuations and dynamics on "ab-initio" level remains a future challenge. In this situation, multiscale modeling can provide a description on all scales using results from one scale as input parameters to the model of the next scale. Thus the "ab-initio" calculations (on a system with a small size) provide the magnetic parameters which will be included in the atomistic simulations. In these atomistic simulations we can take into account the temperature effects and obtain the temperature dependence of the magnetic parameters. The thermodynamic evaluation of macroscopic parameters such as temperature-dependent magnetization $Ms(T)$, anisotropy $K(T)$ [126] and exchange stiffness $A(T)$ [139] can be used later as an input to large-scale micromagnetic simulations, based, for example on open source programs such as Magpar [140] or OOMMF [141]. This "hierarchichal" multiscale scheme was proposed in Ref. [121]. A scheme of this model is represented in Fig. 6.1.

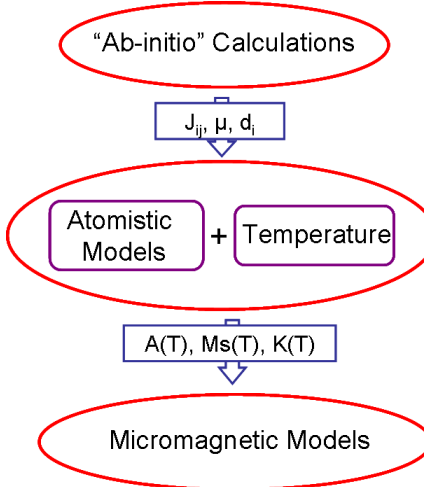


Figure 6.1: Scheme showing a hierarchical multiscale model .

In this chapter we will describe the properties of magnetic thin films in the framework of a generalised Heisenberg model for localized magnetic moments with additional magnetostatic interactions and uniaxial anisotropy.

$$\mathcal{H} = -\frac{1}{2} \sum_{i,j} \sum_{\alpha,\beta} S_i^\alpha J_{ij}^{\alpha,\beta} S_j^\beta + \sum_i \mathbf{d}(\mathbf{S}_i) + H_{MAG}; \alpha, \beta = x, y, z, \quad (6.1)$$

Here $J_{ij}^{\alpha,\beta}$ are the elements of the exchange tensor \mathcal{J}_{ij} between the spins located at sites i and j , α and β represent the coordinates x, y, z . $\mathbf{d}(\mathbf{S}_i)$ is the anisotropy matrix, and \mathbf{S}_i is the spin vector at site i , ($|\mathbf{S}_i| = 1$). First we determine the parameters appearing in the model from the first principle calculations and then study the thermodynamical macroscopic properties by means of the constrained Monte Carlo method [126], presented in chapter 4.

The self-consistent "ab-initio" calculations are performed in terms of the fully relativistic screened Khon-Korringa-Rostocker (SKKR) method [86]. Within this method, spin-polarization and relativistic effects (in particular, spin-orbit coupling) are treated on equal theoretical footing by solving the Kohn-Sham-Dirac equation. We employed the technique to map the electronic structure calculations into the Heisenberg model following L. Uvdardi *et. al* [142]. The anisotropy energies have been extracted from the difference of the layer resolved band energies for the magnetization perpendicular and parallel to the surface. Since the spin-orbit coupling plays a key role in the magnetic anisotropy energy, the calculations were done by a fully relativistic spin polarized code, which was supplied by Dr. L. Szunyogh of the Budapest University of Technology and Economics, and henceforth we will call it the Budapest-Vienna Code.

6.2 Density functional theory

Probably the most widely used theory for quantitative prediction in condensed matter physics is the density functional theory (DFT), originally developed by Hohenberg and Kohn [143]. This theory has the advantage that it does not require adjustable parameters from experiments, in principle only fundamental constants as the speed of light in vacuum, Planck's constant, electron charge, etc. are taken from the experiment. DFT allows to calculate the ground-state properties of materials: total energy, ground-state lattice constants, electronic structure etc. In magnetism it appeared to be particularly useful for calculation of spin-dependent band structure in transition metals, such as Co.

Density functional theory promotes the electron density $n(\mathbf{r})$ instead of the many particle wave function as the key variable, on which the calculation of all other observables can be based.

6.2.1 Hohenberg-Kohn theorems

Density functional theory relies on the theorems of Hohenberg and Kohn [144]. These two theorems could be summarized in the following: (I) That the ground state of a many-electron system (under the effects of an external potential) is uniquely defined by the ground-state electron density, and (II) The existence of an energy functional of the density $E[n]$ that is minimal for the ground state density $n_0(\mathbf{r})$ giving the ground state energy.

6.2.2 Kohn-Sham scheme

The electron density corresponding to the ground state can be calculated using a variational principle, we know that every $n \neq n_0$ has $E[n] > E_0 = E[n_0]$. In this way Kohn and Sham added a tremendous addendum in 1965 [144], within their variational scheme an auxiliary system of non-interacting electrons is introduced. It is assumed that the ground state density of this hypothetical non-interacting electrons system is the same as that of the original interacting system.

In addition, the Kohn-Sham approach to the interacting electrons problem is to rewrite the Hohenberg-Kohn expression for the energy functional corresponding to the ground state as follows:

$$E_{KS} = T_{NI}[n] + E_{ext}[n] + E_H[n] + E_{xc}[n], \quad (6.2)$$

where T_{NI} is the kinetic energy of the non-interacting electron system. E_{ext} is the energy due to the external potential (external potential means that it is due to the atomic nuclei), and it has the following form:

$$E_{ext}[n] = \int d^3r V_{ext}(\vec{r})n(\vec{r}), \quad (6.3)$$

E_H is the Hartree energy, which can be expressed as a functional of the electron density of the system as follows:

$$E_H[n] = -\frac{e^2}{2} \int d^3r \int d^3(\vec{r}') \frac{n(\vec{r})n(\vec{r}')}{|\vec{r} - \vec{r}'|}, \quad (6.4)$$

and finally, E_{xc} is the so called exchange correlation energy term which includes "all remaining" contributions.

We have to note that in practice the correct E_{xc} term is unknown, for this reason the determination of such functional requires some approximation, and it is this approximation which determines the accuracy of the method.

6.2.3 Approximation for the exchange-correlation energy $E_{xc}[n]$

In the literature one can find several approximations of the $E_{xc}[n]$, for instance, the local density approximation (LDA) [144, 145], the general gradient approximation (GGA) [146], etc. LDA is a rather simple approximation which has yielded accurate results in many cases, and may be expressed in the form:

$$E_{xc}[n] \approx E_{xc}^{LDA}[n] = \int n(\vec{r}) \epsilon_{xc}^{LDA}(n(\vec{r})) d^3r \quad (6.5)$$

where ϵ_{xc}^{LDA} is the exchange-correlation energy per particle for a homogeneous electron gas of density $n(\vec{r})$. Within this approximation it is assumed that the energy E_{xc} of a system with an inhomogeneous electron distribution $n(\vec{r})$ at each point (\vec{r}) has the same value as in the case of homogeneous electron gas with the same density.

We are working with a magnetic system, therefore we have to use an approximation that takes into account the spin-polarization of the system, for this reason we used a generalization of the LDA approximation for a spin polarized system: local spin density approximation (LSDA) [147]. In the case of spin-polarized calculations, the spin density $\vec{m}(\vec{r})$ has to be included and the non-spin polarized density n is replaced by the density matrix $\mathbf{n}(\vec{r})$. The density matrix can be expressed as:

$$\mathbf{n}(\vec{r}) = n(\vec{r}) \cdot \mathbf{1} + \tilde{\sigma} \cdot \vec{m}(\vec{r}); \quad (6.6)$$

$\tilde{\sigma}$ represents the Pauli matrices and $\mathbf{1}$ is the unit matrix.

In this context the Kohn-Sham equation (KSE) may be expressed by:

$$\left(-\frac{\hbar^2}{2m} \nabla^2 + V_{eff}(\vec{r}) + \tilde{\sigma} \cdot \vec{B}_{eff}(\vec{r}) - E_i \right) \begin{pmatrix} \psi_{i\uparrow}(\vec{r}) \\ \psi_{i\downarrow}(\vec{r}) \end{pmatrix} = 0 \quad (6.7)$$

where $\psi_{i\uparrow;\downarrow}(\vec{r})$ are the resulting eigenfunctions of the auxiliary non-interacting system. These eigenstates are dependent on the eigenenergy E_i and on the spin up or down ($\uparrow; \downarrow$) configuration, with respect to the local magnetization direction $\mu(\vec{r})$ along the effective magnetic field $\vec{B}_{eff}(\vec{r})$. $V_{eff}(\vec{r})$ is the effective potential which collects the contributions

of the external potential, the Hartree and the exchange-correlation potentials, the last one in practice is unknown and must be approximated.

We have to complete the set of Kohn-Sahm equations with the charge and spin density ones:

$$n(\vec{r}) = \sum_{E_i \leq E_F} (|\psi_{i\uparrow}(\vec{r})|^2 + |\psi_{i\downarrow}(\vec{r})|^2) \quad (6.8)$$

$$\vec{m}(\vec{r}) = \mu(\vec{r}) \sum_{E_i \leq E_F} (|\psi_{i\uparrow}(\vec{r})|^2 - |\psi_{i\downarrow}(\vec{r})|^2) \quad (6.9)$$

Another condition that has to be satisfied is the charge conservation. This requirement allows us to determine the Fermi level E_F , from the next relation:

$$N = \int n(\vec{r}) d^3r = \int d^3r \sum_{E_i \leq E_F} (|\psi_{i\uparrow}(\vec{r})|^2 + |\psi_{i\downarrow}(\vec{r})|^2) \quad (6.10)$$

The equations (6.7-6.10) are the set of equations that must be solved self-consistently in the DFT calculations to obtain the ground state energy of the system.

Note that in principle the Kohn-Sham equation corresponds to a non-relativistic formulation of the DFT. If we work within the relativistic DFT for instance, in the case where the spin-orbit coupling (SOC) can not be treated as a perturbation term, we have to replace the Kohn-Sham equation by the corresponding Kohn-Sham-Dirac equation (KSDE).

6.2.4 Screened Korringa-Kohn-Rostoker Green's function method

The Korringa-Kohn-Rostoker (KKR) method was developed initially by Korringa in 1947 [148] who used the *multiple-scattering theory* to solve the Schrödinger equation and determine the band structure of a periodic solid. Seven years later Kohn and Rostoker [149] proposed a method equivalent to the Korringa one but using Green's functions, called in our days the Korringa-Kohn-Rostoker (KKR) method. Perhaps the most important characteristic of the KKR method is that its formal structure does not change when going from non-relativistic to relativistic description.

The KKR method has undergone several improvements since the late forties. One of these improvements is the so-called screened Korringa-Kohn-Rostoker (SKKR) method. The SKKR method allows to calculate the electronic properties of surface, interface and in general layered systems with periodicity only in two dimensions, within the framework of multiple-scattering theory without any further approximations.

In multiple scattering theory the scattering path operator ($\tau(E)$) from which the Green function and electronic properties are calculated, is given in terms of the structure constant $\mathbf{G}(E)$, and the single-site scattering matrix $\mathbf{t}(E)$:

$$\tau(E) = \left[\mathbf{t}^{-1}(E) - \mathbf{G}(E) \right]^{-1}. \quad (6.11)$$

2D periodicity leads in principle to infinite matrix. However, the screening method allows to transform $\mathbf{G}(E)$ to the screened structure constants, which have spatial short-range. In general the screening results in the fact that layers interact only up to a certain number of neighboring layers. For a layered structure it is convenient to divide the parent lattice in three regions, a left semi-infinite system (L), a right semi-infinite (R), and an intermediate interface region, the properties of which to be calculated. This formal partitioning of the parent infinite system implies that the inverse of the scattering path operator \mathcal{M} also has the form [150]:

$$\mathcal{M} = \begin{pmatrix} \mathcal{M}_{LL} & \mathcal{M}_{LI} & 0 \\ \mathcal{M}_{IL} & \mathcal{M}_{II} & \mathcal{M}_{IR} \\ 0 & \mathcal{M}_{RI} & \mathcal{M}_{RR} \end{pmatrix}. \quad (6.12)$$

This shape is a direct consequence of the short-range of the structure constant. Using the concept of principal layer [151], which is defined so that it interacts only with nearest-neighbors principal layers, one can rewrite the structure constants, and consequently the inverse of the scattering path operators, in tridiagonal form. From them the Green function of the system can be calculated from a decimation technique [152, 153].

The free energy derived in the frame work of the fully relativistic SKKR method at zero temperature is approximated by:

$$\mathcal{F} = \int_{-\infty}^{E_F} d\varepsilon (\varepsilon - E_F) n(\varepsilon) = - \int_{-\infty}^{E_F} d\varepsilon N(\varepsilon), \quad (6.13)$$

where E_F is the Fermi energy of the system, $n(\varepsilon)$ is the density of states (DOS), and $N(\varepsilon)$ is the integrated density of states. Using the Lloyd's formula [154], the free energy can be written as follow:

$$\mathcal{F} = -\frac{1}{\pi} Im \int_{-\infty}^{E_F} d\varepsilon Tr \ln \tau(\varepsilon), \quad (6.14)$$

where $\tau(\varepsilon) = \{\tau_{ij}(\varepsilon)\}$ is the site-angular momentum representation of the scattering path operator, which can be expressed as a function of the site-diagonal single scattering matrix $\mathbf{t}(\varepsilon) = \{t_i(\varepsilon)\delta_{ij}\}$ and the structure constants $\mathbf{G}_0(\varepsilon) = \{G_{0,ij}(\varepsilon)(1 - \delta_{ij})\}$, in the following way:

$$\tau(\varepsilon) = \left(\mathbf{t}^{-1}(\varepsilon) - \mathbf{G}_0(\varepsilon) \right)^{-1}. \quad (6.15)$$

6.3 "Ab-initio" modeling of bulk Co and its interfaces

The "ab-initio" calculations presented in this thesis are based on the fully relativistic Screened Korringa-Kohn-Rostoker (SKKR) Green's function method [86]. Within this method the spin-polarization and the relativistic effects are treated on equal theoretical

footing by solving the Kohn-Sham-Dirac equation. We used the local spin-density approximation (LSDA) for the exchange-correlation term and the effective potential and field were treated within the atomic sphere approximation (ASA), with an angular momentum cutoff of $l = 2$.

In ASA the effective potential is of a muffin-tin type, surrounding each atom there is a sphere of radius S_{MT} outside of which the potential has a value equal to a constant, and within the sphere the potential is assumed to be spherically symmetric leaving only a radial dependence of the potential. Within ASA, the effective potential V_{eff} , at one atomic site can be written as:

$$V_{eff} \approx V_{MT} = \begin{cases} v(r) & r \leq S_{MT} \\ V_{MTZ} & r > S_{MT}, \end{cases} \quad (6.16)$$

here V_{MT} is the Muffin-Tin potential, where V_{MTZ} is the muffin-tin zero potential, which is defined as the value of the muffin-tin potential at a distance S_{MT} ($V_{MTZ} = v(r = S_{MT})$) and $v(r)$ is the spherical potential inside the muffin-tin sphere.

Henceforth we will apply a spin-polarized relativistic version of the screened Korringa-Kohn-Rostoker Green's function method to calculate the magnetic properties: spin and orbital moments, exchange constants, and magnetocrystalline anisotropy energy. Once reached this point, we would like to point out some issues, which will be important throughout this chapter:

- The system simulated in "ab-initio" calculations presents a 2D periodicity.
- The Budapest-Vienna Code, can provide layered resolve spin and orbital magnetic moments, exchange parameters and magneto-crystalline energy.
- The Budapest-Vienna Code has not implemented the option to evaluate the structural relaxation of the lattice in a self-consistent way. There are other codes like SIESTA which has implemented these possibilities.

The theoretical and computational details of the SKKR method used in our calculations can be found in the Weinberger book [155].

First we will discuss the results of a self-consistent calculation of the work function, the spin and orbital moments in the Co/Ag layered system, after that we will analyze the results for the exchange interaction and the magneto-crystalline anisotropy (MCA) energy, obtained using the "magnetic force theorem". Finally we will study the magnetic behavior of a particular system $Co(111) \setminus Ag_1$ with the temperature.

6.3.1 The studied system

We have calculated the magnetic properties for a system of Co fcc (bulk), as well as semi-infinite system with surface terminations $Co(111)$, $Co(100)$, $Co(100) \setminus Ag_n$ and $Co(111) \setminus Ag_n$, where n is the number of the atomic layers of Ag ($n = 1$, or 2).

We would like to indicate that the coordinate system has been chosen in such form that the Z axis is perpendicular to (100) or (111) plane depending the case under study.

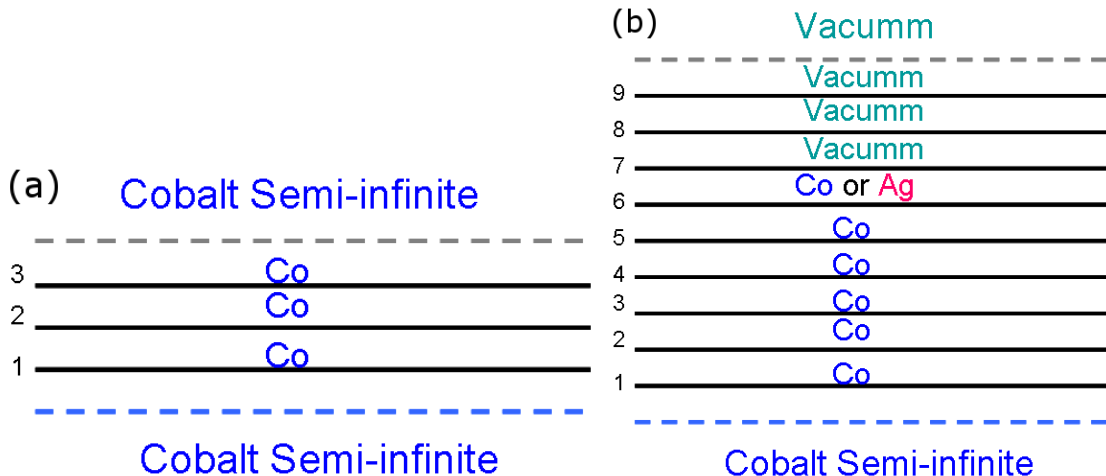


Figure 6.2: Sketch of the systems studied in the calculations (a) Cobalt bulk system; (b) Films systems. The systems are divided in three regions, one corresponding to a semi-infinite substrate of Co, a intermediate region which correspond to: 3 atomic layer of Co in the case of a Co bulk system or, in the case of film systems, several (up to six) atomic layers of Co with or without a Ag capping and 3 Vacumm layers. The last region corresponds to a semi-infinite Co capping in Co bulk, or a Vacuum region in film systems.

The system under study is divided in three regions, see Fig. 6.2, corresponding to a semi-infinite substrate of Co, an intermediate region which corresponds to: 3 atomic layers of Co in the case of a Co bulk system or, in the case of semi-infinite systems, several (up to six) atomic layers of Co with or without Ag capping and 3 Vacumm layers. The last region corresponds to a semi-infinite Co capping in Co bulk, or a Vacuum region in film systems. We have to note that only interactions between spins belonging to the intermediate region are evaluated.

In our calculations when capping layers of Ag on Co exists, it is assumed that the Ag layer(s) adjust to the in-plane lattice parameter of Co fcc. However the lattice parameter of fcc Ag is bigger than that of Co. Then with the aim to deal with this mismatch between the lattice constants of the Co fcc and the Ag, we supposed a "rigid relaxation" of the lattice. In our "rigid relaxation", we kept the in-plane lattice constant of Co fixed, for the whole system since we are modeling epitaxial growth of Ag on Co fcc, and relax the perpendicular lattice constant. For normal-to-plane distance relaxation of the Ag layer(s), we consider an expansion of the interlayer distances, d_{Co-Ag} and d_{Ag-Ag} of $r\%$ with respect to the bulk Co lattice constant. The relaxation (r) was considered to range from 6 to 12 %, depending on the system.

With the aim to have an estimation of the actual relaxation of the system we have compared it with the relaxation obtained for these system with SIESTA code [156],

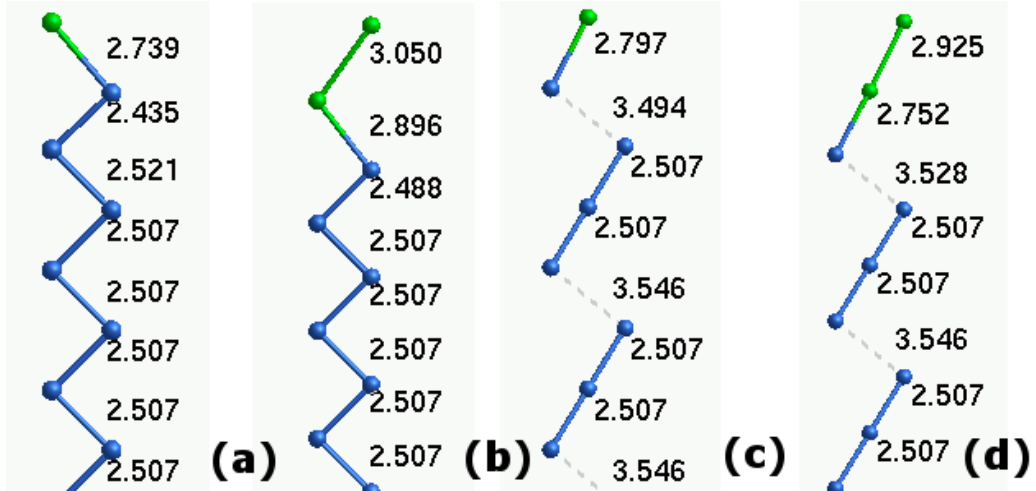


Figure 6.3: Calculated relaxation of the lattice in the systems:(a) $Co(100) \setminus Ag_1$; (b) $Co(100) \setminus Ag_2$; (c) $Co(111) \setminus Ag_1$ and (d) $Co(111) \setminus Ag_2$. This calculations have been performed with the code SIESTA [156].

see Fig. 6.3. The first thing that we can conclude from these results is that the relaxation of the lattice in these layered systems is complex. In the SIESTA results we can observe not only a relaxation of the lattice in the surface layer but also there is a contraction between the subsurface layers of Co. In the cases of one ML of Ag capping, the relaxation of the lattice range from 9.25% to 11.56 %. Therefore, it is always in the range assumed in the study with the Budapest-Vienna code.

In what follows the value of the relaxation which is selected in the multiscale study is $r = 10\%$. This relaxation of the lattice has been chosen because this value coincides with the one which provides the minimum of the total energy and it is close to the SIESTA results. It should be noted that the value of the relaxation has little effect on the spin and orbital magnetic moments, and the influence on the work function and anisotropy will be discussed separately.

6.3.2 Work function

The work function (WF) is one of the important characteristics of surface physics. This quantity, usually denoted by Φ is defined as the minimum work that must be done to remove an electron from the surface at $T = 0K$. The WF could be extracted from experimental measurements and therefore it is often used as a control parameter in simulations. Nevertheless there are no systematic experimental studies which can be used as a proper reference for our theoretical study. The most popular experimental study about the work function is the H.B. Michaelson one [157], and corresponds mostly to polycrystalline samples. In that study we can find experimental values of the work function for 44 elements, including Co, Fe, Ni, Ag etc. Next we study how the work

function depends on the surface's orientation and the relaxation of the lattice.

WF dependence on the surface

We have simulated a semi-infinite system of cobalt fcc and evaluated the value of the work function for different crystal faces, (100) and (111). The obtained results are presented in Tab. 6.1. As we can see, the value of the WF of the face (100) is slightly larger than that corresponding to the face (111), the increment of the work function of the cobalt's face (100) being only about 1%. Smoluchowski et. al. [158] have studied the case of a simple cubic lattice in simple metals. They obtained the result that the lowest work function corresponds to the least densely packed face among those considered. Our results presented in Tab. 6.1 show analogous values but slightly lower for the (111) case.

System	Interface	Work Function (eV)
Cobalt (fcc)	(100)	5.51
Cobalt (fcc)	(111)	5.46

Table 6.1: Work function for semi-infinite system of Co fcc with surface (100) or (111).

Dependence of the WF with the structural relaxation

As we have mention previously, the Budapest-Vienna code does not allow us to include structural relaxation in the self-consistent procedure. For this reason, throughout this chapter when we address the case of semi-infinite fcc cobalt with a capping of an atomic monolayer of Ag, we will suppose that the lattice of the system has experimented "rigid relaxation", and we assume different values of r .

In Fig. 6.4 we present the WF of a semi-infinite cobalt fcc system capped with a monolayer of Ag, for two different interfaces: (100) and (111) as a function of the rigid relaxation of the Ag lattice. As we can see, the work function changes with the crystal face as it has been reported previously in metals in Ref. [159], and also it is affected by the relaxation of the lattice. Nevertheless the variation of the value of the WF is lower than a 5% of the un-relaxed one.

6.3.3 Spin and orbital moments

In this section we will evaluate the spin and orbital magnetic moments: first for a Co fcc bulk system, later we simulate a perfect semi-infinite Co system and finally we study the case of a semi-infinite Co system with a capping of one atomic monolayer of Ag.

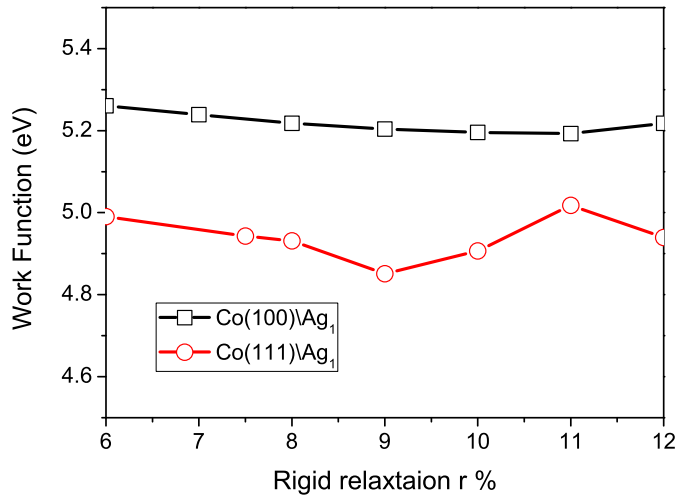


Figure 6.4: Calculated Work Function, in eV, as a function of the relaxation of the volume of the silver atom in the systems: $Co(100) \setminus Ag_1$; $Co(111) \setminus Ag_1$.

Spin and orbital moments on Co bulk system

The self-consistent calculations provide the spin and orbital atomic moments for Co (bulk), which values are: $\mu_s \approx 1.66\mu_B$ and $\mu_L \approx 0.078\mu_B$, see Tab. 6.2, μ_B is the Bohr magneton. As we can expect in the case of a d metal the value of the magnetic moment is practically due to the spin, since μ_L is two orders of magnitude lower than μ_s . The value obtained by us of the spin moment of Co (bulk) coincides with those reported in the literature, which oscillate from $\mu_s = 1.64\mu_B$ [160] to $\mu_s = 1.724\mu_B$ [161]. However the orbital one is smaller than the reported value $\mu_L = 0.14\mu_B$ [160].

Spin and orbital moments on pure Co surface

We have simulated a semi-infinite system of cobalt fcc with (100) or (111) surface. The self-consistent calculations provide the layered resolved spin and orbital atomic moments, see Fig. 6.5. This allows us to establish that there exists an increment of the spin and orbital moments on the cobalt surface and the increment is sensitive to the surface type. Both the spin and the orbital magnetic moments are smaller in the case of the surface (111) than those in the case of the surface (100). The system experiences an increment of the spin and orbital moments on the surface layer, such increment is approximately 10% of the bulk value in the case of Co(100) surface and 5% in the Co(111).

It is well known that the orbital moments of a delocalized state closely depend on the shape and the width of the density of states (DOS). The main reason for an

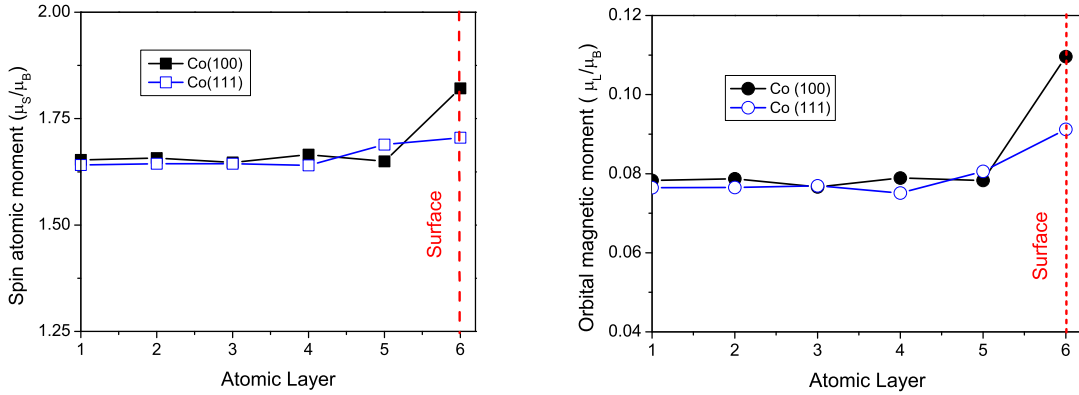


Figure 6.5: The layered resolved spin (left) and orbital (right) moments for a semi-infinite fcc $Co(100)$ and $Co(111)$ system, where the surface is at the atomic layer number 6.

increment of the orbital and spin moments at the surface is the modification of DOS [161]. This can have different origins as for example:

- (i) The reduction of the crystal field at the surface leads to an enhancement of the orbital moment.
- (ii) The d band becomes narrower at the surface due to the reduce number of nearest-neighbors.

Spin and orbital moments on $Co \setminus Ag_1$ interface

Unfortunately, a perfect free layer of a Co is difficult to obtain at ambient condition due to oxidation, lattice imperfection, etc. With the purpose of exploring its experimental properties it is often covered by another protective layer. "A-priori" the orbital and spin moments could be affected by this protective capping. We have analyzed how the Ag capping over the Co semi-infinite system can affect the orbital and spin moment.

In Fig. 6.6 we show the layered resolved values of the spin and orbital moments for a semi-infinite Co capped by a monolayer of Ag: $Co(100) \setminus Ag_1$ and $Co(111) \setminus Ag_1$. It is seen that both the spin and orbital moments are affected by the existence of the Ag capping. The orbital and spin moments of Co experience a variation with respect to the volume one, such modification depends on the orientation of the interface of $Co \setminus Ag$. We can observe that the spin magnetic moment in the case of Co with a monolayer capping of silver presents a reduction of its value with respect to the Co bulk one, on both (100) and (111) interfaces. In contrast to the spin moment, the orbital magnetic moment is increased in the same systems.

With the aim to summarize our results, we present in Tab. 6.2 the spin and orbital atomic moments of Co in several systems. We can observe that Co presents different

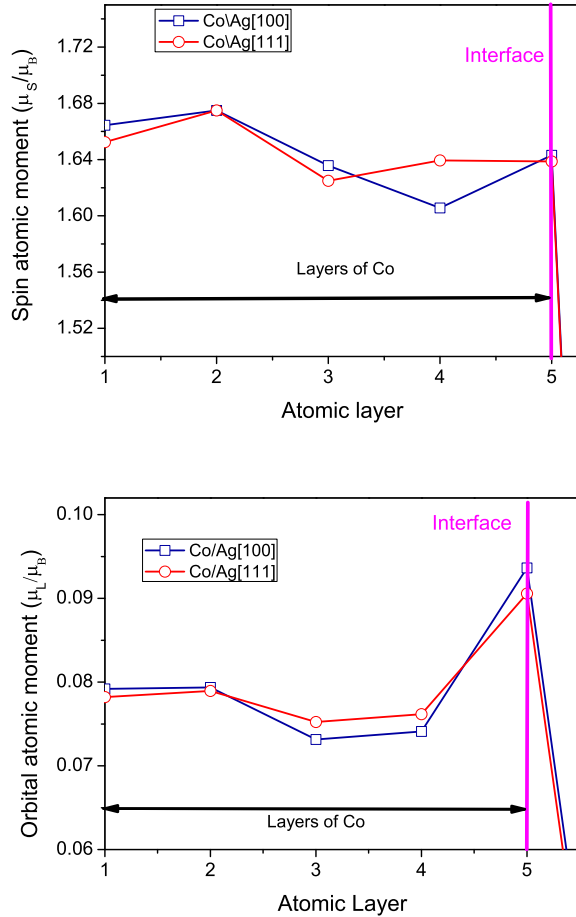


Figure 6.6: The layered resolved spin and orbital magnetic moments, top and bottom graphics respectively, for a $Co(100) \setminus Ag_1$ and $Co(111) \setminus Ag_1$, where the interface between de Co and Ag is the atomic layer number 5.

spin and orbital moments depending on the chemical environment or the existence of a surface. This effect has been reported in the literature, both in theoretical [162, 163] and experimental studies [9, 164, 165]. For example, in Co overlayer on Cu(100) an increment about the double of the bulk value of the Co orbital moment has been observed by Tischer et.al. The authors suggested that this increment could have its origin in an increased spin moment or an increased value of DOS at the Fermi level [161].

The Ag has nearly filled $4d^{10}$ bands and it is diamagnetic in the absence of hybridization, nevertheless we have observed an appearance of a small orbital moment of the Ag layer, see Tab. 6.3. This result suggests us that the Ag layer has become polarized by Co layer, similar to the result reported by N. Joaquin et. al for Fe/Ag

Quantity	$Co(fcc(100), bulk)$	$Co(fcc, surface(100))$	$Co(100) \setminus Ag_1$
μ_L	0.078	0.11	0.094
μ_s	1.663	1.821	1.643
Quantity	$Co(fcc(111), bulk)$	$Co(fcc, surface(111))$	$Co(111) \setminus Ag_1$
μ_L	0.078	0.091	0.091
μ_s	1.658	1.705	1.639

Table 6.2: The μ_s and μ_L values (in Bohr magneton μ_B) obtained in the self-consistent calculations. In the second column we can find the value of the orbital and spin moment of a Co(bulk), in the third column we present the value at a free surface Co(100) and Co(111), in the last column there are the results of μ_S and μ_L at the interface $Co(100) \setminus Ag_1$ and $Co(111) \setminus Ag_1$.

multilayers [166]. On the other hand, we have observed that Ag spin magnetic moment is practically zero.

System	Interface	μ_L/μ_B
Ag monolayer on Co(fcc)	(100)	0.0089
Ag monolayer on Co(fcc)	(111)	0.0057

Table 6.3: The orbital magnetic moment of Ag, obtained in the self-consistent calculation for $Co(100) \setminus Ag_1$ and $Co(111) \setminus Ag_1$ systems.

6.3.4 Exchange interactions

Evaluation of the Exchange tensor

There are different methods in the literature to map the first principle calculations to the exchange coupling parameters entering in a Heisenberg-like spin Hamiltonian. We have used in this chapter the magnetic "force theorem" [86, 167, 168]. It states that for the frozen ground state potential and small perturbations in the electron and magnetization densities ($n(\vec{r})$, $m(\vec{r})$), the variation of the total energy of the system can be approximated by the difference of the occupied single-particle state energies (E_B , called band energy). Within the adiabatic approach the fast motion of the itinerant electrons is decoupled from the slow motion of the spins. This means that the electronic system is assumed to be at any instant in its ground state with respect to the orientation S_i . This approximation is valid if the time scale of the precession of the magnetic moment is larger compared to that of the motion of electrons. It has been shown that in terms of the rigid-spin approximation the adiabatic dynamics of the local spin

moments is described by the Landau-Lifshitz equation [169].

$$M_{ri} \dot{\mathbf{S}}_{ri} = -\frac{2\mu_B}{\hbar} \frac{\delta \mathcal{F}}{\delta \mathbf{S}_{ri}} \times \mathbf{S}_{ri} \quad (6.17)$$

where M_{ri} is the magnitude of the spin-moment of the spin i of the atomic layer r , \mathbf{S}_{ri} is a unit vector pointing along the spin-quantization axis in the cell at site i of layer r , \mathcal{F} is the free-energy of the system and \hbar is the reduced Planck constant.

We will rewrite Eq. (6.17) into spherical coordinates $(\theta_{ri}; \varphi_{ri})$, with polar and azimuthal angles, respectively, measured from the spin-quantization axis. Selecting the corresponding reference system and adopting the harmonic approximation, we can expand the Hamiltonian up to the second order of the free-energy \mathcal{F} in angular variables¹. After that we can relate such Hamiltonian with a generalized Heisenberg Hamiltonian and determine the exchange matrix.

The exchange matrix can be determined in ferromagnetic states by calculating the derivatives of the free energy, with respect to three orthogonal directions of the magnetization: X , Y and Z , see Ref. [142]. Then we get the following results for the magnetization parallel to the X direction:

$$\frac{\delta^2 \mathcal{F}}{\delta \varphi_i \delta \varphi_j} = J_{ij}^{yy}; \quad \frac{\delta^2 \mathcal{F}}{\delta \theta_i \delta \theta_j} = J_{ij}^{zz}; \quad \frac{\delta^2 \mathcal{F}}{\delta \varphi_i \delta \theta_j} = -J_{ij}^{yz}; \quad \frac{\delta^2 \mathcal{F}}{\delta \theta_i \delta \varphi_j} = -J_{ij}^{zy}.$$

For the magnetization parallel to the Y direction:

$$\frac{\delta^2 \mathcal{F}}{\delta \varphi_i \delta \varphi_j} = J_{ij}^{xx}; \quad \frac{\delta^2 \mathcal{F}}{\delta \theta_i \delta \theta_j} = J_{ij}^{zz}; \quad \frac{\delta^2 \mathcal{F}}{\delta \varphi_i \delta \theta_j} = -J_{ij}^{xz}; \quad \frac{\delta^2 \mathcal{F}}{\delta \theta_i \delta \varphi_j} = -J_{ij}^{zx}.$$

For the magnetization parallel to the Z direction:

$$\frac{\delta^2 \mathcal{F}}{\delta \varphi_i \delta \varphi_j} = J_{ij}^{yy}; \quad \frac{\delta^2 \mathcal{F}}{\delta \theta_i \delta \theta_j} = J_{ij}^{xx}; \quad \frac{\delta^2 \mathcal{F}}{\delta \varphi_i \delta \theta_j} = -J_{ij}^{yx}; \quad \frac{\delta^2 \mathcal{F}}{\delta \theta_i \delta \varphi_j} = -J_{ij}^{xy}.$$

Here i and j are different spin sites. In the way described above we have calculated the exchange tensor \mathcal{J}_{ij} within the SKKR method using a full-relativistic description.

The exchange tensor \mathcal{J}_{ij} is a matrix 3×3 , its elements can be noted by $J_{ij}^{\alpha\beta}$ where $\alpha, \beta = x, y, z$. It \mathcal{J}_{ij} can be decomposed into three terms as in Ref. [142]:

$$\mathcal{J}_{ij} = J_{ij}\mathcal{I} + \mathcal{J}_{ij}^S + \mathcal{J}_{ij}^A, \quad (6.18)$$

where \mathcal{I} is the unit matrix and J_{ij} is the isotropic part of the exchange tensor:

$$J_{ij} = \frac{1}{3} \sum_{\alpha} J_{ij}^{\alpha\alpha}; \quad \alpha = x, y, z. \quad (6.19)$$

This term is the parameter normally used as a classical exchange constant.

¹See Refs. [142, 155] or appendix A.1 for more details

The second term \mathcal{J}_{ij}^S is the traceless symmetric anisotropic exchange tensor and it is defined by

$$\mathcal{J}_{ij}^S = \frac{1}{2}(\mathcal{J}_{ij} + \mathcal{J}_{ij}^T) - J_{ij}\mathcal{I}, \quad (6.20)$$

where \mathcal{J}_{ij}^T is the transpose of the exchange tensor.

The third term \mathcal{J}_{ij}^A is the antisymmetric exchange matrix and it is given by

$$\mathcal{J}_{ij}^A = \frac{1}{2}(\mathcal{J}_{ij} - \mathcal{J}_{ij}^T). \quad (6.21)$$

Then we can rewrite the exchange part of the Hamiltonian (6.1) as a function of the isotropic, symmetric anisotropic and antisymmetric exchange as follows:

$$\mathcal{H}^{ex} = -\frac{1}{2} \sum_{i,j} \mathbf{S}_i (J_{ij}\mathcal{I} + \mathcal{J}_{ij}^S + \mathcal{J}_{ij}^A) \mathbf{S}_j \quad (6.22)$$

This equation could be simplified in the following form:

$$\mathcal{H}^{ex} = -\frac{1}{2} \sum_{i,j} J_{ij} \mathbf{S}_i \mathbf{S}_j - \frac{1}{2} \sum_{i,j} \mathbf{S}_i \mathcal{J}_{ij}^S \mathbf{S}_j - \frac{1}{2} \sum_{i,j} \mathbf{S}_i \mathcal{J}_{ij}^A \mathbf{S}_j. \quad (6.23)$$

The corresponding inter-site antisymmetric exchange interaction can be cast in the form, known as the Dzyaloshinsky-Moriya interaction.

$$\mathbf{S}_i \mathcal{J}_{ij}^A \mathbf{S}_j = \mathbf{D}_{ij} (\mathbf{S}_i \times \mathbf{S}_j), \quad (6.24)$$

where \mathbf{D}_{ij} is the Dzyaloshinsky-Moriya vector.

Finally,

$$\mathcal{H}^{ex} = -\frac{1}{2} \sum_{i,j} J_{ij} \mathbf{S}_i \mathbf{S}_j - \frac{1}{2} \sum_{i,j} \mathbf{S}_i \mathcal{J}_{ij}^S \mathbf{S}_j - \frac{1}{2} \sum_{i,j} \mathbf{D}_{ij} (\mathbf{S}_i \times \mathbf{S}_j). \quad (6.25)$$

Isotropic exchange interactions

The first term in equation (6.25) represents the isotropic exchange contribution. Usually the exchange interaction is a short-range interaction, and practically vanishes beyond the fifth nearest neighbors as we can see in Fig. 6.7.

The calculated values of the isotropic exchange interactions are shown as a function of the distance between Co atoms in a bulk Co fcc system and a semi-infinite Co fcc with (100) surface. In both cases we observe that the first nearest-neighbor exchange pair interactions have a ferromagnetic character, also we can see the oscillating behavior of the parameter J_{ij} with the distance. The order of magnitude of the isotropic exchange interaction is in agreement with those presented in Refs. [170, 171] for the cases of thin films of Co on Cu(001) and for Co bulk [40, 172].

We have to note the increment of the exchange pair interaction when the spins are close to the surface. This effects is clearly observed in the right pannel of Fig. 6.7.

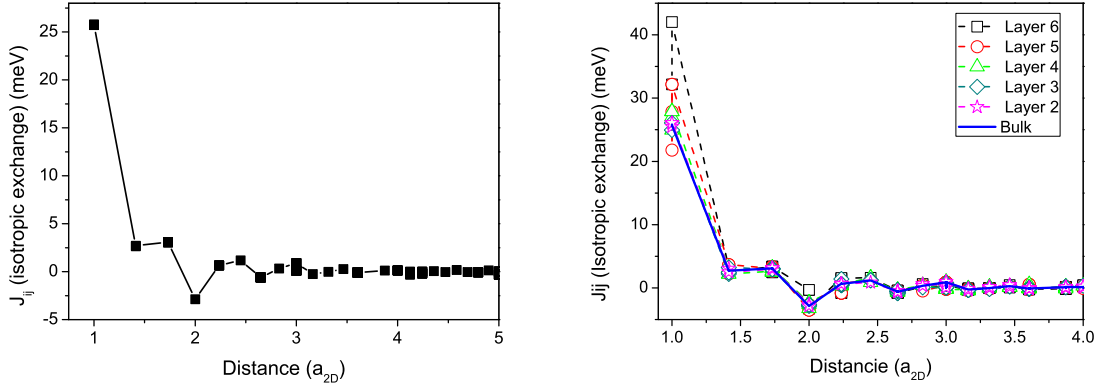


Figure 6.7: Calculated isotropic exchange interaction values J_{ij} (in meV) as a function of the distance between spins for Co bulk (left) and a Co(100) surface (right). The distance is evaluated in unit of lattice parameter in 2D lattice a_{2D} . In the case of a semi-infinite Co(100) we have plotted the isotropic exchange interaction evaluated at last five atomic layers, and compared these results with that of the bulk case.

If we analyze in detail the graphic, we see that there is a decrease in the value of J_{ij} with the distance from the surface. Similar behaviour also occurs in $Co \setminus Ag$ system. Clearly, the isotropic exchange interaction values for nearest neighbors (NNs) depend on the position of the spin i , specifically on the atomic layer to which it belongs. The values of the isotropic exchange between NNs are also different if these NNs spins are coplanar or if they belong to different atomic layers.

With the aim to represent the behavior of the isotropic exchange interaction, we define two parameters $J_{ip,jq}$ and z_i . $J_{ip,jq}$ is the isotropic exchange interaction between the spin i at layer p , and the spin j at layer q , and z_i is the distance from the surface of the atomic layer of spin i . Here $z_i = p - n_s$, where n_s represents the label of the atomic surface (interface) layer, and p is the plane index of the spin i . We have to note that when $z_i = p - n_s = 0$ the spin i belongs to the surface or the interface, depending of the studied case.

Then we can analyze the behavior of $J_{ip,jq}$ with the proximity of the surface.

In Fig. 6.8 we plotted the calculated isotropic exchange interaction strength between the nearest neighbors in the same layer $J_{ip,jp}$ (left graph) and in different layers $J_{ip,jq}$ (right graph) (in meV) as a function of z_i . The results are presented for Co(100) surface, $Co(100) \setminus Ag_1$ and $Co(111) \setminus Ag_1$. In both cases, for NN in the same or in different atomic layer, the isotropic exchange parameter increases in the proximity of the surface.

Despite the fact that an increase in J_{ij} on the surface described above exists, it is possible that the total exchange interaction will be smaller at the surface due to the loss of neighbors in that layer. With this aim we introduce an effective exchange

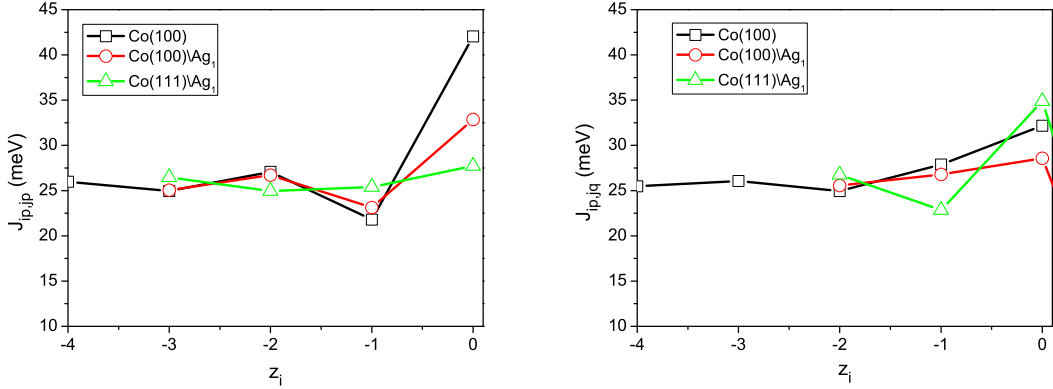


Figure 6.8: Calculated isotropic exchange interaction between nearest neighbors in the same layer $J_{ip,jp}$ and in different layers $J_{ip,jq}$ (in meV) as a function of z_i is the distance from the surface of the atomic layer of spin i , in the left and right side respectively. The results are presented for $Co(100)$ surface, $Co(100) \setminus Ag_1$ and $Co(111) \setminus Ag_1$.

interaction parameter, $J_0(z_i)$, defined as:

$$J_0(z_i) = \sum_j \left(\frac{1}{3} \sum_{\alpha} J_{ij}^{\alpha\alpha} \right); \alpha = x, y, z \quad (6.26)$$

The parameter $J_0(z_i)$ corresponds to the energy cost of flipping a spin located at a layer z_i from the surface.

In the left side of Fig. 6.9 we present this effective exchange interaction parameter as a function of the distance from the surface (interface) atomic layer (z_i), in the various systems: Co (bulk), Co(100) surface, $Co(100) \setminus Ag_1$ and $Co(111) \setminus Ag_1$. Fig 6.9 shows that the $J_0(z_i)$ parameter has practically the bulk value (black line) in the central atomic layers, but at surfaces its value decreases. This comes from the fact that at the surface or interface the number of the neighbors is drastically reduced. However the exchange interaction decays rapidly with the distance between neighbors, thus the surface effects are practically negligible at two atomic layers from the surface.

The effective layer-resolved Curie temperature can be calculated from the value of the "effective" exchange interaction parameter using the mean-field expression:

$$T_c^{eff}(z_i) = \frac{J_0(z_i)}{3 \cdot K_B} \quad (6.27)$$

In the right side of Fig. 6.9, we plotted the values of the "effective" Curie temperature evaluated at different atomic layers. The black line represents the value of the Curie temperature evaluated from our effective exchange parameter for Co(bulk) which corresponds to $T_c = 1430K$ and the dash line indicates the experimental value $T_c = 1389K$. From that values we can conclude that our calculations provide a slightly larger value (less than 3%).

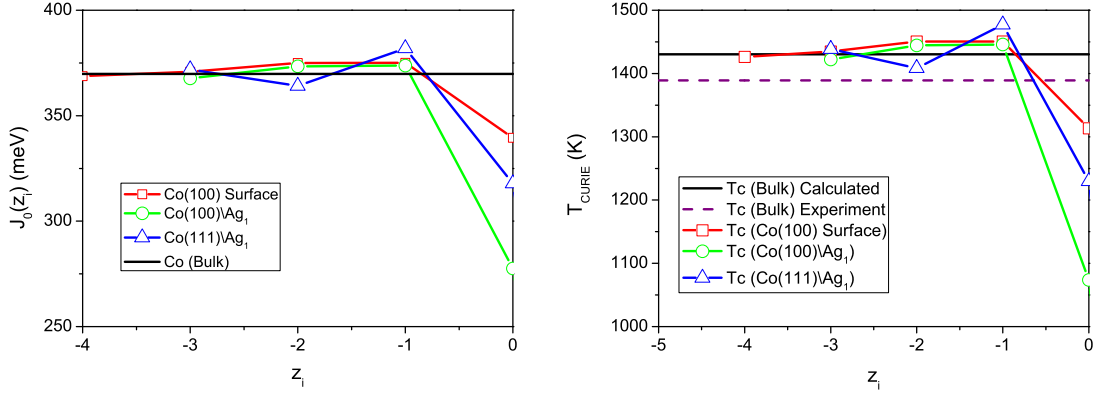


Figure 6.9: Calculated effective exchange interaction parameter $J_0(z_i)$ (in meV) and effective Curie temperature T_c^{eff} (left and right side respectively) layered resolved for Co(bulk), Co(100), $Co(100) \setminus Ag_1$ and $Co(111) \setminus Ag_1$ systems. Here z_i represents the distance from the surface or interface of the system.

Symmetric anisotropic exchange tensor

The second term in equation (6.25) represents the symmetric anisotropic exchange coupling (similar to that described in Refs. [107, 173]) and it is known as an "anisotropic exchange" or a "two-site anisotropy". We defined it previously as:

$$\mathcal{J}_{ij}^S = \frac{1}{2}(\mathcal{J}_{ij} + \mathcal{J}_{ij}^T) - J_{ij}\mathcal{I}.$$

As it will be seen later, \mathcal{J}_{ij}^S is one of the important contributions to the macroscopic anisotropy. For example, in the case of $FePt$, \mathcal{J}_{ij}^S term is the key for the understanding of the deviation in the exponent of the power-law dependence of the anisotropy with the magnetization $K \propto M^{2.09}$ [107, 174], from the theoretical $K \propto M^3$ law given by the Callen-Callen theory [106, 129].

The contribution of the symmetric part of the exchange matrix interaction to the Hamiltonian (\mathcal{H}^{SExc}) can be written as follows:

$$\mathcal{H}^{SExc} = -\frac{1}{2} \sum_{i,j} \mathbf{S}_i \mathcal{J}_{ij}^S \mathbf{S}_j.$$

The double sum is over all $i \neq j$. Now we try to analyze the effective symmetric exchange contribution of the exchange matrix interaction at a layer z_i . For this purpose we define $\mathcal{J}_{z_i}^S$ as:

$$\mathcal{J}_{z_i}^S = \sum_j \mathcal{J}_{ij}^S, \quad (6.28)$$

We have evaluated the effective symmetric exchange contributions for $Co(100)$, $Co(100) \setminus Ag_1$ and $Co(111) \setminus Ag_1$ systems ².

²In the systems under study the Z axis is perpendicular to the surface

In the first place, we would like to comment the characteristic features of these contributions: In the case of $Co(100)$ and $Co(100) \setminus Ag_1$, we observe that the symmetric anisotropic exchange matrix has the form:

$$\mathcal{J}_{z_i}^S = A_{z_i} \begin{pmatrix} -\frac{1}{2} & 0 & 0 \\ 0 & -\frac{1}{2} & 0 \\ 0 & 0 & 1 \end{pmatrix} \quad (6.29)$$

and could lead to an effective uniaxial anisotropy in the direction perpendicular to the plane of the surface, which could be one of the principal contributions to the effective anisotropy ³.

In the $Co(111) \setminus Ag_1$ system, we observe a little different behavior. In this system the effective symmetric exchange contribution $\mathcal{J}_{Z_i}^S$ is a matrix whose non-diagonal elements are in practice negligible, and it has the following form:

$$\mathcal{J}_{z_i}^S = \begin{pmatrix} A_{11}^{z_i} & 0 & 0 \\ 0 & A_{22}^{z_i} & 0 \\ 0 & 0 & A_{33}^{z_i} \end{pmatrix} \quad (6.30)$$

Here unlike what happens in the cases of a semi-infinite $Co(100)$ and a $Co(100) \setminus Ag_1$ systems, the diagonal elements have the property $A_{11}^{z_i} \neq A_{22}^{z_i} \neq A_{33}^{z_i}$. Also we have observed that $|A_{33}^{z_i}| > |A_{11}^{z_i}|$ and $|A_{33}^{z_i}| > |A_{22}^{z_i}|$ and $A_{33}^{z_i}$ has an opposite sign than the other two elements.

Antisymmetric anisotropic exchange tensor

The third term in equation (6.25) represents the Dzyaloshinsky-Moriya (DM) interaction [175, 176]. The DM contribution to the Hamiltonian of the system has the following form:

$$\mathcal{H}_{DM}^{ex} = -\frac{1}{2} \sum_{i,j} \mathbf{D}_{ij} (\mathbf{S}_i \times \mathbf{S}_j), \quad (6.31)$$

where the \mathbf{D}_{ij} is Dzyaloshinsky-Moriya vector and is defined as:

$$\begin{aligned} D_{ij}^x &= \frac{1}{2}(J_{ij}^{yz} - J_{ij}^{zy}) \\ D_{ij}^y &= \frac{1}{2}(J_{ij}^{xz} - J_{ij}^{zx}) \\ D_{ij}^z &= \frac{1}{2}(J_{ij}^{xy} - J_{ij}^{yx}) \end{aligned}$$

\mathbf{D}_{ij} is zero if sites i and j experience an inversion symmetry. Therefore, this contribution is practically zero in bulk system. Nevertheless the DM term can be enhanced near the magnetic surface due to the reduction of the symmetry. It also tends to lower

³See appendix A.2 for a detailed description of the derivation of the effective uniaxial anisotropy

the energy of the system upon inducing a non-collinear spin-structure [177, 178]. To clarify the DM contribution in different systems, we present in Tab. 6.4 the value of the module of DM vector for the first nearest neighbors, in Co (fcc, bulk) and for the surface layer or the interface in $Co(100)$, $Co(100) \setminus Ag_1$ and $Co(111) \setminus Ag_1$.

System	$Co(\text{bulk})$	$Co(100)$	$Co(100) \setminus Ag_1$	$Co(111) \setminus Ag_1$
$ D_{ij} $	0.0	0.475	0.58	0.408

Table 6.4: Calculated module of the DM vectors $| D_{ij} |$ (all in meV) for the first nearest neighbors in Co (fcc, bulk) surface of Co fcc (100), $Co(100) \setminus Ag_1$ and $Co(111) \setminus Ag_1$.

As we have expected in the case of a Co bulk system the DM is zero. From the results for $| D_{ij} |$ presented in Tab. 6.4 we can conclude that the Dzyaloshinsky-Moriya interaction is modified, if the surface of $Co(100)$ is capped by an Ag layer. In this case the module of a DM vector between nearest neighbors is increased, but it decays more rapidly than in the case of free $Co(100)$ surface, and the direction of the DM vector at second nearest neighbors is changed (see Fig. 6.10).

The increment of $| D_{ij} |$ in the case of $Co(100) \setminus Ag_1$ with respect to the corresponding value in $Co(100)$ surface could be due to the pure effect of the Ag capping and also due to the existence of a relaxation in the lattice. We can find cases where the relaxation affects the value of the DM interaction, for example we can mention the case of $Fe_2 \setminus W(110)$, in this case as the relaxation of the lattice is decreased from 26% to 10%, the magnitude of the main DM interaction is reduced by about three times [178].

The Dzyaloshinsky-Moriya contribution to the total exchange matrix is much smaller, approximately two orders of magnitude lower, than the isotropic exchange one. However it is comparable to that of the on-site anisotropy. Therefore we have to study in each particular case how important is this contribution in the effective magnetic anisotropy energy of the system.

The calculated DM vectors for three systems are displayed in Fig. 6.10 (a) $Co(100)$ surface, (b) $Co(100) \setminus Ag_1$ interface and (c) $Co(111) \setminus Ag_1$. For the cases of $Co \setminus Ag$ systems the lattice relaxation is $r = 10\%$, the arrows indicate the directions of the DM vectors, and the values are normalized to the maximum value of DM vectors module $| D_{ij} |$ for each system (shows in Tab. 6.4). In the cases (a-b) which correspond to the (100) surface/ interface, the DM vectors lie in the surface/interface plane, which implies that an orientation of the Co spins perpendicular to the surface/interface is favored. While in the case (c) (111) interface, the DM vectors are oriented practically perpendicular to the interface, which favors an in-plane orientation of the Co spins at the interface. As we have mentioned above, the DM vectors in Fig. 6.10 are normalized, this allows us to note that DM interaction, in the same way as values of J_{ij} , diminishes very rapidly with the distance between the spins i and j .

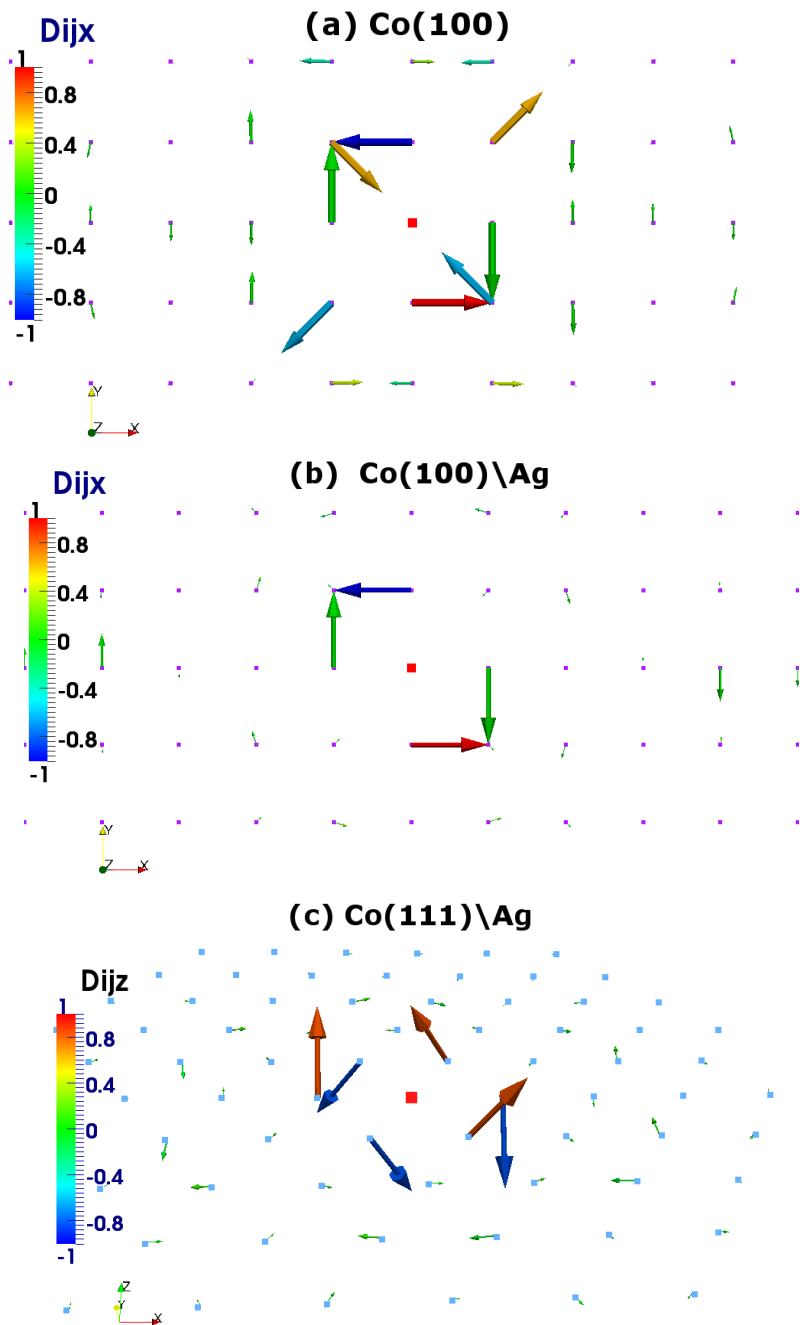


Figure 6.10: Sketch of the DM vectors for (a) $Co(100)$ surface, (b) $Co(100) \backslash Ag_1$ interface and (c) $Co(111) \backslash Ag_1$ interface. For the cases of $Co \backslash Ag$ systems the lattice relaxation is of 10%, the arrows indicate the direction of the DM vectors, and the values are normalized to the maximum of DM module ($|D_{ij}|$ for each system.)

6.3.5 Magneto-crystalline anisotropy energy

The magneto-crystalline anisotropy (MCA) energy has its origin in the spin-orbit coupling under the ordering imposed by the crystalline lattice of the material. In the most general case, the magnetocrystalline anisotropy matrix d_i can be written as a function of its eigenvectors (corresponding to the easy axes) u_i^α and eigenvalues $d_i^{\alpha\alpha}$:

$$\mathbf{d}_i = \sum_{\alpha=1,2,3} d_i^{\alpha\alpha} u_i^\alpha (u_i^\alpha)^T \quad (6.32)$$

In this general case we have a triaxial anisotropy. This sort of anisotropy could be present in a system with a reduced symmetry such as surfaces, edges, etc. The contribution due to the on-site anisotropy to the total energy has the following form:

$$\mathcal{H}_{ani} = \sum_i \mathbf{d}(\mathbf{S}_i) = \sum_i \mathbf{S}_i \mathbf{d}_i \mathbf{S}_i = \sum_i \sum_{\alpha=1,2,3} d_i^{\alpha\alpha} (\mathbf{S}_i \cdot u_i^\alpha)^2 \quad (6.33)$$

Epitaxially grown systems present usually uniaxial anisotropy. If we suppose that in this case the easy axis is parallel to the Z axis, then the on-site anisotropy has the form:

$$\mathcal{H}_{ani} = \sum_i d_i^{zz} (\mathbf{S}_i \cdot e_z)^2 \quad (6.34)$$

We have only described the on-site magneto-crystalline anisotropy. However, there could exist other contributions to the magnetic anisotropy of the system, as e.g. the two-site magnetic anisotropy, mentioned already above and discussed later in this chapter.

Evaluation of the total magneto-crystalline anisotropy

The evaluation of the total magneto-crystalline anisotropy energy with the Budapest-Vienna SKKR code is based on the so-called "force theorem" [86, 142, 167]. Within this approximation, for each system two calculations were performed, using the previously determined self-consistent potentials. Namely the first calculation with the magnetic field perpendicular to the surface (\perp) and the second with the magnetic field pointing along X axis, which is one of the crystalline axis contained in the plane of the surface (\parallel).

$$\Delta E_B = E_B^{\parallel} - E_B^{\perp}, \quad (6.35)$$

Typically the MCA energy in transition metals is small, of the order of a few tens of μeV , and this is the real difficulty in performing such calculations with a good accuracy of the results. For this reason it is necessary to perform a previous study of the convergence of the value of ΔE_B with respect to the number of k (wave number) points for energies close to the Fermi energy E_F . Such stability study has been done for all the systems which we have analyzed. Once we have obtained the value of the MCA

System	Interface	ΔE_B (meV)
Cobalt bulk(fcc)	(100)	8.63e-4
Cobalt (fcc)	(100)	-0.09
Cobalt (fcc)	(111)	0.12
Ag monolayer on Co(fcc)	(100)	0.03
Ag monolayer on Co(fcc)	(111)	0.22
2 Ag ML on Co(fcc)	(100)	-0.01
2 Ag ML on Co(fcc)	(111)	0.06

Table 6.5: In this table we present the values of the band energies difference ΔE_B (in meV) for different systems of Co (bulk), Co (100), Co (111), Co (100) \ Ag_n and Co (111) \ Ag_n .

energy, we can extract the corresponding value of the effective anisotropy constant K^{eff} . The anisotropy constant is an energy density and can be described as:

$$K^{eff} = \frac{\Delta E_B}{V}, \quad (6.36)$$

where V represents the volume of the system.

In the next sections we will discuss the MCA behavior with different surface's orientations and cappings. Later, we will obtain the layer resolved MCA for different systems. The next point in our study will be to understand how the MCA is affected with the relaxation of the lattice. To conclude this section we will analyze different contributions to the MCA energy for a particular system Co (111) \ Ag_1 .

Magneto-crystalline anisotropy energy dependence on the interface and cappings.

It is well known that the magneto-crystalline anisotropy energy could be affected by the reduction of the symmetry of the system such as the existence of interfaces, relaxation of the lattice or the presence of the capping in the system. We have tried to analyze how these effects contribute the MCA energy of our systems.

In Tab. 6.5 we present the results of the total MCA energy calculated from the difference of the band energies. We have evaluated the MCA energy in Co fcc (bulk), semi-infinite Co fcc with (100) or (111) surface, and semi-infinite Co fcc with a capping of one or two Ag atomic monolayers (MLs) and (100) or (111) interfaces.

The first thing that we observe is that the bulk value of the MCA is lower than $1\mu eV$, this value is in the limit of the accuracy of our method. For this reason we should take this value just as the order of magnitude of the MCA for cobalt bulk. Then, from the results of MCA energy shown in Tab. 6.5 we can assert that the MCA energy of the surface of semi-infinite Co systems suffers a huge increment from the bulk value.

From equation (6.35) we can conclude that $\Delta E > 0$ means that the energy of the system is lower when the moments of the system are oriented in the direction perpendicular to the surface, therefore the magnetization prefers to align perpendicular to the surface. In the opposite situation, when $\Delta E < 0$ the magnetization of the system prefers to align parallel to the surface of the sample. In the case of a *Co(100)* system, $\Delta E < 0$, this implies that the easy axis of the system is contained in the plane of the surface of the sample. At the same time, the magnitude of the MCA energy has increased two order of magnitude with respect to the bulk case. Now if we cover this system with an atomic monolayer of silver, an abrupt change of MCA energy occurs and the easy axis becomes perpendicular to the surface of the sample.

On the other hand, in the case of a *Co(111)* system, $\Delta E > 0$ then the easy axis of the system is perpendicular to the surface of the sample, and the value of the MCA is higher than that of the *Co(100)*. Now we analyze what happens with the MCA energy if we coat the system with a ML of Ag, we find that the easy axis of the system does not change, being also in this case perpendicular to the surface.

Our calculations of the MCA energy of the Co (fcc) system with one atomic monolayer of Ag capping suggest us that the existence of this capping induces an increase in the MCA energy and favors a perpendicular orientation of the magnetization. Nevertheless, if the width of the Ag capping is increased up to *2MLs* the MCA energy is reduced with respect to the case of a capping by one ML of Ag and is close to the results of the corresponding pure surface.

In brief, the MCA energy depends closely on the proximity and characteristics of the surface or interface. The MCA energy is larger in the case of (111) surface or interface than in the (100) case.

Understanding the origin of the MCA is a complex task, due to the difficulty that involve this kind of studies. Nevertheless several authors suggest an interpretation of the MCA as a function of the symmetry breaking or asymmetry of the bonding at magnetic surface or interface [179]. The concept of Bruno suggests that under certain assumptions the magnetic anisotropy energy is related with an anisotropy of the orbital moment and the anisotropy bonding [45], see section 1.4.2. In the case of fcc lattice with surface/interface (111) the number of NN in the surface/interface is 6 in contrast to the 4 NN in surface/interface (100). Then the effect of the ligand field is stronger in the case of (111) than in the case of (100), this suggests that the orbital moment of the surface/interface (111) is more quenched than of the surface/interface (100), in agreement with our calculated μ_L for this surface. Therefore the variation of the magnetic moment in-plane and out-of-plane is stronger in the (111) case. Basing on the Bruno's model this fact can explain the larger value of the MCA energy on (111) surface/ interface.

Layer-resolved magneto-crystalline anisotropy energy

The Budapest-Vienna Code allows us to obtain the layer resolved MCA energy values. This tool gives us the opportunity to analyze the spacial distribution of the magneto-crystalline anisotropy energy. In Fig. 6.11 we present the layered resolved

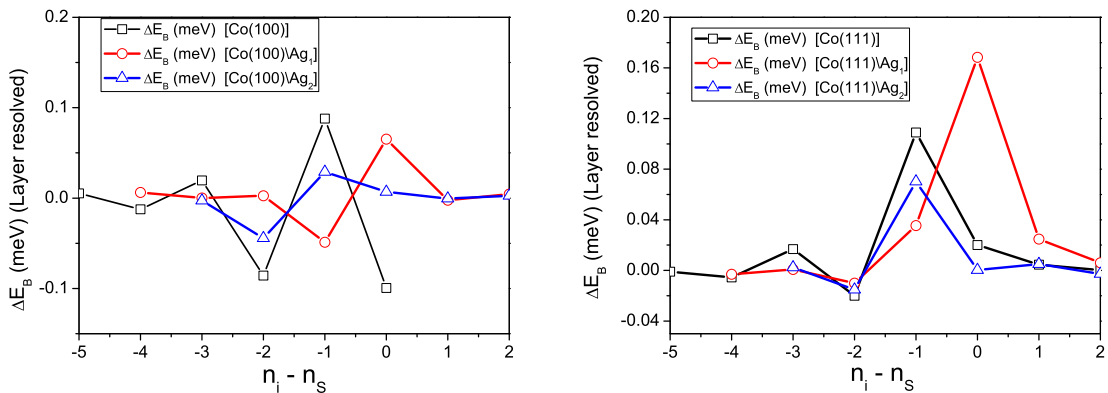


Figure 6.11: The layered resolved ΔE_B calculated for: semi-infinite Co, $Co \setminus Ag_1$ and $Co \setminus Ag_2$ systems with surface or interface (100) and (111) in the left and right graphs respectively. We have to note that for the system with Ag capping we have supposed a rigid relaxation of the lattice $r = 10\%$. Here n_S indicates the index of the atomic layer of the surface or the interface of the system and n_i is the label of the atomic layer, in this way $n_i - n_s = 0$ corresponds to the surface or the interface.

ΔE_B calculated for: semi-infinite Co, $Co \setminus Ag_1$ and $Co \setminus Ag_2$ systems with surface or interface (100) and (111) in the left and right graphs respectively.

In first place, we would like to point out that the layer resolved MCA energy shows an oscillating behavior due to the existence of the surface. The principal contribution to the crystalline anisotropy energy comes from the subsurface layer. We can also conclude that approximately 3 – 4 layers have their local anisotropy different from that of the bulk. For example in the case of the Co(111) surface the contribution to MCA energy of the surface layer is approximately two orders of magnitude larger than the MCA energy for a bulk Co (fcc).

Magneto-crystalline anisotropy energy as a function of the lattice relaxation.

At this point we would like to address the question on how the MCA energy is affected by the relaxation of the lattice. For this purpose, we have calculated the MCA energy of $Co \setminus Ag$ system at the interfaces (100) and (111) as a function of the rigid relaxation of the lattice. The results are plotted in Fig. 6.12.

The relaxation of the lattice is ranged from 0% to 12%. We observe that in all cases

the MCA energy at the interface $Co \setminus Ag$ (111) is almost an order of magnitude higher than in the case of (100) interface. The value of the MCA energy is affected by the

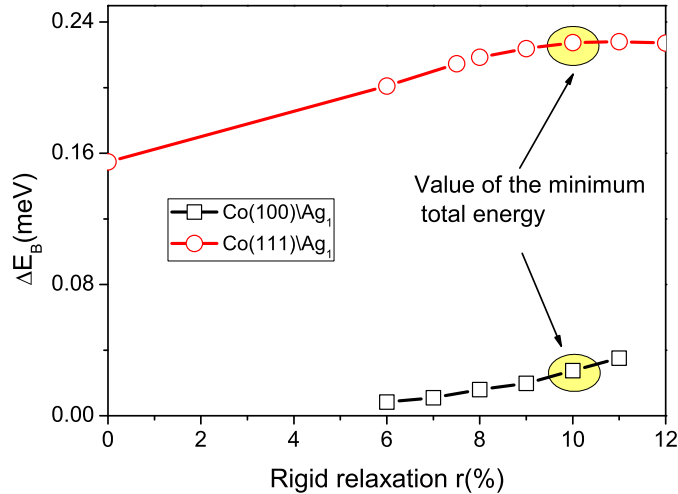


Figure 6.12: The MCA energy, ΔE_B , calculated for a $Co(100) \setminus Ag_1$ and $Co(111) \setminus Ag_1$ as a function of the rigid relaxation parameter r .

relaxation of the lattice. For all studied cases, for the (100) interface the MCA suffers an increment when the relaxation of the system is increased. In the systems with (111) interface the behavior is slightly different. Initially when the relaxation is changed from 6% to 11%, the MCA is increased, starting from this point if the relaxation increases, the MCA energy manifests a slight decrease.

Magneto-crystalline anisotropy energy of a $Co(111) \setminus Ag_1$ thin films

Here we present a detailed study of the MCA energy for a particular system of $Co(111) \setminus Ag_1$. The first step is to obtain the angular dependence of the energy. In Fig. 6.13, we show the band energy of the system $Co(100) \setminus Ag_1$ as a function of the angle (θ) from the Z axis (axis perpendicular to the surface of the thin film). The value obtained from SKKR calculation has been compared with the analytical expression of the angular dependence of the uniaxial anisotropy energy, showing that both adjust perfectly.

$$E(\theta) = E_0 - \Delta E \cos^2(\theta) \quad (6.37)$$

From the analysis of this result we can suppose that the $Co(111) \setminus Ag_1$ system presents an uniaxial anisotropy whose easy axis is perpendicular to the surface of the system,

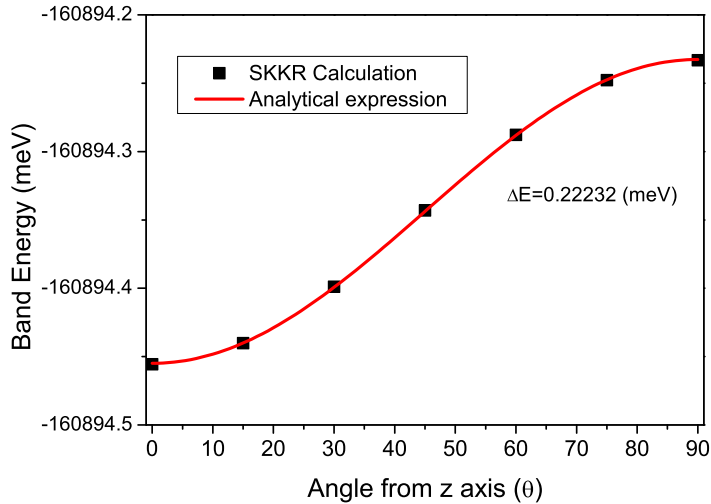


Figure 6.13: Band energy as a function of the angle of the magnetization axis from the Z axis of the system.

and the on-site anisotropy has the following form.

$$\sum_i \mathbf{S}_i d_i \mathbf{S}_i = - \sum_i d_i^{zz} (\mathbf{S}_i \cdot \mathbf{e}_z)^2 \quad (6.38)$$

Henceforth, we omit the super-index (zz) of the on-site anisotropy constant.

As we presented in previous section (6.3.5), the effective anisotropy constant extracted from the "ab-initio" calculations is related to the difference of the band energy between the magnetic moments configuration oriented at different directions, $\{\vec{S}_i\}||\vec{x}$ and $\{\vec{S}_i\}||\vec{z}$. The problem appears when we try to figure out which are different contributions to this effective anisotropy. In the first place, we have an on-site contribution (d_i). As we mentioned in section (6.3.4) the anisotropic part of the exchange tensor interaction also contributes to the anisotropy, with a two-site anisotropy contribution, in a such way that:

$$\Delta E = Eb_x - Eb_z \approx -\frac{1}{2} \sum_{i,j} J_{ij}^{S,xx} + \frac{1}{2} \sum_{i,j} J_{ij}^{S,zz} + \sum_i d_i \quad (6.39)$$

In the way reported in the appendix ⁴ we can get the layer-resolved on-site anisotropy constant d_i for $Co(111) \setminus Ag_1$, which we plotted in Fig. 6.14 together with the values of ΔE_b . We observe a huge increment of the macroscopic magneto-crystalline anisotropy on the surface. However the discrepancy between the values of ΔE_b and the on-site anisotropy contribution suggests us that a large contribution of the two-site anisotropy to the total MCA energy should exist.

⁴See Appendix A.3 for a detailed derivation of the on-site anisotropy from E_B

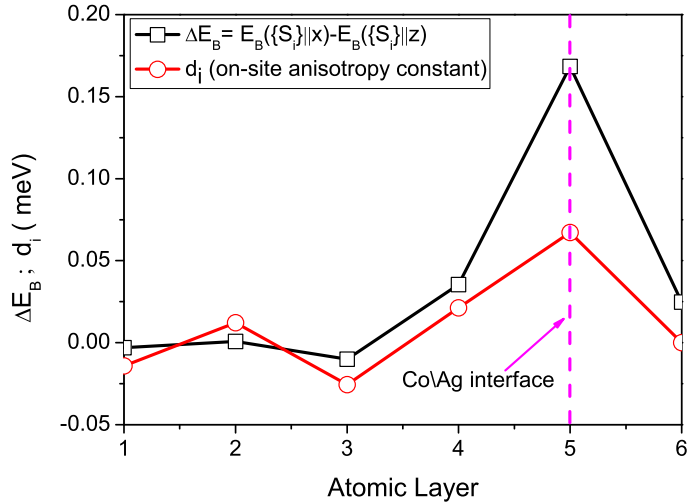


Figure 6.14: The layer-resolved MCA energy and the on-site anisotropy energy for $Co(111)\backslash Ag_1$ films.

6.4 Temperature-dependent macroscopic properties

At this point, we linked the physical magnitudes extracted from the "ab-initio" simulations where the electronic structure has been explicitly taken into account to an atomistic semiclassical model, in which every magnetic parameter: magnetic moment, anisotropy constant, exchange coupling etc., has its value at the atom site. This can be described as follows:

$$\mathcal{H} = -\frac{1}{2} \sum_{i,j} \mathbf{S}_i \mathcal{J}_{ij} \mathbf{S}_j + \sum_i \mathbf{S}_i d_i \mathbf{S}_i + \mathcal{H}_{MAG} + \mathcal{H}_{Zeeman}. \quad (6.40)$$

Here the exchange interaction and on-site anisotropy (\mathcal{J}_{ij} and d_i) are expressed in a general form, where they are 3×3 matrices. The Hamiltonian of the system has the form of a generalized Heisenberg Hamiltonian, where the first term corresponds to various exchange contributions, and in the double sum of the exchange interactions terms the indices i y j range from 1 to N excluding the case $i = j$, where N represents the total number of the spins in the system. The second term is the on-site anisotropy energy, \mathcal{H}_{MAG} is the magnetostatic energy term, and the last term \mathcal{H}_{Zeeman} corresponds to the Zeeman energy.

In this section we focus our efforts on the study of the magnetic behavior of a thin film of $Co(111) \backslash Ag_1$ with fcc lattice structure. From the first principle calculations we have extracted the magnetic parameters that are used to perform temperature-dependent simulations. We also make some assumptions:

1. We assume that the Ag magnetic moments, exchange and anisotropy are negligible due to their small values. Then the Hamiltonian takes into account Co moments only.
2. In our simulations there are no external applied magnetic field, therefore the Zeeman contribution to the total energy is zero.
3. Although the "ab-initio" results (see section 6.3.3) showed some increment of the spin and orbital Co moments at the interface of the $Co(111) \setminus Ag$ system, in the first approximation to the problem we assume that the cobalt's moments are the same as those in the bulk system. As is shown in Table (6.2) these modifications are in practice negligible.

6.4.1 Magnetostatic interaction

The magnetostatic self energy is the interaction of a distribution of a magnetization vector with the magnetic field created by this distribution itself. This energy term is normally written in the following way:

$$E_M = -\frac{1}{2} \int \mathbf{M} \cdot \mathbf{H}' dv, \quad (6.41)$$

where the integration is over the volume of the ferromagnetic system, taken as a continuum. Due to its long range character, the magnetostatic interaction generally depends on the shape of the system, and it is responsible for the existence of magnetic domains. Usually this contribution leads to the commonly called shape anisotropy, and becomes important in thin films where it often produces in-plane alignment of moments. The proper calculation of the magnetostatic energy belongs to the area of micromagnetism and is computationally costly.

As a first approximation of the magnetostatic anisotropy energy, we used a simplified version of the demagnetization factor approach valid for thin films with homogeneous magnetization [180]. Then the density of energy per volume could be written as an additional anisotropy term [181, 182].

$$\mathcal{E}_M = K_{SH} \cdot \cos^2(\theta), \quad (6.42)$$

where $K_{SH} = 2\pi M_s^2$ in c.g.s. unit system. The magnetization makes an angle (θ) to the plane normal. The magnetostatic anisotropy energy is thus minimized for an angle of $\theta = \pi/2$, this implies all the moments lying in the plane of the thin film.

The saturation magnetization M_s is related at $T = 0K$ to the atomic magnetic moment μ through:

$$M_s = \frac{\mu}{V_0}, \quad (6.43)$$

V_0 represents the atomic volume. In the case of an fcc lattice the atomic volume is related with the lattice parameter a as $V_0 = a^3/4$ (for Co $a = 0.3548$ nm). As we can see

in section 6.3.3, the orbital magnetic moment in Co system is practically zero, because of that the atomic magnetic moment in this case is taken as: $\mu = \mu_{Co} \approx 1.66\mu_B$. Then we obtain that $M_s = 1377.24$ (emu/cc) at $T = 0K$.

The expression (6.42) represents the magnetostatic energy for a thin films with a homogeneous magnetization. In our case we have a layered system with a total magnetostatic energy in the form similar to that described in Ref. [115]:

$$E_M = 2\pi M_s^2 \sum_i \frac{a_i}{L_z} V_i (\vec{m}_i \cdot \vec{e}_{mag})^2, \quad (6.44)$$

here the sum is up to the total number of spin N, M_s is the saturation magnetization, a_i is the width of the atomic layer i , L_z is the thickness of the thin film, V_i is the atomic volume of the spin i , $\vec{m}_i = \frac{\vec{M}_i}{M_s}$ is the unit vector in the direction of the magnetization at site i , \vec{e}_{mag} is the magnetostatic anisotropy axis, in the case of thin films, \vec{e}_{mag} is perpendicular to the plane of the surface, which favors the orientation of the magnetization in plane.

In our case, the direction perpendicular to the surface of the thin films is parallel to Z axis. The expression above is reduced to the following one:

$$E_M = 2\pi M_s^2 \sum_i \frac{a_i}{L_z} V_i m_{z,i}^2. \quad (6.45)$$

In the approximation described above we implicitly supposed that the $|\mathbf{M}| = M_s$, this means that it is an athermal approximation. Nevertheless in our work we want to analyze the magnetic behavior of our system at $T \neq 0$, therefore we have to introduce the temperature effects on the magnetostatic energy. In this case the value of M_s should be substituted by $M_s \langle m_i(T) \rangle$. In this way the magnetostatic energy can be written as:

$$E_M = 2\pi M_s^2 \sum_i \frac{a_i}{L_z} V_i \langle m_{z,i}(T) \rangle^2, \quad (6.46)$$

here $\langle m_{z,i}(T) \rangle$ is the average z component of the magnetization at the atomic plane to which the spin i belongs for a temperature T.

6.4.2 Implementation of the exchange tensor interaction

Unfortunately, to take into account all exchange contributions in atomistic simulations is very time consuming for a reasonable system size. Due to the properties of the exchange tensor interactions (oscillatory character) it is necessary to take into account not only first neighbors in the calculations. At the same time the exchange is a short-range interaction which falls off sufficiently fast with distance, as clearly seen in the left side of Fig. 6.7, so that only a finite number of neighbors j has to be considered. In other words, we consider that the exchange double sum is over the neighbors whose distance is below a certain cutoff, in our case the cutoff is $5 \cdot (a_{2D})$, being a_{2D} the

lattice parameter in the 2D fcc lattice. We call this approximation the **Truncated Exchange Tensor (TET)**.

The widely used approximation in the literature [172, 183] is the use of the **Isotropic exchange constant (IEC)**. In this approximation it is considered that the exchange tensor interaction J_{ij} is replaced by an exchange constant J_{ij} , in a similar way as it was used by L. Szunyogh et al. in Ref. [173]. This way \mathcal{H}^{ex} could be written in the next form:

$$\mathcal{H}^{ex} = -\frac{1}{2} \sum_{i,j} J_{ij} \mathbf{S}_i \mathbf{S}_j \quad (6.47)$$

where J_{ij} is the isotropic exchange parameter (see section 6.3.4). The J_{ij} constant depends on the pair of spins i, j . Also in this case we take as neighbors of spin i all other spins j , which are located at a distance smaller than $5 \cdot (a_{2D})$.

This approximation involves a modification in the uniaxial anisotropy constant. With the aim to reproduce the correct anisotropy of the system, we replace the value of the on-site anisotropy constant by the effective anisotropy constant evaluated in the same form that in the case in the section 6.3.5 and having contributions from the anisotropic exchange tensor interaction.

6.4.3 Temperature-dependent magnetization

In order to calculate the temperature dependent magnetization of $Co(111) \setminus Ag_1$ system, we have modeled a thin film system with 5 atomic layers and a total of $N = 845$ spins. We apply the constrained Monte Carlo method described in chapter 4 to evaluate the temperature dependence of macroscopic parameters. In Fig. 6.15, we present the average magnetization as a function of the temperature for the two approximations described above.

We can see that the two models of the exchange interaction reproduce the same dependence of the magnetization with temperature, giving the same Curie temperature and adjust perfectly. This is a natural fact since it is known that the Curie temperature is defined by the total exchange strength only. The calculated Curie temperature has been interpolated as $T_c \approx 1200K$, compared to the known experimental value $T_c = 1388 - 1403K$ [184], our calculated value is smaller. As we showed in Chapter 4 this is due to the loss of neighbors for the surface spins.

6.4.4 Temperature-dependent anisotropy

In chapter 4 we presented the constrained Monte Carlo method and we showed that this method is a powerful tool to determine the temperature dependence of the effective anisotropy of the system. Below we present the results for the temperature-dependent anisotropy for a $Co(111) \setminus Ag_1$ thin films.

In the left side of Fig. 6.16 the temperature-dependent effective anisotropy is plotted. In contrast to what happens in the temperature-dependent magnetization case,

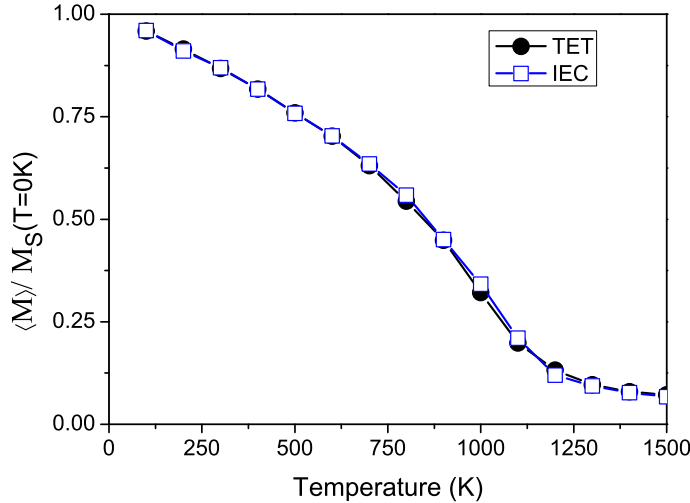


Figure 6.15: Magnetization versus temperature for a thin film with 5 magnetic layers, such the parameters correspond to the values extracted for the $Co(111) \setminus Ag_1$ system. Two approximations of the exchange interactions (TET and IEC) are used.

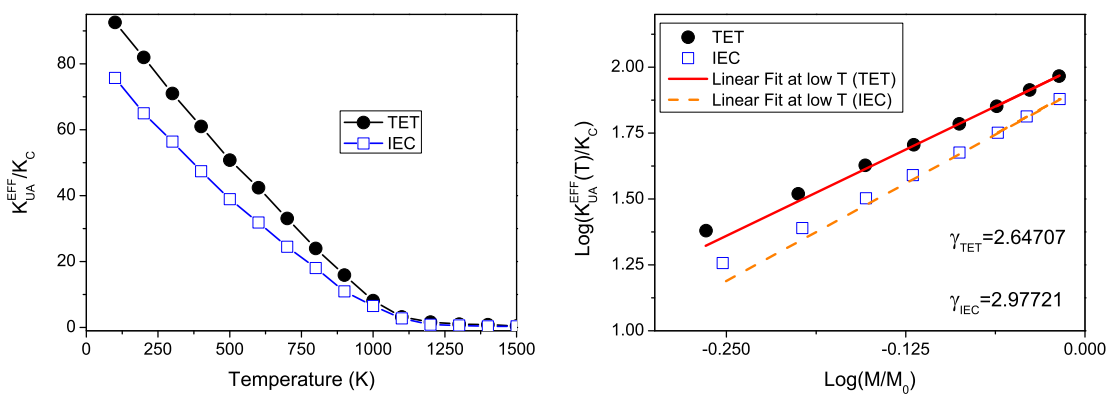


Figure 6.16: Effective anisotropy constant versus temperature (left) and critical exponent at low temperatures (right) for a $Co(111) \setminus Ag_1$ thin films with 5 magnetic layer for the two approximations of the exchange interactions (TET and IEC).

the use of the isotropic exchange constant modifies the results.

The effective value at $T = 0K$ is also different being larger in the case of full but truncated exchange tensor than for the isotropic exchange constant approximation. Such an increment of the initial effective anisotropy is due to the fact that in the first case the "two-site" anisotropy and the DM interaction are included explicitly. The DM interaction favors the orientation of the magnetization in plane, leading to a reduction of the anisotropy out-of-plane, but the contribution of the "two-site" anisotropy favors the anisotropy perpendicular to the surface of the sample and this contribution is more important leading to a net increment of the anisotropy out-of-plane. The IEC approximation includes these contributions in a modified "uniaxial anisotropy" which is obviously wrong.

We have also calculated the low-temperature scaling exponents γ of the anisotropy with magnetization and we have observed that in the case of TET $\gamma \approx 2.69$ and in the case of IEC $\gamma \approx 3$. That discrepancy of the results is due to that in TET case and differently to IEC approximation we have taken into account the total exchange matrix, which has an important contribution of the "two-site" anisotropy. As it has been shown by Mryrasov et al. [185] this term is responsible of the deviation from $\gamma = 3$ exponent (typical for uniaxial anisotropy) in the case of $FePt$.

6.5 Conclusions

From our results we can conclude the following:

- We have constructed an effective semiclassical (spin localized) Heisenberg Hamiltonian, passing the magnetic information from "ab-initio" calculations to the atomistic level.
- We have shown that the magnetic moment in Co thin films is affected by the existence of the surface and the capping. In the case of $Co \setminus Ag$ thin films we observed a polarization of the Ag layer. However, the modifications of the spin and the orbital magnetic moment of Ag are small.
- We have obtained the layer resolved effective anisotropy constant and observed that it has experienced a huge increment due to the breaking of symmetry on the surface. Also we have shown that its character could be changed by the surface capping. A transformation from a system with easy axis perpendicular to the plane to the one with easy plane anisotropy by one or two layers of Ag capping has been predicted.
- The symmetry breaking of the surface induces an increment in the value of the exchange interaction. Also it leads to an asymmetry of the exchange tensor interaction in the direction Z perpendicular to the surface. This, together

with the Dzyaloshinsky-Moriya interaction contributes to an overall macroscopic anisotropy.

- In the case of a thin film $Co(111) \setminus Ag_1$ we have discussed different exchange interaction contributions, and the temperature dependence of the macroscopic magnetization and anisotropy. We have observed that the magnetization dependence on the temperature can be reproduced both with the truncated exchange tensor and within the isotropic exchange constant approximation . Nevertheless the dependence of the anisotropy on the temperature is highly dependent on the correct account of the exchange interaction. This indicates that the IEC is not able to provide a correct temperature dependence of the magnetic properties of the system, in this case we should use a total exchange matrix.

Conclusiones

Para resumir, hemos realizado un estudio multiescala de las propiedades magnéticas de diversos sistemas. En primer lugar obtuvimos los parámetros magnéticos locales del Co semi-infinito con superficies (100) y (111), $Co(100) \setminus Ag_n$ y $Co(111) \setminus Ag_n$ con $n=1,2$, utilizando para ello simulaciones "ab-initio". Posteriormente haciendo uso del algoritmo CMC estudiamos el comportamiento magnético de una lámina delgada $Co(111) \setminus Ag_1$. A continuación indicamos las principales conclusiones de este estudio:

- En primer lugar hemos observado que el momento magnético del Co se ve afectado por la existencia de la superficie o del recubrimiento de Ag, variando su valor con respecto al de volumen. En el caso de láminas delgadas de $Co \setminus Ag$ se detectó una pequeña polarización de la capa de Ag. Aún así, la modificación del momento orbital de la plata y del espín del Co son en general pequeños.
- Hemos obtenido la energía magneto-cristalina resuelta por capas y observamos que ésta experimenta un gran aumento en la superficie. Además mostramos que el carácter de la anisotropía efectiva puede ser alterado por el recubrimiento de plata, observando una reorientación del eje fácil magnético del sistema al recubrir el Co con una o dos capas atómicas de Ag.
- La ruptura de simetría cristalina en la superficie induce un incremento del valor de la interacción de canje, así como una asimetría en la interacción de canje en la dirección Z (dirección perpendicular a la superficie). Estos factores conjuntamente con la interacción Dzyaloshinsky-Moriya contribuyen a la anisotropía global del sistema.
- En láminas delgadas de $Co(111) \setminus Ag_1$ donde existe una ruptura abrupta de la simetría cristalina hemos encontrado que la principal contribución a la anisotropía magnética global del sistema no es la anisotropía "on-site" sino la "two-site".
- En el caso de una lámina delgada de $Co(111) \setminus Ag_1$ discutimos las diferentes contribuciones de canje y la dependencia con la temperatura de la imanación y la anisotropía macroscópica. En el estudio de la dependencia térmica de la imanación, se observó que este comportamiento puede ser reproducido tanto si tomamos la interacción de canje con su naturaleza exacta, como una interacción tensorial a multiples vecinos, o si la tomamos de una forma aproximada como una constante de canje renormalizada (IEC). Sin embargo la dependencia térmica de la anisotropía se ve afectada sustancialmente con la aproximación utilizada para la interacción de canje. Esto indica que la aproximación (IEC) no es capaz de proporcionar una correcta dependencia térmica de la anisotropía global del sistema.

- Hemos mostrado que aunque nos encontramos en los primeros pasos de nuestro estudio tenemos la capacidad de realizar un estudio multiescla desde cálculos "ab initio" hasta un modelo atomístico de las propiedades macroscópicas de láminas delgadas.

A

Appendix A

A.1 Hamiltonian of the spin system in the adiabatic approximation

Within the rigid-spin approximation the adiabatic dynamics of local spin moments is described by the Landau-Lifshitz equation.

$$M_{ri} \dot{\mathbf{S}}_{ri} = -\frac{2\mu_B}{\hbar} \frac{\delta \mathcal{F}}{\delta \mathbf{S}_{ri}} \times \mathbf{S}_{ri} \quad (\text{A.1})$$

where \mathbf{S}_{ri} is a unit vector pointing along the spin-quantization axis in the atomic cell at the site i of the layer r , M_{ri} is the magnitude of the spin moment and \mathcal{F} is the free energy of the system. If we are working in spherical coordinates then we can write \mathbf{S}_{ri} as a function of the polar and azimuthal angles θ_{ri} and φ_{ri} respectively.

$$\mathbf{S}_{ri} = (\sin \theta_{ri} \cos \varphi_{ri}, \sin \theta_{ri} \sin \varphi_{ri}, \cos \theta_{ri}) \quad (\text{A.2})$$

Rewriting the dynamical equation into spherical coordinates, the equations of motion for the angles θ_{ri} and φ_{ri} are given by:

$$M_r \dot{\varphi}_{ri} \sin \theta_{ri} = \frac{2\mu_B}{\hbar} \frac{\delta \mathcal{F}}{\delta \theta_{ri}} \quad (\text{A.3})$$

$$-M_r \dot{\theta}_{ri} \sin \theta_{ri} = \frac{2\mu_B}{\hbar} \frac{\delta \mathcal{F}}{\delta \varphi_{ri}}, \quad (\text{A.4})$$

implicitly in these equations we supposed that the magnitude of the spin moment M_{ri} depends only on the atomic layer for the spins i .

If we choose the polar axis of the reference system (Z) perpendicular to the magnetization in the ferromagnetic state, the system of equations (A.3 and A.4) can be linearized

$$M_r \dot{\varphi}_{ri} = \frac{2\mu_B}{\hbar} \frac{\delta \mathcal{F}}{\delta \theta_{ri}} \Big|_{\theta=\frac{\pi}{2}, \varphi=0} \quad (\text{A.5})$$

$$-M_r \dot{\theta}_{ri} = \frac{2\mu_B}{\hbar} \frac{\delta \mathcal{F}}{\delta \varphi_{ri}} \Big|_{\theta=\frac{\pi}{2}, \varphi=0} \quad (\text{A.6})$$

These equations are the canonical equations for the generalized coordinates q_{ri} and momenta p_{ri} which are defined as:

$$q_{ri} = \left(\frac{M_r}{\mu_B} \right)^{1/2} \varphi_{ri} \quad (\text{A.7})$$

$$p_{ri} = \left(\frac{M_r}{\mu_B} \right)^{1/2} \theta_{ri} \quad (\text{A.8})$$

Therefore doing an expansion up to the second order of the free energy in the angular variables, the corresponding Hamiltonian can be written as:

$$\mathcal{H} = \frac{1}{\hbar} \sum_{ri,sj} (q_{ri} A_{ri,sj} q_{sj} + q_{ri} B_{ri,sj} p_{sj} + p_{ri} B_{sj,ri} q_{sj} + p_{ri} C_{ri,sj} p_{sj}), \quad (\text{A.9})$$

with

$$A_{ri,sj} = \left(\frac{M_r}{\mu_B} \right)^{1/2} \frac{\delta^2 \mathcal{F}}{\delta \varphi_{ri} \delta \varphi_{sj}} \Big|_{\theta=\frac{\pi}{2}, \varphi=0} \left(\frac{M_s}{\mu_B} \right)^{1/2} \quad (\text{A.10})$$

$$B_{ri,sj} = \left(\frac{M_r}{\mu_B} \right)^{1/2} \frac{\delta^2 \mathcal{F}}{\delta \varphi_{ri} \delta \theta_{sj}} \Big|_{\theta=\frac{\pi}{2}, \varphi=0} \left(\frac{M_s}{\mu_B} \right)^{1/2} \quad (\text{A.11})$$

$$C_{ri,sj} = \left(\frac{M_r}{\mu_B} \right)^{1/2} \frac{\delta^2 \mathcal{F}}{\delta \theta_{ri} \delta \theta_{sj}} \Big|_{\theta=\frac{\pi}{2}, \varphi=0} \left(\frac{M_s}{\mu_B} \right)^{1/2} \quad (\text{A.12})$$

A.2 Contribution to total uniaxial anisotropy due to "two-site" anisotropy

In chapter 6 we have shown that the contribution of the symmetric part of the exchange matrix interaction to the Hamiltonian (\mathcal{H}^{SExc}) can be written as follows:

$$\mathcal{H}^{SExc} = -\frac{1}{2} \sum_{i,j} \mathbf{S}_i \mathcal{J}_{ij}^S \mathbf{S}_j. \quad (\text{A.13})$$

The double sum is over all $i \neq j$. If we analyze only the contribution of the spin i , we obtain that it is described by:

$$\mathcal{H}_i^{SExc} = -\frac{1}{2} \sum_j \mathbf{S}_i \mathcal{J}_{ij}^S \mathbf{S}_j = -\frac{1}{2} \mathbf{S}_i \left(\sum_j \mathcal{J}_{ij}^S \mathbf{S}_j \right). \quad (\text{A.14})$$

In the case when the state of the system has the ferromagnetic order, where all the unit vectors \mathbf{S}_i are pointing out in the same direction, we can rewrite the last expression as:

$$\mathcal{H}_i^{SExc} = -\frac{1}{2}\mathbf{S}_i(\sum_j \mathcal{J}_{ij}^S)\mathbf{S}_j, \quad (\text{A.15})$$

being $(\sum_j \mathcal{J}_{ij}^S)$ the effective symmetric contribution of the exchange interaction at layer z_i , it has been defined previously as \mathcal{J}_{zi}^S . As we have shown in the chapter 6.3.4, for Co(100) and Co(100) \ Ag₁ the \mathcal{J}_{zi}^S has the following form:

$$\mathcal{J}_{zi}^S = \sum_j \mathcal{J}_{ij}^S = A_{zi} \begin{pmatrix} -\frac{1}{2} & 0 & 0 \\ 0 & -\frac{1}{2} & 0 \\ 0 & 0 & 1 \end{pmatrix} \quad (\text{A.16})$$

This expression can be separated in two contributions,

$$\mathcal{J}_{zi}^S = A_{zi} \begin{pmatrix} -\frac{1}{2} & 0 & 0 \\ 0 & -\frac{1}{2} & 0 \\ 0 & 0 & 1 \end{pmatrix} = \frac{-A_{zi}}{2} \begin{pmatrix} 1 & 0 & 0 \\ 0 & 1 & 0 \\ 0 & 0 & 1 \end{pmatrix} + A_{zi} \begin{pmatrix} 0 & 0 & 0 \\ 0 & 0 & 0 \\ 0 & 0 & \frac{3}{2} \end{pmatrix} \quad (\text{A.17})$$

Therefore we have that:

$$\mathcal{H}_i^{SExc} = \frac{A_{zi}}{4}\mathbf{S}_i\mathbf{S}_j - A_{zi}\mathbf{S}_i \begin{pmatrix} 0 & 0 & 0 \\ 0 & 0 & 0 \\ 0 & 0 & \frac{3}{2} \end{pmatrix} \mathbf{S}_j, \quad (\text{A.18})$$

This formula can be simplified as:

$$\mathcal{H}_i^{SExc} = \frac{A_{zi}}{4}\mathbf{S}_i\mathbf{S}_j - \frac{3A_{zi}}{4}S_{i,z}S_{j,z}, \quad (\text{A.19})$$

The first term on the right hand side (r.h.s) of this equation is isotropic and does not contribute to the anisotropy of the system, but it can modify the isotropic part of the exchange interaction. If we remember the initial hypothesis of the ferromagnetic state of the system, the second term in the (r.h.s.) of the equation A.19 can be expressed as: $-\frac{3A_{zi}}{4}S_{i,z}^2$ and this formula is analogous to that of the expression for the uniaxial anisotropy with easy axis parallel to the Z axis.

In conclusion the "two-site" anisotropy can contribute to the effective uniaxial anisotropy under the assumptions mentioned above.

A.3 Determination of one-site anisotropy energy

Suppose that we describe the properties of a magnetic system with an anisotropic Heisenberg Hamiltonian as follows:

$$\mathcal{H} = -\frac{1}{2}\sum_{i,j} \mathbf{S}_i \mathcal{J}_{ij} \mathbf{S}_j - \sum_i d(\mathbf{S}_i) \quad (\text{A.20})$$

where \mathcal{J}_{ij} and $d(\mathbf{S}_i)$ are matrices 3×3 . If we assume that the on-site anisotropy is uniaxial and its easy axis is parallel to Z axis, we can rewrite the Hamiltonian as:

$$\mathcal{H} = -\frac{1}{2} \sum_{i,j} \mathbf{S}_i \mathcal{J}_{ij} \mathbf{S}_j - \sum_i \mathbf{S}_i d_i \mathbf{S}_i \quad (\text{A.21})$$

$$d_i = \begin{pmatrix} 0 & 0 & 0 \\ 0 & 0 & 0 \\ 0 & 0 & d_i^{zz} \end{pmatrix} \quad (\text{A.22})$$

In spherical coordinates we can write \mathbf{S}_i as a function of the polar and azimuthal angles θ_i and φ_i , respectively.

$$\mathbf{S}_i = (\sin \theta_i \cos \varphi_i, \sin \theta_i \sin \varphi_i, \cos \theta_i) \quad (\text{A.23})$$

and evaluate the second derivatives with respect to the polar and azimuthal angles.

$$\frac{\partial^2 \mathbf{S}_i}{\partial \theta_i^2} = -(\sin \theta_i \cos \varphi_i, \sin \theta_i \sin \varphi_i, \cos \theta_i) = -\mathbf{S}_i \quad (\text{A.24})$$

$$\frac{\partial^2 \mathbf{S}_i}{\partial \varphi_i^2} = -(\sin \theta_i \cos \varphi_i, \sin \theta_i \sin \varphi_i, 0) \quad (\text{A.25})$$

If the spin i belongs to the plane XY then Eq. (A.25) is reduced to :

$$\frac{\partial^2 \mathbf{S}_i}{\partial \varphi_i^2} = -\mathbf{S}_i \quad (\text{A.26})$$

Now we evaluate the second derivatives with respect to the polar and azimuthal angles of the energy:

$$\frac{\partial^2 E\{\mathbf{S}_i\}}{\partial \theta_i^2} = -\frac{\partial^2}{\partial \theta_i^2} (\mathbf{S}_i d_i \mathbf{S}_i) - \frac{1}{2} \sum_{j,j \neq i} \frac{\partial^2 \mathbf{S}_i}{\partial \theta_i^2} \mathcal{J}_{ij} \mathbf{S}_j - \frac{1}{2} \sum_{j,j \neq i} \mathbf{S}_i \mathcal{J}_{ij} \frac{\partial^2 \mathbf{S}_j}{\partial \theta_i^2} \quad (\text{A.27})$$

$$\frac{\partial^2 E\{\mathbf{S}_i\}}{\partial \varphi_i^2} = -\frac{\partial^2}{\partial \varphi_i^2} (\mathbf{S}_i d_i \mathbf{S}_i) - \frac{1}{2} \sum_{j,j \neq i} \frac{\partial^2 \mathbf{S}_i}{\partial \varphi_i^2} \mathcal{J}_{ij} \mathbf{S}_j - \frac{1}{2} \sum_{j,j \neq i} \mathbf{S}_i \mathcal{J}_{ij} \frac{\partial^2 \mathbf{S}_j}{\partial \varphi_i^2} \quad (\text{A.28})$$

Due to the fact that the spin variables are independent, the equations above can be reduced to:

$$\frac{\partial^2 E\{\mathbf{S}_i\}}{\partial \theta_i^2} = -\frac{\partial^2}{\partial \theta_i^2} (\mathbf{S}_i d_i \mathbf{S}_i) - \frac{1}{2} \sum_{j,j \neq i} \frac{\partial^2 \mathbf{S}_i}{\partial \theta_i^2} \mathcal{J}_{ij} \mathbf{S}_j \quad (\text{A.29})$$

$$\frac{\partial^2 E\{\mathbf{S}_i\}}{\partial \varphi_i^2} = -\frac{\partial^2}{\partial \varphi_i^2} (\mathbf{S}_i d_i \mathbf{S}_i) - \frac{1}{2} \sum_{j,j \neq i} \frac{\partial^2 \mathbf{S}_i}{\partial \varphi_i^2} \mathcal{J}_{ij} \mathbf{S}_j \quad (\text{A.30})$$

The free energy of the system \mathcal{F} is related with the second derivatives above:

$$\mathcal{F}(\theta_i, \varphi_i) = \frac{\partial^2 E\{\mathbf{S}_i\}}{\partial \theta_i^2} - \frac{\partial^2 E\{\mathbf{S}_i\}}{\partial \varphi_i^2} = -\left(\frac{\partial^2}{\partial \theta_i^2} - \frac{\partial^2}{\partial \varphi_i^2}\right)(\mathbf{S}_i \mathbf{d}_i \mathbf{S}_i) - \sum_{j,j \neq i} \left(\frac{\partial^2 \mathbf{S}_i}{\partial \theta_i^2} - \frac{\partial^2 \mathbf{S}_i}{\partial \varphi_i^2}\right) \mathcal{J}_{ij} \mathbf{S}_j \quad (\text{A.31})$$

Taking into account the hypothesis that the on-site anisotropy is uniaxial Eq. (A.22), this expression can be reduced to:

$$\mathcal{F}(\theta_i, \varphi_i) = -\left(\frac{\partial^2}{\partial \theta_i^2} - \frac{\partial^2}{\partial \varphi_i^2}\right)(d_i^{zz} \cos^2 \theta_i) - \sum_{j,j \neq i} \left(\frac{\partial^2 \mathbf{S}_i}{\partial \theta_i^2} - \frac{\partial^2 \mathbf{S}_i}{\partial \varphi_i^2}\right) \mathcal{J}_{ij} \mathbf{S}_j \quad (\text{A.32})$$

Therefore we can calculate the on-site anisotropy constant d_i^{zz} evaluating the free energy at $\theta_i = \pi/2$

$$\mathcal{F}(\theta_i, \varphi_i) \Big|_{\theta_i=\pi/2} = 2d_i^{zz} \cos(2\theta) \Big|_{\theta_i=\pi/2} = -2d_i^{zz} \quad (\text{A.33})$$

with

$$d_i^{zz} = -\frac{1}{2} \mathcal{F}(\theta_i, \varphi_i) \Big|_{\theta_i=\pi/2} \quad (\text{A.34})$$

Bibliography

- [1] C. Desvaux, C. Amiens, P. Fejes, P. Renaud, M. Respaud, P. Lecante, E. Snoeck, and C. Bruno. *Multimillimetre-large superlattices of air-stable iron-cobalt nanoparticles*. Nat. Mater. **4**, 750 (2005).
- [2] S. Sun, C. B. Murray, D. Weller, L. Folks, and A. Moser. *Monodisperse FePt nanoparticles and ferromagnetic FePt nanocrystal superlattices*. Science **287**, 1989 (2000).
- [3] S. Rusponi, T. Cren, N. Weiss, M. Epple, P. Buluschek, L. Claude, and H. Brune. *The remarkable difference between surface and step atoms in the magnetic anisotropy of two-dimensional nanostructures*. Nat. Mater **2**, 546 (2003).
- [4] P. Tartaj, M. del Puerto Morales, S. Veintemillas-Verdaguer, T. González-Carreño, and C. J. Serna. *The preparation of magnetic nanoparticles for applications in biomedicine*. J. Phys. D: Appl. Phys. **36**, R182 (2003).
- [5] A. K. Gupta and M. Gupta. *Synthesis and surface engineering of iron oxide nanoparticles for biomedical applications*. Biomaterials **26**, 3995 (2005).
- [6] V. Skumryev, S. Stoyanov, Y. Zhang, G. Hadjipanayis, D. Givord, and J. Nogues. *Beating the superparamagnetic limit with exchange bias*. Nature **423**, 850 (2003).
- [7] R. F. L. Evans, R. Yanes, O. Mryasov, R. W. Chantrell, and O. Chubykalo-Fesenko. *On beating the superparamagnetic limit with exchange bias*. Europhys. Lett. **88**, 57004 (2009).
- [8] F. Luis, J. M. Torres, L. M. García, J. Bartolomé, J. Stankiewicz, F. Petroff, F. Fettar, J.-L. Maurice, and A. Vaurès. *Enhancement of the magnetic anisotropy of nanometer-sized Co clusters: Influence of the surface and of interparticle interactions*. Phys. Rev. B **65**, 094409 (2002).
- [9] J. Bartolomé, L. M. García, F. Bartolomé, F. Luis, R. López-Ruiz, F. Petroff, C. Deranlot, F. Wilhelm, A. Rogalev, P. Bencok, N. B. Brookes, L. Ruiz, and J. M. González-Calbet. *Magnetic polarization of noble metals by Co nanoparticles in M -capped granular multilayers (M = Cu , Ag, and Au): An X-ray magnetic circular dichroism study*. Phys. Rev. B **77**, 184420 (2008).

- [10] F. Luis, F. Bartolomé, F. . Petroff, J. Bartolomé, L. M. García, C. Deranlot, H. Jaffrè, M. J. Martínez, P. Bencok, F. Wilhelm, A. Rogalev, and N. B. Brookes. *Tuning the magnetic anisotropy of Co nanoparticles by metal capping*. *Europhys. Lett.* **76**, 142 (2006).
- [11] F. Garcia-Sanchez, O. Chubykalo-Fesenko, O. Mryasov, P. Asselin, and R. W. Chantrell. *Switching and thermal stability properties of bilayer thin films: Single versus multigrain cases*. *J. Appl. Phys.* **103**, 07F505 (2008).
- [12] G. R. Aranda, O. Chubykalo-Fesenko, R. Yanes, J. Gonzalez, J. J. del Val, R. W. Chantrell, Y. K. Takahashi, and K. Hono. *Coercive field and energy barriers in partially disordered FePt nanoparticles*. *J. Appl. Phys.* **105**, 07B514 (2009).
- [13] G. Salazar-Alvarez, J. Qin, V. Sepelák, I. Bergmann, M. Vasilakaki, K. N. Trohidou, J. D. Ardisson, W. A. A. Macedo, M. Mikhaylova, M. Muhammed, M. D. Baró, and J. Nogués. *Cubic versus spherical magnetic nanoparticles: The role of surface anisotropy*. *J. Am. Chem. Soc.* **130**, 13234 (2008). <http://pubs.acs.org/doi/pdf/10.1021/ja0768744>.
- [14] M. Jamet, W. Wernsdorfer, C. Thirion, V. Dupuis, P. Mélinon, A. Pérez, and D. Mailly. *Magnetic anisotropy in single clusters*. *Phys. Rev. B* **69**, 024401 (2004).
- [15] X. Batlle and A. Labarta. *Finite-size effects in fine particles: magnetic and transport properties*. *J. Phys. D: Appl. Phys.* **35**, R15 (2002).
- [16] A. Weddemann, I. Ennen, A. Regtmeier, C. Albon, A. Wolf, K. Eckstädt, N. Mill, J. Peter, Michaeland Mattay, C. Plattner, and A. Sewald, Norbert andfd Hütten. *Review and outlook: from single nanoparticles to self-assembled monolayers and granular GMR sensors*. *Beilstein J. Nanotechnol.* **1**, 75 (2010).
- [17] J. Frenkel and J. Doefman. *Spontaneous and induced magnetisation in ferromagnetic bodies*. *Nature* **126**, 274 (1930).
- [18] R. Evans, U. Nowak, F. Dorfbauer, T. Shrefl, O. Mryasov, R. W. Chantrell, and G. Grochola. *The influence of shape and structure on the Curie temperature of Fe and Co nanoparticles*. *J. Appl. Phys.* **99**, 08G703 (2006).
- [19] A. G. Roca, R. Costo, A. F. Rebolledo, S. Veintemillas-Verdaguer, P. Tartaj, T. González-Carreño, M. P. Morales, and C. J. Serna. *Progress in the preparation of magnetic nanoparticles for applications in biomedicine*. *J. Phys. D: Appl. Phys.* **42**, 224002 (2009).
- [20] M. Jamet, W. Wernsdorfer, C. Thirion, D. Mailly, V. Dupuis, P. Mélinon, and A. Pérez. *Magnetic anisotropy of a single cobalt nanocluster*. *Phys. Rev. Lett.* **86**, 4676 (2001).

- [21] J. M. D. Coey, K. Wongsaprom, J. Alaria, and M. Venkatesan. *Charge-transfer ferromagnetism in oxide nanoparticles.* J. Phys. D: Appl. Phys. **41**, 134012 (2008).
- [22] L. F. Cotica, I. A. Santos, E. M. Girotto, E. V. Ferri, and A. A. Coelho. *Surface spin disorder effects in magnetite and poly(thiophene)-coated magnetite nanoparticles.* J. Appl. Phys. **108**, 064325 (2010).
- [23] W. H. Meiklejohn and C. P. Bean. *New magnetic anisotropy.* Phys. Rev. **105**, 904 (1957).
- [24] S. A. Makhlof, H. Al-Attar, and R. Kodama. *Particle size and temperature dependence of exchange bias in NiO nanoparticles.* Solid State Commun. **145**, 1 (2008).
- [25] W. H. Meiklejohn and C. P. Bean. *New magnetic anisotropy.* Phys. Rev. **102**, 1413 (1956).
- [26] J. Nogués and I. K. Schuller. *Exchange bias.* J. Magn. Magn. Mat. **192**, 203 (1999).
- [27] O. Iglesias, X. Batlle, and A. Labarta. *Modelling exchange bias in core/shell nanoparticles.* J. Phys.: Condens. Matter **19**, 406232 (2007).
- [28] F. Liu, M. R. Press, S. N. Khanna, and P. Jena. *Magnetism and local order: Ab initio tight-binding theory.* Phys. Rev. B **39**, 6914 (1989).
- [29] S. N. Khanna and S. Linderoth. *Magnetic behavior of clusters of ferromagnetic transition metals.* Phys. Rev. Lett. **67**, 742 (1991).
- [30] S. E. Apsel, J. W. Emmert, J. Deng, and L. A. Bloomfield. *Surface-enhanced magnetism in nickel clusters.* Phys. Rev. Lett. **76**, 1441 (1996).
- [31] K. W. Edmonds, C. Binns, S. H. Baker, S. C. Thornton, C. Norris, J. B. Goedkoop, M. Finazzi, and N. B. Brookes. *Doubling of the orbital magnetic moment in nanoscale Fe clusters.* Phys. Rev. B **60**, 472 (1999).
- [32] M. Respaud, J. M. Broto, H. Rakoto, A. R. Fert, L. Thomas, B. Barbara, M. Verelst, E. Snoeck, P. Lecante, A. Mosset, J. Osuna, T. O. Ely, C. Amiens, and B. Chaudret. *Surface effects on the magnetic properties of ultrafine cobalt particles.* Phys. Rev. B **57**, 2925 (1998).
- [33] A. E. Berkowitz, W. J. Schuele, and P. J. Flanders. *Influence of crystallite size on the magnetic properties of acicular γ - Fe_2O_3 particles.* J. Appl. Phys. **39**, 1261 (1968).

- [34] J. M. D. Coey. *Noncollinear spin arrangement in ultrafine ferrimagnetic crystallites*. Phys. Rev. Lett. **27**, 1140 (1971).
- [35] R. H. Kodama. *Magnetic nanoparticles*. J. Magn. Magn. Mat. **200**, 359 (1999).
- [36] F. Bødker, S. Mørup, and S. Linderoth. *Surface effects in metallic iron nanoparticles*. Phys. Rev. Lett. **72**, 282 (1994).
- [37] E. Tronc, A. Ezzir, R. Cherkaoui, C. Chanéac, M. Noguès, H. Kachkachi, D. Fiorani, A. Testa, J. Grenèche, and J. Jolivet. *Surface-related properties of γ -Fe₂O₃ nanoparticles*. J. Magn. Magn. Mat. **221**, 63 (2000).
- [38] J. E. Lima, E. D. Biasi, M. V. Mansilla, M. E. Saleta, F. Effenberg, L. M. Rossi, R. Cohen, H. R. Rechenberg, and R. D. Zysler. *Surface effects in the magnetic properties of crystalline 3 nm ferrite nanoparticles chemically synthesized*. J. Appl. Phys. **108**, 103919 (2010).
- [39] M. Hamedoun, K. Bouslykhane, H. Bakrim, A. Hourmatallah, and N. Benzakour. *Coupling and surface effects in magnetic thin films*. Physica A **358**, 102 (2005).
- [40] L. Szunyogh, L. Udvardi, J. Jackson, U. Nowak, and R. Chantrell. *Atomistic spin model based on a spin-cluster expansion technique: Application to the IrMn₃/Co interface*. Phys. Rev. B **83**, 024401 (2011).
- [41] I. Apostolova and J. M. Wesselinowa. *Possible low-T_c nanoparticles for use in magnetic hyperthermia treatments*. Solid State Commun. **149**, 986 (2009).
- [42] J. H. van Vleck. *On the anisotropy of cubic ferromagnetic crystals*. Phys. Rev. **52**, 1178 (1937).
- [43] U. Gradmann. *Magnetism in oligatomic films*. J. Appl. Phys. **40**, 1182 (1969).
- [44] J. G. Gay and R. Richter. *Spin anisotropy of ferromagnetic films*. Phys. Rev. Lett. **56**, 2728 (1986).
- [45] P. Bruno. *Tight-binding approach to the orbital magnetic moment and magnetocrystalline anisotropy of transition-metal monolayers*. Phys. Rev. B **39**, 865 (1989).
- [46] R. H. Victora and J. M. MacLaren. *Theory of magnetic interface anisotropy*. Phys. Rev. B **47**, 11583 (1993).
- [47] L. Néel. *Anisotropie magnétique superficielle et surstructures d'orientation*. J. Phys. Radium **15**, 225 (1954).
- [48] L. Stöhr and H. Siegmann. *Magnetism from: fundamentals to nanoscale dynamics* (Springer, 2006).

- [49] C. Andersson, B. Sanyal, O. Eriksson, L. Nordström, O. Karis, D. Arvanitis, T. Konishi, E. Holub-Krappe, and J. H. Dunn. *Influence of ligand states on the relationship between orbital moment and magnetocrystalline anisotropy.* Phys. Rev. Lett. **99**, 177207 (2007).
- [50] G. Schütz, W. Wagner, W. Wilhelm, P. Kienle, R. Zeller, R. Frahm, and G. Materlik. *Absorption of circularly polarized x-rays in iron.* Phys. Rev. Lett. **58**, 737 (1987).
- [51] J. Stöhr. *Exploring the microscopic origin of magnetic anisotropies with X-ray magnetic circular dichroism (XMCD) spectroscopy.* J. Magn. Magn. Mat. **200**, 470 (1999).
- [52] A. Ney, P. Poulopoulos, M. Farle, and K. Baberschke. *Absolute determination of Co magnetic moments: Ultrahigh-vacuum high- T_c SQUID magnetometry.* Phys. Rev. B **62**, 11336 (2000).
- [53] W. F. Brown. *Thermal fluctuations of a single-domain particle.* Phys. Rev. **130**, 1677 (1963).
- [54] P. Bruno and J. P. Renard. *Magnetic surface anisotropy of transition metal ultra-thin films.* Appl. Phys. A **49**, 499 (1989).
- [55] H. J. Elmers and U. Gradmann. *Magnetic anisotropies in Fe(110) films on W(110).* Appl. Phys. A **51**, 255 (1990).
- [56] A. P. N. Dinia and H. Danan. *Spectral-density method for classical systems: Heisenberg ferromagnet.* J. App. Phys. **84**, 5668 (1998).
- [57] E. Tronc, D. Fiorani, M. Noguès, A. Testa, F. Lucari, F. D’Orazio, J. Grenèche, W. Wernsdorfer, N. Galvez, C. Chanéac, D. Mailly, and J. Jolivet. *Surface effects in non-interacting and interacting γ -Fe₂O₃ nanoparticles.* J. Magn. Magn. Mat. **262**, 6 (2003).
- [58] U. Gradmann. *Magnetic surface anisotropies.* J. Magn. Magn. Mat. **54-57**, 733 (1986).
- [59] G. Bochi, C. A. Ballentine, H. E. Inglefield, C. V. Thompson, and R. C. O’Handley. *Evidence for strong surface magnetoelastic anisotropy in epitaxial Cu/Ni/Cu(001) sandwiches.* Phys. Rev. B **53**, R1729 (1996).
- [60] Z. Kurant, R. Gieniusz, A. Maziewski, M. Tekielak, W. Stefanowicz, I. Sveklo, V. Zablotskii, A. Petrouitchik, L. Baczewski, and A. Wawro. *Changes in magnetic properties of ultrathin cobalt films as induced by Mo, V, Au overlayers.* J. Magn. Magn. Mat. **316**, e511 (2007).

- [61] T. Shinjo, N. Nakayama, I. Moritani, and Y. Endoh. *Monolayer of ferromagnetic MnSb*. J. Phys. Soc. Jpn. **55**, 2512 (1986).
- [62] F. den Broeder, W. Hoving, and P. Bloemen. *Magnetic anisotropy of multilayers*. J. Magn. Magn. Mat. **93**, 562 (1991).
- [63] B. Schulz and K. Baberschke. *Crossover from in-plane to perpendicular magnetization in ultrathin Ni/Cu(001) films*. Phys. Rev. B **50**, 13467 (1994).
- [64] D. Wilgocka-Ślęzak, K. Freindl, A. Kozioł, K. Matlak, M. Rams, N. Spiridis, M. Ślęzak, T. Ślęzak, M. Zajac, and J. Korecki. *Thickness-driven polar spin reorientation transition in ultrathin Fe/Au(001) films*. Phys. Rev. B **81**, 064421 (2010).
- [65] N. C. Koon, B. T. Jonker, F. A. Volkenning, J. J. Krebs, and G. A. Prinz. *Direct evidence for perpendicular spin orientations and enhanced hyperfine fields in ultrathin Fe(100) films on Ag(100)*. Phys. Rev. Lett. **59**, 2463 (1987).
- [66] R. Allenspach and A. Bischof. *Magnetization direction switching in Fe/Cu(100) epitaxial films: Temperature and thickness dependence*. Phys. Rev. Lett. **69**, 3385 (1992).
- [67] Y. Yafet and E. M. Gyorgy. *Ferromagnetic strip domains in an atomic monolayer*. Phys. Rev. B **38**, 9145 (1988).
- [68] C. Won, Y. Z. Wu, J. Choi, W. Kim, A. Scholl, A. Doran, T. Owens, J. Wu, X. F. Jin, H. W. Zhao, and Z. Q. Qiu. *Magnetic stripe melting at the spin reorientation transition in Fe/Ni/Cu(001)*. Phys. Rev. B **71**, 224429 (2005).
- [69] M. Carubelli, O. V. Billoni, S. A. Pighín, S. A. Cannas, D. A. Stariolo, and F. A. Tamarit. *Spin reorientation transition and phase diagram of ultrathin ferromagnetic films*. Phys. Rev. B **77**, 134417 (2008).
- [70] A. Hubbert and R. Schaffer. *Magnetic domains* (Springer, 1998).
- [71] Y. Xie and J. A. Blackman. *Magnetocrystalline anisotropy and orbital polarization in ferromagnetic transition metals*. Phys. Rev. B **69**, 172407 (2004).
- [72] Y. Xie and J. A. Blackman. *Magnetic anisotropy of nanoscale cobalt particles*. J. Phys.: Condens. Matter **16**, 3163 (2004).
- [73] H. Kachkachi. *Effects of spin non-collinearities in magnetic nanoparticles*. J. Magn. Magn. Mat. **316**, 248 (2007).
- [74] D. A. Garanin and H. Kachkachi. *Surface contribution to the anisotropy of magnetic nanoparticles*. Phys. Rev. Lett. **90**, 065504 (2003).

- [75] H. Kachkachi and H. Mahboub. *Surface anisotropy in nanomagnets: transverse or Néel?* J. Magn. Magn. Mat. **278**, 334 (2004).
- [76] R. Yanes, O. Chubykalo-Fesenko, H. Kachkachi, D. A. Garanin, R. Evans, and R. Chantrell. *Effective anisotropies and energy barriers of magnetic nanoparticles with Néel surface anisotropy.* Phys. Rev. B **76**, 064416 (2007).
- [77] L. Berger, Y. Labaye, M. Tamine, and J. M. D. Coey. *Ferromagnetic nanoparticles with strong surface anisotropy: Spin structures and magnetization processes.* Phys. Rev. B **77**, 104431 (2008).
- [78] J. Mazo-Zuluaga, J. Restrepo, F. Munoz, and J. Mejia-Lopez. *Surface anisotropy, hysteretic, and magnetic properties of magnetite nanoparticles: A simulation study.* J. Appl. Phys. **105**, 123907 (2009).
- [79] A. Cabot, A. P. Alivisatos, V. F. Puntes, L. Balcells, O. Iglesias, and A. Labarta. *Magnetic domains and surface effects in hollow maghemite nanoparticles.* Phys. Rev. B **79**, 094419 (2009).
- [80] O. Chubykalo-Fesenko and R. W. Chantrell. *Multidimensional energy barrier distributions of interacting magnetic particles evaluated at different magnetization states.* J. Appl. Phys. **97**, 10J315 (2005).
- [81] O. Chubykalo-Fesenko, K. Guslienko, T. Klemmer, X. Wu, R. Chantrell, and D. Weller. *A computational and experimental study of exchange coupling in FePt self-organized magnetic arrays.* Physica B: Condensed Matter **382**, 235 (2006).
- [82] H. Kronmüller, R. Fischer, M. Seeger, and A. Zern. *Micromagnetism and microstructure of hard magnetic materials.* J. Phys. D: Appl. Phys. **29**, 2274 (1996).
- [83] F. Garcia-Sanchez, O. Chubykalo-Fesenko, O. Myrasov, R. W. Chantrell, and K. Y. Guslienko. *Exchange spring structures and coercivity reduction in FePt/FeRh bilayers: A comparison of multiscale and micromagnetic calculations.* Appl. Phys. Lett. **87**, 122501 (2005).
- [84] R. Evans, F. Dorfbauer, O. Myrasov, O. Chubykalo-Fesenko, T. Schrefl, and R. Chantrell. *The effects of surface coating on the structural and magnetic properties of CoAg core-shell nanoparticles.* IEEE Trans. Magn. **43**(6), 3106 (2007).
- [85] F. Dorfbauer, R. Evans, M. Kirschner, O. Chubykalo-Fesenko, R. Chantrell, and T. Schrefl. *Effects of surface anisotropy on the energy barrier in cobalt-silver core-shell nanoparticles.* J. Magn. Magn. Mat. **316**, e791 (2007).
- [86] L. Szunyogh, B. Újfalussy, and P. Weinberger. *Magnetic anisotropy of iron multilayers on Au(001): First-principles calculations in terms of the fully relativistic spin-polarized screened KKR method.* Phys. Rev. B **51**, 9552 (1995).

- [87] H. Kachkachi and E. Bonet. *Surface-induced cubic anisotropy in nanomagnets.* Phys. Rev. B **73**, 224402 (2006).
- [88] J. M. Vargas and R. D. Zysler. *Tailoring the size in colloidal iron oxide magnetic nanoparticles.* Nanotechnology **16**, 1474 (2005).
- [89] G. Chouhan, D. Wang, and H. Alper. *Magnetic nanoparticle-supported proline as a recyclable and recoverable ligand for the CuI catalyzed arylation of nitrogen nucleophiles.* R. Soc. Chem. (Suppl. Mater. (ESI)Chem. Communic.) (2007).
- [90] H. Kachkachi and M. Dimian. *Hysteretic properties of a magnetic particle with strong surface anisotropy.* Phys. Rev. B **66**, 174419 (2002).
- [91] H. Kachkachi, A. Ezzir, M. Noguès, and E. Tronc. *Surface effects in nanoparticles: application to maghemite.* Eur. Phys. J. B **14**, 681 (2000).
- [92] O. Iglesias and A. Labarta. *Finite-size and surface effects in maghemite nanoparticles: Monte Carlo simulations.* Phys. Rev. B **63**, 184416 (2001).
- [93] D. Fiorani, ed. *Surface effects in magnetic nanoparticles* (Springer Science, 2005).
- [94] R. H. Kodama and A. E. Berkowitz. *Atomic-scale magnetic modeling of oxide nanoparticles.* Phys. Rev. B **59**, 6321 (1999).
- [95] M. S. Daw and M. I. Baskes. *Semiempirical, quantum mechanical calculation of hydrogen embrittlement in metals.* Phys. Rev. Lett. **50**, 1285 (1983).
- [96] F. Dorfbauer, T. Schrefl, M. Kirschner, G. Hrkac, D. Suess, O. Ertl, and J. Fidler. *Nanostructure calculation of CoAg core-shell clusters.* J. Appl. Phys. **99**, 08G706 (2006).
- [97] H. Kachkachi and D. M. Garanin. Unpublished .
- [98] A. Aharoni. *Introduction to the theory of ferromagnetism* (Oxford University Press, 1996).
- [99] E. Paz, F. Garcia-Sanchez, and O. Chubykalo-Fesenko. *Numerical evaluation of energy barriers in nano-sized magnetic elements with lagrange multiplier technique.* Physica B: Condens. Matter **403**, 330 (2008).
- [100] F. Bartolomé, F. Luis, F. Petroff, L. M. García, J. Bartolomé, V. Cros, and H. Jaffrè. *XMCD study of the anisotropy of nanometric Co clusters in insulating and metallic matrices.* J. Magn. Magn. Mater. **272-276**, E1275 (2004). Proceedings of the International Conference on Magnetism (ICM 2003).

- [101] F. Luis, J. Bartolome, F. Bartolome, M. J. Martinez, L. M. Garcia, F. Petroff, C. Deranlot, F. Wilhelm, and A. Rogalev. *Enhancement of the magnetic anisotropy of Co clusters by Au capping.* J. Appl. Phys. **99**, 08G705 (pages 3) (2006).
- [102] Y. Labaye, O. Crisan, L. Berger, J. M. Grenache, and J. M. D. Coey. *Surface anisotropy in ferromagnetic nanoparticles.* J. Appl. Phys. **91**, 8715 (2002).
- [103] D. A. Dimitrov and G. M. Wysin. *Magnetic properties of spherical fcc clusters with radial surface anisotropy.* Phys. Rev. B **51**, 11947 (1995).
- [104] G. H. O. Daalderop, P. J. Kelly, and M. F. H. Schuurmans. *Magnetic anisotropy of a free-standing Co monolayer and of multilayers which contain Co monolayers.* Phys. Rev. B **50**, 9989 (1994).
- [105] B. Újfaluassy, L. Szunyogh, P. Bruno, and P. Weinberger. *First-principles calculation of the anomalous perpendicular anisotropy in a co monolayer on au(111).* Phys. Rev. Lett. **77**, 1805 (1996).
- [106] H. Callen and E. Callen. *The present status of the temperature dependence of magnetocrystalline anisotropy, and the $l(l+1)/2$ law.* J. Phys. Chem. Solids **27**, 1271 (1966).
- [107] O. N. Mryasov, U. Nowak, K. Y. Guslienko, and R. W. Chantrell. *Temperature-dependent magnetic properties of FePt: Effective spin Hamiltonian model.* Europhys. Lett. **69**, 805 (2005).
- [108] R. Skomski, A. Kashyap, and D. Sellmyer. *Finite-temperature anisotropy of PtCo magnets.* IEEE Trans. Magn. **39**, 2917 (2003).
- [109] H. F. Hamann, Y. C. Martin, and H. K. Wickramasinghe. *Thermally assisted recording beyond traditional limits.* Appl. Phys. Lett. **84**, 810 (2004).
- [110] R. Rottmayer, S. Batra, D. Buechel, W. Challener, J. Hohlfeld, Y. Kubota, L. Li, B. Lu, C. Mihalcea, K. Mountfield, K. Pelhos, C. Peng, T. Rausch, M. Seigler, D. Weller, and X. Yang. *Heat-assisted magnetic recording.* IEEE Trans. Magn. **42**, 2417 (2006).
- [111] T. W. McDaniel. *Ultimate limits to thermally assisted magnetic recording.* J. Phys.: Condens. Matter. **17**, R315 (2005).
- [112] A. Lyberatos and K. Y. Guslienko. *Thermal stability of the magnetization following thermomagnetic writing in perpendicular media.* J. Appl. Phys. **94**, 1119 (2003).

- [113] F. G. Sanchez, O. Chubykalo-Fesenko, O. Mryasov, and R. Chantrell. *Multiscale modelling of hysteresis in FePt/FeRh bilayer*. Physica B: Condensed Matter **372**, 328 (2006).
- [114] J.-U. Thiele, S. Maat, and E. E. Fullerton. *FeRh/FePt exchange spring films for thermally assisted magnetic recording media*. Appl. Phys. Lett. **82**, 2859 (2003).
- [115] K. Y. Guslienko, O. Chubykalo-Fesenko, O. Mryasov, R. Chantrell, and D. Weller. *Magnetization reversal via perpendicular exchange spring in FePt/FeRh bilayer films*. Phys. Rev. B **70**, 104405 (2004).
- [116] U. Atxitia, O. Chubykalo-Fesenko, N. Kazantseva, D. Hinzke, U. Nowak, and R. W. Chantrell. *Micromagnetic modeling of laser-induced magnetization dynamics using the Landau-Lifshitz-Bloch equation*. Appl. Phys. Lett. **91**, 232507 (2007).
- [117] A. Berger and H. Hopster. *Nonequilibrium magnetization near the reorientation phase transition of Fe/Ag(100) films*. Phys. Rev. Lett. **76**, 519 (1996).
- [118] I.-G. Baek, H. G. Lee, H.-J. Kim, and E. Vescovo. *Spin reorientation transition in Fe(110) thin films: The role of surface anisotropy*. Phys. Rev. B **67**, 075401 (2003).
- [119] A. Enders, D. Peterka, D. Repetto, N. Lin, A. Dmitriev, and K. Kern. *Temperature dependence of the surface anisotropy of Fe ultrathin films on Cu(001)*. Phys. Rev. Lett. **90**, 217203 (2003).
- [120] M. Farle. *Ferromagnetic resonance of ultrathin metallic layers*. Rep. Progr. Phys. **61**, 755 (1998).
- [121] N. Kazantseva, D. Hinzke, U. Nowak, R. W. Chantrell, U. Atxitia, and O. Chubykalo-Fesenko. *Towards multiscale modeling of magnetic materials: Simulations of FePt*. Phys. Rev. B **77**, 184428 (2008).
- [122] B. C. Chuang D.S. and O. R.C. *Surface and step magnetic anisotropy*. Phys. Rev. B **51**, 11947 (1995).
- [123] N. Metropolis, A. Rosenbluth, M. Rosembuth, A. Teller, and E. Teller. *Equation of state calculations by fast computing machines*. J. Chem. Phys. **21**, 1087 (1953).
- [124] J. M. González, O. A. Chubykalo, and R. S. Rueda. *A micromagnetic approach, based on the Monte Carlo algorithm, to the thermally activated magnetization reversal processes*. J. Magn. Magn. Mat. **203**, 18 (1999).
- [125] R.Evans. Ph.D. thesis, University of York,UK (2009).

- [126] P. Asselin, R. F. L. Evans, J. Barker, R. W. Chantrell, R. Yanes, O. Chubykalo-Fesenko, D. Hinzke, and U. Nowak. *Constrained Monte Carlo method and calculation of the temperature dependence of magnetic anisotropy*. Phys. Rev. B **82**, 054415 (2010).
- [127] L. S. Campana, A. C. D'Auria, M. D'Ambrosio, U. Esposito, L. De Cesare, and G. Kamieniarz. *Spectral-density method for classical systems: Heisenberg ferromagnet*. Phys. Rev. B **30**, 2769 (1984).
- [128] G. A. Baker, H. E. Gilbert, J. Eve, and G. S. Rushbrooke. *High-temperature expansions for the spin 1/2 Heisenberg model*. Phys. Rev. **164**, 800 (1967).
- [129] C. Zener. *Classical theory of the temperature dependence of magnetic anisotropy energy*. Phys. Rev. **96**, 1335 (1954).
- [130] K. Binder and P. C. Hohenberg. *Surface effects on magnetic phase transitions*. Phys. Rev. B **9**, 2194 (1974).
- [131] T. Kaneyoshi. *Surface magnetism; magnetization and anisotropy at a surface*. J. Phys.: Condens. Matter **3**, 4497 (1991).
- [132] C. Chappert and P. Bruno. *Magnetic anisotropy in metallic ultrathin films and related experiments on cobalt films*. J. Appl. Phys. **64**, 5736 (1988).
- [133] G. André, A. Aspelmeier, B. Schulz, M. Farle, and K. Baberschke. *Temperature dependence of surface and volume anisotropy in Gd/W(110)*. Surface Science **326**, 275 (1995).
- [134] M. Farle, W. Platow, A. N. Anisimov, B. Schulz, and K. Baberschke. *The temperature dependence of magnetic anisotropy in ultra-thin films*. J. Mag. Magn. Matt. **165**(74), 4 (1997).
- [135] A. Buruzs, P. Weinberger, L. Szunyogh, L. Udvardi, P. I. Chleboun, A. M. Fischer, and J. B. Staunton. *Ab initio theory of temperature dependence of magnetic anisotropy in layered systems: Applications to thin Co films on Cu(100)*. Phys. Rev. B **76**, 064417 (2007).
- [136] J. B. Staunton, L. Szunyogh, A. Buruzs, B. L. Gyorffy, S. Ostanin, and L. Udvardi. *Temperature dependence of magnetic anisotropy: An ab initio approach*. Phys. Rev. B **74**, 144411 (2006).
- [137] D. Pescia and V. L. Pokrovsky. *Perpendicular versus in-plane magnetization in a 2D Heisenberg monolayer at finite temperatures*. Phys. Rev. Lett. **65**, 2599 (1990).

- [138] B. Dieny and A. Vedyayev. *Crossover from easy-plane to perpendicular anisotropy in magnetic thin films: canted anisotropy due to partial coverage or interfacial roughness.* Europhys. Lett. **25**, 723 (1994).
- [139] U. Atxitia, D. Hinzke, O. Chubykalo-Fesenko, U. Nowak, H. Kachkachi, O. N. Myrasov, R. F. Evans, and R. W. Chantrell. *Multiscale modeling of magnetic materials: Temperature dependence of the exchange stiffness.* Phys. Rev. B **82**, 134440 (2010).
- [140] URL <http://www.magpar.net/>.
- [141] URL <http://math.nist.gov/oommf/>.
- [142] L. Udvardi, L. Szunyogh, K. Palotás, and P. Weinberger. *First-principles relativistic study of spin waves in thin magnetic films.* Phys. Rev. B **68**, 104436 (2003).
- [143] P. Hohenberg and W. Kohn. *Inhomogeneous Electron Gas.* Phys. Rev. **136**, B864 (1964).
- [144] W. Kohn and L. J. Sham. *Self-consistent equations including exchange and correlation effects.* Phys. Rev. **140**, A1133 (1965).
- [145] L. Hedin and B. I. Lundqvist. *Explicit local exchange-correlation potentials.* J. Phys. C: Solid State Phys. **4**, 2064 (1971).
- [146] J. P. Perdew, J. A. Chevary, S. H. Vosko, K. A. Jackson, M. R. Pederson, D. J. Singh, and C. Fiolhais. *Atoms, molecules, solids, and surfaces: Applications of the generalized gradient approximation for exchange and correlation.* Phys. Rev. B **46**, 6671 (1992).
- [147] U. von Barth and L. Hedin. *A local exchange-correlation potential for the spin polarized case.* J. Phys. C: Solid State Phys. **5**, 1629 (1972).
- [148] J. Korringa. *On the calculation of the energy of a Bloch wave in a metal.* Physica **13**, 392 (1947).
- [149] W. Kohn and N. Rostoker. *Solution of the Schrödinger equation in Periodic Lattices with an Application to Metallic Lithium.* Phys. Rev. **94**, 1111 (1954).
- [150] L. Szunyogh, B. Újfalussy, P. Weinberger, and J. Kollár. *Self-consistent localized KKR scheme for surfaces and interfaces.* Phys. Rev. B **49**, 2721 (1994).
- [151] M. C. Muñoz, V. R. Velasco, and F. Garcia-Moliner. *Surface and interface electronic structure calculations with empirical tight binding models.* Physica Scripta **35**, 504 (1987).

- [152] M. P. L. Sancho, J. M. L. Sancho, J. M. L. Sancho, and J. Rubio. *Highly convergent schemes for the calculation of bulk and surface green functions*. J. Phys. F: Met. Phys. **15**(4), 851 (1985).
- [153] M. C. Muñoz, V. R. Velasco, and F. García-Moliner. *Electronic structure of AlAs-GaAs superlattices*. Phys. Rev. B **39**, 1786 (1989).
- [154] P. Lloyd. *Wave propagation through an assembly of spheres: II. The density of single-particle eigenstates*. Proc. Phys. Soc. **90**(1), 207 (1967).
- [155] J. Zabloud, R. Hammerling, L. Szunyogh, and P. Weinberger. *Electron Sacttering in Solid Matter: A Theoretical and Computational treatise*, vol. 147 of *Series in solid state science* (Springer, 2005).
- [156] N. S. González, S. Gallego, and M. C. Muñoz. Private communication .
- [157] H. B. Michaelson. *The work function of the elements and its periodicity*. J. Appl. Phys. **48**, 4729 (1977).
- [158] R. Smoluchowski. *Anisotropy of the electronic work function of metals*. Phys. Rev. **60**, 661 (1941).
- [159] N. D. Lang and W. Kohn. *Theory of metal surfaces: Work function*. Phys. Rev. B **3**, 1215 (1971).
- [160] P. Söderlind, O. Eriksson, B. Johansson, R. C. Albers, and A. M. Boring. *Spin and orbital magnetism in Fe-Co and Co-Ni alloys*. Phys. Rev. B **45**, 12911 (1992).
- [161] M. Tischer, O. Hjortstam, D. Arvanitis, J. Hunter Dunn, F. May, K. Baberschke, J. Trygg, J. M. Wills, B. Johansson, and O. Eriksson. *Enhancement of orbital magnetism at surfaces: Co on Cu(100)*. Phys. Rev. Lett. **75**, 1602 (1995).
- [162] O. Eriksson, A. M. Boring, R. C. Albers, G. W. Fernando, and B. R. Cooper. *Spin and orbital contributions to surface magnetism in 3d elements*. Phys. Rev. B **45**, 2868 (1992).
- [163] R. Wu, D. Wang, and A. J. Freeman. *First principles investigation of the validity and range of applicability of the X-ray magnetic circular dichroism sum rule*. Phys. Rev. Lett. **71**, 3581 (1993).
- [164] N. Nakajima, T. Koide, T. Shidara, H. Miyauchi, H. Fukutani, A. Fujimori, K. Iio, T. Katayama, M. Nývlt, and Y. Suzuki. *Perpendicular magnetic anisotropy caused by interfacial hybridization via enhanced orbital moment in Co/Pt multilayers: Magnetic circular x-ray dichroism study*. Phys. Rev. Lett. **81**, 5229 (1998).

- [165] H. A. Dürr, S. S. Dhesi, E. Dudzik, D. Knabben, G. van der Laan, J. B. Goedkoop, and F. U. Hillebrecht. *Spin and orbital magnetization in self-assembled Co clusters on Au(111)*. Phys. Rev. B **59**, R701 (1999).
- [166] N. Jaouen, F. Wilhelm, A. Rogalev, J. Goulon, L. Ortega, J. M. Tonnerre, and A. Yaresko. *Electronic and magnetic interfacial states of Ag in an Ni₈₁Fe₁₉/Ag coupled multilayer*. J. Phys.: Condens. Matter **20**, 095005 (2008).
- [167] A. I. Liechtenstein, M. I. Katsnelson, V. P. Antropov, and V. A. Gubanov. *Local spin density functional approach to the theory of exchange interactions in ferromagnetic metals and alloys*. J. Magn. Magn. Mat. **67**, 65 (1987).
- [168] B. L. Gyorffy, A. J. Pindor, J. Staunton, G. M. Stocks, and H. Winter. *A first-principles theory of ferromagnetic phase transitions in metals*. J. Phys. F: Metal Phys. **15**, 1337 (1985).
- [169] V. P. Antropov, M. I. Katsnelson, B. N. Harmon, M. van Schilfgaarde, and D. Kusnezov. *Spin dynamics in magnets: Equation of motion and finite temperature effects*. Phys. Rev. B **54**, 1019 (1996).
- [170] L. Szunyogh and L. Udvardi. *Ab initio calculation of Heisenberg parameters in thin magnetic films*. Philosophical Magazine B **78**, 617 (1998).
- [171] L. Szunyogh and L. Udvardi. *Ab initio calculation of Heisenberg parameters and Curie temperatures in thin magnetic films*. J. Magn. Magn. Mat. **198-199**, 537 (1999).
- [172] P. Mavropoulos. *Multiscale modelling of magnetic materials: From the total energy of the homogeneous electron gas to the Curie temperature of ferromagnets*. Multiscale Sim. Met. Mol. Science **42**, 271 (2009).
- [173] L. Szunyogh, B. Lazarovits, L. Udvardi, J. Jackson, and U. Nowak. *Giant magnetic anisotropy of the bulk antiferromagnets IrMn and IrMn₃ from first principles*. Phys. Rev. B **79**, 020403 (2009).
- [174] J. B. Staunton, S. Ostanin, S. S. A. Razee, B. L. Gyorffy, L. Szunyogh, B. Ginatempo, and E. Bruno. *Temperature dependent magnetic anisotropy in metallic magnets from an ab initio electronic structure theory: L1₀-ordered FePt*. Phys. Rev. Lett. **93**, 257204 (2004).
- [175] I. Dzyaloshinsky. *A thermodynamic theory of "weak" ferromagnetism of antiferromagnetics*. J. Phys. Chem. Solids **4**, 241 (1958).
- [176] T. Moriya. *Anisotropic superexchange interaction and weak ferromagnetism*. Phys. Rev. **120**, 91 (1960).

- [177] A. Crépieux and C. Lacroix. *Dzyaloshinsky-Moriya interactions induced by symmetry breaking at a surface*. J. Magn. Magn. Mat. **182**, 341 (1998).
- [178] A. Antal, B. Lazarovits, L. Balogh, L. Udvardi, and L. Szunyogh. *Multiscale studies of complex magnetism of nanostructures based on first principles*. Philosoph. Magazine **88**, 2715 (2008).
- [179] D.-S. Wang, R. Wu, and A. J. Freeman. *First-principles theory of surface magnetocrystalline anisotropy and the diatomic-pair model*. Phys. Rev. B **47**, 14932 (1993).
- [180] C. Kittel. *Theory of the structure of ferromagnetic domains in films and small particles*. Phys. Rev. **70**, 965 (1946).
- [181] R. Drautz and M. Fähnle. *Spin-cluster expansion: Parametrization of the general adiabatic magnetic energy surface with ab initio accuracy*. Phys. Rev. B **69**, 104404 (2004).
- [182] R. Drautz and M. Fähnle. *Parametrization of the magnetic energy at the atomic level*. Phys. Rev. B **72**, 212405 (2005).
- [183] M. Pajda, J. Kudrnovský, I. Turek, V. Drchal, and P. Bruno. *Ab initio calculations of exchange interactions, spin-wave stiffness constants, and Curie temperatures of Fe, Co, and Ni*. Phys. Rev. B **64**, 174402 (2001).
- [184] R. Skomski. *Nanomagnetics*. J. Phys.: Condens. Matter **15**(20), R841 (2003).
- [185] A. B. Shick and O. N. Mryasov. *Coulomb correlations and magnetic anisotropy in ordered L₁₀ CoPt and FePt alloys*. Phys. Rev. B **67**, 172407 (2003).

List of Publications of R. Yanes

- [1] R. Yanes, O. Chubykalo-Fesenko, H. Kachkachi, D. A. Garanin, R. Evans, and R. W. Chantrell *"Effective anisotropies and energy barriers of magnetic nanoparticles with Néel surface anisotropy"*, Phys. Rev. B, vol. **40**, page 2140, (2007).
- [2] M. Jaafar, R. Yanes ,A. Asenjo, O. Chubykalo-Fesenko, M. Vázquez, E.M. González y J. L. Vicent. *"Field induced vortex dynamics in magnetic Ni nanotriangles"*, Nanotechnology , vol. **19**, page 285717, (2008).
- [3] G.R. Aranda; O. Chubykalo-Fesenko; R. Yanes; J. González; J.J. del Val; R. W. Chantrell; Y. K. Takahashi and K. Huno. *"Coercive field and Energy Barriers in partially disordered FePt nanoparticle"*. J. Appl. Phys., vol. **105**, page 07B514, (2009).
- [4] R. Yanes and O. Chubykalo-Fesenko. *"Modelling of the influence of the Néel surface anisotropy on the enhancement of the magnetic anisotropy in Co nanoparticle"*. J. Phys. D: Appl. Phys, vol. **42**, page 055013, (2009).
- [5] R. Yanes , R. Rozada, F. Garcia-Sanchez, O. Chubykalo-Fesenko,P. M. Pimentel, B. Leven, B. Hillebrands. *"Modeling of microwave-assisted switching in micron-size magnetic ellipsoids"*. Phys. Rev. B, vol. **79**, page 224427, (2009).
- [6] R.F.L. Evans, R. Yanes, O. Mryasov, R.W. Chantrell and O. Chubykalo-Fesenko. *"On beating the superparamagnetic limit with exchange bias"*. EPL, vol. **88**, page 57004, (2009).
- [7] M. Jaafar, R. Yanes, D. Perez de Lara, O. Chubykalo-Fesenko, A. Asenjo, E.M. Gonzalez, J.V. Anguita, M. Vazquez and J.L. Vicent. *"Control of the chirality and polarity of magnetic vortices in triangular nanodots"*. Phys. Rev. B, vol. **81**, page 054439, (2010.)
- [8] P. Asselin, R.F.L. Evans, J. Barker, R.W. Chantrell, R. Yanes, O. Chubykalo-Fesenko, D. Hinzke and U. Nowak. *"Constrained Monte Carlo method and calculation of the temperature dependence of magnetic anisotropy"*. Phys. Rev. B, vol. **82**, page 054415, (2010).

- [9] R. Yanes, O. Chubykalo-Fesenko, R.F.L. Evans and R.W. Chantrell "*Temperature dependence of the effective anisotropies in magnetic nanoparticles with Néel surface anisotropy*". J. Phys. D: Appl. Phys, vol. **43**, page 474009, (2010).

Agradecimientos

Esta es la sección más gratificante de toda esta tesis, es en este punto donde puedo expresar mi agradecimiento a todas esas personas que me han ayudado a lo largo de estos años.

En primer lugar me gustaría darle las gracias a mi directora de tesis Oksana Fesenko por brindarme la posibilidad de entrar en este mundo, por sus valiosos consejos, por su confianza y en esta última fase por entender mi frustración en los malos momentos.

Me gustaría agradecer a mi tutor Dr. Farkhad Aliev por su disponibilidad.

Gracias a los Prof. Hamid Kachkachi, Prof. Roy W. Chantrell. y Prof. Laszlo Szunyogh por sus discusiones sobre física y por su calurosa acogida en mis estancias.

También me gustaría agradecer a Dr. J. Palomares, Dr. F. Cebollada, y Prof. J. González, su acogida en el grupo y su apoyo a lo largo de estos años.

Esta tesis no se podría haber llevado a cabo sin la ayuda inestimable de Juan Manuel Rodríguez Puerta (Juanma), por acudir con una sonrisa en mi ayuda cada vez que el cluster o MAGPAR me ponía contra las cuerdas, muchas gracias.

Gracias a Felipe becario senior a mi llegada al grupo ahora flamante post-doc por haberme facilitado la entrada en el mundo del magnetismo y por su ayuda con todos mis problemas de compilación.

Gracias a Silvia Gallego y M. Carmen Muñoz por su ayuda intentando que entendiera algo de los cálculos SKKR.

Gracias a Elvira (la mejor DJ) por su visión entusiasta de la vida.

Gracias a Unai por ser tan buen compañero, a pesar de sus chistes.

Gracias a Virginia por compartir este duro camino de la tesis, por convencerme para hacer el camino de Santiago y sobre todo por su amistad.

Gracias a Samuel, Rafa y Jesús mis compis del despacho 168 con ellos compartí grandes momentos, escuché muchas horas de Radio 3 y aprendí mucho.

Gracias a Rubén, Almudena, Laura, Yorexis, Ezzouhra, Javier compañeros temporales o permanentes del despacho 159, por conseguir que todos los días tengan una sonrisa.

Estos agradecimientos no estarían completos si no menciono a Javier Mendez, Jorge Iribas, Arturo Baró, Nacho Jiménez, María Moreno con los que he compartido muchas bromas y risas en la hora de la comida, gracias a todos por aceptar a esta becaria en su grupo y permitirme conocer a unas bellísimas personas.

Gracias a mis amigos del ICMM Aldo, Ramón, Karin, Lucía, Lidia, Mercedes, Karla, Miriam, Wagner, así como a los amigos que encontré en mis estancias Richard, Natalia, Attila, Eva por los gratos momentos.

Y cómo existe vida más allá del ICMM, gracias a Conchi por su amistad, por su apoyo continuo y sincero, y por escuchar todas mis charlas aunque creo que la aburrían, en definitiva por estar ahí. Gracias también a Mar, Manolo y Noemí por las cenas y las paellitas los domingos, me habéis hecho sentir en casa.

Por último no puedo dejar de agradecer a mi familia. Agradecer a esas personas que me han dado su afecto y su cariño desde que no levantaba un palmo del suelo, a mis padres Pedro y Josefa, por todo el amor que me han dado. Gracias a mis hermanos Natalia, Pedro y Jose por sus consejos, su cariño y su apoyo incondicional.